J/Ψ production in ultra-peripheral proton-lead and lead-lead collisions with CMS

By

Ayman Ahmad Al-bataineh

Submitted to the graduate degree program in Department of Physics and Astronomy and the Graduate Faculty of the University of Kansas in partial fulfillment of the requirements for the degree of Doctor of Philosophy.

Committee members

Murray, Michael J., Chairperson

Baringer, Philip S.

Fischer, Chris

Tapia Takaki, Daniel

Laird, Brian Bostian

Date defended: September 01, 2017

The Thesis Committee for Ayman Ahmad Al-bataineh certifies
that this is the approved version of the following thesis :

J/Ψ production in ultra-peripheral proton-lead and lead-lead collisions with CMS

Murray, Michael J., Chairperson

Date approved: December 05, 2017

Abstract

This thesis reports on photoproduction of exclusive J/ψ mesons in ultra-peripheral PbPb and pPb collisions at $\sqrt{s_{NN}} = 2.76$ TeV, and 5.02 TeV, respectively, from the CMS experiment at the LHC. For PbPb collisions, there is a correlation between the directions of the produced J/ψ and the neutron emitted by the struck nucleus. For J/ψ mesons with $p_T > 100$ MeV/c, the ratio of the p_T distributions for J/ψ is moving in the opposite direction as the neutrons emitted from the target nucleus to those for J/ψ is moving in the same direction as the neutrons, suggests significant shadowing in the lead nucleus.

For pPb collisions, the distributions of the J/ψs in transverse momentum have a similar form to previous measurements at HERA. The average p_T increases with the photon-proton center of mass energy W. This implies that the spatial distribution of the gluons within the proton depends upon the gluon momentum. The cross section also increases as W increases from 57 to 439 GeV implying that the proton become more and more opaque to photons as the photon energy increases. Parametrizing the growth of the cross section by the form $\sigma(W) \propto W^{\delta}$ yields a value of $\delta = 0.636 \pm 0.063$. This result is consistent with the world average and has a precision comparable to other experiments.

Acknowledgements

I want to thank my supervisor Michael Murray for his support, guidance and patience. He was like a father and big brother to me in this long and difficult journey to get this degree. Thanks also to Stephen J. Sanders, Royon Christophe, Daniel Takaki for their ideas and advice. Many thanks to my friends in the nuclear group at the University of Kansas and also CMS for their help, and the beautiful time we spent together in this long trip. Thanks to the faculty, staff and graduate students in the Department of Physics and Astronomy for giving me this chance to complete my PhD. Thanks to all my friends at the University of Kansas and in Lawrence for their help and for spending fun times together. Last but not least, I want to thank my father, my mother, my sisters, my brothers, my wife and my children for their support and their encouragement.

Contents

List of Figures

List of Tables

Chapter 1

Introduction

About 14 billion years ago, the universe was created in an event called the Big Bang. It is currently believed that after a period of rapid inflation and then reheating the gravitational, electro-weak and strong forces that we know today were operating but the universe was too hot for nucleons to exist. At first it is thought the universe would have been a electro-weak plasma and that quarks were formed from the decays of the vector bosons. This was the status after about 10^{-12} seconds. From this time until $\approx 3 \cdot 10^{-6}$ seconds the universe was in a hot and dense state, where the quarks and gluons were free and left- and right-handed quarks behaved symmetrically. This state is called the quark gluon plasma (QGP). As the universe expanded and cooled the quarks and gluons eventually became confined into nucleons and the chiral symmetry between left- and right-handed quarks was broken. Later the nucleons formed the hydrogen and helium from which our universe was built. This sequence is shown in Figure 1.1.

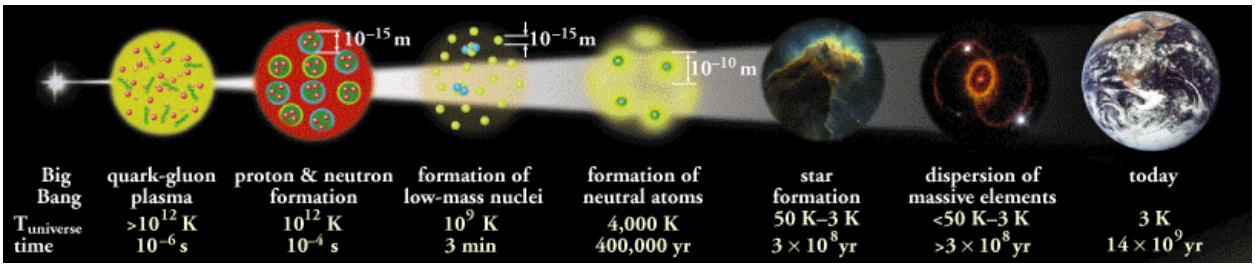

Figure 1.1: Development and expansion of the universe from the Big Bang to the present day [1].

1.1 Large Hadron Collider (LHC)

The Large Hadron Collider (LHC) is the most powerful particle accelerator in the world. It is a 27 km ring of superconducting magnets and accelerating radio frequency cavities that sits in an underground tunnel, at a mean depth of 100 meters below the surface near Geneva. There are four main detectors in the LHC: A Large Ion Collider Experiment (ALICE), A Toroidal LHC Apparatus (ATLAS), the Compact Muon Solenoid (CMS) and Large Hadron Collider beauty (LHCb). ALICE, ATLAS, CMS, and LHCb are installed in four huge underground caverns, at the four collision points of the beams as shown in Figure 1.2. The LHC has two beams of particles that travel in opposite directions in separate circular beam pipes. The particles are boosted to be close to the speed of light and focused by superconducting quadrupoles to increase the luminosity and the probability of the collisions between the particles at the interaction points.

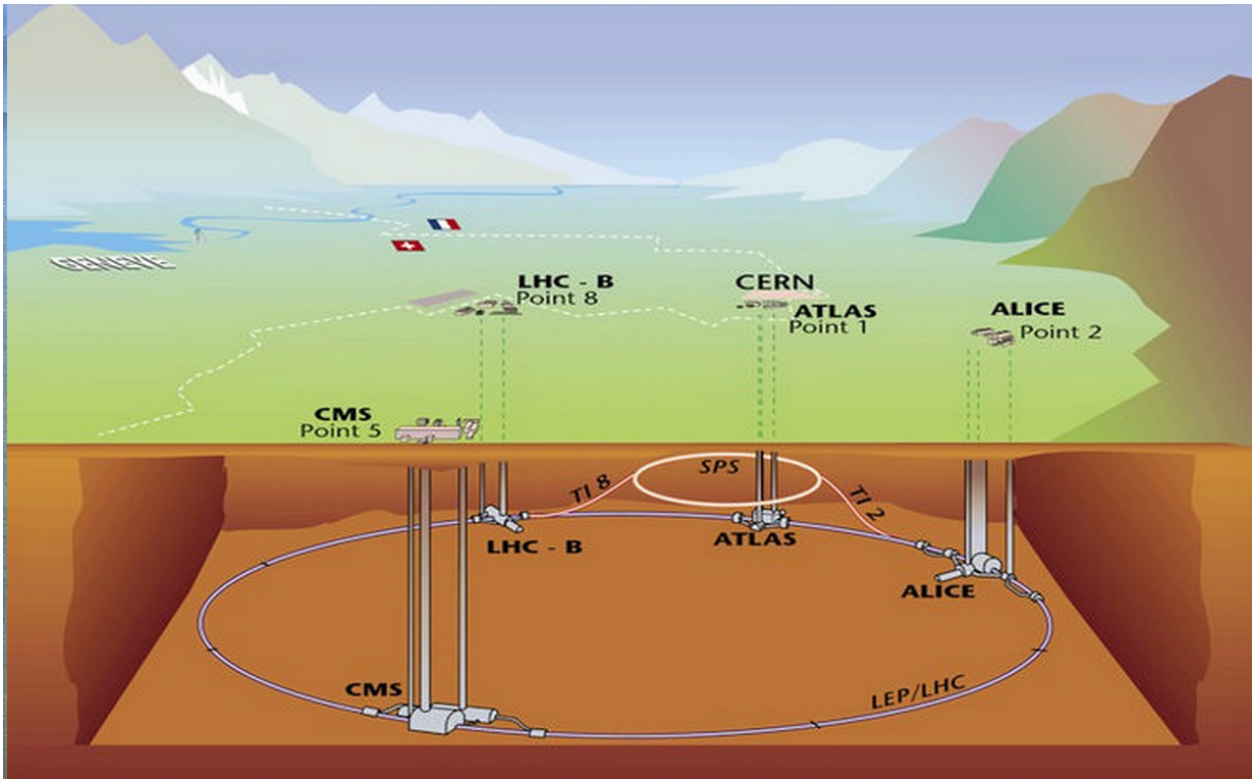

Figure 1.2: layout of the LHC ring and the four main experiments [2].

The LHC is able to make a small version of the quark gluon plasma by accelerating and colliding two beams of nuclei at very high energies. The life time and volume of this state are very

small, since it quickly decays into hadrons and other particles. The detector's role is to observe the production of these particles and so deduce the properties of the QGP. This process is shown in Figure 1.3.

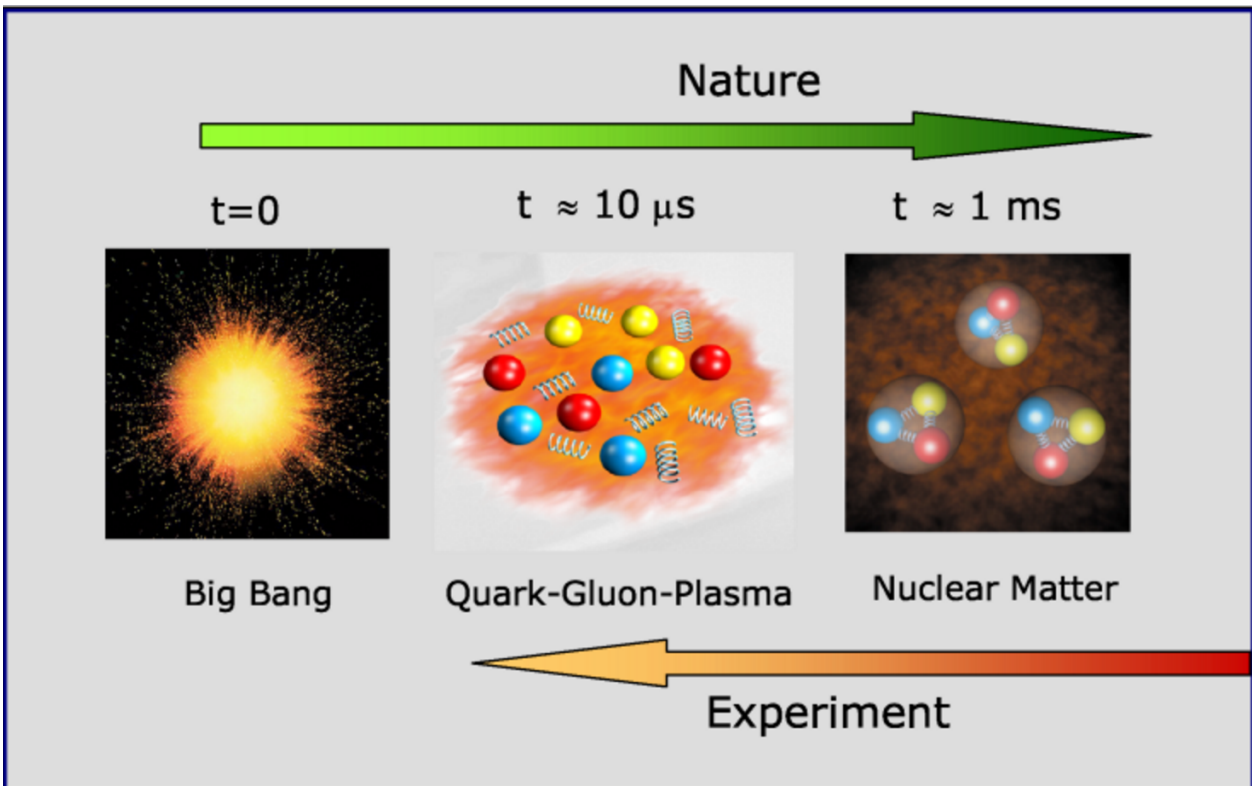

Figure 1.3: The expansion of the universe and the experiment's role to study the early era of the universe [3].

1.2 Kinematic Variables

Galileo developed a set of transformations to describe the coordinates of a system $K^{'}$ that is moving with velocity v along the z axis of system K.

$$x^{'} = x \tag{1.1}$$

$$y^{'} = y \tag{1.2}$$

$$z^{'} = (z - vt) \tag{1.3}$$

$$t^{'} = t \tag{1.4}$$

These transformations work well at low speeds but was contradicted by the experiments of Michelson and Morley that found the speed of light to be constant in all reference frames. The Lorentz transformations were designed to keep the speed of light constant in all frames of reference. They are

$$x^{'} = x \tag{1.5}$$

$$y^{'} = y \tag{1.6}$$

$$z^{'} = \gamma(z - vt^{'}) \tag{1.7}$$

$$ct^{'} = \gamma(ct - \beta x) \tag{1.8}$$

where $\beta = \frac{v}{c}$ and $\gamma = \frac{1}{\sqrt{1-\beta^2}}$. In order to present experimental results in a meaningful way it is important to describe them in terms of Lorentz invariant quantities.

Velocity is not invariant under Lorentz transformations and so it is important to find a measure of velocity that is. The rapidity is a logarithmic measure of direction and velocity. The rapidity in terms of E and p_z is written as:

$$y = \frac{1}{2}\ln(\frac{E + p_z c}{E - p_z c}) \tag{1.9}$$

The rapidity is zero when a particle is close to transverse to the beam axis, but tends to $\pm\infty$ when a particle is moving close to the beam axis in either direction. It is related to the angle between the XY plane and the direction of emission of a product of the collision. The rapidity of the particle can be written in terms of its velocity, if we define its direction of motion to be along the z axis. Then

$$y = \tanh^{-1}(\frac{v}{c}) = \frac{1}{2}(\frac{1+v/c}{1-v/c}) \tag{1.10}$$

Rapidity itself is not Lorentz invariant but differences in rapidity are Lorentz invariant.

For particles with $pc >> mc^2$ the rapidity can be approximated by the pseudorapidity η

$$\eta = \frac{1}{2}\ln(\frac{p+p_z}{p-p_z}) \tag{1.11}$$

$$= \frac{1}{2}\ln(\frac{p+p\cos(\theta)}{p-p\cos(\theta)}) \tag{1.12}$$

$$= -\ln(\tan(\frac{\theta}{2})). \tag{1.13}$$

where θ is the scattering angle of a particle with respect to the beam line. Since η depends only upon the polar angle of the particle it is easier to measure experimentally than the rapidity. From Equation 1.13 it is clear that $\eta = 0$ at $\theta = 90^\circ$, and $\eta = \infty$ at $\theta = 0^\circ$.

The transverse momentum of a particle p_T, is that component of the momentum perpendicular to the beam axis. It is defined by

$$p_T = \sqrt{p_x^2 + p_y^2} \tag{1.14}$$

Since p_x and p_y are Lorentz invariant under transformations along the z axis, p_T is also Lorentz invariant. A related quantity is the transverse mass which is defined by

$$m_T^2 c^4 = p_T^2 c^2 + m^2 c^4 \tag{1.15}$$

The total energy and longitudinal momentum along the beam line p_L can then be written as:

$$E = m_T c^2 \cosh y \tag{1.16}$$

$$p_z c = \sqrt{E^2 - m_T^2 c^4} = m_T c^2 \sinh y \tag{1.17}$$

For any $2 \rightarrow 2$ collision process where particle 1 collides with particle 2 producing particle 3 and particle 4 there are three Lorentz invariant Mandelstam variables defined by

$$s = (E_1 + E_2)^2 - c^2(\overrightarrow{p_1} + \overrightarrow{p_2})^2 \tag{1.18}$$

$$t = (E_1 - E_3)^2 - c^2(\overrightarrow{p_1} - \overrightarrow{p_3})^2 \tag{1.19}$$

$$u = (E_1 - E_4)^2 - c^2(\overrightarrow{p_1} - \overrightarrow{p_4})^2 \tag{1.20}$$

where s, t, and u are Lorentz invariant, and related to each other by the equation

$$s + t + u = m_1^2 + m_2^2 + m_3^2 + m_4^2 \tag{1.21}$$

In the center of mass system $\overrightarrow{p_1} + \overrightarrow{p_2} = 0$ and so s can be written as:

$$s = (E_1 + E_2)^2. \tag{1.22}$$

Thus $\sqrt{s}$ is the center of mass energy for the collision between two particles.

1.3 Quantum Chromodynamics

Quantum chromodynamics, QCD, is a gauge theory of the strong interaction. It is similar to quantum electrodynamics (QED) which describes the force between electrically charged particles by the exchange of photons. The quarks inside protons carry both electric and “color" charge. QCD describes the force between colored quarks and anti-quarks by the exchange of gluons which are themselves colored. This makes QCD a much richer and more complex theory than QED [57].

Quarks and anti-quarks are fundamental constituents of matter. Quarks have various intrinsic properties such as electric charge, color charge, spin, and mass. The color charge for quarks can have three different values known as red, green, and blue. The gluons are the mediators of the strong interaction. Gluons in QCD do the same job as photons in QED, but the differences between the photon and the gluon are that the gluon interacts with itself and that there are eight types of gluons as opposed to only one kind of photon. Figure 1.4 shows the standard model of the quarks, mediators (Gauge bosons), and leptons.

The strengths of the electric and strong forces are given by the coupling constants α_e and α_s respectively. Since $\alpha_e \sim \frac{1}{137} << 1$, perturbation theory can be used to make calculations in QED for all ranges of energy. In QCD, at low energy perturbation theory can not be used, because $\alpha_s \sim 1$, so the QCD calculations are difficult. At high energy the force weakens and perturbation theory can be used. This effect is known as the running of the QCD coupling constant and is shown quantitatively in Figure 1.5. This running of the coupling constant implies that quarks are confined within hadrons at low energies but become asymptotically free at high energy. The data shown in Figure 1.5 are consistent with a coupling that is proportional to $\frac{1}{\ln Q/\Lambda_{QCD}}$. The parameter Λ_{QCD} sets the scale of confinement in QCD and has a value of about 217 MeV.

Asymptotic freedom means that at small distances (high energy) the interaction between quarks is weak, so the quarks move almost freely inside the hadrons. On the other hand, color confinement means that at large distances (low energy) the interaction between quarks is strong. This forces the quarks to combine to form neutral color particles such as mesons and baryons and is the reason that no free quarks have been observed despite many searches [58]. All hadrons are color neutral combinations of quarks. Mesons (pion, J/ψ, etc) are combinations of quarks and antiquarks with a given color/anti-color to make the neutral color charge. Baryons (protons, neutrons, etc) are composed of three quarks, each of which has a different color (red, green, blue, ...) to form a color neutral state. For example a red c quark and anti-red $\bar{c}$ quark could form a J/ψ while a green u quark, blue u quark and red d quark could form a proton. Recently there has even been evidence for pentaquarks states [59]. Experimentally no isolated quarks have been observed in nature [58].

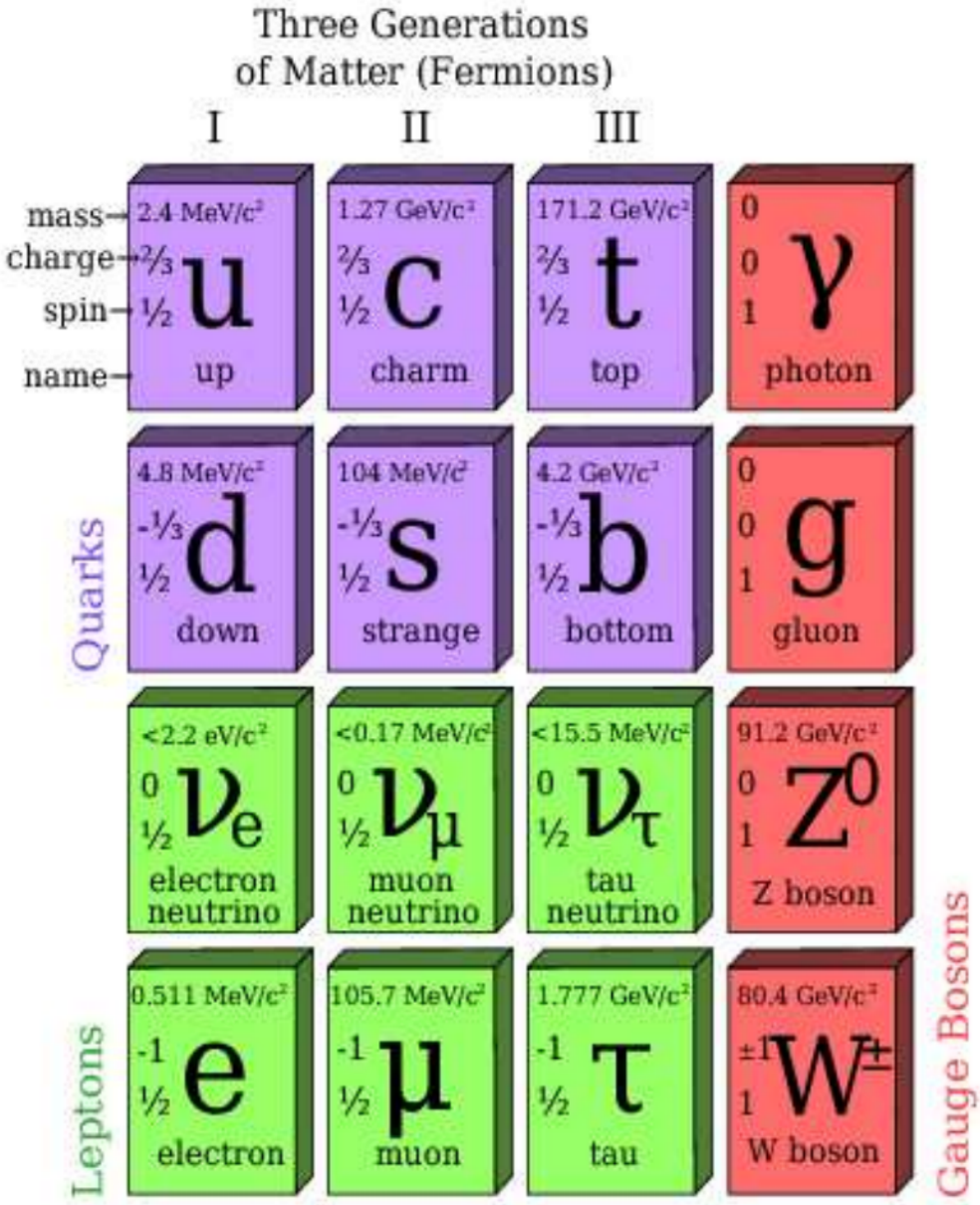

Figure 1.4: Three generation of matter particles in the standard model, and the mediator particles (Gauge bosons) [4]

If the distance between two quarks is increased, the interaction between them will be stronger and stronger until the stored energy is sufficient to create a new $q\bar{q}$ pair. The aim of relativistic heavy ion experiments is to produce a very hot and dense medium where quarks and gluons may move freely over an extended volume.

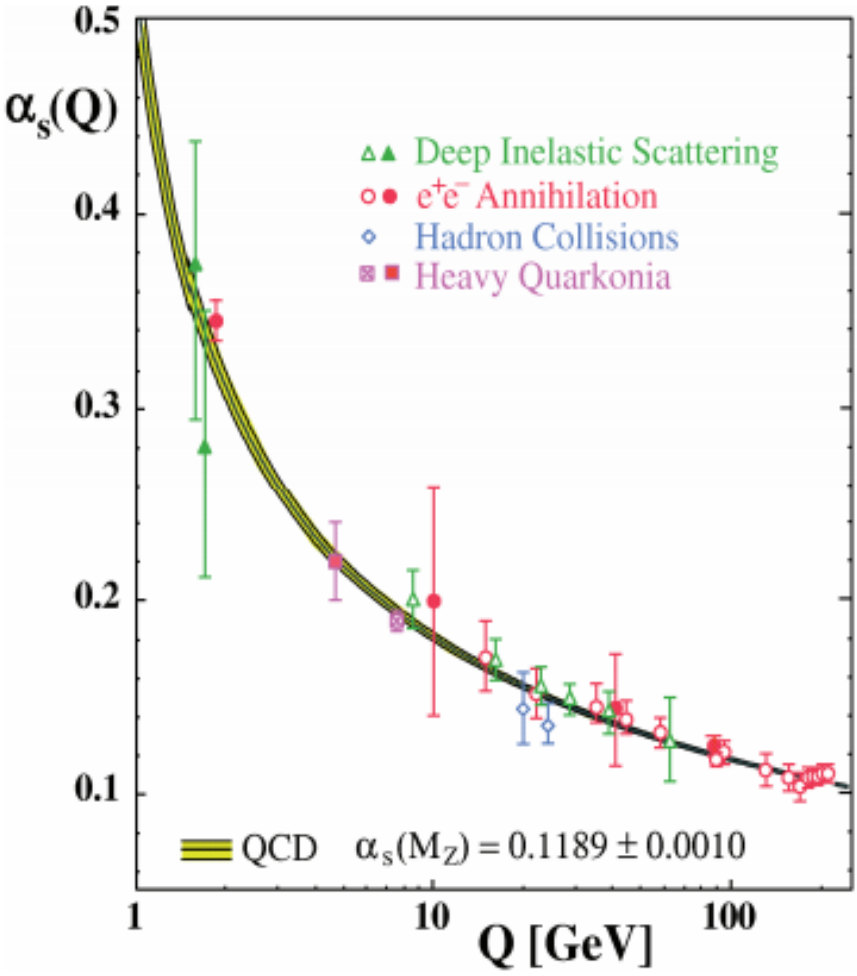

Figure 1.5: The coupling constant $\alpha_s(Q)$ versus energy scale Q. The curve that slopes downwards is a prediction of QCD. The curve agrees with the measurements [5]

1.4 Relativistic heavy ion collisions

Figure 1.6 shows a timeline of a head-on collision of two relativistic heavy ions. The ions in the LHC are moving at about 99.99998% of the speed of light and appear as flat disks in the laboratory frame because of the very strong Lorentz contraction along the z axis. This initial state of the system serves as a boundary condition for the subsequent evolution of the system and is actually the main topic of this thesis. In this state, time dilation effects are very strong since $\gamma \approx 1700$ and the quarks and gluons are essentially frozen in a particular configuration. Such an individual

configuration may be very different from the smooth average wave function of the nucleus. It has been suggested that the soft gluons in such a nucleus may overlap to form a saturated glass-like state known as the Color Glass Condensate (CGC). Right after impact the system is in a prequilibrium state where many hard scatterings are occurring. The system quickly approaches a thermal equilibrium and starts to behave like an almost perfect fluid of deconfined quark matter. The system then rapidly expands and cools until the quark matter finally freezes out into hadrons, photons and leptons that can be detected by experiments.

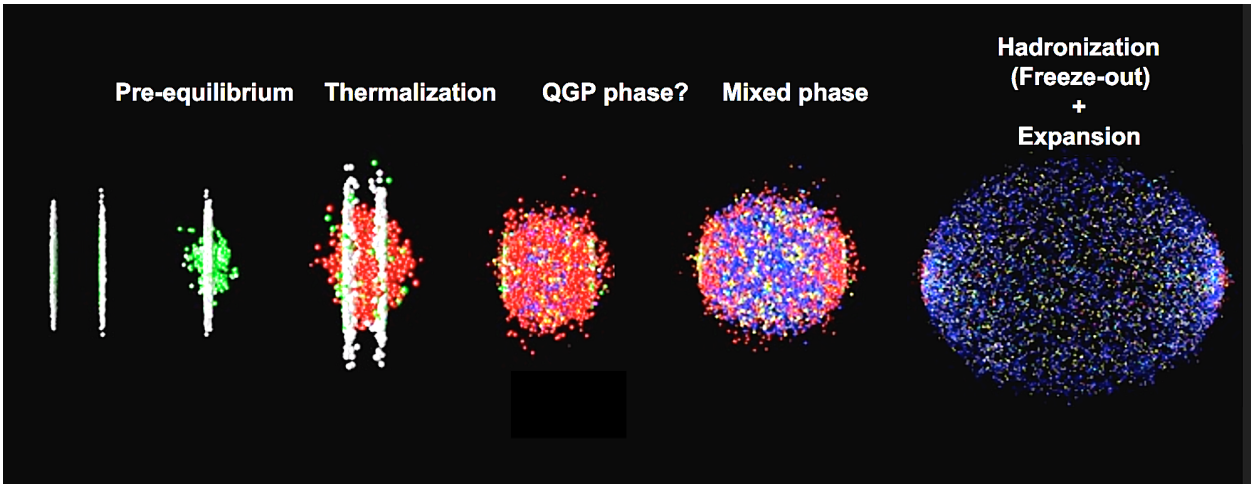

Figure 1.6: Stages of a Relativistic Heavy Ion Collision [6]

1.5 Quark Gluon Plasma stage

There are many experimental signatures of the Quark Gluon Plasma (QGP), such as the quarkonia suppression (a color screening of deconfined quarks and gluons in short range around the quark and around the anti-quark making the binding between them weak), jets quenching (high transverse momentum p_T partons that propagate through the medium (QGP) and lose energy), and the azimuthal asymmetries.

1.5.1 Quarkonia suppression (dissociation)

In 1986 Matsui and Satz predicted that the yield of $c\bar{c}$ mesons would be suppressed in relativistic heavy ion collisions due to the Debye screening of the attractive force between the charmed quarks by deconfined light quarks [60]. Such a suppression of the J/ψ was reported by the NA38 collaboration. Since then several experiments have measured the suppression of both charm and beauty mesons. Although other effects can also reduce the yield of such mesons there is very strong evidence of Debye screening at both RHIC and LHC energies [61].

One way to quantify this suppression is to take the ratio of the yield of a given particle (jets, hadrons, quarkonia) in heavy ion collisions with that expected by scaling up the yield from proton proton collisions at the same beam energy per nucleon. The nuclear modification factor R_{AA} is defined as

$$R_{AA}(y, p_T) = \frac{1}{< N_{coll} >} \frac{N_{AA}(y, p_T)}{N_{pp}(y, p_T)}, \tag{1.23}$$

where $N_{AA}(y, p_T)$ and $N_{pp}(y, p_T)$ are the Lorentz invariant yields in AA and pp collisions respectively in a given rapidity y and transverse momentum p_T interval and $< N_{coll} >$ is the average number at binary nucleon-nucleon collisions in heavy ion collisions. R_{AA} measures the modification of particle yields in the nuclear medium. R_{cp} is used for the same purpose but is the ratio of particle production in central collisions compared to scaled peripheral heavy ion collisions.

Figure 1.7 shows R_{AA} for J/ψ versus N_{part} (left), where N_{part} is interaction volume that the nucleons are participating in the collision, and p_T (right) at two different beam energies. The J/ψ yield is suppressed at both $\sqrt{s_{NN}} = 0.2$ TeV and $\sqrt{s_{NN}} = 2.76$ TeV. The suppression is stronger for more central collisions, higher N_{part}, and at higher p_T. Figure 1.8 shows R_{AA} for the Upsilon family at $\sqrt{s_{NN}} = 2.76$ TeV. As N_{part} increases the suppression becomes more pronounced. As expected from models of Debye screening $R_{AA}^{\Upsilon(1S)} > R_{AA}^{\Upsilon(2S)} > R_{AA}^{\Upsilon(3S)}$ since the binding energy of the $\Upsilon(1S)$ is greater than that of $\Upsilon(2S)$ which in turn is more strongly bound than the $\Upsilon(3S)$.

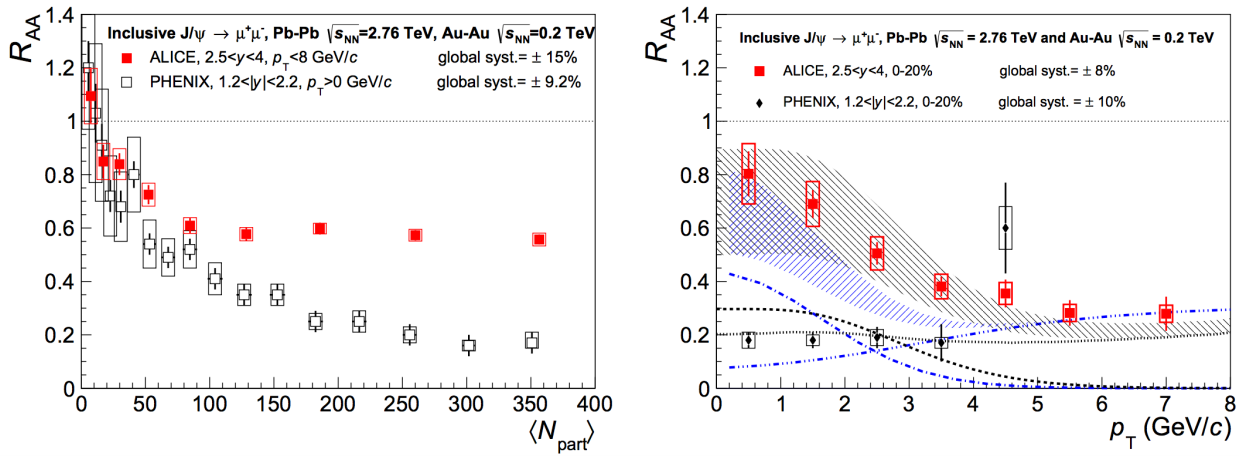

Figure 1.7: R_{AA} for inclusive J/ψ measured in PbPb collisions $\sqrt{s_{NN}} = 2.76$ TeV and forward rapidity by ALICE [7] and in AuAu collisions at $\sqrt{s_{NN}} = 0.2$ TeV and central rapidity by PHENIX. The left panel shows the N_{part} dependence and the right panel the p_T-dependence of R_{AA}.

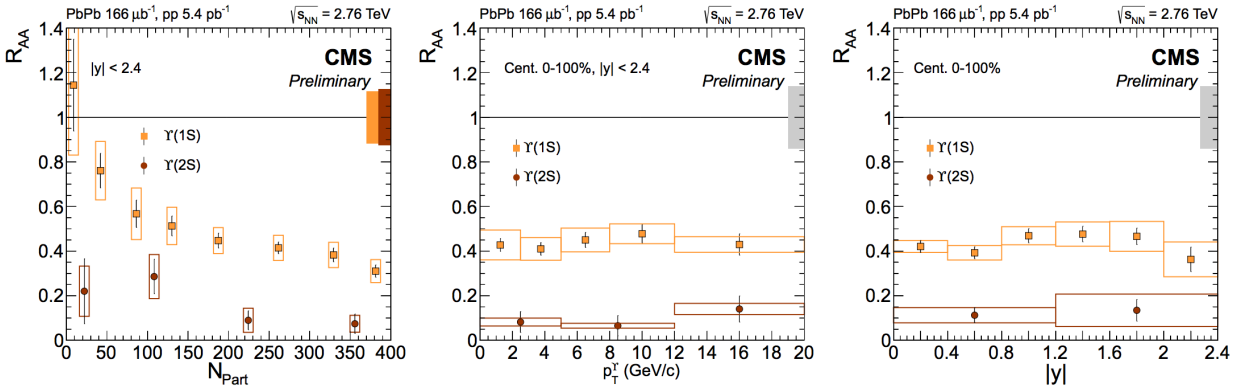

Figure 1.8: R_{AA} for $\Upsilon(1S)$ and $\Upsilon(2S)$ measured by CMS at $y < 2.4$ versus N_{part} (Left) increasing with centrality, p_T (Center) and rapidity (Right) [8] . The R_{AA} for $\Upsilon(3S)$ is consistent with zero.

1.5.2 Azimuthal asymmetries

In non-central heavy-ion collisions, the initial shape of the created fireball has a geometrical anisotropy which induces different pressure gradients in the medium and a collective flow of the matter. As a consequence, an anisotropy of the azimuthal distributions of the produced particles arises. The coefficients of a Fourier expansion of such distributions [62] can be used to characterize the observed asymmetry. The azimuthal distribution of produced particles can be represented

as a Fourier series

$$\frac{d^3N}{dp_T dy d\phi'} \propto (1 + 2v_1\cos(\phi') + 2v_2\cos(2\phi')...) \tag{1.24}$$

where $\phi' = \phi - \Psi_R$ is the particle's azimuthal angle, where Ψ_R is the reaction plane angle that points along the direction of impact parameter. In this equation v_1 is known as direct flow, v_2 elliptic flow, and v_3 triangular flow, etc. The coefficients of this expansion in Equation 1.24, i.e. the v_n, are strongly related to the pressure gradients, equation of state of the medium and on the geometric fluctuations of the initial state.

The observation of large v_2 values at low p_T is in good agreement with ideal hydrodynamic calculations (i.e. zero viscosity) in semi-central and central heavy ion collisions and strongly suggests that the matter produced in heavy ion collisions behaves as an ideal liquid [61]. Figure 1.9 shows v_2 versus p_T and centrality for PbPb collisions at $\sqrt{s_{NN}} = 2.76$ TeV. The fast rise of v_2 with p_T at low p_T is understood in terms of ideal hydrodynamics. The slow fall of v_2 at high p_T is thought to be due to jet quenching, see Section 1.5.3 below.

The integral of $v_2(p_T)$ over p_T depends upon the "stiffness" of the fluid produced. This is expected to depend upon the temperature of the matter produced in heavy ion collisions. Figure 1.10 shows the energy dependence of integrated v_2. Positive values mean that the matter feels a repulsion while negative values indicate an attraction. At very low energies the matter is repelled by the Coulomb force. At intermediate energies the matter experiences an attraction. It is thought that this is due to the attraction between baryons. At high energies the matter is hot enough to become a quark liquid and so the matter feels a repulsion due to the pressure in the liquid.

1.5.3 High p_T suppression and jet quenching

One of the most important measurements at RHIC was the suppression of high p_T particles and the disappearance of back-to-back correlations [63]. These results showed that the medium produced in nucleus-nucleus collisions was very dense and made up of colored partons. In such a medium

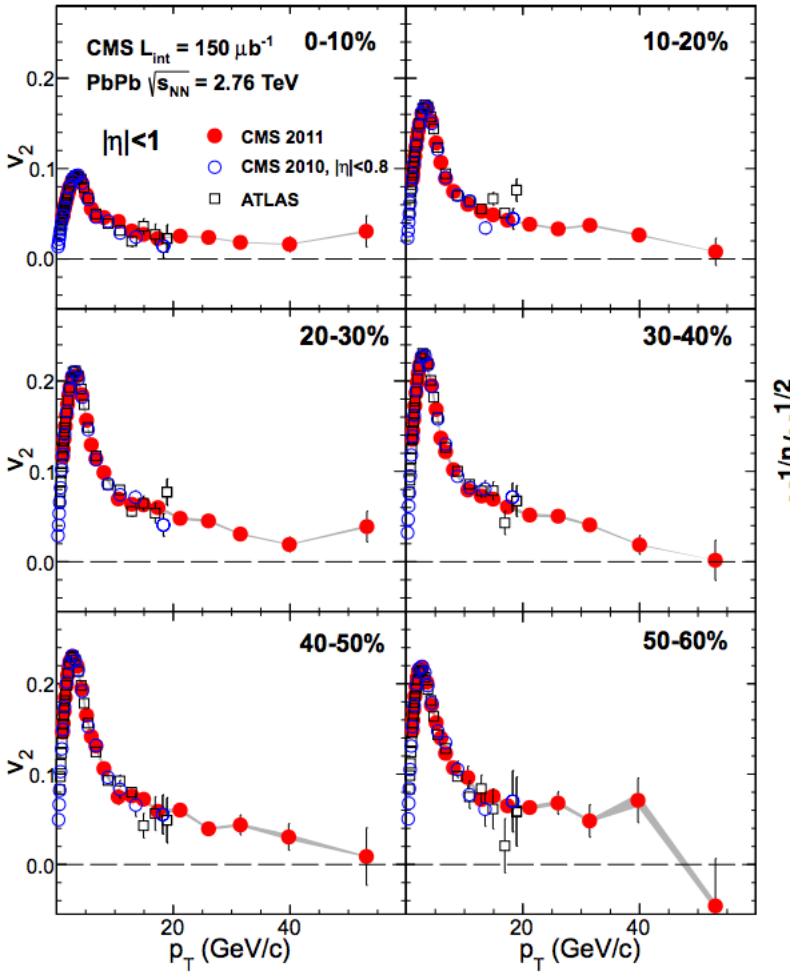

Figure 1.9: The elliptic flow parameter v_2 versus p_T and centrality in PbPb collisions at $\sqrt{s_{NN}} = 2.76$ TeV, measured by CMS [9]. Error bars denote the statistical uncertainties, while the grey bands correspond to the small systematic uncertainties. The centrality is shown in the top right of each panel. Results from ATLAS are also shown.

high momentum quarks may lose energy by gluon exchange with the many lower momentum quarks and gluons in the medium. At the LHC, analogous results to RHIC have been found for the nuclear modification factor and for the suppression of back-to-back correlations [61]. Figure 1.11 shows the nuclear modification factor R_{AA} for charged particles versus p_T and N_{part}. For $p_T < 2.5$ GeV the suppression is dominated by flow but at higher p_T values quark energy loss becomes important.

Jets are sprays of hadrons and the closest objects to partons that can be properly defined in QCD. The study of jet modification inside a colored medium is a sensitive proof of the mechanisms

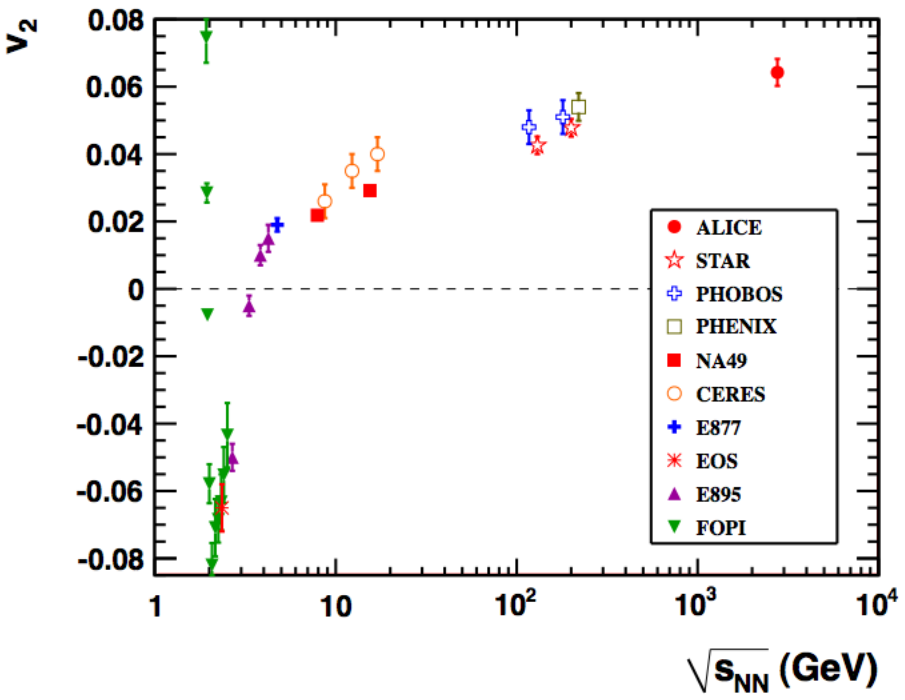

Figure 1.10: The ALICE result on p_T-integrated elliptic flow for PbPb collisions at $\sqrt{s_{NN}} = 2.76$ TeV in the 20% to 30% centrality class [10] compared with results from lower energies taken at similar centralities [11].

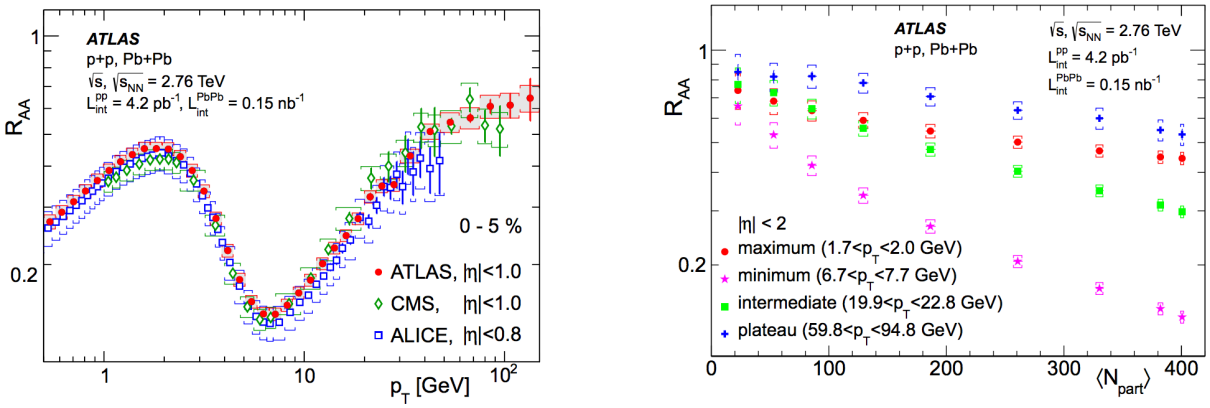

Figure 1.11: The nuclear modification factor R_{AA} for charged particles measured by ATLAS [12] and compared to CMS [13] and ALICE results [14]. The left panel shows the p_T dependence and the right panel the dependence on N_{part}.

of energy loss, of the interaction strength with the medium and of its density [61]. Figure 1.12 shows the nuclear modification factor of central collisions compared to peripheral ones R_{cp}, for charged jets, fully reconstructed jets and charged hadrons for PbPb collisions at $\sqrt{s_{NN}} = 2.76$ TeV.

High p_T particles or jets from central collisions are significantly suppressed relative to peripheral ones over a very wide range of momentum. This is consistent with central collisions producing a hotter and denser medium than peripheral ones which causes high momentum quarks from central collisions to lose more energy than in peripheral ones.

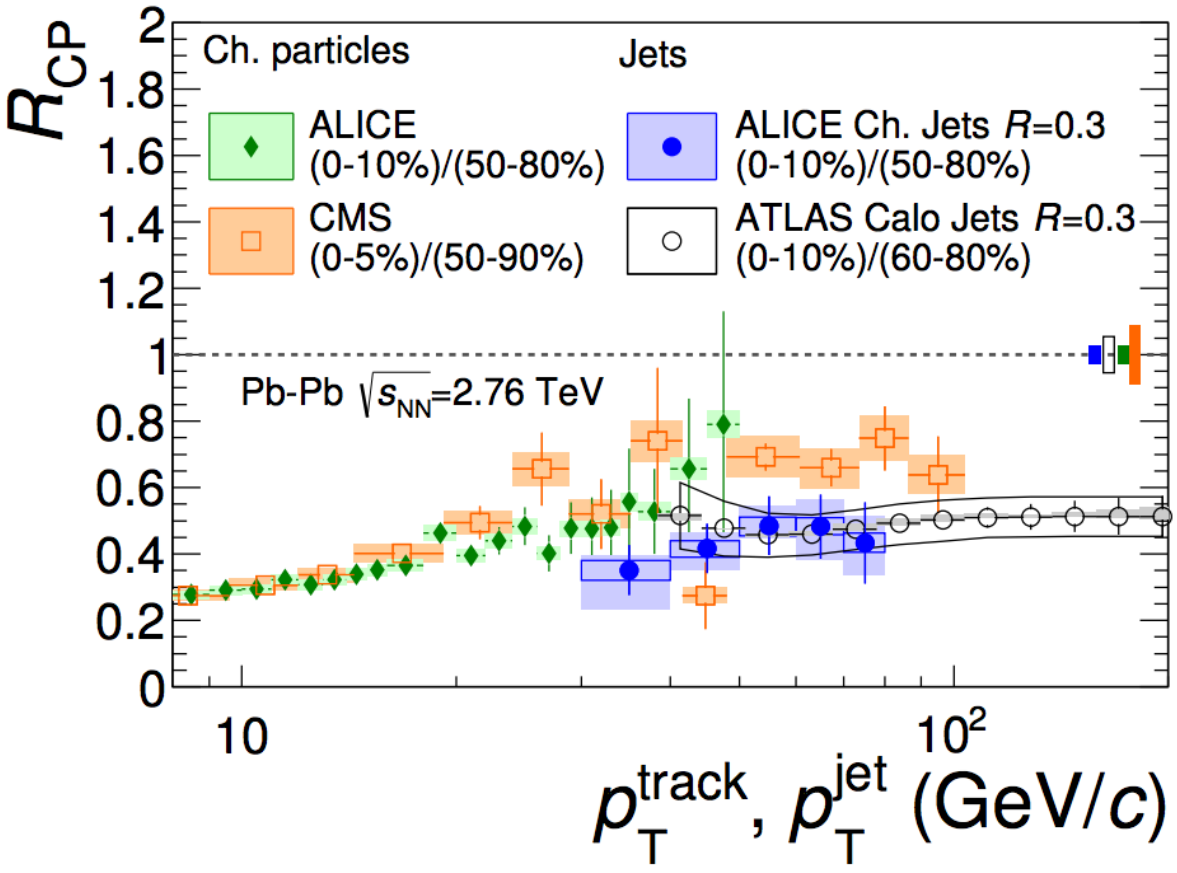

Figure 1.12: Nuclear modification factor of central collisions compared to peripheral ones R_{cp}, for charged jets, fully reconstructed jets and charged hadrons, versus the p_T of the jet or hadron [15].

1.5.4 Heavy flavor suppression

Heavy quarks are an important probe of the medium created in nuclear collisions. Because their mass is much larger than the temperature of the system, they are not created or destroyed in the medium, but rather produced by hard scattering in the early stage of the collision process. Therefore, they are particularly sensitive to the QGP phase. For p_T smaller than their mass the heavy

quarks are expected to have a significantly different pattern of energy loss than the light quarks. This means that the study of R_{AA} and v_2 can give new information on the degree of thermalization of the medium and the mechanism of energy loss [61]. Figure 1.13 shows R_{AA} of D-mesons and charged pions versus N_{part} measured by ALICE in PbPb collisions at $\sqrt{s_{NN}} = 2.76$ TeV [16]. For both particles the suppression increases with N_{part}. Within the current statistics the suppression the charmed D mesons is consistent with that of pions. Further studies using mesons containing b quarks are in progress. Figure 1.14 shows v_2 and R_{AA} versus p_T for D-mesons from PbPb collisions at $\sqrt{s_{NN}} = 2.76$ TeV [8]. The data are compared to a variety of models that handle quark energy loss in different ways. The combined v_2 and R_{AA} data are a very strong constraint for the models.

1.6 Initial state: Parton Distribution Function

The first evidence for quarks as real objects inside the proton came from electron-proton experiments at SLAC in the early 1970s [64]. In 1979 the gluon was discovered by the production of 3 jet events at the e^+e^- collider PETRA [65]. The term parton is used to mean either a quark, antiquark or a gluon. The quarks which give particles their quantum numbers are known as valance quarks while the quark-antiquark pairs that do not contribute to the quantum numbers are known as sea quarks.

Parton distribution function (PDF) is the parton distribution or density inside the proton or the nucleus. Partons are characterized by their transverse size and their momentum. The transverse size is proportional to $\frac{\bar{h}^2}{Q^2}$ where $\bar{h}$ is Planck's constant and Q^2 is the momentum transferred to the scattered electron. Bjorken-x is the fraction of the proton's longitudinal momentum carried by a single parton. It is defined as

$$x = \frac{p_z^i}{p_{hadron}} \tag{1.25}$$

where p_z^i is the longitudinal momentum carried by parton i. If $g(x)$ is the number of partons with

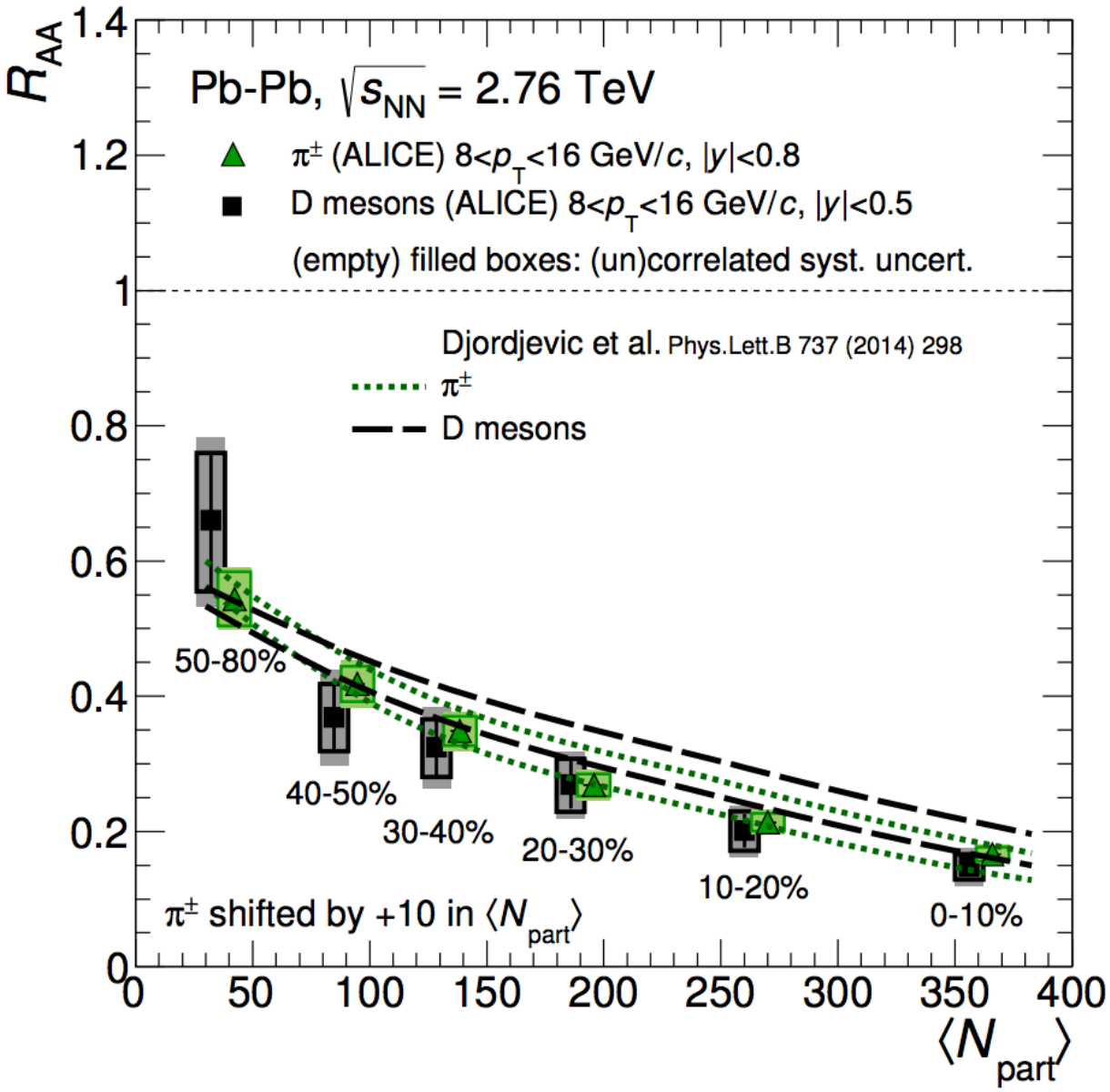

Figure 1.13: R_{AA} of D-mesons and charged pions measured by ALICE in PbPb collisions at $\sqrt{s_{NN}} = 2.76$ TeV[16]

momentum fraction between x and $x+dx$ the Parton Distribution Function or PDF is defined as

$$PDF(x,Q^2) = x \cdot g(x,Q^2) \tag{1.26}$$

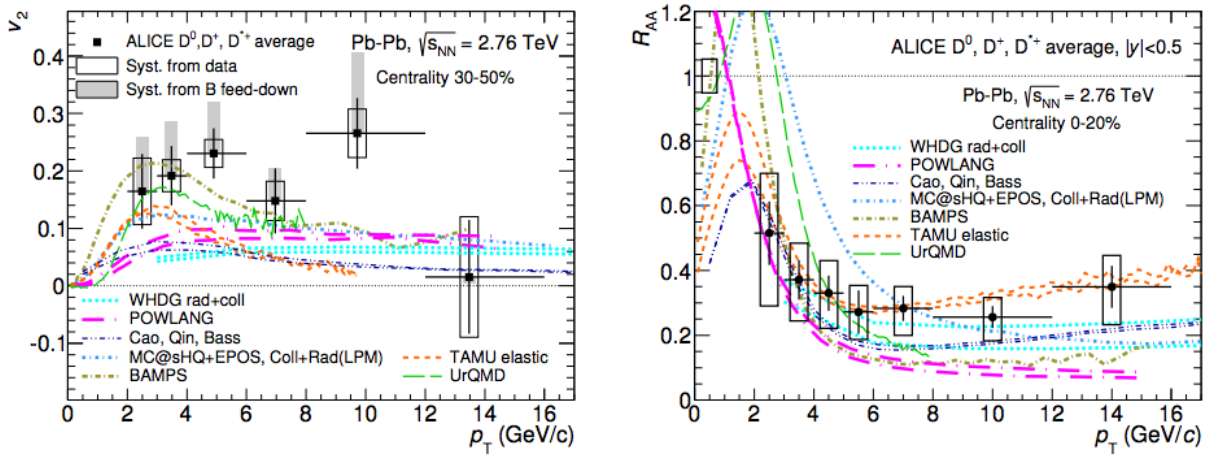

Figure 1.14: Left: the average D-meson v_2 in the 30- 50% centrality class, measured by ALICE[8]. Right: the average D-meson R_{AA} on the 0-20% centrality class, measured by ALICE [8]. Both results refer to PbPb collisions at $\sqrt{s_{NN}} = 2.76$ TeV, and are compared to theoretical models

1.6.1 Proton parton distribution function

The best data on the distribution of partons inside the proton come from deep inelastic scattering experiments (DIS) at the HERA collider. By measuring the momenta of the scattered electron and the other particles produced in the event it is possible to calculate the momentum of the object that the electron hit. These experiments have shown that at very high energy the proton contains many quarks, anti-quarks and gluons.

Figure 1.15 shows the distribution of the gluon, sea quark, and valence quark distributions versus x for $Q^2 = 10$ GeV^2, as measured at HERA (combined H1 and ZEUS analysis [17]). The gluons dominate below $x = 0.01$. As Bjorken-x decreases there is a rapid increase in the density of sea quarks and gluons. This means that at very high energies the proton wave-function is dominated by gluons.

Figure 1.16 shows the parton density for three different resolution scales $Q^2 = 5$ GeV^2, $Q^2 = 20$ GeV^2, and $Q^2 = 200$ GeV^2 [18]. At high x the distributions are independent of Q^2. As x decreases the parton density increases rapidly and this increase is stronger at higher Q^2. Figure 1.17 shows a schematic description of the parton distribution data at various x and Q^2 values shown in Figure 1.16. If the parton distribution at a given x and Q^2 is known, the Balitsky-Fadin-

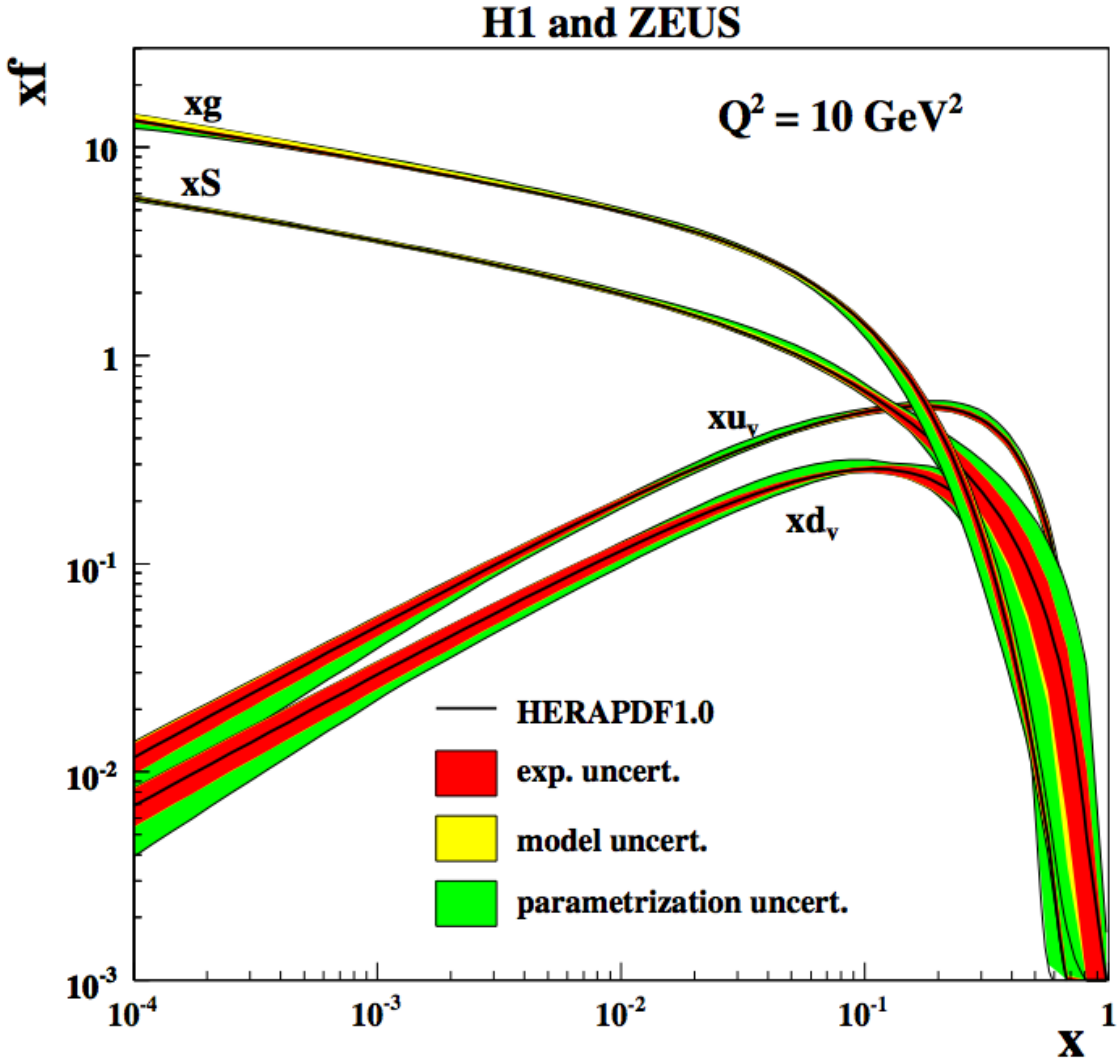

Figure 1.15: Proton parton density versus x. By decreasing x, there is evolution of the gluon, sea quark, and valence quark distributions for $Q^2 = 10GeV^2$, as measured at HERA (combined H1 and ZEUS analysis [17]).

Kuraev-Lipatov (BFKL) theory can be used to calculate (or evolve) the parton density at the same resolution scale Q^2 but different x (x, becomes smaller, the number of partons increases, but their size stays the same) [66].

On the other hand the Dokshitzer-Gribov-Lipatov-Altarelli-Parisi (DGLAP) theory describes the evolution of the parton numbers with Q^2 at a specific x (the number of partons rises but their size decreases) [66]. Both of these models have been inspired by HERA data. For a given Q^2 the

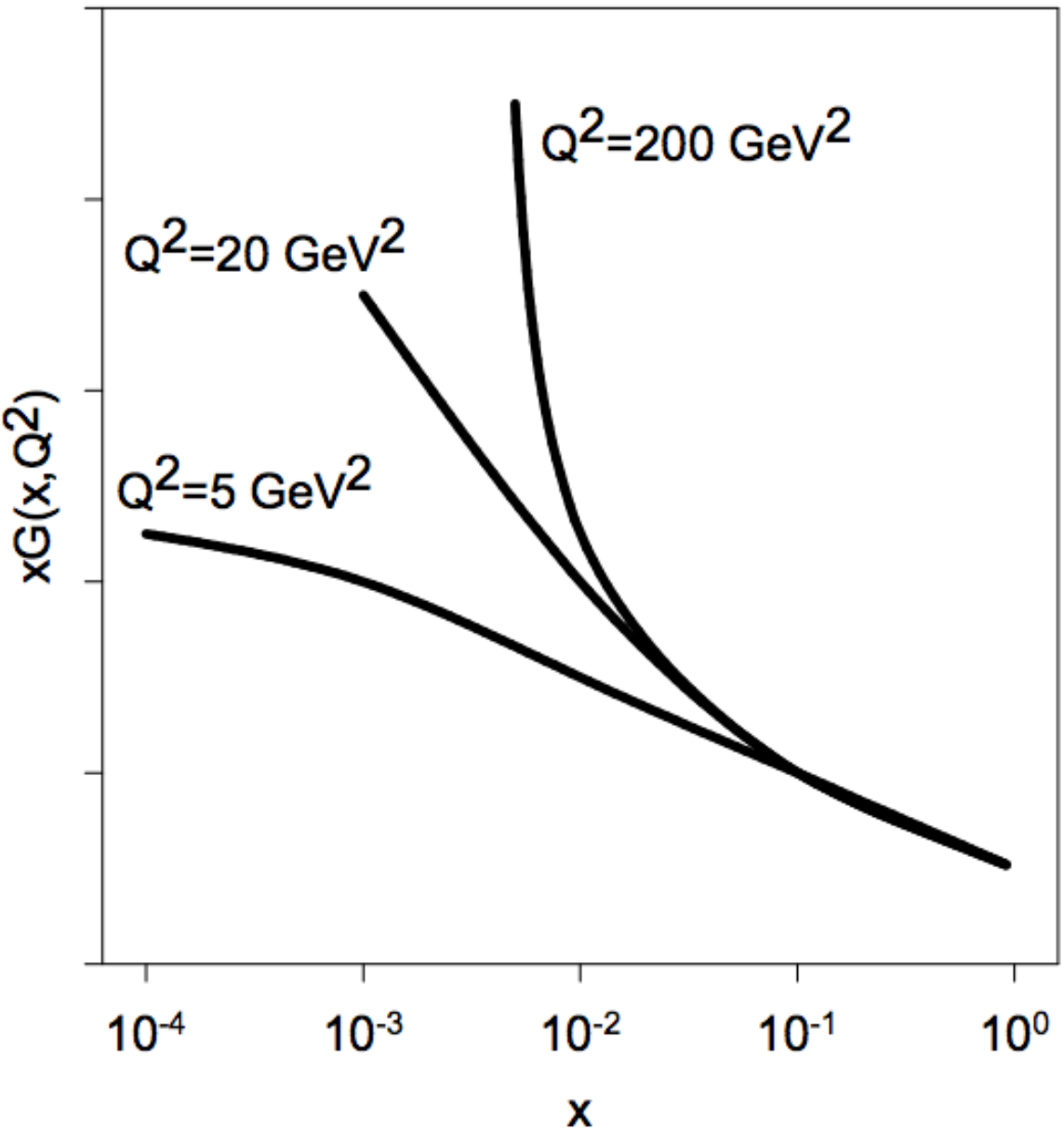

Figure 1.16: Parton density versus x at three different resolution scales [18].

density of partons increases as x decreases. For a given x the size of the partons decreases and their number increases as Q^2 increases.

Physically, the rapid increase in parton density as x decreases, shown in Figure 1.16, cannot go on forever since the probability for a particle to scatter off a proton is finite. This is known as the unitary limit and can be understood in terms of the packing of partons into a disk. At some

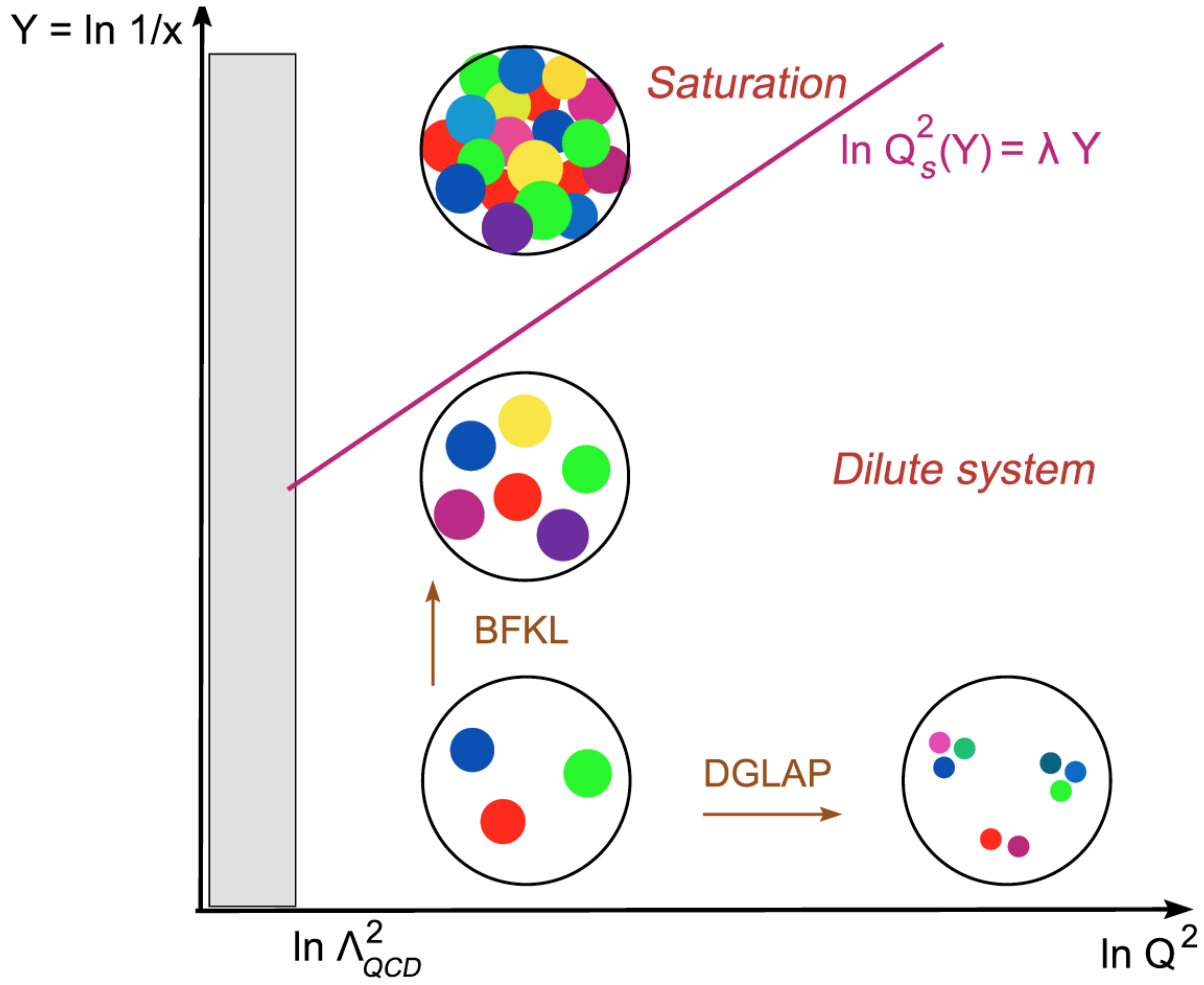

Figure 1.17: Schematic diagram of the parton density within a proton or nucleus at different values of x and Q^2. Each colored area represents a parton with transverse area $\sim \frac{\bar{h}^2}{Q^2}$ and longitudinal momentum fraction x.The straight line $\ln Q_s^2(x) = \lambda Y$ represents the value of x below which the density of partons with a given Q^2 saturates [19]

.

point it is not possible to fit another parton of transverse area $\sim \pi \cdot \frac{\bar{h}^2}{Q_s^2}$ into the proton without it overlapping and merging with another parton. This transverse momentum Q_s is known as the saturation scale and is a function of x. When two partons merge they form a new parton whose transverse momentum Q is the sum of the other two partons. Since higher momentum partons are smaller it is possible to pack them more tightly into a disk and so Q_s increases as x decreases. Analysis of HERA data suggests that instead of being a function of two variables, x and Q^2, the parton density depends only upon the ratio $\frac{Q^2}{Q_s^2(x)}$ where $Q_s(x)$ increases as the logarithm of $\frac{1}{x}$. The

line on the QCD diagram in figure 1.17 represents the x value for which gluon saturation starts to occur at a particular Q^2.

1.6.2 Nuclear Parton Distribution Function

For a nucleus, the saturation effects described above are expected to be stronger. Because of Lorentz contraction all the nucleons are very close to each other. This means that partons from one nucleon at the back face of the nucleus can overlap with partons at the front. This overlapping of partons means that at very high energy (low x) heavy ions can be treated as a condensed wall of colored gluons. Due to the very strong time dilation the gluons in the moving nucleus are essentially frozen compared to an incoming probe. Because of the combination of a high density of gluons and strong time dilation, it has been proposed that the system may behave like a glass [18]. This proposed new state of matter is called the Color Glass Condensate. Figure 1.18 shows a map of the saturation domain as a function of x and A. The saturation scale rises as the atomic mass increases and x decreases. Note that for $x \sim 10^{-3}$ the saturation momentum Q_s can be 4 GeV for lead nuclei.

Because of the effects described above the nuclear parton distribution function (nPDF) of a nucleus with A nucleons is not the superposition of A independent $PDFs$ of individual nucleons. This modification of the nuclear gluon density $g_A(x,Q^2,A)$ is expressed by the nuclear ratio $R(x,Q^2,A)$, which is the ratio of the nuclear parton distribution function $g_A(x,Q^2,A)$ and the nucleon parton distribution function $g^N(x,Q^2)$. The nuclear ratio $R(x,Q^2,A)$ is defined as:

$$R(x,Q^2,A) = \frac{g_A(x,Q^2,A)}{g_N(x,Q^2)}. \tag{1.27}$$

Figure 1.19 shows a calculation of R versus x for a lead nucleus at a given value of Q [21]. For $x > 0.8$, the parton density of the nucleus is greater than the parton density of the nucleon $g_A > g_N$. This effect is due to the Fermi motion of the individual nucleons within a nucleus. In the range $0.3 < x < 0.8$, the parton density of nucleus is less than the parton density of the nucleon $g_A < g_N$.

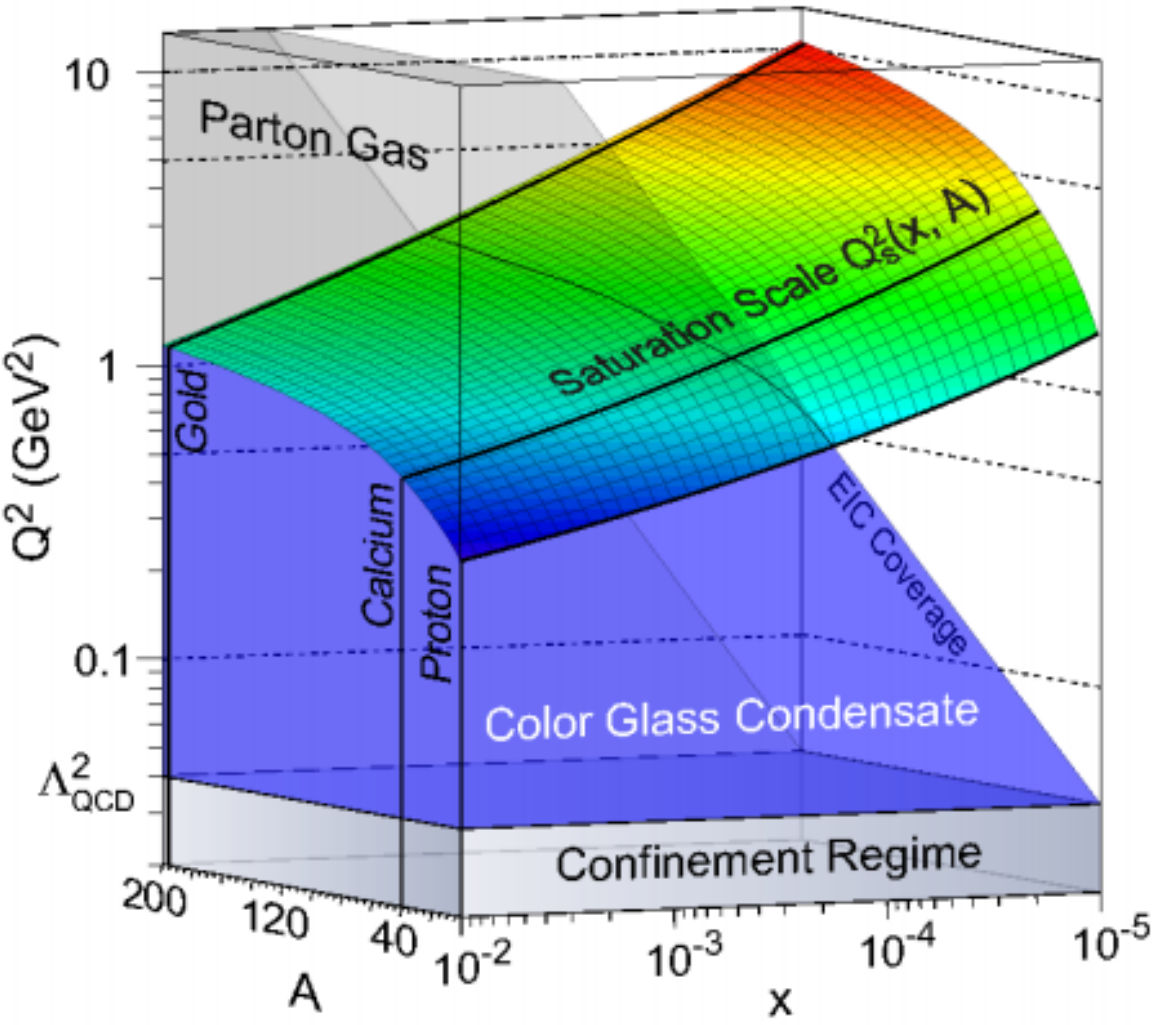

Figure 1.18: Saturation domain as a function of x and A [20].

This effect, known as shadowing, was first measured by the European Muon Collaboration which measured the scattering of muons off nuclear targets [67]. In the range $3 \times 10^{-2} < X < 3 \times 10^{-1}$, the parton density of the nucleus is greater than the parton density of the nucleon $g_A > g_N$, this effect is called anti-shadowing. As x decreases below 3×10^{-2}, the parton density in the nucleus is more and more suppressed compared to that of the proton. In this model the suppression is due to the recombination of low x partons within the nucleus.

Figure 1.20 shows a comparison of the average valence and sea quark, and gluon modifications at $Q^2 = 1.69$ GeV^2 for a Pb nucleus from a LO global DGLAP analyses EKS98 [22] [23], EPS08

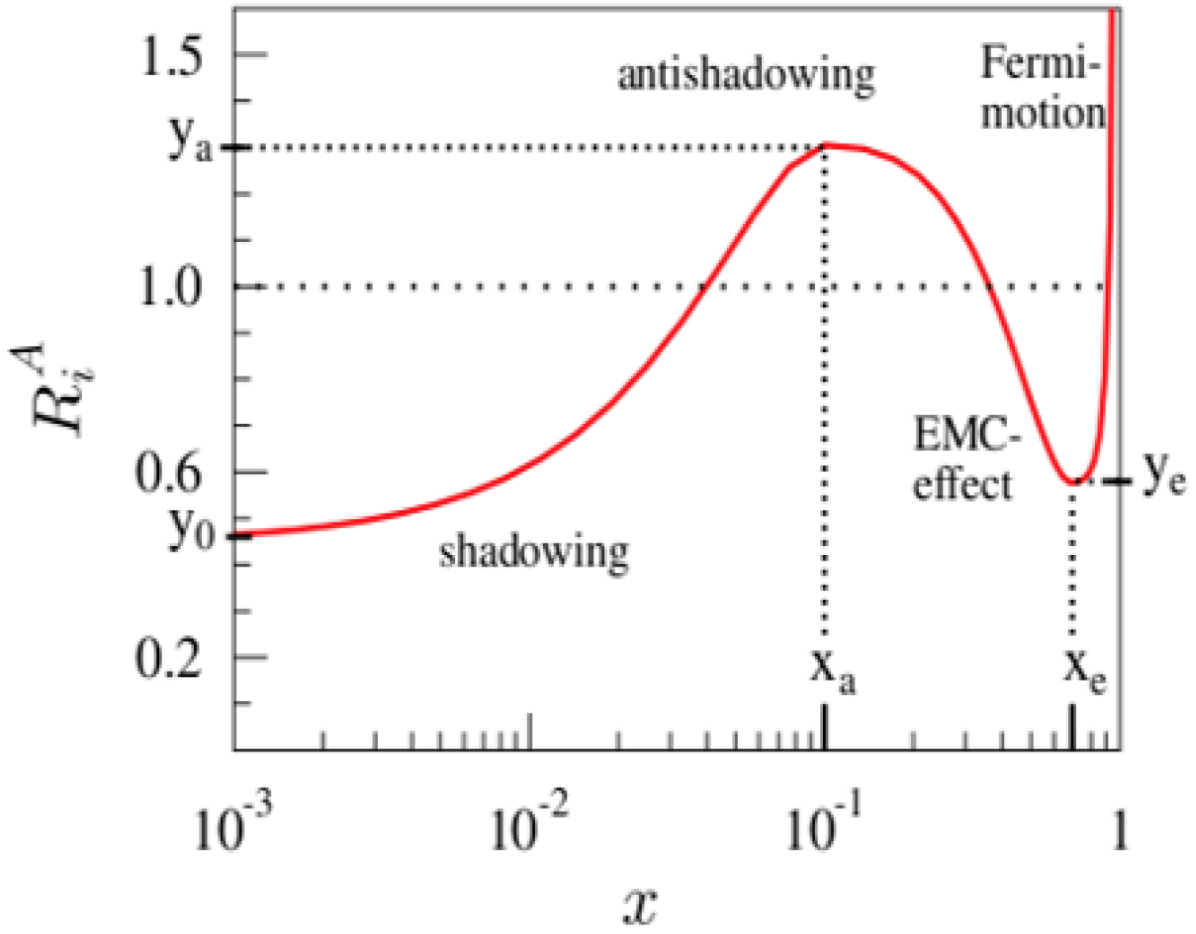

Figure 1.19: A sample calculation of the ratio of the parton distribution function for a lead nucleus to that of a proton as a function of x [21]

[24], nDS [25], HKN07 [26], and EPS09LO [21]. At x less than 3×10^{-2}, the HKN07 and nDS calculations indicate little shadowing, the EKS98 and EPS09 calculations suggest moderate shadowing, while the EPS08 calculation gives strong shadowing. In the shadowing range, where x is less than 3×10^{-2}, the uncertainties in R for valence and sea quarks is small with relative to the gluons, because DIS is the tool used to probe the nucleus.

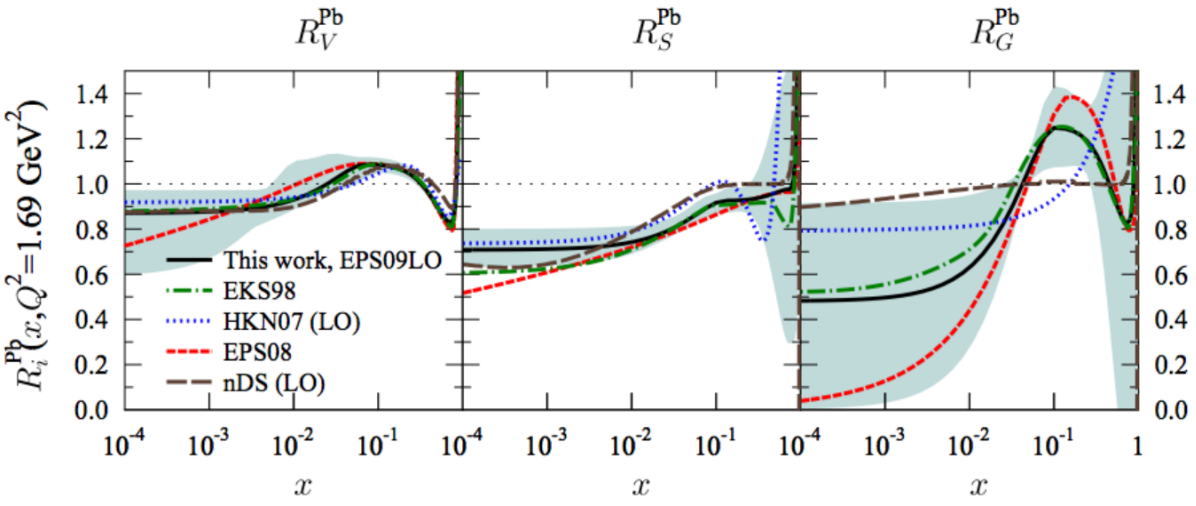

Figure 1.20: Average valence and sea quark, and gluon modifications at $Q^2 = 1.69 GeV^2$ for Pb nucleus from LO global DGLAP analyses EKS98 [22] [23], EPS08 [24], nDS [25], HKN07 [26], and EPS09LO[21]

1.7 Ultra-peripheral collisions (UPCs)

One of the best probes of the initial state of a nucleus is the photon. A lead nucleus with a charge of +82 times the electron charge and a velocity of 99.99998% of the speed a light produces a huge flux of photons. If the two nuclei in a heavy ion collision are further than twice the nuclear radius apart they can interact only via the exchange of photons. Such events are called ultra-peripheral collisions. In such collisions it can be shown that the cross section for the production of the vector mesons ($\rho, J/\psi, \Upsilon, ...$) with no other accompanying particles depends upon the square of the gluon density. This thesis will concentrate on the production of J/ψ mesons in PbPb and pPb collisions.

The J/ψ is a bound state of a pair of $c\bar{c}$ quarks with mass 3096.916 ± 0.011MeV and full width $\Gamma = 92.9 \pm 2.8$ KeV. The charge and the spin of the J/ψ are 0 and 1 respectively. The J/ψ has a lifetime of $7.2 \times 10^{-21} s$ and so it cannot be detected directly. The J/ψ can decay to a muon pair $J/\psi \rightarrow \mu^- \mu^+$ which can be detected. This process has a branching ratio ($5.961 \pm 0.033\%$). Figure 1.21 shows an event display of a J/ψ decaying into two muons within CMS. Using information from the muon chambers and tracker it is possible to identify both tracks as muons and then calculate their momentum and charge from the curvature of the tracks in the

magnetic field.

Once the momenta of the tracks are measured the invariant mass of the dimuon pair is given by

$$m^2_{\mu\mu} = E^2_{J/\psi} - p^2_{J/\psi} = (E_{\mu_1} + E_{\mu_1})^2 - (\overrightarrow{p}_{\mu_1} + \overrightarrow{p}_{\mu_1})^2, \tag{1.28}$$

$$m^2_{\mu\mu} = E^2_{\mu_1} + E^2_{\mu_2} - 2E_{\mu_1}E_{\mu_2} - p^2_{\mu_1} - p^2_{\mu_2} - 2\overrightarrow{p}_{\mu_1} \cdot \overrightarrow{p}_{\mu_2}, \tag{1.29}$$

$$m_{\mu\mu} = \sqrt{m^2_{\mu} + m^2_{\mu} - 2E_{\mu_1}E_{\mu_2} - 2\overrightarrow{p}_{\mu_1} \cdot \overrightarrow{p}_{\mu_1}}. \tag{1.30}$$

If the dimuon mass is consistent with that of a J/ψ we can infer that we have observed a J/ψ decaying into two muons.

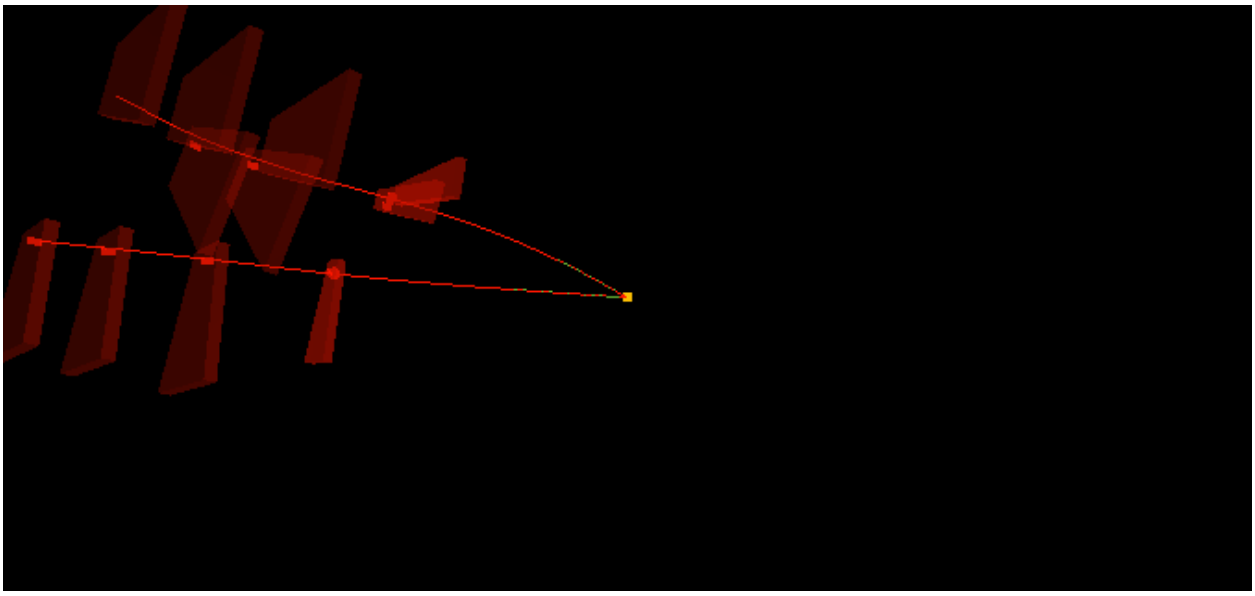

Figure 1.21: An event display of mother particle J/ψ decaying to daughters (two muons) in ultra-peripheral pPb collision in CMS detector.

Figure 1.22 shows the nuclear ratio versus x for a lead nucleus at a resolution scale $Q = M_{J/\psi}$ and the cross section versus rapidity for J/ψ production in ultra-peripheral PbPb collisions for several theoretical *nPDFs*. The stronger the suppression of the nuclear density the lower the cross section for J/ψ production. Thus the cross section for exclusive ρ, J/ψ, and Υ production in ultra-peripheral collisions offers a unique possibility for determining the gluon density.

Figure 1.23 shows the cross section of exclusive photoproduction J/ψ(left) and ρ (right) from PbPb collisions at $\sqrt{s_{NN}} = 2.76$ TeV as measured by ALICE. Both results are consistent with

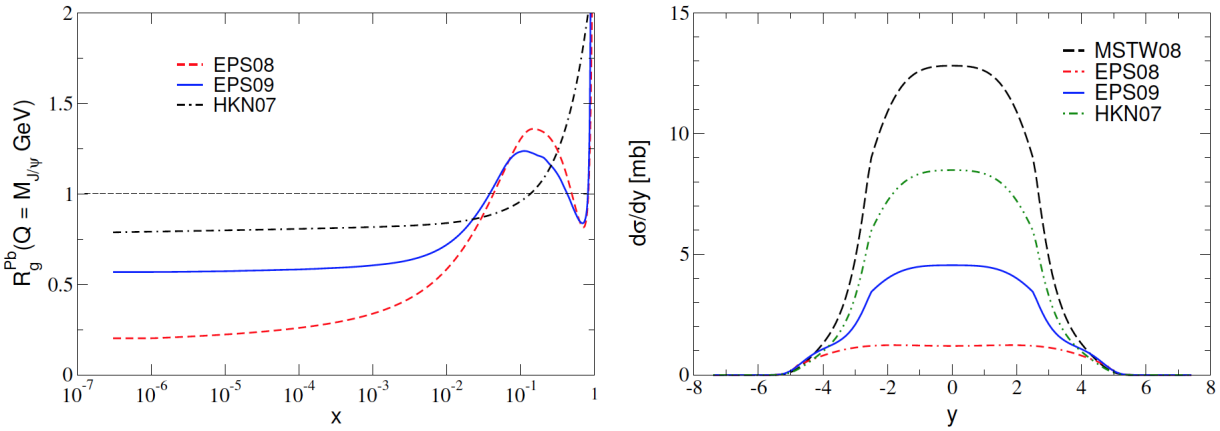

(a) (b)

Figure 1.22: Left: Modification of the nuclear parton density for a lead nucleus with a resolution scale of $Q = M_{J/\psi}$ for different theoretical models Right: the cross section for J/ψ production in ultra-peripheral PbPb collisions versus rapidity for the same models.[27]

significant gluon shadowing in the lead nucleus. Figure 10.2 shows the combined CMS and ALICE data for exclusive photoproduction J/ψ. Again the experimental results are consistent with models, which assume shadowing in the nPDF at low x.

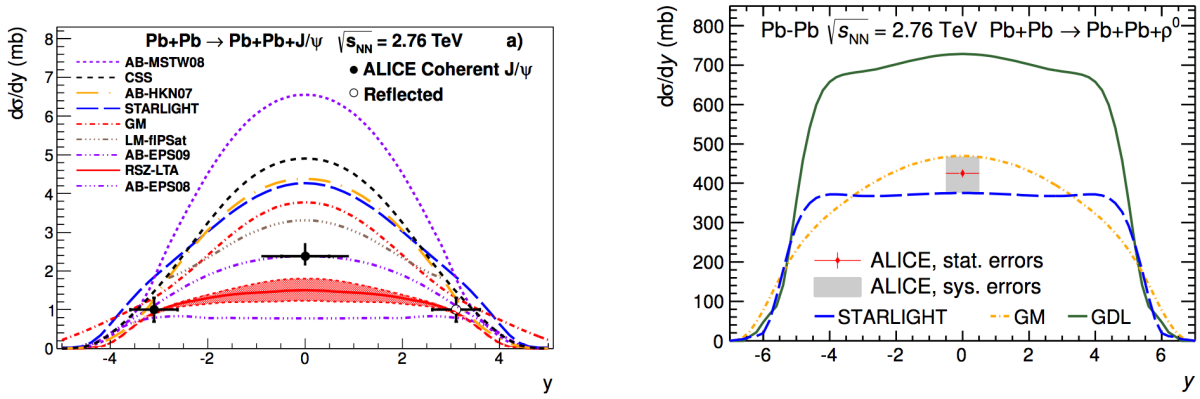

Figure 1.23: Left: measured cross section for coherent exclusive J/ψ production versus rapidity in ultraperipheral PbPb collisions at $\sqrt{s_{NN}} = 2.76$ TeV by the ALICE collaboration, compared to theoretical calculations [28]. Right: measured cross section for coherent exclusive ρ^0 production versus rapidity in ultraperipheral PbPb collisions at $\sqrt{s_{NN}} = 2.76$ TeV by the ALICE collaboration, compared to theoretical calculations [29]

In this thesis, we present a search for saturation in the proton and the shadowing in lead nuclei

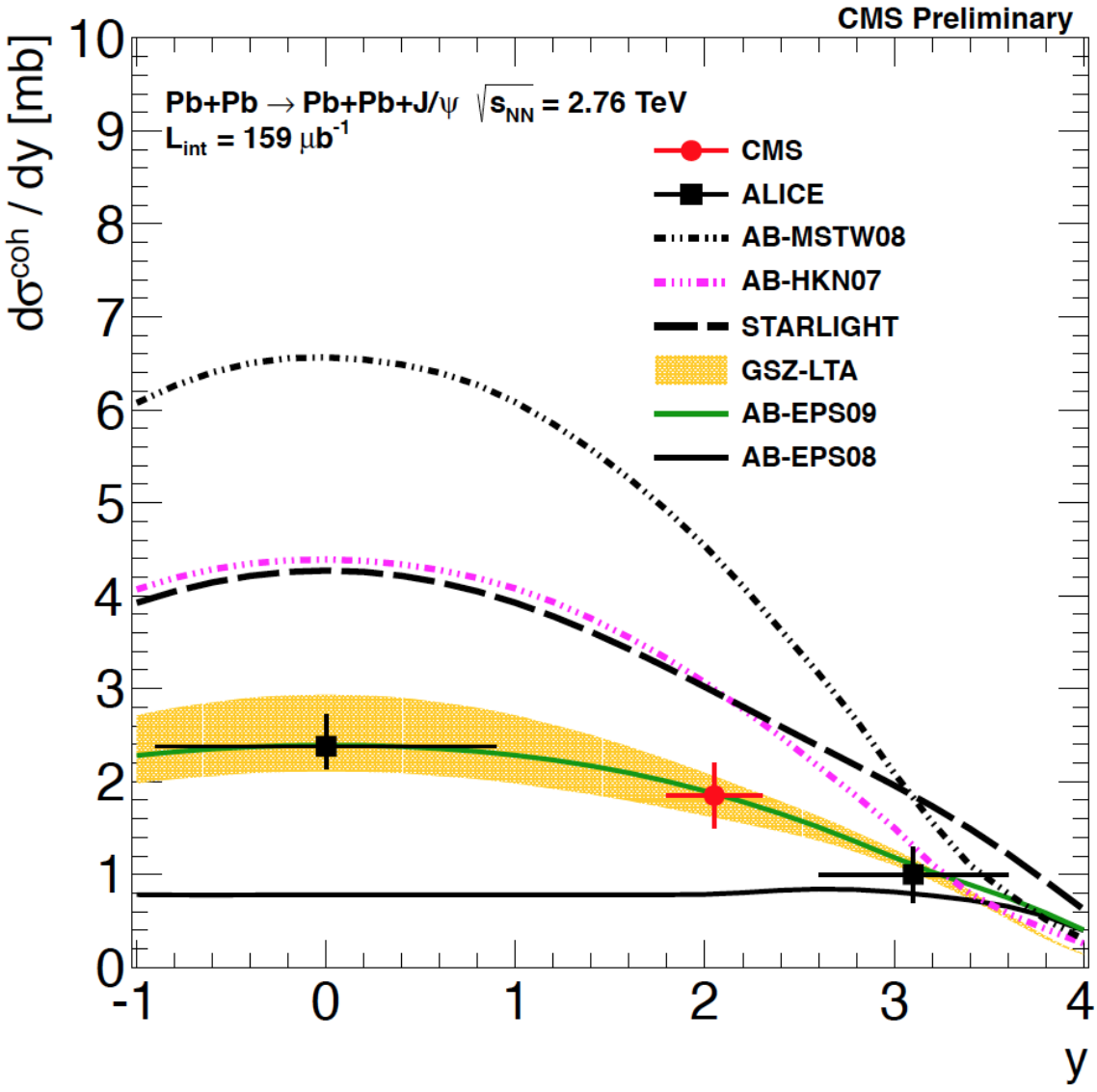

Figure 1.24: Cross section for coherent exclusive J/ψ production versus rapidity in ultraperipheral PbPb collisions at $\sqrt{s_{NN}} = 2.76$ TeV from the CMS and ALICE collaboration compared to theoretical calculations [30].

using exclusive J/ψ photoproduction in very high energy ultra-peripheral pPb and PbPb collisions. This will be done over a range of x and Q^2 by measuring the p_T spectra of exclusive J/ψ at different rapidities. Chapter 2 describes the physics of ultra-peripheral PbPb and pPb collisions, theoretical models, and summarizes previous experimental results on J/ψ photoproduction. Chapter 3 and 4 describe the CMS detector and its trigger system respectively. Chapter 5 contains the

analysis of J/ψ photoproduction for PbPb collisions at $\sqrt{s_{NN}} = 2.76$ TeV. Chapter 6, 7, and 8 contain the analysis of J/ψ photoproduction for pPb collisions at $\sqrt{s_{NN}} = 5.02$ TeV, the comparison with Monte Carlo simulation of UPCs (STARLIGHT), and the corrections (acceptance and trigger efficiency) respectively. Chapter 9 describes studies of systematic uncertainties and cross checks of J/ψ photoproduction for pPb collisions. Finally, chapter 10 provides the results, discussions, and a summary of J/ψ photoproduction for PbPb and pPb collisions.

Chapter 2

The Physics of Ultra-Peripheral Collisions

2.1 Introduction

Ultra-peripheral collisions are defined as interactions between two accelerated charged ions (the projectile and the target) which are separated by an impact parameter b larger than the sum of their radii. Because of this large separation they miss each other and do not interact hadronically. They can however interact through the exchange of photons.

For ions moving close to the speed of light the strong Lorentz contraction compresses the electric field lines into a very thin sheet. The electric field points radially away from the ion and the magnetic field is perpendicular to it. The idea of treating the electromagnetic field of a moving charged particle as a flux of virtual photons was first introduced by Enrico Fermi in 1924 [68]. A decade later Weizsacker and Williams extended this treatment to relativistic charged particles as the Weizsacker-Williams method [69]. The relativistic charged particle (nucleus, proton ..) generates a flux of virtual photons $n(\omega)$ where $\hbar\omega$ is the energy of an individual photon. The photon spectrum $n(\omega)$ is the Fourier transform of the time-dependent electromagnetic field.

In ultra-peripheral collisions, there are two kinds of interactions. The first case is a photon-photon interaction, $\gamma\gamma$, in which the radiated photon of the projectile interacts with a photon from the target. The second case, photo-nuclear interaction, γA, occurs when a photon from the projectile particle hits the target ion itself.

The photo-nuclear interaction is a two-stage process. First the photon fluctuates into a $q\bar{q}$ pair, then these quarks interact with the target. The lifetime of the $q\bar{q}$ fluctuation is large compared with the interaction time scale. For interactions that are energetic enough to produce a heavy vector

meson such as a J/ψ or Υ, the process is hard and perturbative QCD (pQCD) can be applied. In leading order pQCD, the interaction of the $q\bar{q}$ pair by exchange of two gluons from the target is shown in Figure 2.1. The photon emitted by the Pb nucleus fluctuates to a $c\bar{c}$ pair. The $c\bar{c}$ pair is then scattered by two gluons producing a J/ψ vector meson. The cross section for the photoproduction of vector mesons depends upon the square of the gluon distribution $[xg_A]^2$ [70]. This makes UPC J/ψ production a very sensitive probe of the low x behavior of the gluons inside the nucleus.

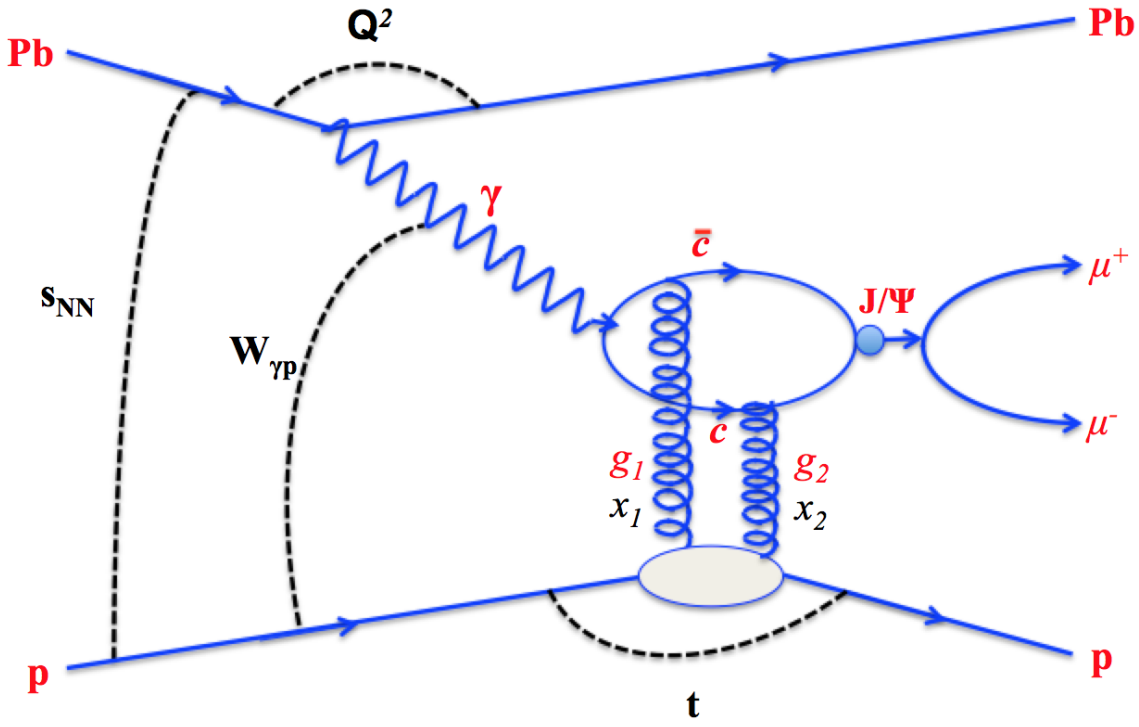

Figure 2.1: The photoproduction of J/ψ in leading order pQCD. In ultra-peripheral pPb collisions, the photon emitted by the lead nucleus can fluctuate into a low p_T $c\bar{c}$ pair. The $c\bar{c}$ pair is scattered by two gluons producing J/ψ vector meson.

2.2 The photon flux

The expression for the electromagnetic field of a relativistic charged particle can be obtained from a Lorentz transformation of the 4-vector potential A^μ. The relativistic effect leads to an increase of

the transverse E-field by the Lorentz factor γ, which is ($\gamma = \frac{1}{\sqrt{1-\frac{v^2}{c^2}}}$) and to a contraction of the E-field in the longitudinal direction by the same factor. The shape of the field is similar to a pancake moving along with the particle. The moving charge also induces a magnetic field perpendicular to the E-field and with the same strength since the velocity is very close to the speed of light. The components of the time-dependent electromagnetic field for a relativistic charged point particle are given by:

$$E_Z(t,b) = \frac{-Ze\gamma vt}{[b^2+(\gamma vt)^2]^{3/2}}, \tag{2.1}$$

$$B_Z(t,b) = 0, \tag{2.2}$$

$$E_T(t,b) = \frac{-Ze\gamma b}{[b^2+(\gamma vt)^2]^{3/2}}, \tag{2.3}$$

$$B_T(t,b) = |v \times \vec{E}_T|. \tag{2.4}$$

Here b is the impact parameter, E_Z is the longitudinal electric field, E_T is the transverse electric field, B_Z is the longitudinal magnetic field, and B_T is the transverse magnetic field. The Weizsacker-Williams method starts by taking the Fourier transformation of the time varying fields $\vec{E}(t,b)$ and $\vec{B}(t,b)$. This gives

$$E_Z(\omega,b) = \sqrt{\frac{2}{\pi}}\frac{eZ}{4\pi\varepsilon_o b^2}\frac{b}{\gamma v}\frac{\omega b}{\gamma v}K_0(\frac{\omega b}{\gamma v}), \tag{2.5}$$

$$E_T(\omega,b) = \sqrt{\frac{2}{\pi}}\frac{\gamma eZ}{4\pi\varepsilon_o b^2}\frac{b}{\gamma v}\frac{\omega b}{\gamma v}K_1(\frac{\omega b}{\gamma v}), \tag{2.6}$$

$$B_Z(\omega,b) = 0, \tag{2.7}$$

$$B_T(\omega,b) = \frac{\vec{E}_T}{c}, \tag{2.8}$$

where K_0, K_1 are modified Bessel functions.

The longitudinal components of the field strengths are small in the limit $v \to c$, i.e., when γ becomes large. To extract the equivalent photon spectrum $n(\omega)$, which depends upon the photon

frequency ω, we have to consider the energy flux of the electromagnetic field through a plane perpendicular to the direction of the moving charge. This is provided by the Poynting vector. The amount of energy projected to the target per unit area in terms of the frequency spectrum of the field is given by:

$$I(\omega,b) = \frac{|\vec{E}(\omega)\times\vec{B}(\omega)|}{4\pi}. \tag{2.9}$$

Using this and considering that each photon has an energy $\hbar\omega$, the photon flux $N(\omega,b)$ is given by Equation 2.10:

$$N(\omega,b) = \frac{dN^2}{d\omega db} = \frac{Z^2\alpha}{\pi^2}\frac{1}{\beta^2}\frac{1}{\omega b^2}x^2\left(K_1^2(x)+\frac{1}{\gamma^2}K_0^2(x)\right), \tag{2.10}$$

where $x = \frac{b\omega}{\beta\gamma}$. The first term, $K_1^2(x)$, gives the flux of photons in the direction transverse to the motion of the ion or proton and the second term, $K_0^2(x)$, is the flux of photons in the longitudinal direction. For ultra-relativistic particles the photon flux in the transverse direction is dominant, i.e., $K_1^2(x) >> \frac{1}{\gamma^2}K_0^2(x)$. Figure 2.2 shows the electric field $E(b)$ of the nucleus at $v = 0$, and at $v \approx c$, and the photon spectrum $n(\omega,b)$ of the nucleus at $v \approx c$. Since the width of the relativistic electric field gets wider as b increases there are fewer high energy photons at large b, i.e. far from the nucleus.

The maximum photon energy will be of order

$$\hbar\omega_{max} \sim \frac{\hbar}{\triangle t} = \frac{\hbar}{\frac{b}{\gamma v}} = \frac{\gamma_L v\hbar}{b}. \tag{2.11}$$

In ultra-peripheral collisions, because the minimum impact parameter is $b_{min} = (R_1 + R_2)$, the maximum photon energy will be $\omega_{max} \sim \frac{\gamma_L\hbar c}{(R_1+R_2)}$. For lead-lead collisions with $R_A \sim 7$ fm the maximum photon energy is about 1.5% of the beam energy per nucleon. For proton-proton collisions with radius $R_p \sim 0.7$ fm the maximum photon energy is about 15% of the proton energy.

In ultra-peripheral ion-ion collisions the total photon flux is obtained by integrating Equa-

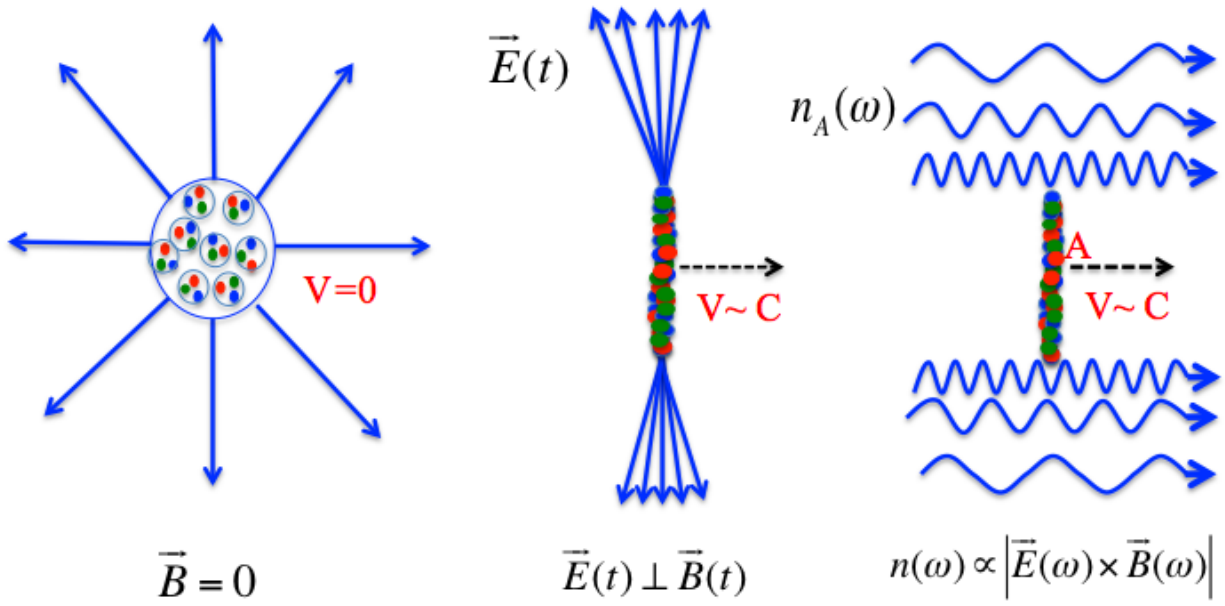

Figure 2.2: Left: the electric field of a nucleus at v=0. Middle:the transverse electric field of a nucleus at $v \approx c$. Right: photon spectrum $n(\omega)$ of a nucleus at $v \approx c$.

tion 2.10 over $b > b_{min} = 2R_A$:

$$n(\omega) = \int_{b>2R_a} N(\omega,b)d^2b = \frac{2Z^2\alpha}{\pi}\frac{1}{E_\gamma}\left(xK_0K_1 - \frac{1}{2}x^2(K_1^2(x) - K_0^2(x))\right) \tag{2.12}$$

where $x = \frac{2RE_\gamma}{\beta\gamma}$.

2.3 Photon-Photon Interactions

Figure 2.3 shows a schematic of an ultra-peripheral $\gamma\gamma$ collision. Each ion emits a photon each of which can have a different energy and momentum. The two photons then collide and form new particles. No hadronic interaction occurs. The total cross section for the gamma gamma, i.e. $\gamma\gamma$, interaction can be written as [71]

$$\sigma_{total} = \int d\omega_1 d\omega_2 \frac{n(\omega_1)}{\omega_1}\frac{n(\omega_2)}{\omega_2}\sigma^{\gamma\gamma\to X}, \tag{2.13}$$

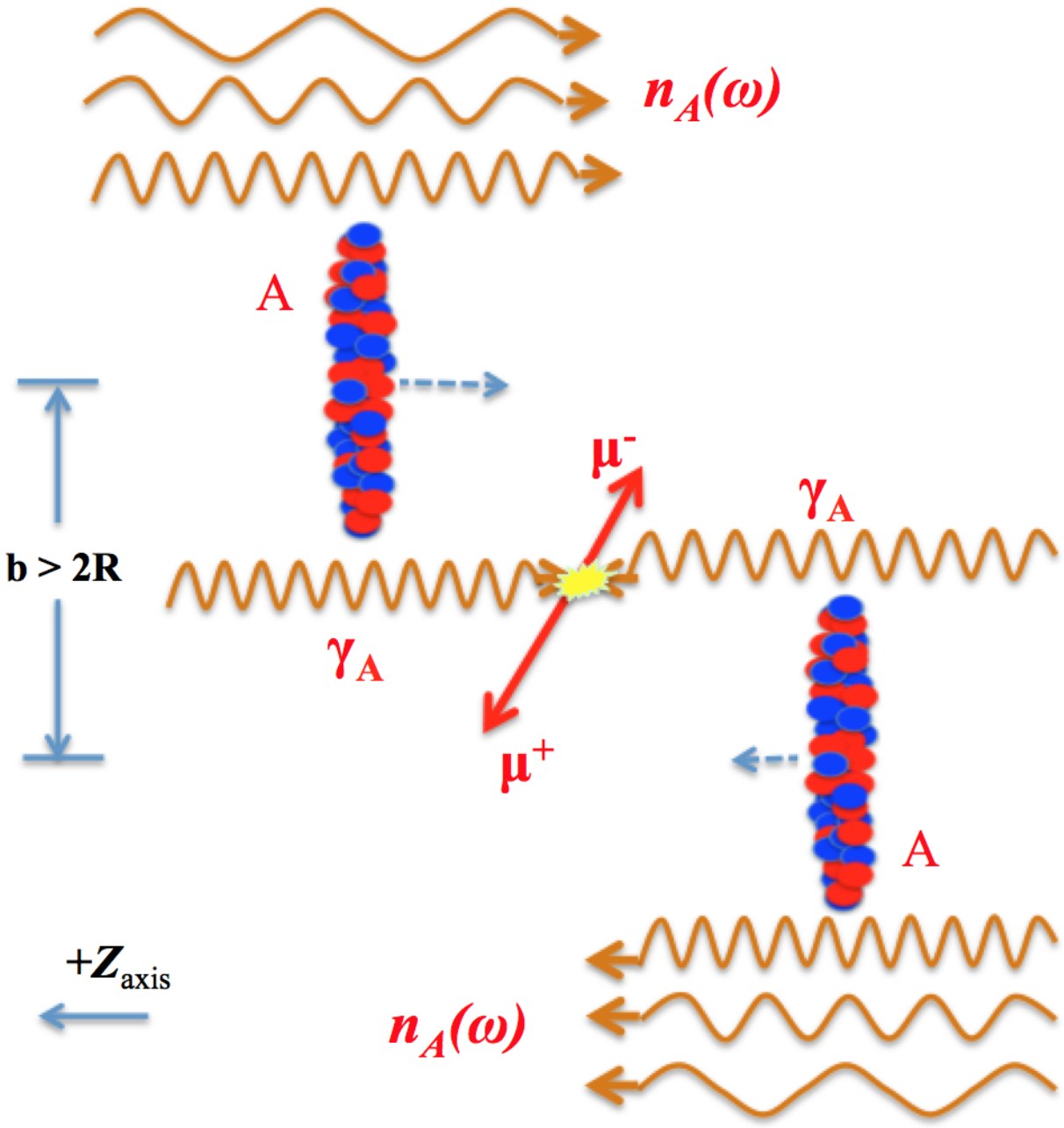

Figure 2.3: An ultra-peripheral gamma gamma $\gamma\gamma$ collision producing two muons.

where $n(\omega_1)$ and $n(\omega_1)$ are the photon densities of the first and second ion respectively, and $\sigma_X^{\gamma\gamma}$ is the cross section for the two photons to interact. Note that the final state X can be lepton pairs such as $\mu^+\mu^-$, e^+e^-,.... or mesonic states such as $f_0(980)$, $f_2(1270)$, ... or ρ^0.

The cross section to produce a pair of leptons with lepton mass m and pair invariant mass W is given by the Breit−Wheeler formula [72]

$$\sigma^{\gamma\gamma\to l^+l^-} = \frac{4\pi\alpha^2}{W^2}\left[\left(2+\frac{8m^2}{W^2}-\frac{16m^4}{W^4}\right)\ln\left(\frac{W+\sqrt{W^2-4m^2}}{2m}\right)-\sqrt{1-\frac{4m^2}{W^2}\left(1+\frac{4m^2}{W^2}\right)}\right] \quad (2.14)$$

The cross-section to produce a single vector meson from two photons is [73]

$$\sigma^{\gamma\gamma\to V} = 8\pi(2J+1)\frac{\Gamma_{\gamma\gamma}\Gamma}{(W^2-M_R^2)^2}, \quad (2.15)$$

where $\Gamma_{\gamma\gamma}$ is the two-photon width, W and M_R are the pair invariant mass and vector meson mass, respectively, Γ and J are the total width and spin, respectively.

2.4 Photon-nuclear interactions

Figure 2.4 shows a schematic picture of an ultra-peripheral photonuclear collision. The electromagnetic field around each nucleus can be thought of a beam of virtual photons, each of which has a very low transverse momentum. One of these photons interacts with the nucleus to produce new particles. In general, the cross section for vector meson production in photon-nuclear interactions is given by:

$$\sigma_{total} = \int d\omega \frac{n(\omega)}{\omega}\sigma^{\gamma A\to V}(\omega), \quad (2.16)$$

where $\hbar\omega$ is the photon energy, $\sigma^{\gamma A\to V}(\omega)$ is the cross section for a photon with energy $\hbar\omega$ to collide with an ion A (proton or nucleus) and to produce vector mesons V, and $n(\omega)$ is the number of photons with a given frequency ω. The photon spectrum $n(\omega)$ depends only upon the electromagnetic force and can be calculated using methods similar to those described in Section 2.2. The discussion in this section focusses on the calculation of $\sigma^{\gamma A\to V}(\omega)$.

In a photon-nucleus collision, the incident photon may first fluctuate into a quark-antiquark pair (or even more complicated partonic configuration) which then interacts hadronically with the target producing a vector meson. Another possibility is that the photon may fluctuate into a virtual

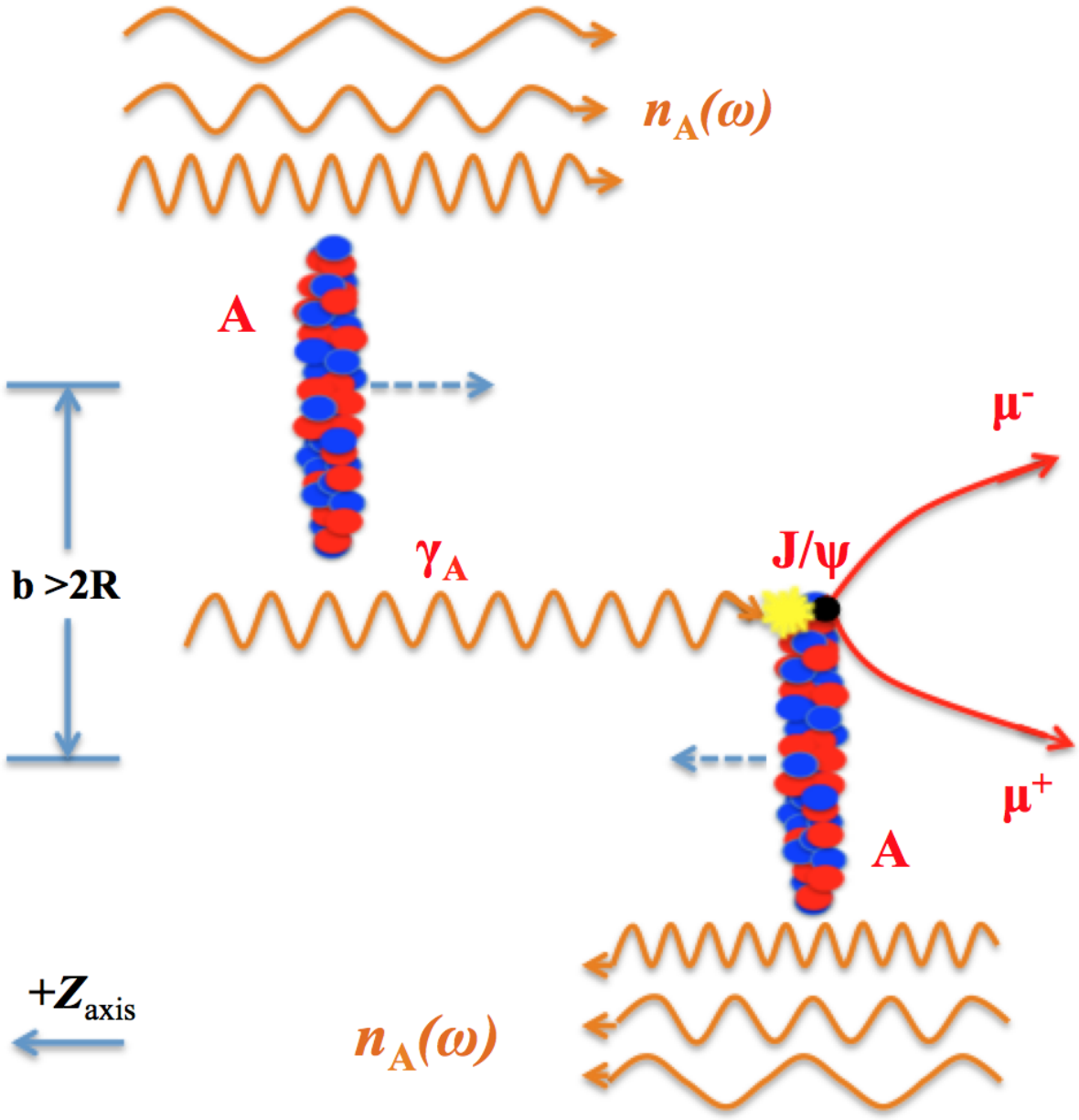

Figure 2.4: Ultra-peripheral photonuclear collision between two heavy ions. The electromagnetic field around each nucleus can be thought of a beam of virtual photons, each of which has a very low transverse momentum. One of these photons interacts with the nucleus to produce new particles.

vector meson (because the V and the photon have same quantum numbers), then the V exchanges momentum with the target nucleus producing a real vector meson after the collision.

In general, the cross section for exclusive elastic photoproduction of a vector meson V on a

target H (nucleus or proton) can be written as:

$$\frac{d\sigma^{\gamma H\to VH}}{dt} = \frac{d\sigma}{dt}\bigg|_{t=0} |F_H(t)|^2, \tag{2.17}$$

where $\frac{d\sigma^{\gamma H\to VH}}{dt}\Big|_{t=0}$ is the forward scattering amplitude and $F_H(t)$ is the form factor. The forward scattering amplitude contains the dynamical information, while the form factor determines the momentum transfer of the elastic scattering. The form factor depends upon the spatial features of the target nucleus, so it equals the Fourier transform of the charge density of the target. For a proton target, the form factor is written as an exponential function,

$$|F_p(t)|^2 = e^{-b|t|}, \tag{2.18}$$

where b is the slope of the distribution. For J/ψ production $b \approx 4$ GeV$^{-2}c^2$. For the target nucleus, the form factor $F_A(t)$ is the Fourier transform of the nuclear density, written as

$$F_A(t) = \int d^3r \rho_A(r) e^{iq.r}, \tag{2.19}$$

where q is the momentum transferred. ρ_A is a Woods-Saxon nuclear distribution. The Woods-Saxon nuclear distribution is written as

$$\rho_A(r) = \frac{\rho_o}{1+e^{\frac{r-R_A}{d}}}, \tag{2.20}$$

where ρ_o is the central nuclear density, R_A and d are the radius and skin depth, respectively. For ^{208}Pb, $\rho_o = 0.16$ fm^3, $R_A = 1.2A^{\frac{1}{3}}$ fm

The forward scattering amplitude for leading order QCD via two-gluon exchange is written as follows:

$$\left.\frac{d\sigma(\gamma H \to VH)}{dt}\right|_{t=0} \propto [x g_H(x,Q^2)]^2, \tag{2.21}$$

where $x = \frac{M_V^2}{W_{\gamma H}^2}$ is the longitudinal fractional momentum carried by the gluons, $g_A(x,Q^2)$ is the gluon nuclear distribution, $g_p(x,Q^2)$ is the gluon proton distribution, which are calculated at a momentum transfer $Q^2 = (\frac{M_{J/\psi}}{2})^2$ for exclusive photoproduction of J/ψ. From equation 2.21, it is clear the exclusive vector meson production is a very sensitive tool to probe the gluon distribution in protons and nuclei.

2.4.1 Exclusive photo-production of J/ψ in PbPb collisions

The total cross section for the photo-production of vector mesons in ultra-peripheral heavy ion collisions is given by,

$$\sigma^{AA\to V} = 2\int d\omega \frac{n(\omega)}{\omega}\sigma^{\gamma A\to V}(\omega) \tag{2.22}$$

In this equation the factor of 2 accounts for the symmetry in the cross section with respect to the target and projectile. The differential cross section with respect to rapidity is given by

$$\frac{d\sigma^{(PbPb\to J/\psi)}}{dy} = n_{Pb}(\omega)\sigma^{\gamma Pb\to J/\psi}(\omega)\Big|_{\omega=\omega_l} + n_{Pb}(\omega)\sigma^{\gamma Pb\to J/\psi}(\omega)\Big|_{\omega=\omega_r} \tag{2.23}$$

where ω_l and ω_r refer to the left-and right-going nuclei separately. The relation between ω and y is $\omega_1 = \frac{M_{J/\psi}}{2}e^{+y}$. $\omega_2 = \frac{M_{J/\psi}}{2}e^{-y}$, $M_{J/\psi}$ is the mass of the J/ψ vector meson.

Exclusive photo-nucleus production can be either coherent or incoherent. Figure 2.5 shows a schematic view of the coherent process. The photon is emitted coherently by all the charges within the projectile and couples coherently with the whole target nucleus. The transverse momentum, p_T, of the J/ψ is small, it is about $< p_T > \sim \frac{\hbar c}{R} = 30$ MeV/c. About 80% of both nuclei (projectile and the target) remain intact after this type of interaction. Figure 2.6 shows a schematic view of the

incoherent process. Here a photon from one nucleus interacts with a single nucleon in the target nucleus. In this case, the target nucleus is excited and generally breaks up, emitting neutrons to a Giant- Dipole Resonance (GDR) with energy $O(10MeV)$ in the forward direction.

The average transverse momentum p_T for the J/ψ in this process is about $< p_T > \sim$ 500 MeV/c.

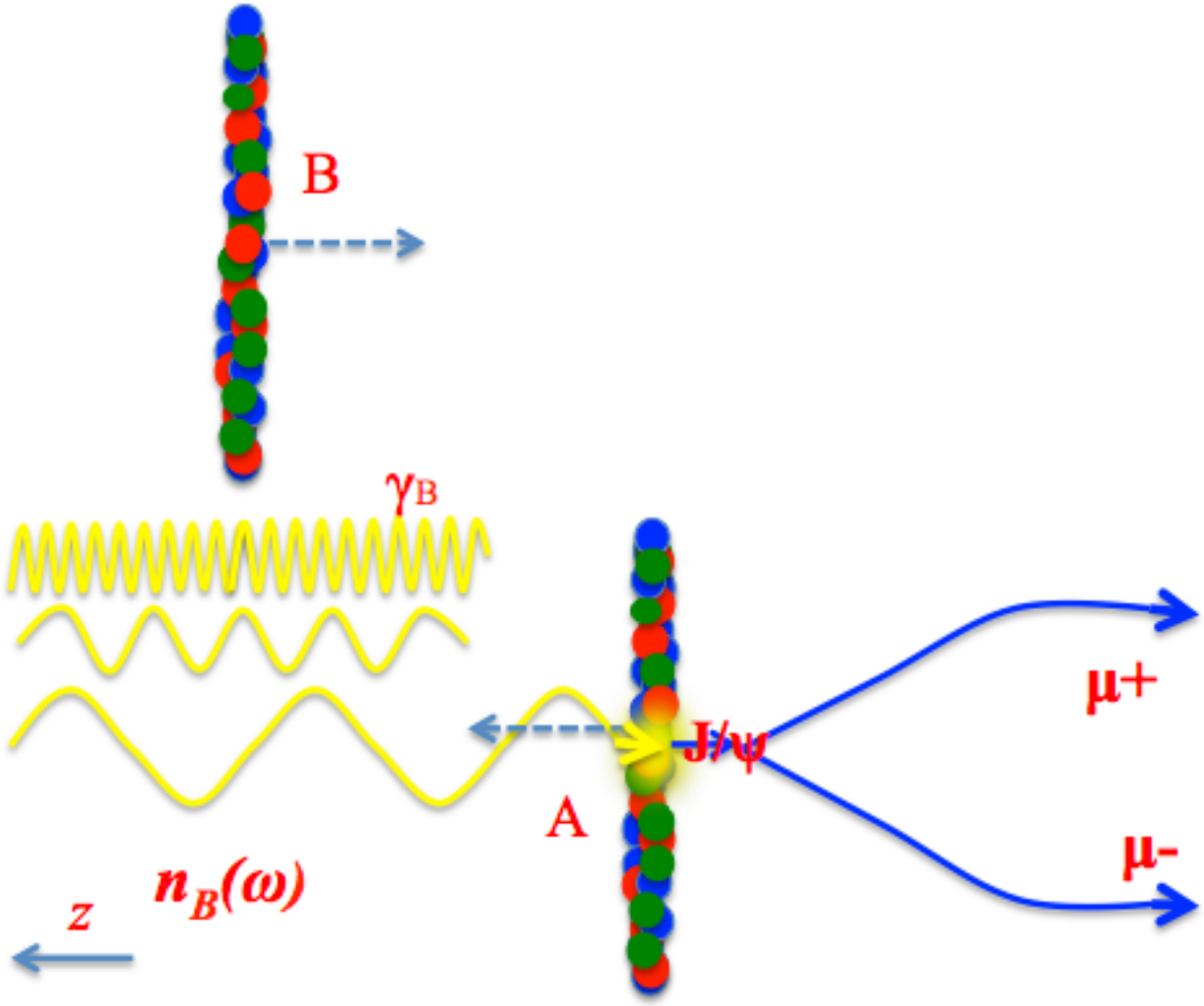

Figure 2.5: Coherent production of J/ψ in ultra-peripheral heavy ion collisions. The photon emitted coherently by the projectile interacts coherently with the whole nucleus. The J/ψ rapidly decays to two muons.

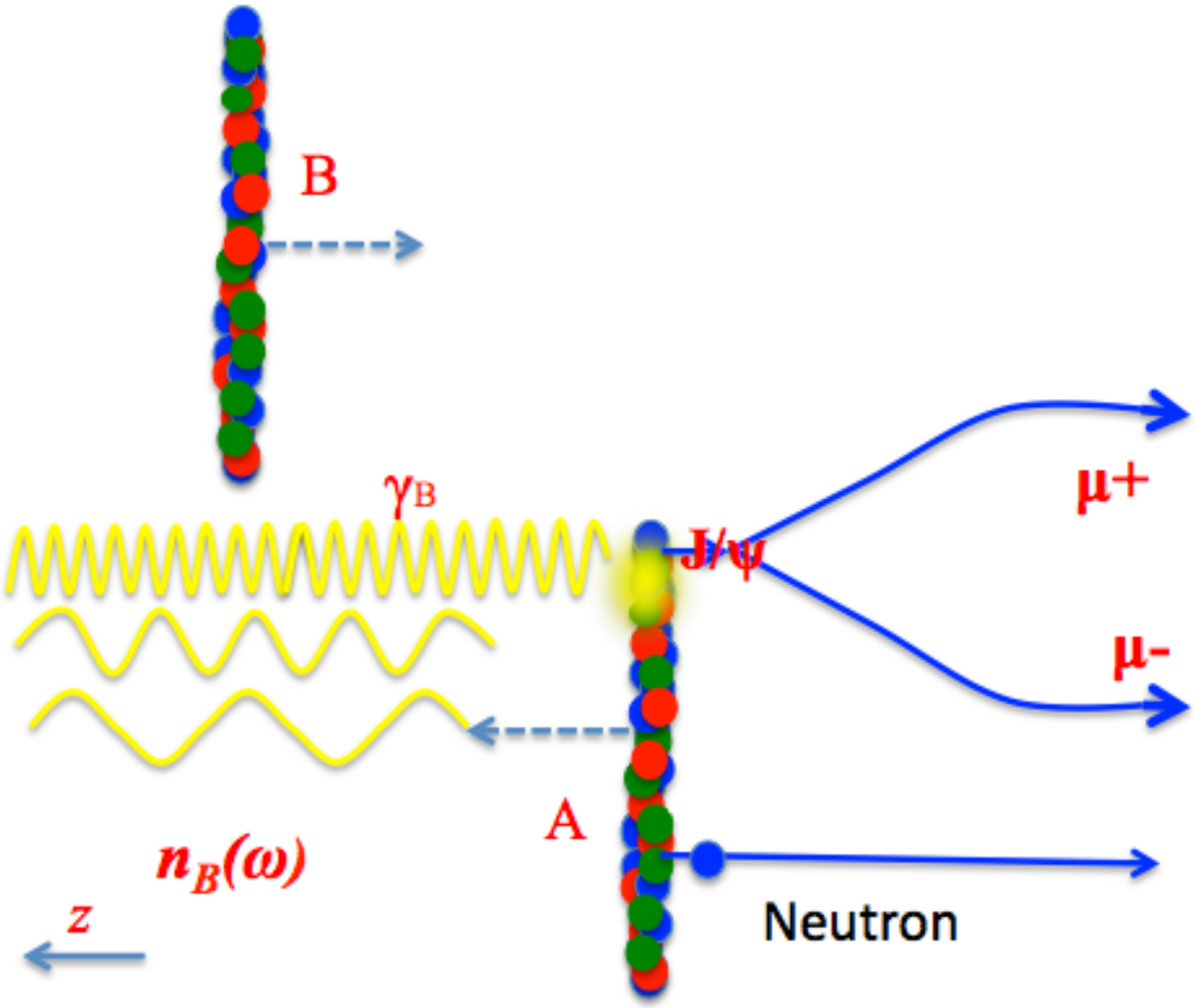

Figure 2.6: Incoherent production of J/ψ mesons in ultra-peripheral heavy ion collisions. The photon emitted by the projectile interacts incoherently with one nucleon in the target. The J/ψ rapidly decays to two muons.

2.4.2 Exclusive photo-production of J/ψ in pPb collisions

In ultra-peripheral p+Pb collisions, the differential cross section for the photoproduction of J/ψ can be written as

$$\frac{d\sigma^{(pPb\to J/\psi)}}{dy} = n_{Pb}(\omega)\sigma^{\gamma p\to J/\psi}(\omega)\Big|_{\omega=\omega_L} + n_p(\omega)\sigma^{\gamma Pb\to J/\psi}(\omega)\Big|_{\omega=\omega_R}. \qquad (2.24)$$

The first term considers the interaction of photons emitted by the lead nucleus with the proton while the second term is due to photons emitted by the proton hitting the nucleus. Because the photon flux is proportional to Z^2 the first term dominates.

2.5 Theoretical models and event generators

Figure 2.1 shows a schematic view of the exclusive production of J/ψ in ultra-peripheral heavy ion collisions. In order to model this cross section it is necessary to understand:

1. The flux of photons; models generally follow the derivations in Section 2.2 and integrate Equation 2.10 over impact parameters greater than the sum of the two nuclear radii.

2. The flux of partons, i.e., the nuclear PDFs. These can either be taken as input as in the AB model, or derived from proton PDFs with some gluon recombination mechanism, i.e., the RSZ model, or simply taken as $A\times$ the proton PDF.

3. The photon's interaction with partons.

The total photoproduction cross section is then obtained by the convolution of the cross section with the photon and parton fluxes.

In ultra-peripheral collisions, the incident photon can interact either as a point-like photon γ_0, a point-like particle as vector meson V, or a fluctuation of a quark-antiquark pair $q\bar{q}$. The photon wave function can be written as [74]:

$$|\gamma\rangle = C_0|\gamma_0\rangle + \sum_{V=\rho,\omega,\phi} C_V\big|V\big\rangle + \sum_{q=u,d,s,c,b} C_q\big|q\bar{q}\big\rangle, \tag{2.25}$$

where $\big|\gamma_0\big\rangle$, $\big|V\big\rangle$, and $\big|q\bar{q}\big\rangle$ are wave functions of the point-like photon, a vector meson, and a quark-antiquark pair respectively. The "bare" photon γ_0 does not interact hadronically, and its contribution to the interaction is small at high energies. C_0 is used to normalized the photon wave function. C_V and C_q represent the hadronic interaction. $\big|C_V\big|^2$ is the probability of a photon to

fluctuate into a vector meson, and $\left|C_q\right|^2$ is the probability of a photon to fluctuate into a $q\bar{q}$ pair. The fluctuation into $q\bar{q}$ works at high-virtuality, and C_q is written as [72]:

$$C_q \approx \frac{\alpha_{em}}{2\pi} 2Q_q^2 \ln(\frac{\mu^2}{k_0^2}), \tag{2.26}$$

where $k_0 = 0.5$ GeV [75]. The $q\bar{q}$ fluctuation can be described by models such as Color Dipole Model, which will be discussed later.

The fluctuation into vector mesons works at low-virtuality, where $k_0 < 0.5$ [72], and can be described by models such as the phenomenological Vector Meson Dominance model (VMD), which will be discussed later. In the VMD model, C_V is given as:

$$C_V^2 = \frac{4\pi\alpha_{em}}{f_V^2}, \tag{2.27}$$

where the decay constants f_V are determined from experimental data on $V \to l^+l^-$. The value of $\frac{f_V^2}{4\pi} = 2.20, 23.6, 18.4$, and 11.5 for ρ^0, ω, ϕ, and J/ψ respectively [72].

2.5.1 Vector Meson Dominance model (VMD)

The KN Model used the VMD model [76] [77] [78]. The photon turns into a virtual vector meson before the interaction. Figure 2.7 [79] shows the schematic representation of elastic V production. The photon fluctuates into a vector meson which scatters from the proton via the exchange of the Pomeron. The parameters of the Pomeron were determined by Donnachie and Landshoff (DL) from a global fit to photoproduction data [80].

For small values of Q^2, the production of light vector mesons ρ^0, ω, ϕ are governed by the exchange of the "soft" Pomeron [81]. For high values of Q^2, the production of heavy vector mesons $J/\psi, \psi(2s), \Upsilon$ are governed by the exchange of two Pomerons [82]. The scattering amplitude for

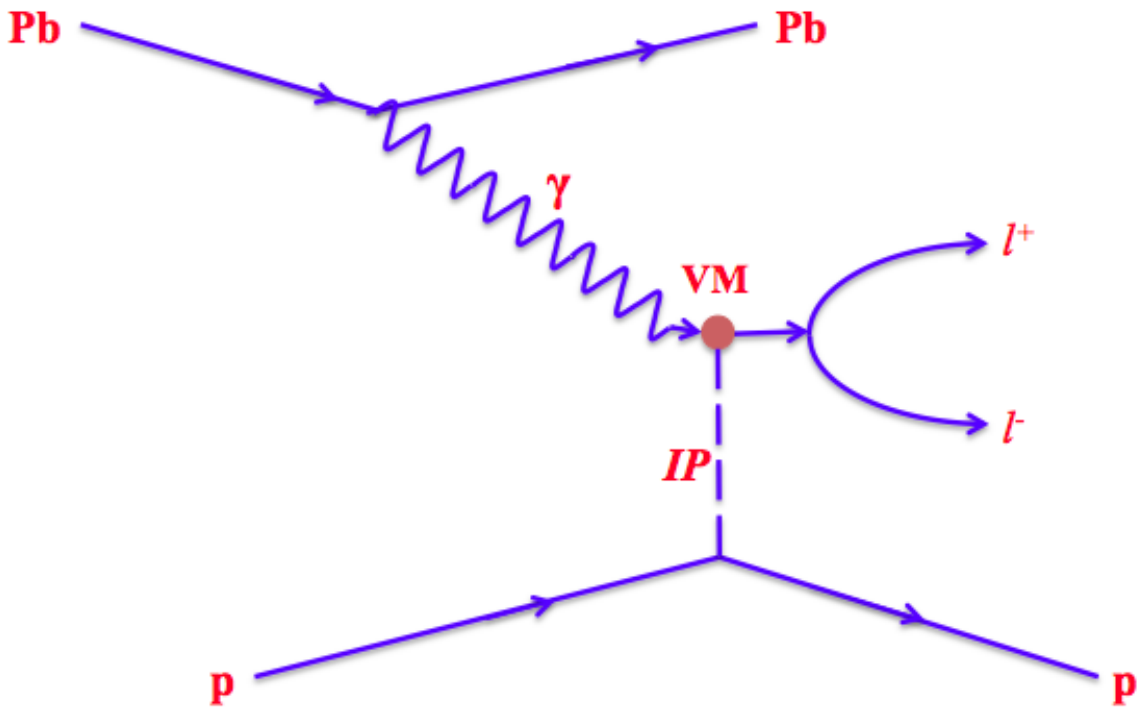

Figure 2.7: Vector meson V production.The photon fluctuates into a vector meson which scatters from the proton via the exchange of a Pomeron IP.

the process $\gamma H \to VH$, where H is a proton p or nucleus A), can then be written

$$|\gamma\rangle H = C_V |V\rangle H. \tag{2.28}$$

In this interaction the scattered vector meson V gets a sufficient momentum transfer to make it real. This means that the photo-production cross section is related to the elastic vector meson cross section by

$$\frac{d\sigma(\gamma H \to VH)}{dt} = C_V^2 \frac{d\sigma(VH \to VH)}{dt}. \tag{2.29}$$

The cross section for exclusive elastic photoproduction of a vector meson V on a target H can be written as:

$$\frac{d\sigma^{\gamma H\to VH}}{dt} = \frac{d\sigma^{\gamma H\to VH}}{dt}\bigg|_{t=0} |F(t)|^2 \tag{2.30}$$

where $\frac{d\sigma^{\gamma H\to VH}}{dt}\Big|_{t=0}$ is the forward scattering amplitude and $F_H(t)$ is the form factor. The forward scattering amplitude contains the dynamical information, while the form factor determines the momentum transfer of the elastic scattering and depends upon the spatial features of the target. One can consider the form factor to be the Fourier transform of the charge density of the target. For a proton target, the form factor is well described by the exponential function,

$$|F(t)|^2 = e^{-b|t|}, \tag{2.31}$$

where b is the slope of the distribution. For J/ψ production $b \approx 4$ GeV$^{-2}c^2$. For nuclear targets, the momentum transfer is much smaller and it is expected that the t dependence of the form factor should be much stronger. For the target nucleus, the forward scattering amplitude $\frac{d\sigma^{\gamma A\to VA}}{dt}\Big|_{t=0}$ is related to total cross section from the optical theorem as follows

$$\frac{d\sigma^{\gamma A\to VA}}{dt}\bigg|_{t=0} = \frac{\alpha\sigma_{tot}^2(VA)}{4f_V^2}. \tag{2.32}$$

The classical Glauber model relates the total cross section for protons to that for nuclei. The relation is written as

$$\sigma_{tot}^{\gamma A\to VA} = \int db^2(1-\exp[-\sigma_{tot}^{\gamma p\to Vp}T_A(b)]). \tag{2.33}$$

Treating the proton as a target, and depending on the optical theorem, the forward scattering amplitude $\frac{d\sigma^{\gamma p\to Vp}}{dt}\Big|_{t=0}$ is related to the total cross section as follows

$$\frac{\alpha\sigma_{tot}^2(\gamma p\to Vp)}{16\pi} = \frac{d\sigma^{\gamma p\to Vp}}{dt}\bigg|_{t=0}, \tag{2.34}$$

and the VMD for a γp collision leads to:

$$\left.\frac{d\sigma^{Vp\to Vp}}{dt}\right|_{t=0} = \frac{1}{C_V^2}\left.\frac{d\sigma^{\gamma p\to Vp}}{dt}\right|_{t=0} = \frac{f_V^2}{4\pi\alpha}\left.\frac{d\sigma^{\gamma p\to Vp}}{dt}\right|_{t=0}, \tag{2.35}$$

where the forward cross section $\left.\frac{d\sigma^{Vp\to Vp}}{dt}\right|_{t=0}$ for $\gamma p \to Vp$ equals an empirical formula, which is written as

$$\sigma(\gamma p) = b_V(XW_{\gamma p}^{\varepsilon} + YW_{\gamma p}^{-\eta}). \tag{2.36}$$

The function $\sigma(\gamma p)$ is fitted to experimental data to obtain the values for the b_V, X, Y, ε , and η parameters. Table 2.1 lists the values of the constants for $\gamma p \to Vp$ production. In equation 2.36, the first term is responsible for the growth of the cross section at high energies, the second term for the drop in the cross section at low energies. This formula was developed by Donnachie and Landshoff (DL) [80] [83].

Meson	b_V	X	ε	Y	η	$\frac{f_V^2}{4\pi\alpha_{em}}$
ρ^0	11	5.0	0.22	26.0	1.23	2.02
ω	10	0.55	0.22	18.0	1.92	23.1
ϕ	7	0.34	0.22	0	0	13.7
J/ψ	4	0.0015	0.80	0	0	10.4

Table 2.1: Constants for $\gamma p \to Vp$ production. The slopes b_V are in GeV^{-2}, while X and Y are in μb, for $W_{\gamma p}$ in GeV [56].

2.5.2 Dipole Approach Models

The CSS [84], LM [85] [86], and GM−GDGM [87] [88] models depend on a dipole model. The virtual photon fluctuates into a quark-antiquark pair (dipole) before the interaction. Figure 2.8 [79] shows the process of a dipole approach to the production of vector mesons. The photon fluctuates into a $q\bar{q}$ pair, forming a color dipole, the color dipole scatters from the proton, and forms a bound state, the vector meson, after scattering on the proton. The life time τ of the fluctuation can be long

relative to the interaction time, depending on the energy uncertainty of the $q\bar{q}$ pair. The fluctuation life time is written as $\tau \approx \frac{1}{M_p x}$, where M_p is the proton rest mass. This time is large with respect to proton radius, so the size of the dipole is constant throughout the interaction with the proton. The interaction of the dipole with the color field of the proton depends on the size of the dipole r , which is proportional to Q^{-1}. If the separation of the quark and antiquark pair is very small (high Q), the proton will be transparent to the dipole and the probability of interaction will be low. At large dipole sizes (low Q), the color dipole interacts strongly with the target. The total cross section of vector meson production, according to the Color Dipole Model, is written as:

$$\sigma(\gamma p \to V p) \propto \left| A(x, Q^2, \Delta) \right|^2, \tag{2.37}$$

where $A(x, Q^2, \Delta)$ is the scattering amplitude. This is written as:

$$A(x, Q^2, \Delta) = \int d\mathbf{r}^2 \int_0^1 dz \Phi_V^*(z, \mathbf{r}) \sigma_{q\bar{q}-p}(x, \mathbf{r}, \Delta) \Phi_\gamma(z, \mathbf{r}, Q^2), \tag{2.38}$$

where $\sigma_{q\bar{q}-p}(x, r, \Delta)$ is the cross section for the scattering of a dipole of size r from the proton, $\Phi_V^*(z, \mathbf{r})$ and $\Phi_\gamma(z, \mathbf{r}, Q^2)$ are the wave functions of the vector meson and the photon respectively, z is the fraction of the photon momentum carried by the quark, Δ denotes the transverse momentum lost by the outgoing proton ($t = -\Delta^2$), and x is the Bjorken variable.

The color dipole interacts with the proton through the exchange of two gluons, so the dipole cross section is sensitive to the gluon density distribution in the proton [89].

2.5.3 Models based on PDF of the target

The Adeluyi and Bertulani, or AB, model is designed to take different nuclear PDFs as input and so allow them to be compared to data [27, 31, 90]. In The MSTW08 model [91], the nPDF has no nuclear effect (no shadowing), the proton and the nucleus have the same density. In the HKN07 model [92] the nPDF has little nuclear effect (little shadowing), in EPS09 model [21] the nPDF

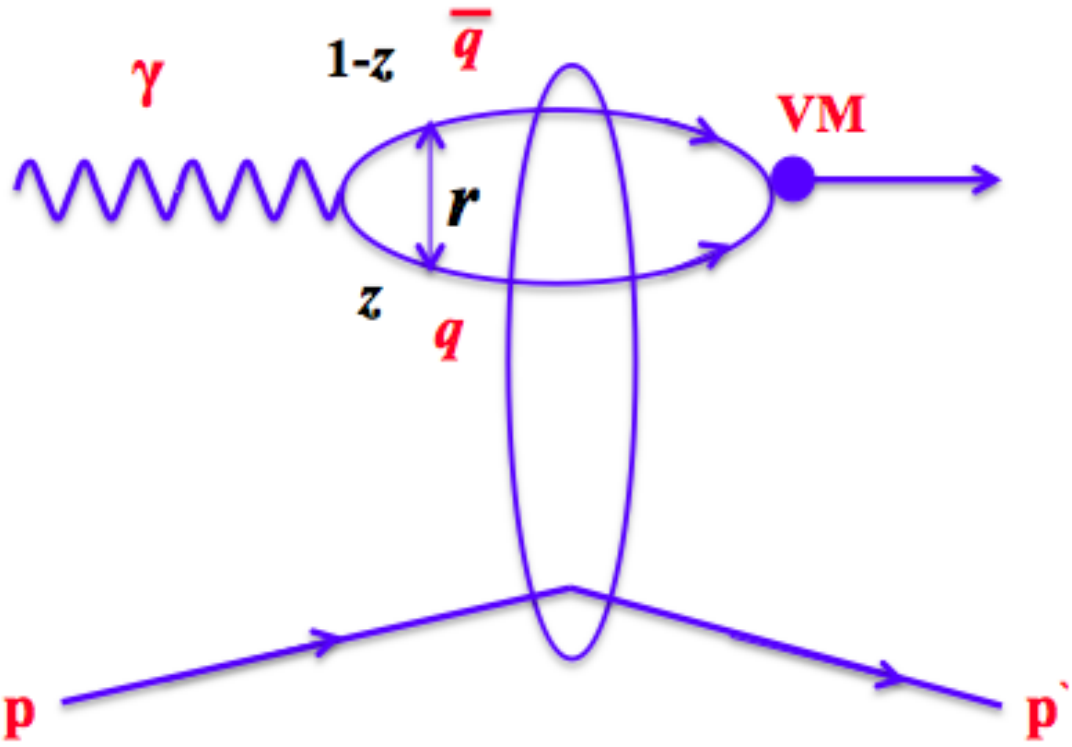

Figure 2.8: A dipole approach to vector meson V production. The photon fluctuates into a $q\bar{q}$ pair, forming a color dipole, the color dipole scatters from the proton, and forms a bound state, the vector meson, after scattering

has a moderate nuclear effect (moderate shadowing), and in the EPS08 model [24], the nPDF has a high nuclear effect (high shadowing). The photon-nucleus cross section is given by the LO *pQCD* formula of the two-gluon exchange with the phenomenological correction for next-to-leading-order effects ζ_V written as

$$\frac{d\sigma^{\gamma A\to VA}}{dt}|_{t=0} = \zeta_V \frac{16\pi^3\alpha_s^2\Gamma_{ee}}{3\alpha M_V^5}[xg_A(x,Q^2)]^2 \tag{2.39}$$

at zero momentum transfer in the interaction vertex (t=0), also called as the forward cross section. This is identical to Equation 2.21 when $g_H(x,Q^2)$ is the nuclear-gluon distribution $g_A(x,Q^2)$. This gluon distribution is evaluated at the scale $Q^2 = M_V$, where M_V is the mass of the vector meson.

The cross section in Equation 2.39 can be extended to other values of t using Equation 2.30.

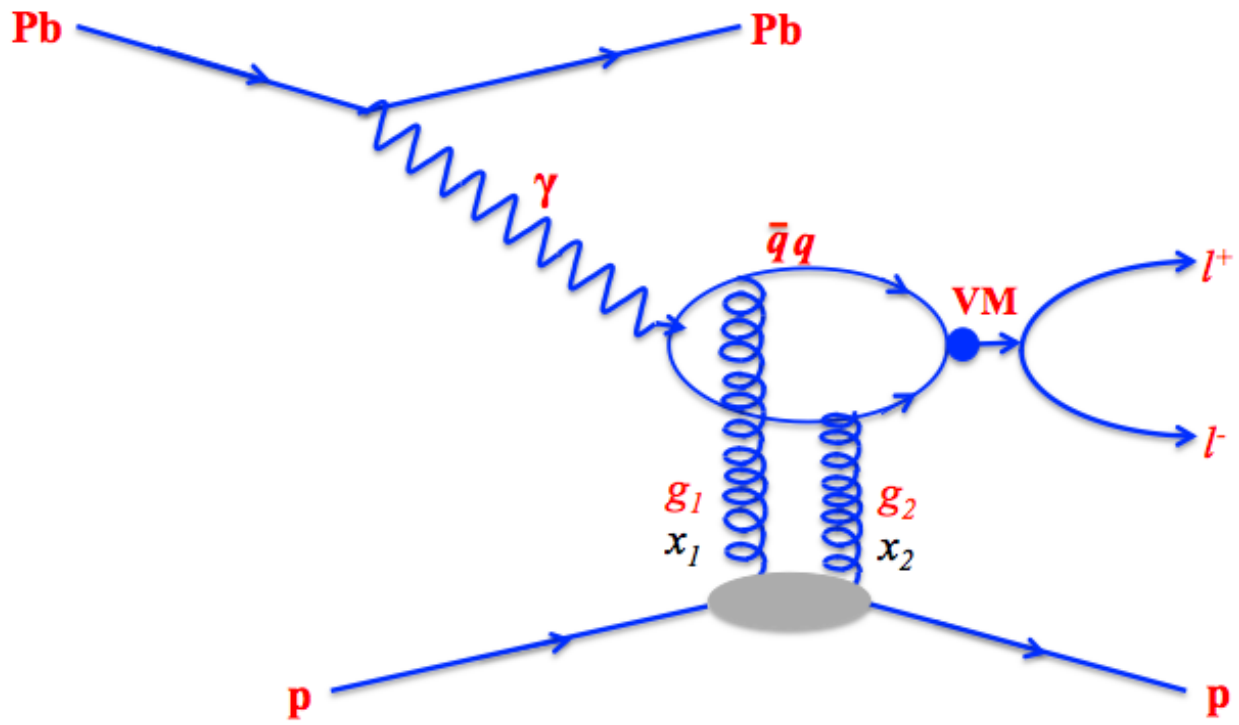

Figure 2.9: Vector meson production in perturbative QCD. The photon fluctuates into a $q\bar{q}$ pair, which scatters from the proton via the exchange of two gluons. The vector meson is created after the interaction.

The total cross section can then be found by integrating over all possible t values.

$$\sigma^{\gamma A\to VA} = \frac{d\sigma^{\gamma A\to VA}}{dt}|_{t=0}\int_{t_{min}(k)=(\frac{M_V^2}{4k\gamma})^2} dt \mid F(t) \mid^2 . \tag{2.40}$$

The AB model uses a simple Wood-Saxon parametrization of the nuclear density which is given by:

$$\rho(r) = \frac{\rho_o}{1+\exp\frac{r-R_A}{d}}, \tag{2.41}$$

where ρ_o is the central density and d is the skin depth. The rapidity y of the produced vector meson is given by the photon wavenumber using the relation $k = \frac{M_V}{2}\exp y$. Figures 2.10, and 2.11 show calculations of exclusive photoproduction of both J/ψ and Υ in PbPb and pPb collisions at $\sqrt{s_{NN}} = 5$ TeV using the AB model with several different nuclear PDFs as input [31]. The PDF

with the strongest shadowing, EPS08, produces the smallest cross section for J/ψ and Υ. On the other hand the MSTW 08 PDF is simply scaled up from the proton PDF with no shadowing and so gives the largest cross section. For pPb collisions the distribution is asymmetric in rapidity. On the proton side, i.e., positive rapidity the yield depends little upon the nuclear PDF while on the lead-going side, i.e., negative rapidity, there is a noticeable dependence of the final yield on the PDFs.

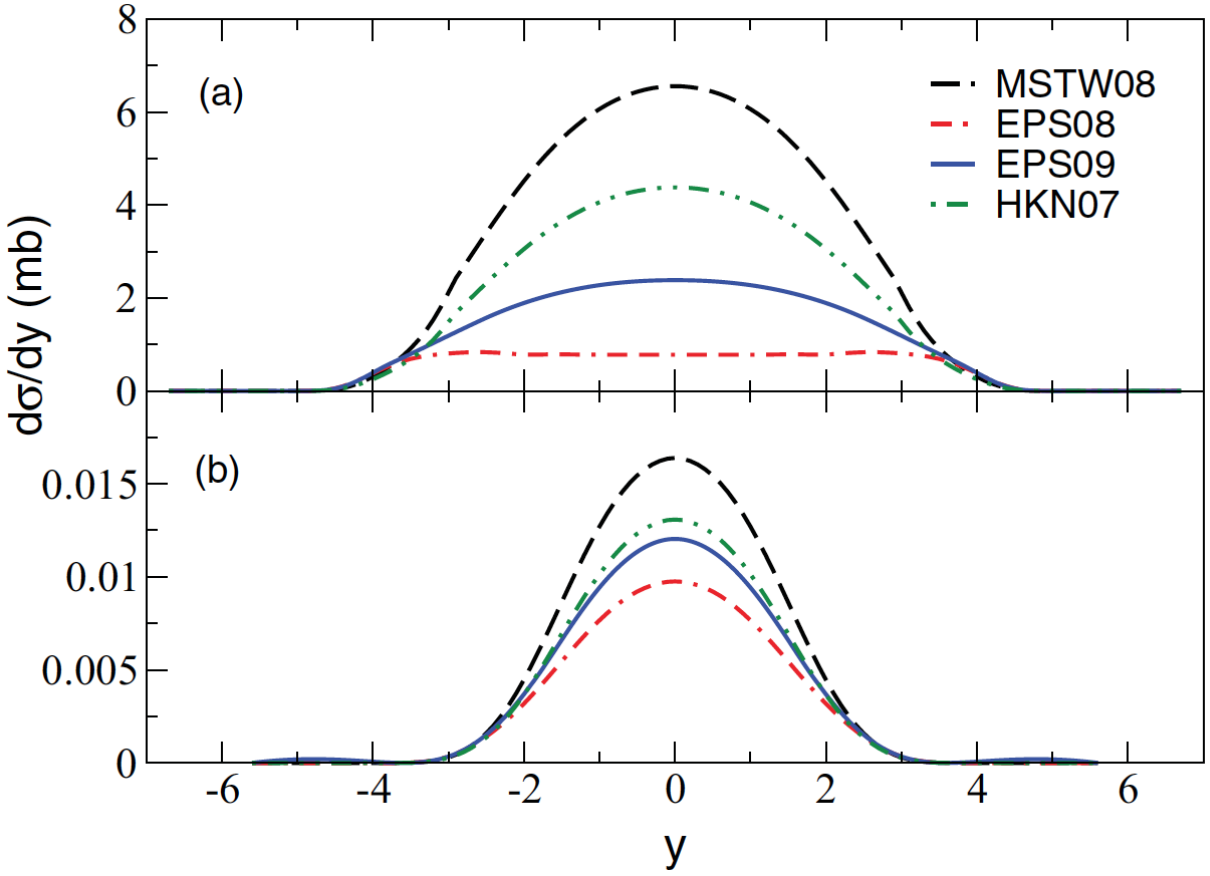

Figure 2.10: Calculation for exclusive photoproduction of J/ψ (top) and Υ (bottom) in PbPb collisions at $\sqrt{s_{NN}} = 5$ TeV using AB model, [31]. Dashed, solid, dash-dotted, and dash-double-dotted lines are results from MSTW08, EPS09, EPS08, and HKN07 parton distributions, respectively.

2.5.4 STARLIGHT

STARLIGHT is a program used to calculate the cross section for a variety of UPC final states via Monte Carlo simulation of two-photon and photon-Pomeron interactions between relativistic

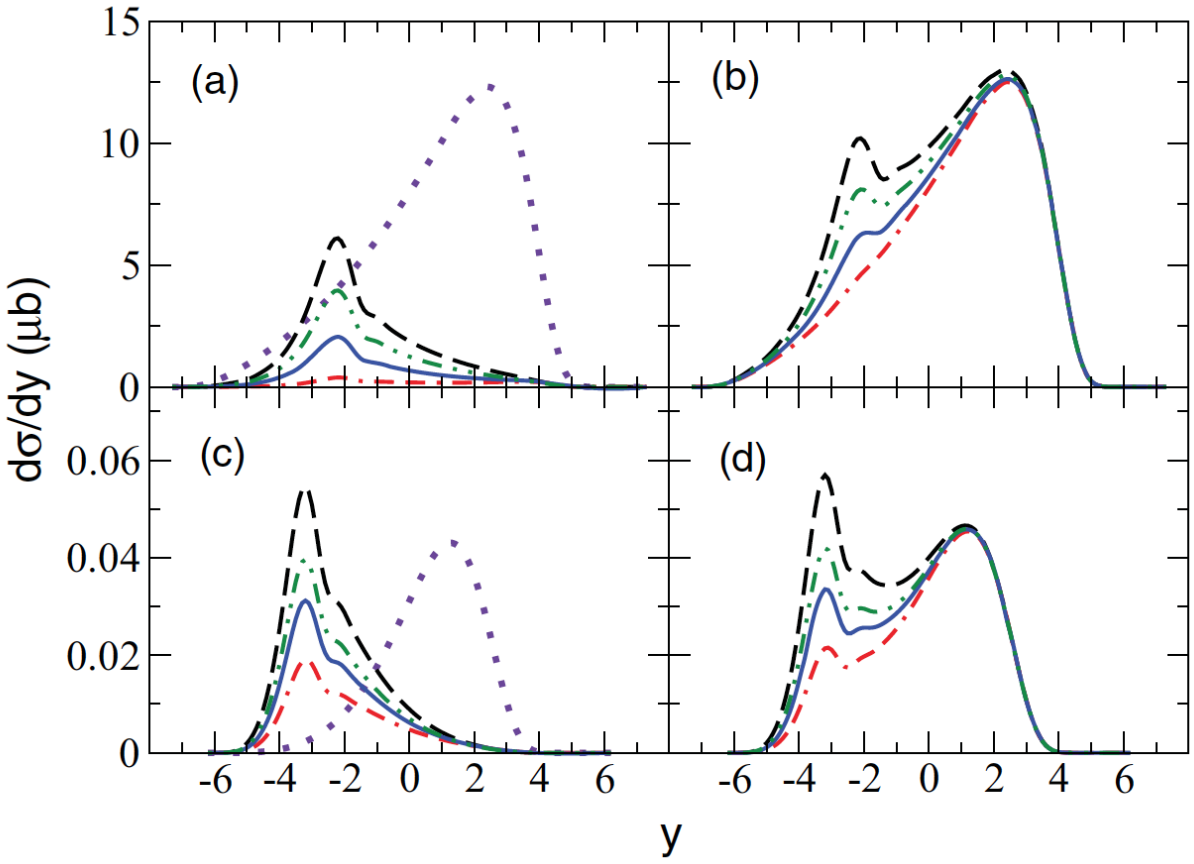

Figure 2.11: Calculation for exclusive photoproduction of J/ψ (top) and Υ (bottom) in pPb collisions at $\sqrt{s_{NN}} = 5$ TeV using AB model, [31]. Dashed, solid, dash-dotted, and dash-double-dotted lines are results from MSTW08, EPS09, EPS08, and HKN07 parton distributions, respectively.

nuclei and protons [93]. The cross sections are mostly based on parameterized HERA data for $\gamma p \to V p$. The J/ψ, ψ', and Υ cross sections, $\sigma(\gamma p \to V p)$, are parameterized as a function of the $W_{\gamma p}$ center-of-mass energy using the equation

$$\sigma(\gamma + p \to V + p) = \sigma_P . \left| 1 - \frac{(m_p + m_V)^2}{W_{\gamma p}^2} \right|^2 W_{\gamma p}^{\varepsilon}, \tag{2.42}$$

where σ_P is the cross section of Pomeron exchange. The value of the parameters were obtained from fitting experimental data. For the J/ψ, $\sigma_P = 4.06$ nb and $\varepsilon = 0.65$. The vector mesons are decayed assuming that the photon polarization is parallel to the beam axis.

The cross sections for coherent production from nuclear targets are determined using:

$$\sigma(AA \to AAV) = 2\int dw \frac{dN_\gamma(w)}{dw}\sigma(\gamma A \to VA) \tag{2.43}$$

$$= 2\int dw \frac{dN_\gamma(w)}{dw}\int dt \frac{d\sigma(\gamma A \to VA)}{dt}|_{t=0}|F(t)|^2, \tag{2.44}$$

where $F(t)$ is the nuclear form factor and $N_\gamma(w)$ is the photon flux obtained by integrating Equation 2.10 over impact parameter space, subject to the condition that there is no hadronic interaction.

The incoherent photonuclear cross section is calculated by assuming vector meson dominance and using the classical Glauber expression for the total inelastic cross section. This gives

$$\sigma(\gamma + A \to V + A) = \frac{4\pi\alpha}{f_V^2}\int (1 - \exp(-\sigma_{VN}T(b))db^2. \tag{2.45}$$

Here the term inside the bracket corresponds to the probability of having at least one vector meson-nucleon interaction at impact parameter b.

2.6 Experimental Results on Exclusive J/ψ Production

2.6.1 Photon-Proton Results

2.6.1.1 $p\bar{p}$ results from CDF experiment of the Tevatron.

The CDF collaboration has measured exclusive photoproduction of J/ψ in $\bar{p}p$ collisions at $\sqrt{s_{NN}} =$ 1.96 TeV. The cross section $\frac{d\sigma}{dy}\big|_{y=0}$ is $3.92 \pm 0.25(stat) \pm 0.52(syst) nb$ [94]. The data are consistent with a power law in $W_{\gamma p}$ with $\delta = 0.72$ [95].

2.6.1.2 ep results from H1 and Zeus at HERA

The H1 detector measured J/ψ photoproduction using electron-proton collisions in the range $40 \leq W_{\gamma p} \leq 305$ GeV and $40 \leq W_{\gamma p} \leq 160$ GeV. The data are consistent with a power law in $W_{\gamma p}$ with $\delta = 0.754 \pm 0.033(stat) \pm 0.032(syst)$, and the results show no Q^2 dependence [96]. Also, the H1 detector measured the cross sections for elastic and proton-dissociative photoproduction of J/ψ mesons in the range $25 \leq W_{\gamma p} \leq 110$ GeV, The data are consistent with a power law in $W_{\gamma p}$ with $\delta = 0.67 \pm 0.03$ [52]. The ZEUS detector measured J/ψ photoproduction using electron-proton collisions in the range $20 \leq W_{\gamma p} \leq 290$ GeV, the data are consistent with a power law in $W_{\gamma p}$ with $\delta = 0.69 \pm 0.02(stat) \pm 0.03(syst)$ [97].

2.6.1.3 pp results from the LHCb experiment

The LHCb collaboration has measured exclusive photoproduction of the J/ψ in proton-proton collisions at $\sqrt{s} = 7$ TeV. The cross section times the branching fraction to two muons with pseudorapidities between 2.0 and 4.5 are measured to be $307 \pm 21 \pm 36$ pb for exclusive J/ψ. The data are consistent with a power law dependence and with the previous results from H1 and ZEUS. Figure 2.12 shows the cross section $\sigma(\gamma + p \rightarrow J/\psi + p)$ versus the photon-proton center of mass energy $W_{\gamma p}$ for LHCb, H1 and ZEUS [32].

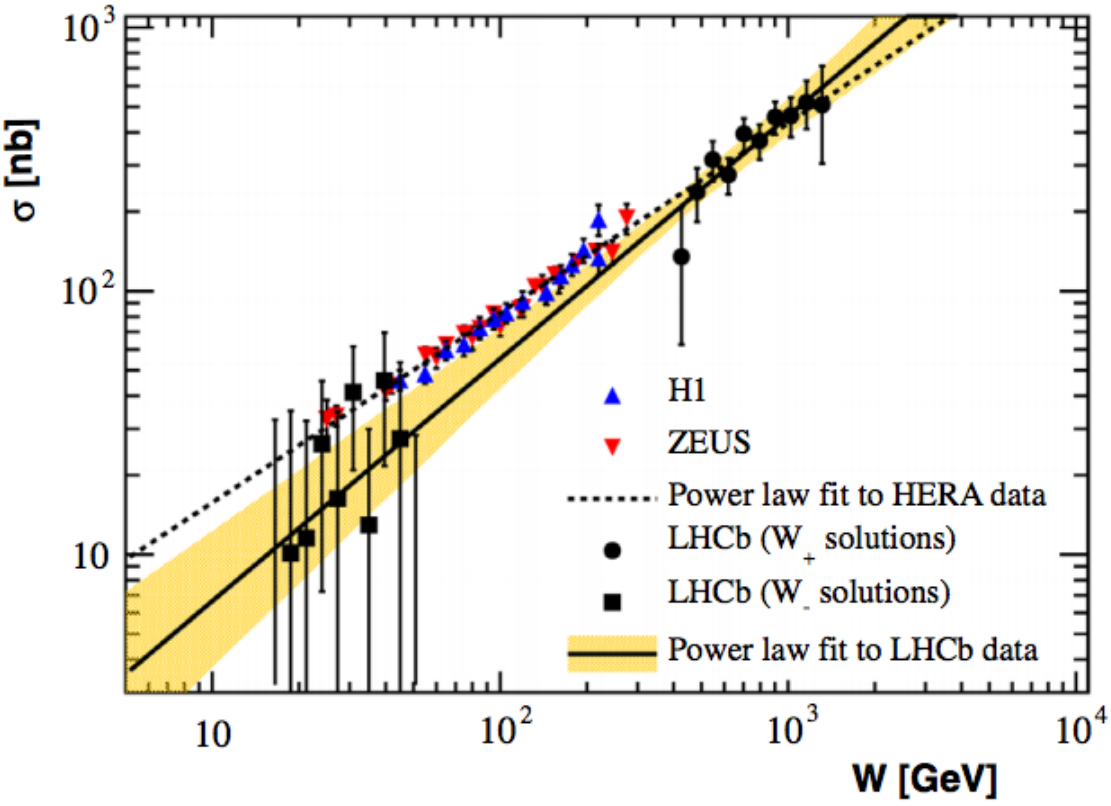

Figure 2.12: J/ψ photoproduction cross section versus the center-of-mass energy of the photon-proton system . The blue (red) triangles represent the data from H1 (ZEUS). The black dots and squares represent the data from LHCb. The dashed and full lines are the power law dependences determined from the HERA and LHCb data, respectively. The uncertainty on the LHCb power law determination is shown by the shaded band [32].

2.6.1.4 pPb results from the ALICE experiment

The ALICE collaboration has measured exclusive photoproduction of J/ψ using ultra-peripheral proton-lead collisions at $\sqrt{s_{NN}} = 5.02$ TeV. The dimuon invariant mass spectra in two rapidity ranges are shown in Figure 2.13. The J/ψ peak is clearly visible in both data sets, and is well described by a Crystal Ball parameterization [55]. The dimuon continuum is well described by an exponential as expected from two-photon production of continuum $\gamma\gamma \to \mu^+\mu^-$. The dimuon p_T spectra for J/ψ candidates are shown in Figure 2.14 together with estimates for the non-exclusive (red), $\gamma\gamma$ (green), and γPb (pink) contributions.

Figure 2.15 shows the cross section $\sigma(\gamma + p \to J/\psi + p)$ versus the photon-proton center of

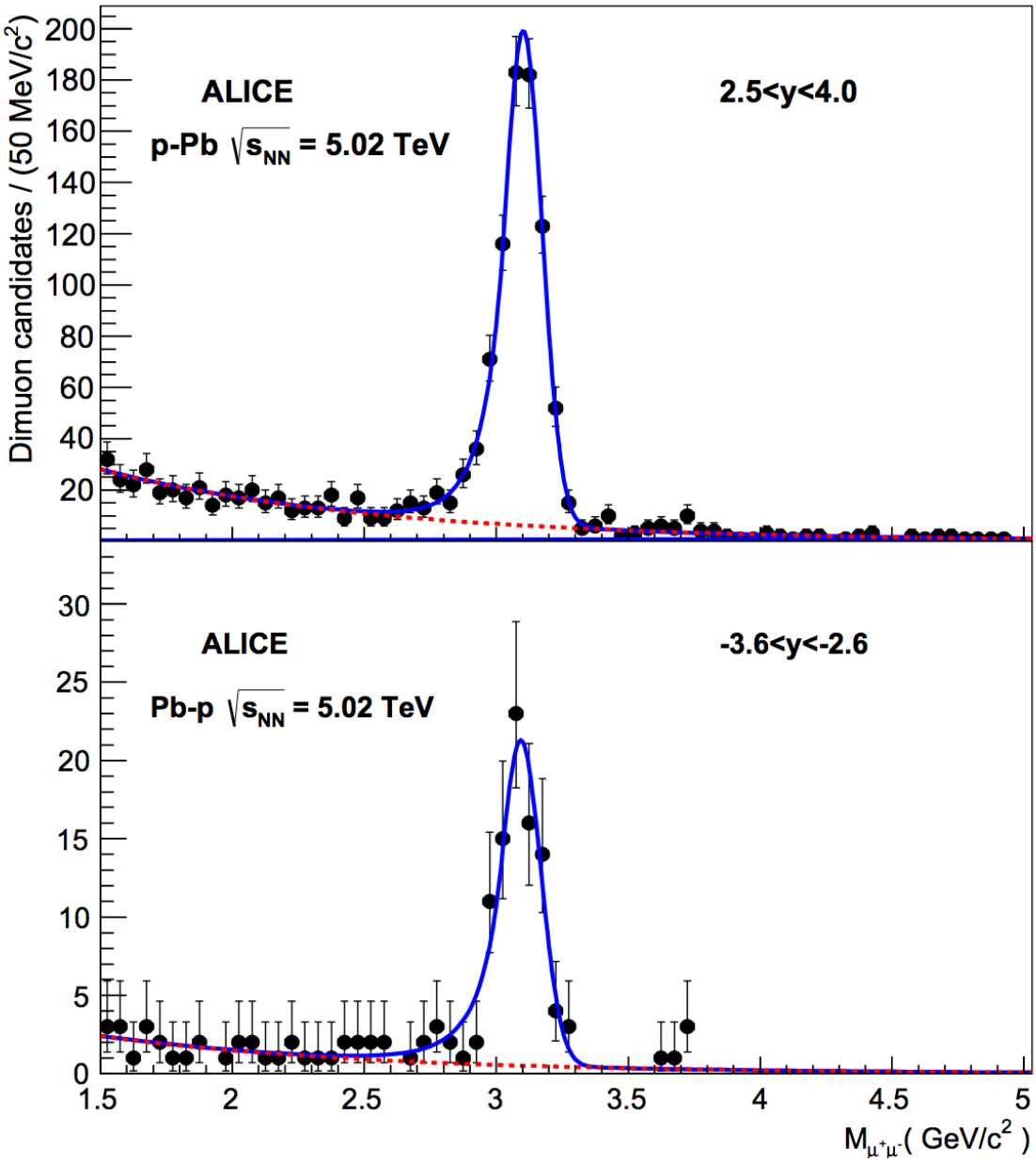

Figure 2.13: Dimuon invariant mass distribution for ultra-peripheral pPb collisions at $\sqrt{s_{NN}} =$ 5.02 TeV for two ranges of rapidity. The peak is fitted by a Crystal Ball function (blue) and the background by an exponential (dashed red) [33]

.

mass energy $W_{\gamma p}$ for both the ALICE data and the H1 and ZEUS measurements from the HERA e-p collider. The predictions of several theoretical models are also shown. The data cover the energy range 20 to 700 GeV, corresponding to values of Bjorken-x between $x \sim 10^{-3}$ and $x \sim 10^{-5}$. The three experiments have also fit their data to a power law of the form, $\sigma \propto W^{\delta}$. A fit to the ALICE

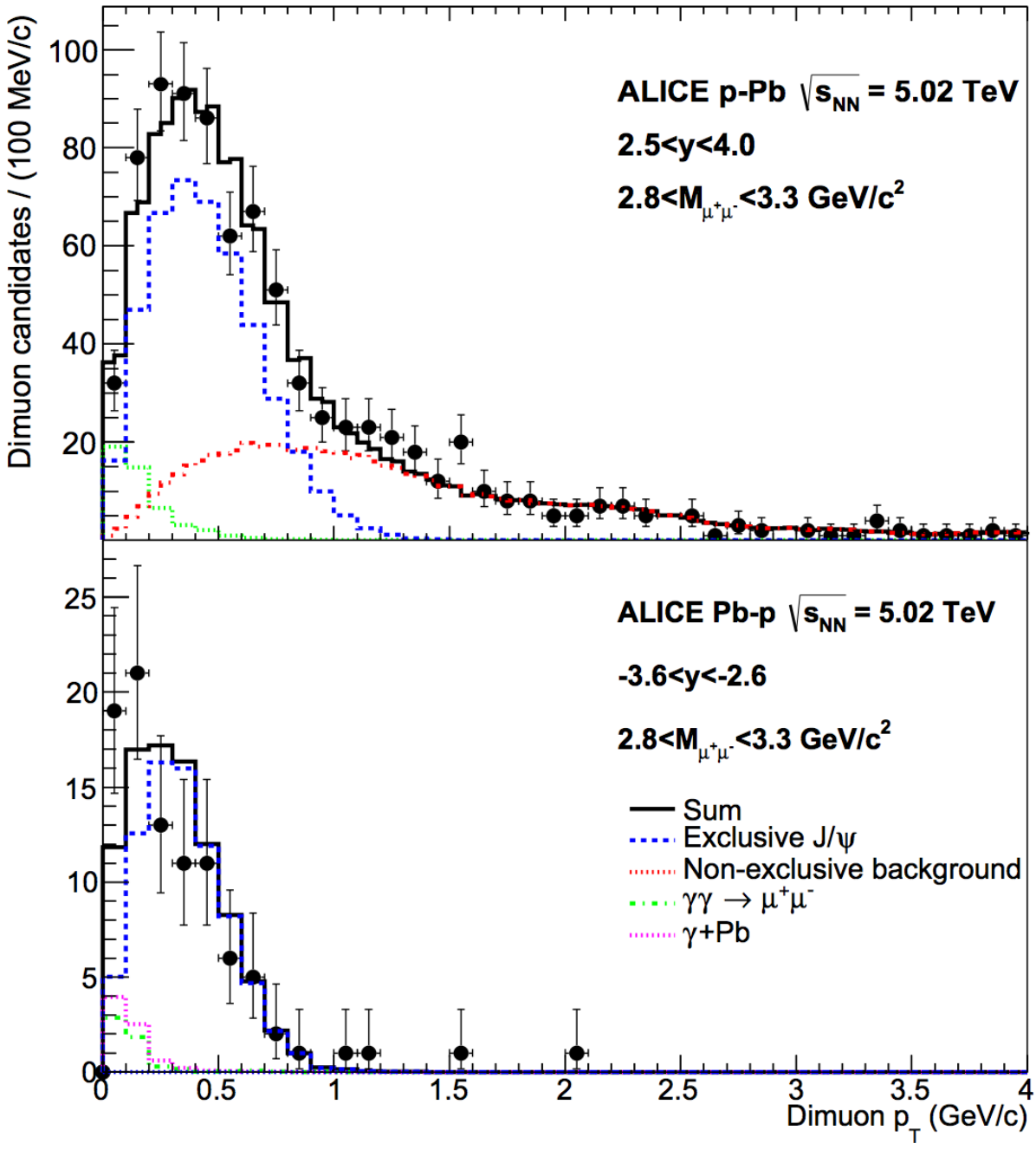

Figure 2.14: The dimuon p_T spectra for J/ψ candidates from ultra-peripheral pPb collisions at $\sqrt{s_{NN}} = 5.02$ TeV in two different rapidity ranges. Also shown are template fits to various processes; exclusive J/ψ (dashed blue), non-exclusive J/ψ (red), $\gamma\gamma$ (green), and γPb (pink) [33]

.

data gives $\delta = 0.68 \pm 0.06$ (stat+syst). Thus, for protons there is no significant change in the evolution of the gluon density between HERA and LHC energies.

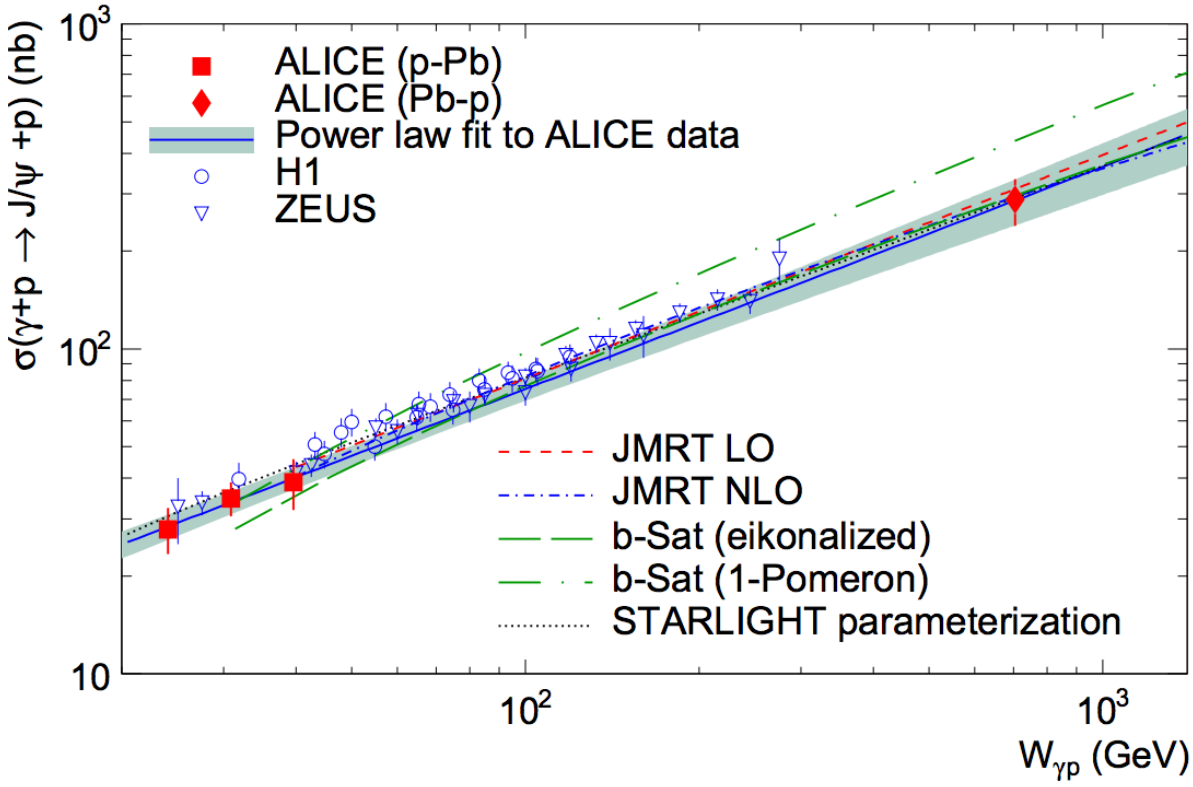

Figure 2.15: The measured cross sections $\sigma(\gamma + p \to J/\psi + p)$ versus center-of mass energy $W_{\gamma p}$ for ALICE, H1 and ZEUS together with several model predictions [33]

.

2.6.2 Heavy Ion Results

The PHENIX collaboration has measured the cross section for the photoproduction of J/ψ in ultra-peripheral AuAu collisions at $\sqrt{s_{\rm NN}} = 200$ GeV at mid-rapidity in coincidence with forward neutrons [34]. Their measurement was done using the $J/\psi \to e^+e^-$ decay channel. Figure 2.16 shows the invariant mass distribution of the e^+e^- pairs. The data show a clear J/ψ peak above an exponential background. Figure 2.17 shows the p_T spectrum of the data. There is an enhancement

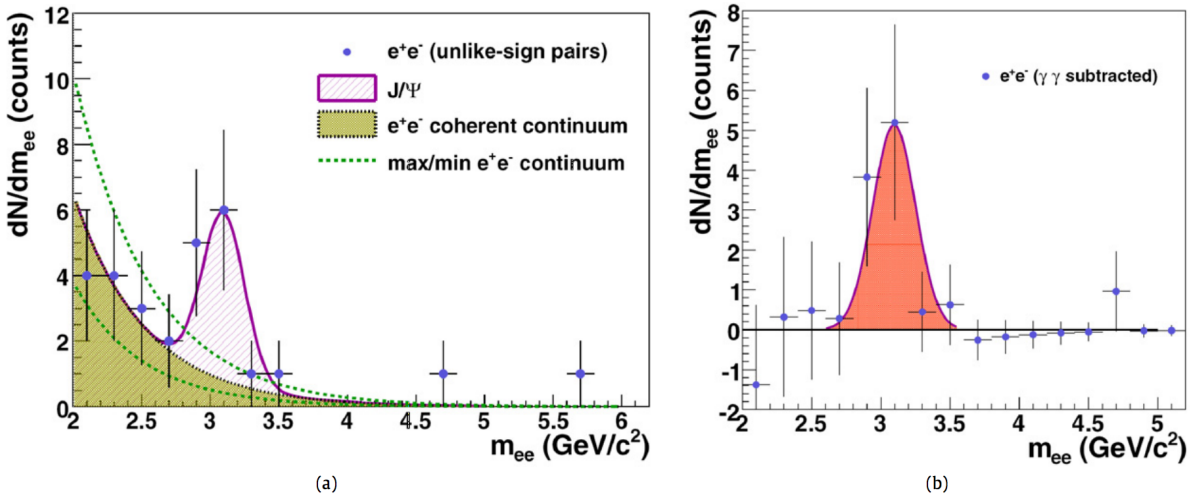

Figure 2.16: e^+e^- invariant mass distribution a) fitted to the combination of a di-electron continuum (exponential) and a J/ψ (Gaussian) signal. b) distribution after subtraction of the fitted di-electron continuum background [34]

of events with very low transverse momentum, consistent with coherent production, but also a significant number of higher p_T events. These are believed to be due to incoherent production, i.e., the interaction of a photon with a single nucleon. Figure 2.18 compares the PHENIX $J/\psi + X_n$ cross section to several theoretical models. Unfortunately, the number of events are too small to allow the data to distinguish between the models.

The ALICE collaboration has measured J/ψ production in ultra-peripheral PbPb collisions at $\sqrt{s_{NN}} = 2.76$ TeV using both the di-muon and di-electron channels at central [28] and forward rapidity [35]. Figure 2.19 shows the invariant mass (left) and p_T spectra (right) for di-muon pairs at forward rapidity from ultra-peripheral PbPb events at $\sqrt{s_{NN}} = 2.76$ TeV. The number of J/ψ events was extracted by fitting the invariant mass distribution in Fig. 2.19 to the sum of a Crys-

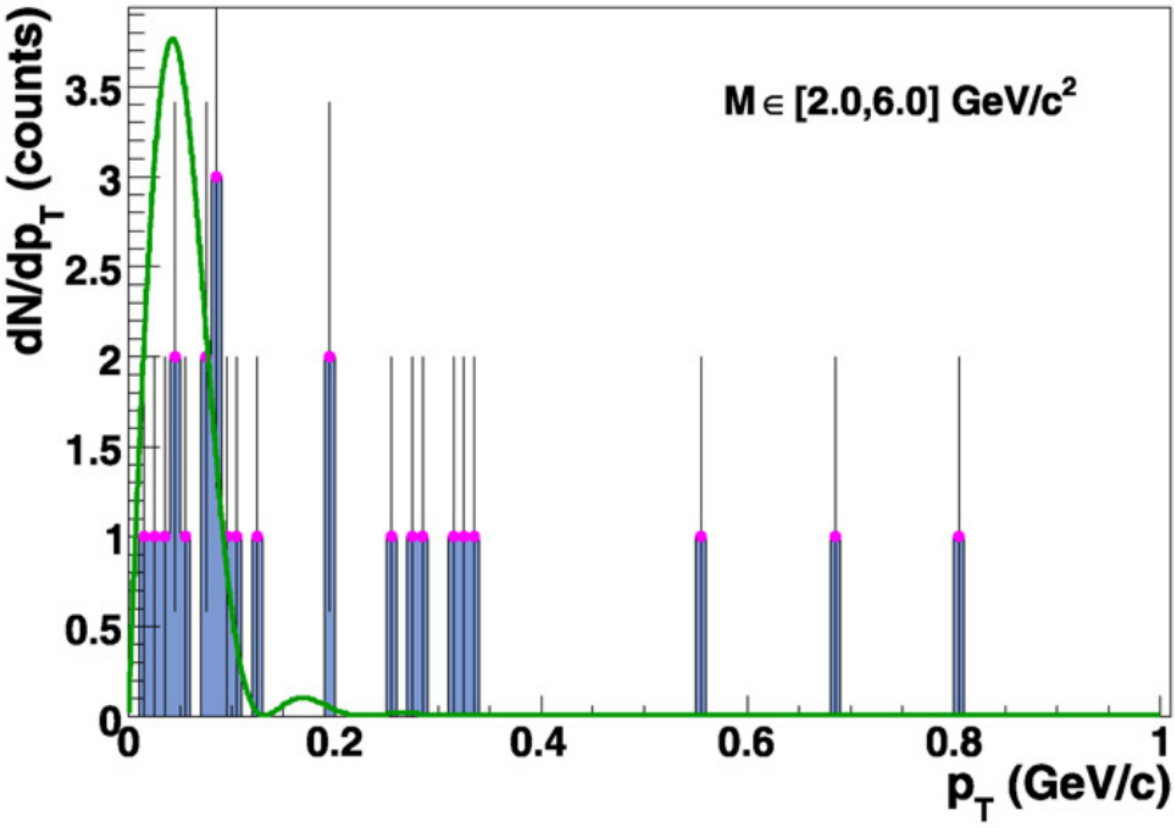

Figure 2.17: Transverse momentum spectrum of e^+e^- pairs produced in ultra-peripheral Au-Au collisions at $\sqrt{s_{NN}} = 200$ GeV [34].

tal Ball function for the signal, and an exponential for the two-photon background. This gave an extracted number of J/ψ events $N_{yield} = 96 \pm 12(stat) \pm 6(syst)$. The systematic error on the yield was obtained by varying the Crystal Ball tail parameters. The right-hand panel of Figure 2.19 shows the p_T distribution of the J/ψ. The histograms show the expected contribution from coherent J/ψ production, incoherent J/ψ production, J/ψ from the decay $\psi' \rightarrow J/\psi + X$, and two-photon production of di-muon pairs. The contribution from hadronic J/ψ production was estimated from the measured yield above $p_T > 1$ GeV/c, where the contribution from photoproduction is insignificant. These estimates showed that the hadronic contribution is negligible for $p_T < 0.3$ GeV/c.

At mid-rapidity ALICE has measured the yield of both coherent and incoherent J/ψ mesons [28]. Figure 2.20 shows the mass distribution for dimuon pairs at central rapidity for coherent,

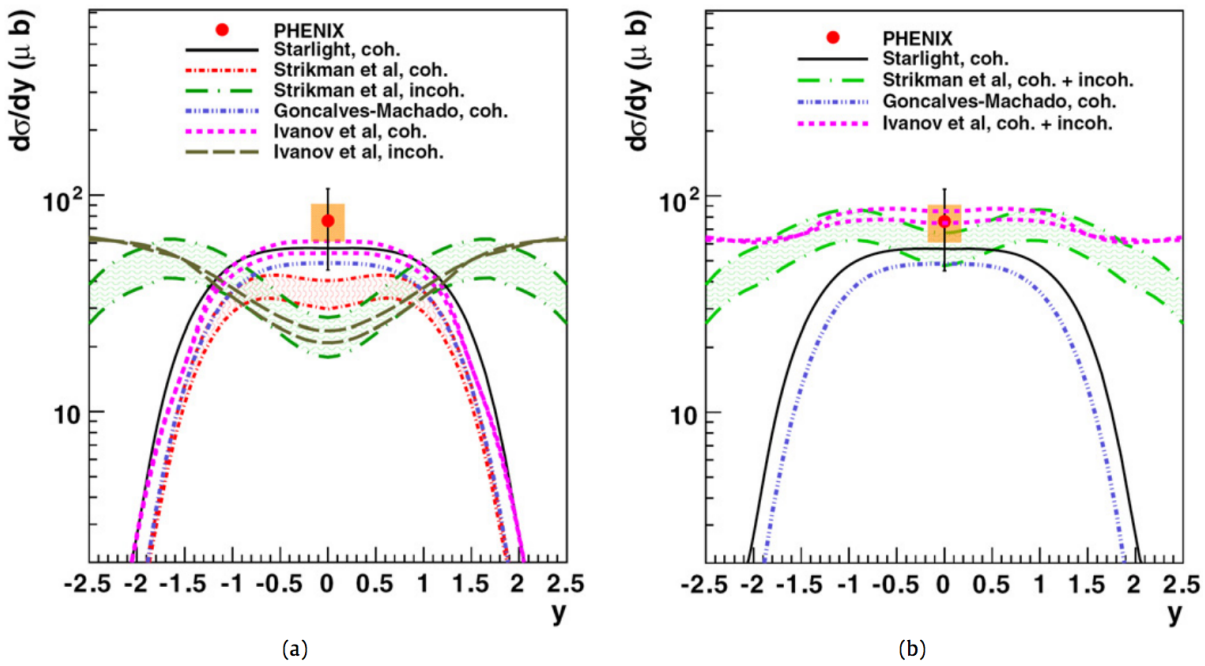

Figure 2.18: Comparison of theoretical calculations with the PHENIX measurement of ultra-peripheral J/ψ production in Au-Au collisions at $\sqrt{s_{NN}} = 200$ GeV. In the left panel, the theoretical coherent and incoherent components are shown separately while in the right panel they are added together [34].

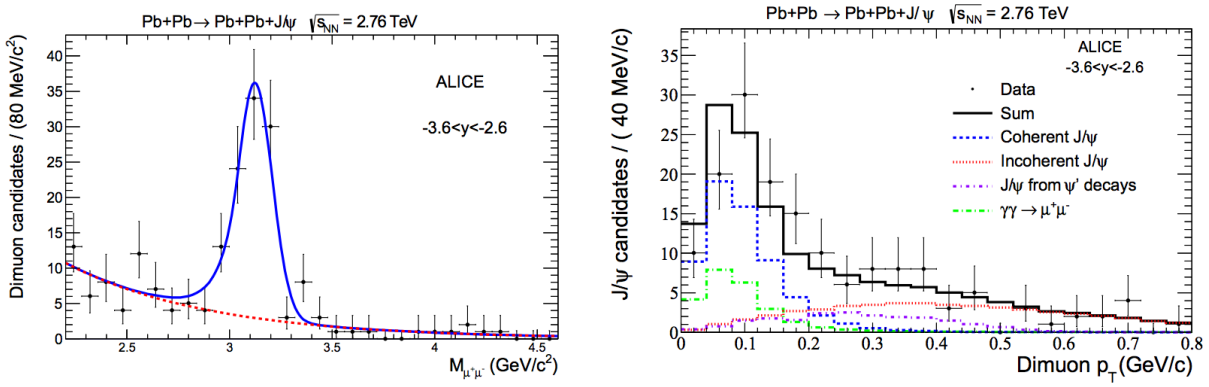

Figure 2.19: Invariant mass distribution (left) and p_T spectrum (right) for di-muons at forward rapidity from ultra-peripheral PbPb collisions at $\sqrt{s_{NN}} = 2.76$ TeV recorded by the ALICE collaboration. The curve in the left panel shows the sum of a Crystal Ball function and an exponential fitted to the data. The right panel shows the p_T distribution for J/ψ candidates with $2.8 < M_{inv} < 3.4$ GeV/c^2 [35]

$p_T^{\mu\mu} < 200$ MeV$/c$, and incoherent $p_T^{\mu\mu} > 200$ MeV$/c$ samples. Clear J/ψ mass peaks are observed. As above, yields were extracted using Crystal Ball fits and cross sections are determined.

Figure 2.21 shows $d\sigma/dy$ for both coherent and incoherent events together with several model comparisons. The data are below the predictions of the STARLIGHT event generator, which has no nuclear effects, and tend to be closer to models such as AB-EPS09 which has moderate gluon shadowing at low x.

CMS has measured the cross section of coherent J/ψ photoproduction accompanied by forward neutrons in ultra-peripheral PbPb collisions at $\sqrt{s_{NN}} = 2.76$ TeV for $1.8 < y < 2.3$. Figure 2.22 shows the dimuon invariant mass and p_T distribution for dimuon pairs produced in ultra-peripheral PbPb collisions at $\sqrt{s_{NN}} = 2.76$ TeV. A clear J/ψ peak is seen in the mass distribution. The p_T spectrum shows a very pronounced coherent peak followed by a tail from incoherent interactions. Since the CMS results were taken with a neutron trigger, in order to compare them to those of ALICE it is necessary to scale them up by the ratio of the cross section with and without neutron production. This was done using the STARLIGHT event generator. STARLIGHT gives a good description of the ratio of the various neutron breakup modes measured by CMS and also of the fraction of coherent J/ψ events with no neutron emitted with respect to the total number of coherent J/ψ events, as measured by ALICE [28]. Figure 2.23 shows the $d\sigma/dy$ distribution for coherent J/ψ production in ultra-peripheral PbPb collisions at $\sqrt{s_{NN}} = 2.76$ TeV from both the ALICE and CMS collaborations.

The impulse approximation calculation uses HERA data for exclusive J/ψ photoproduction in γp interactions to estimate coherent J/ψ production in γ-nucleus collisions [36]. It neglects all nuclear effects and significantly overestimates the data. The leading twist calculation includes a mechanism for the merging of low x gluons within a nucleus [37]. It is consistent with the data at all rapidities. This suggests that gluon shadowing is present in heavy nuclei.

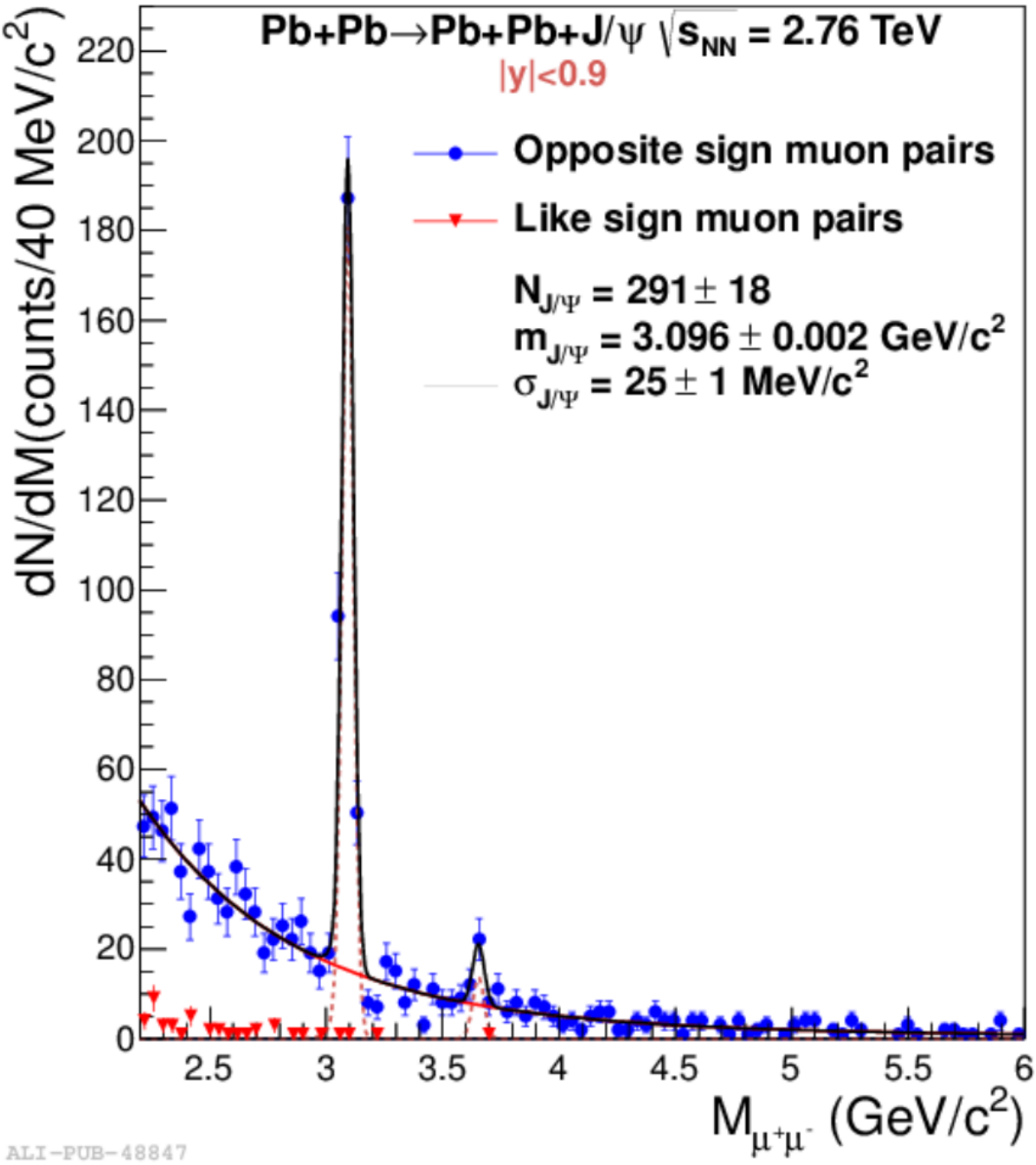

Figure 2.20: Invariant mass spectrum of muon pairs at mid-rapidity for events with less than 6 forward neutrons for ultra-peripheral PbPb collisions at $\sqrt{s_{NN}} = 2.76$ TeV as measured by ALICE [28].

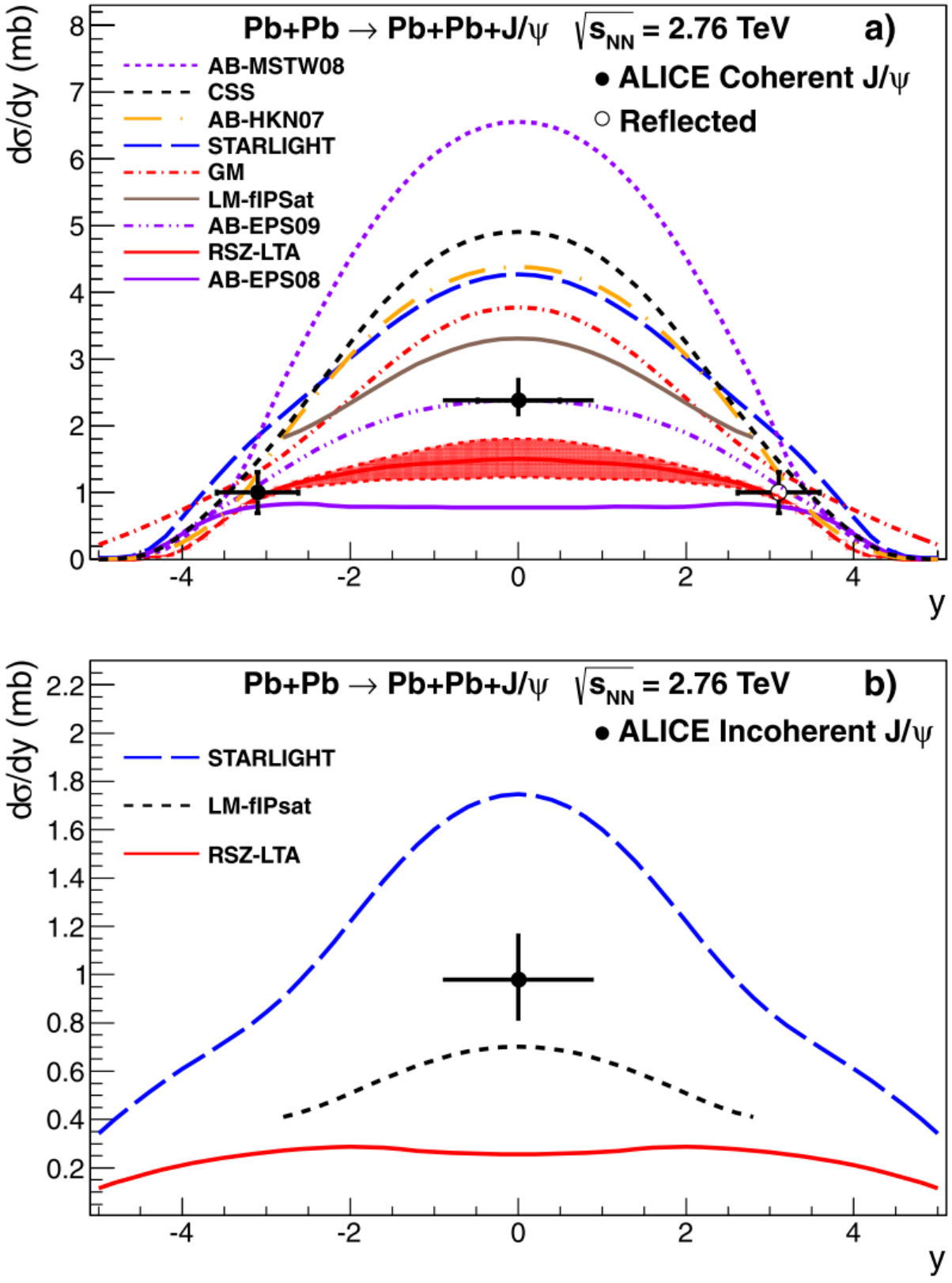

Figure 2.21: Measured differential cross section of J/ψ photoproduction at $0.9 < y < 0.9$ in ultra-peripheral PbPb collisions at $\sqrt{s_{NN}} = 2.76$ TeV as measured by ALICE for coherent (top) and incoherent (bottom) events [28]. The error bar is the quadratic sum of the statistical and systematic errors.

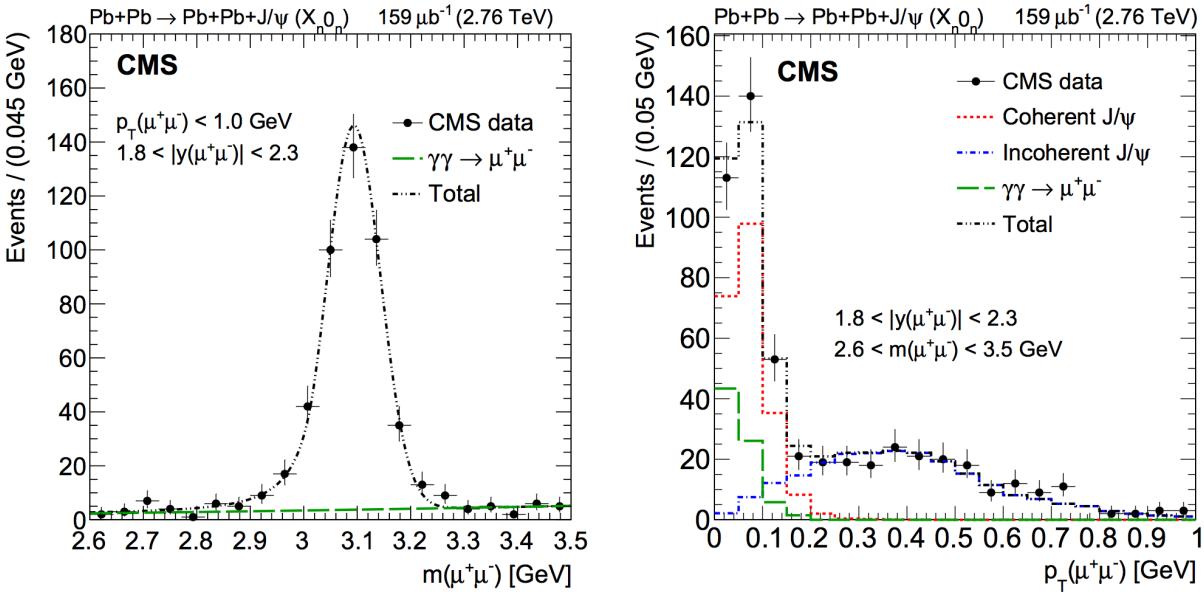

Figure 2.22: Invariant mass (left) and p_T (right) distributions from $\mu^+\mu^-$ pairs from ultra-peripheral PbPb collisions at $\sqrt{s_{NN}} = 2.76$ TeV for the X_n0_n break-up mode. Template fits to the $\gamma\gamma$ (green), incoherent J/ψ (blue) and coherent J/ψ (red) are also shown. The data are not corrected by acceptance and efficiencies, and the MC templates are folded with a simulation of the detector response [30]

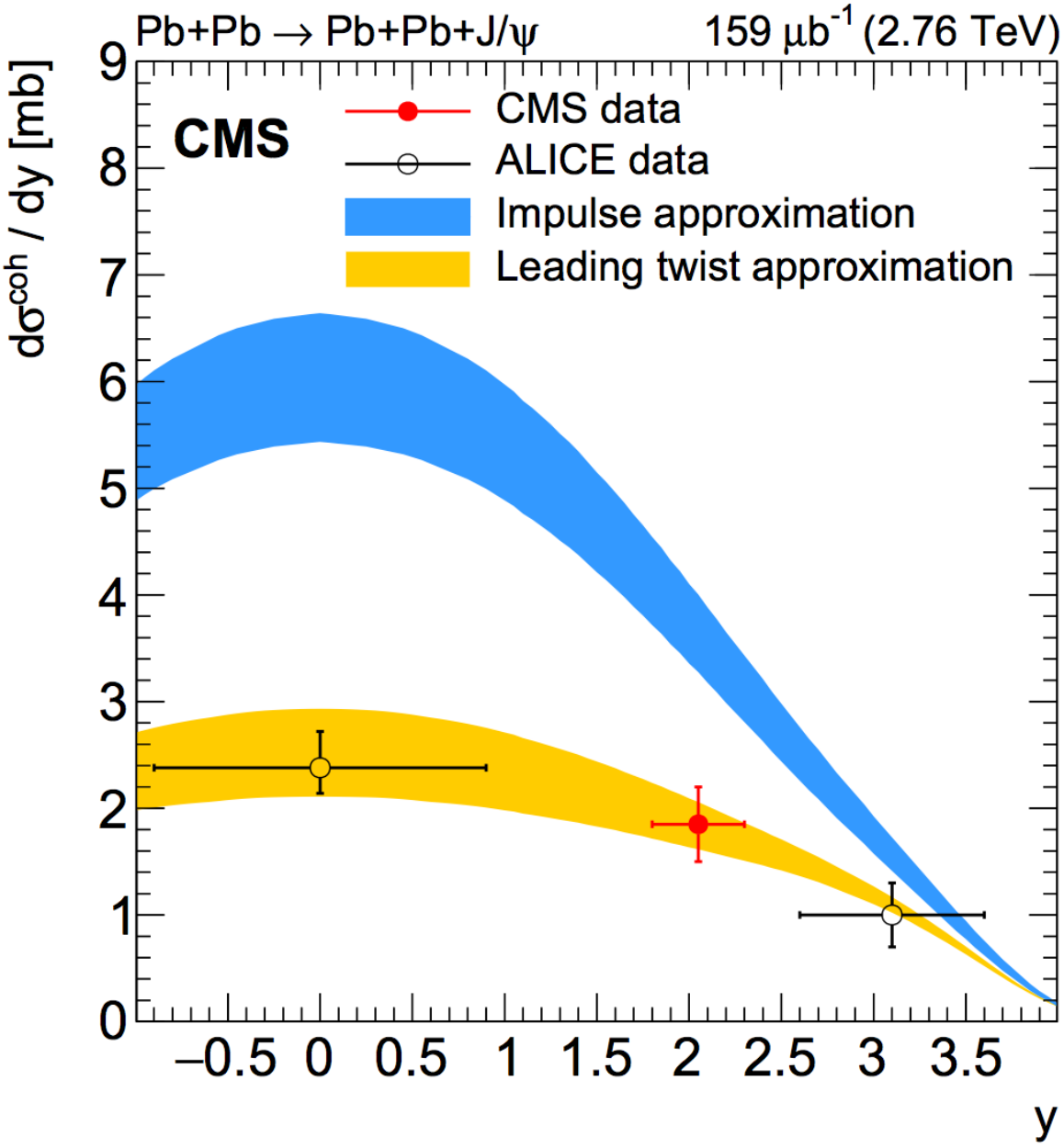

Figure 2.23: Differential cross section versus rapidity for coherent J/ψ production in ultra-peripheral PbPb collisions at $\sqrt{s_{NN}} = 2.76$ TeV, measured by ALICE at mid rapidity [28] and forward rapidity [35] and CMS at forward rapidity [30]. The vertical error bars include the statistical and systematic uncertainties added in quadrature, and the horizontal bars represent the range of the measurements in y. Calculations based upon the impulse [36] and leading twist approximations [37] are also shown.

Chapter 3

The Compact Muon Solenoid

3.1 Introduction

CMS is a general-purpose detector, which is designed to cover the widest possible range of physics, from the Higgs boson to supersymmetry (SUSY) and extra dimensions. CMS is a technologically advanced detector comprised of many layers. The length is 21m, the diameter is 15m and the weight is 14000 tons. It is one of the four LHC experiments, sitting at a depth of 100m underground near the French village of Cessy as shown in Figure 3.1.

Figure 3.2 shows a perspective view of CMS. The magnet is the core of CMS. This magnet is a huge superconducting solenoid. Inside the solenoid, working outward from the beam, are a silicon tracker, a lead tungstate crystal electromagnetic calorimeter (ECAL), and a brass/scintillator hadron calorimeter (HCAL). Each calorimeter has a barrel and two endcaps. Outside the solenoid, there are muon detectors with a barrel and two endcaps. They are imbedded in the steel flux-return yoke. On either side of the main detector, there is an attached Hadronic Forward calorimeter (HF) at distance 11m, and a Zero Degree Calorimeter (ZDC) at a distance of 140 m from the interaction point IP [41] [98].

A transverse slice of the CMS detector is shown in Figure 3.3. Figure 3.3 also shows the response of the subdetectors to different particles emerging from proton-proton and heavy ion collisions. The silicon tracker measures the positions of the charged particles to record their paths. The ECAL measures the energies of photons and electrons. The HCAL measures the energies of the hadrons (for example, neutrons, protons, and charged pions). The muon detectors track the positions of the muons to measure their momentum.

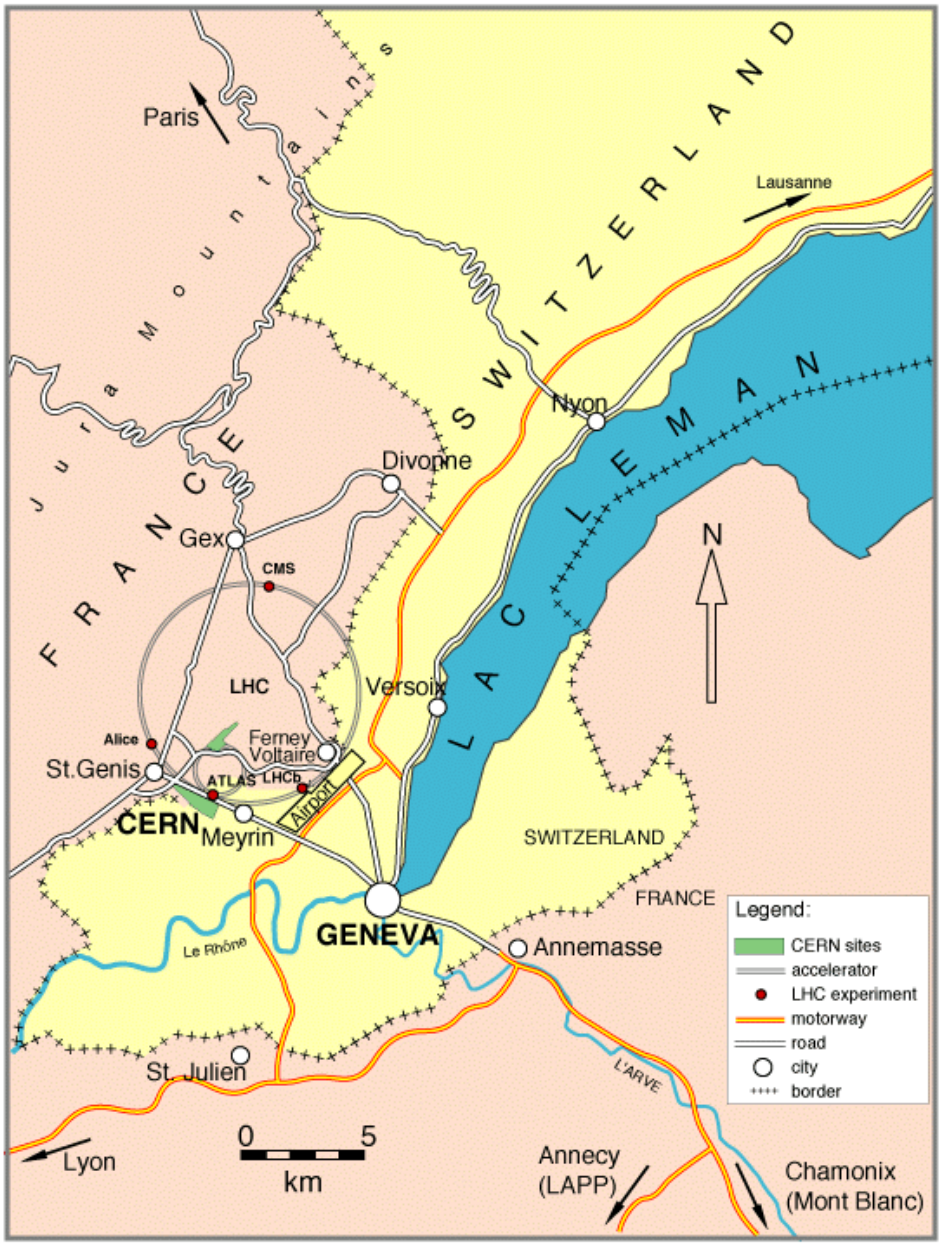

Figure 3.1: The map shows the location of LHC experiments: ALICE, ATLAS, CMS, and LHCb [38]

In general, the responses of subdetectors are continuously translated to electric signals, the signals are amplified, integrated every 25 ns, digitalized, and then synchronized to the same event. Because there are billions of events per second, it is impossible to read and store all of them, so CMS uses a trigger system to store only events of potential interest.

The origin of CMS is centered at the nominal collision point inside the experiment, the y-axis

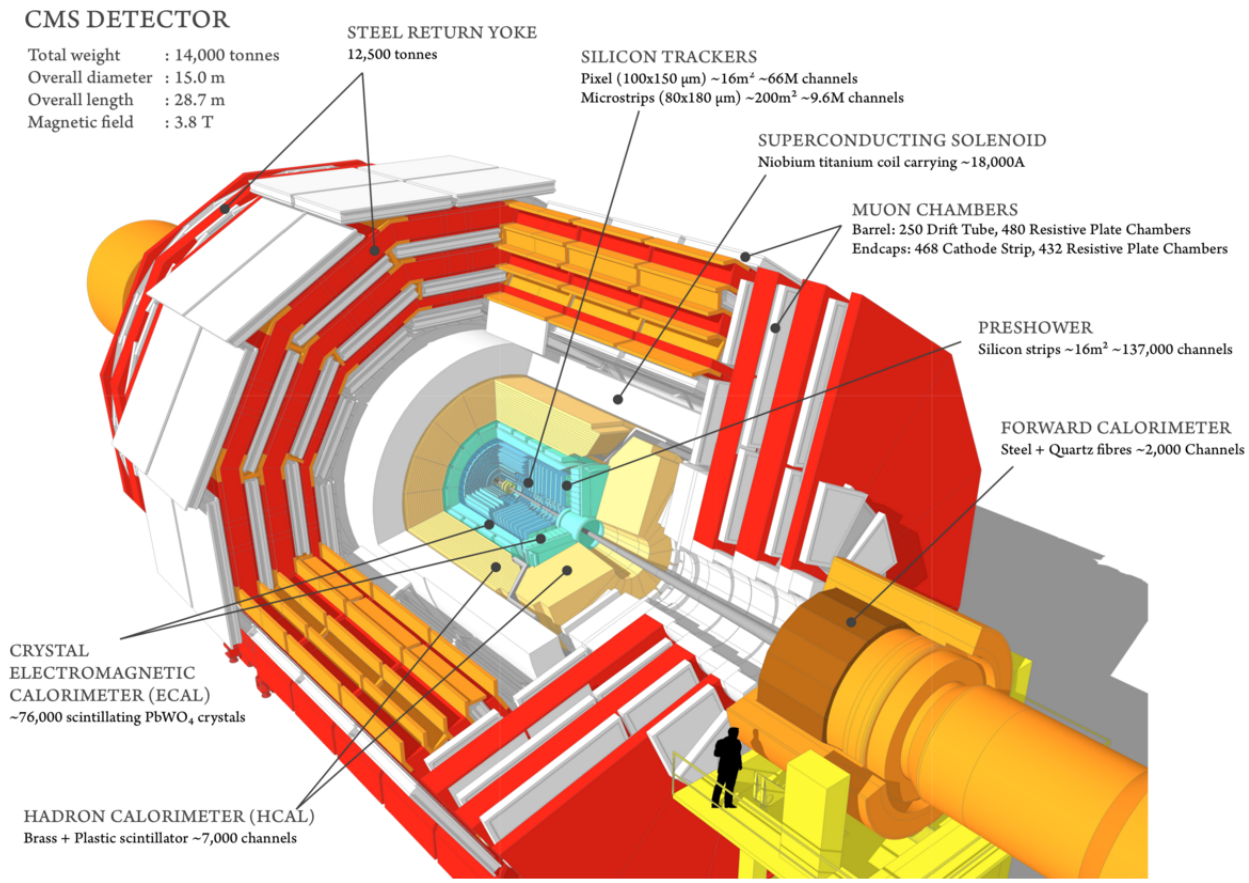

Figure 3.2: A perspective view of the CMS detector [39]

points vertically upward, the x-axis points radially inward toward the center of the LHC, and the z-axis points along the beam direction toward the Jura mountains in France from LHC Point 5, as shown in the map 3.1. The azimuthal angle ϕ is measured counter-clockwise from the x-axis. The polar angle θ is measured from the z-axis, and the pseudorapidity is defined as $\eta = -ln[tan(\theta/2)]$.

3.2 The Magnet

The magnet consist of three parts: a superconducting cylindrical coil, a vacuum tank, and a magnetic steel yoke. The cylindrical solenoid generates a magnetic field of 4T. It has a length of 12.5m and a 6m diameter. The magnet consists of 5 modules, each with length 2.5m. Each module has 4 layers and each layer has 109 turns to make a total of 2180 turns. Figure 3.4 shows the super-conducting solenoid of CMS and Table 3.1 lists the parameters of the magnet. The yoke is

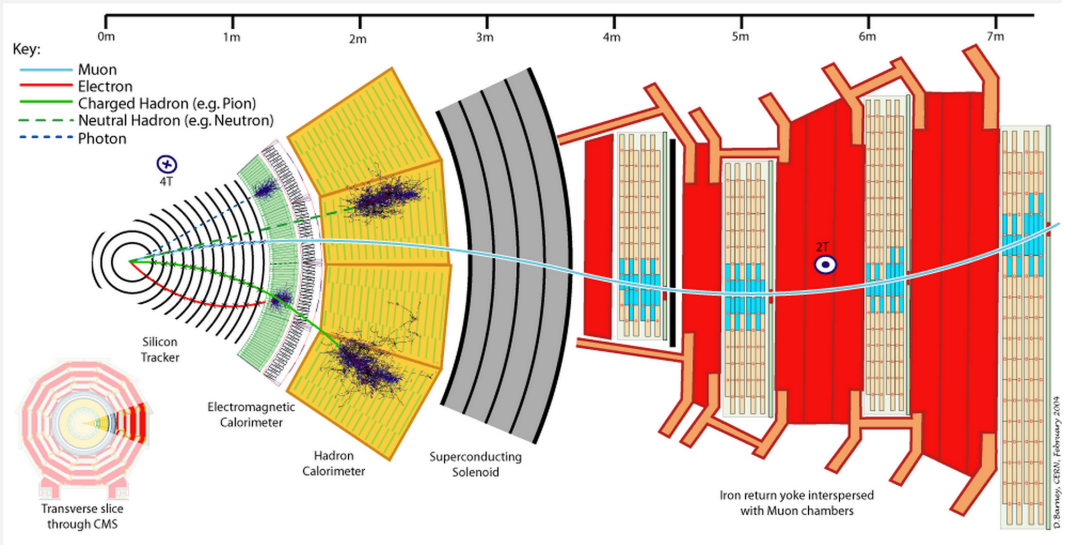

Figure 3.3: A slice of the CMS detector [40]

constructed from the iron of the muon system. The iron works as both the flux return yoke of the magnetic field and as an absorber to shield the muon detectors. The yoke weighs 10,000 tons. It consists of a barrel and two endcaps. The barrel consists of 5 wheels (YB-2, YB-1, YB0, YB+1, YB+2), each wheel has three dodecagon steel layers, with rectangular muon chambers embedded between these layers. Each endcap consists of three disks ($YE \pm 1, YE \pm 2, YE \pm 3$), with trapezoidal muon chambers interleaved between them [98]. Figure 3.5 shows magnetic flux density on a longitudinal section of the CMS detector. Approximately two thirds of the magnetic flux return through the barrel yoke [42].

Parameter	Value
Field	4T
Field in the yoke	2T
Inner Bore	5.9m
Length	12.9m
Number of Turns	2168
Current	19.5 kA
Stored energy	2.7 GJ
Hoop stress	64 atm

Table 3.1: Parameters of the CMS super-conducting solenoid [43].

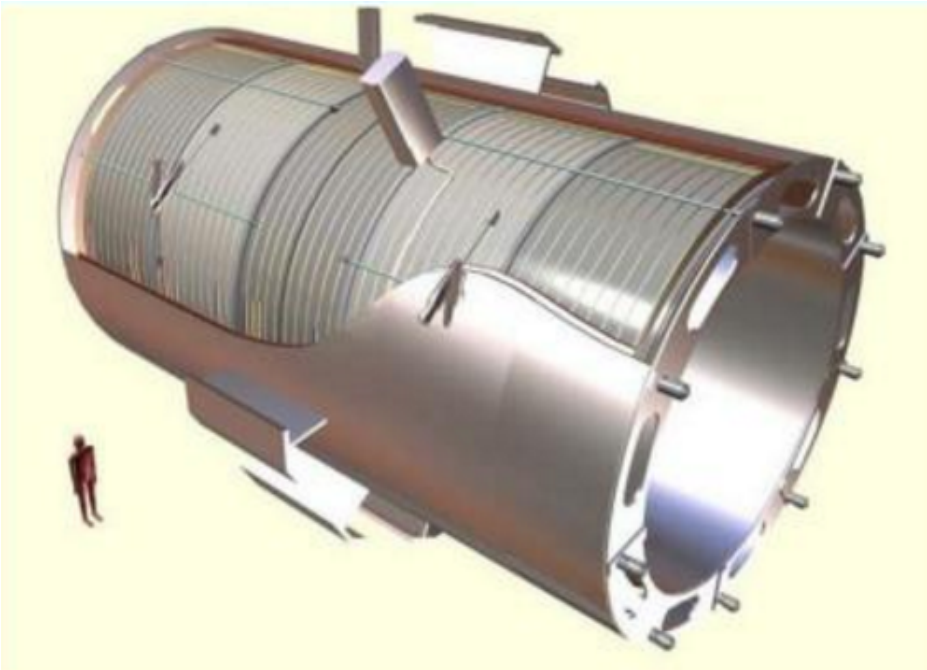

Figure 3.4: The magnet of the CMS detector [41].

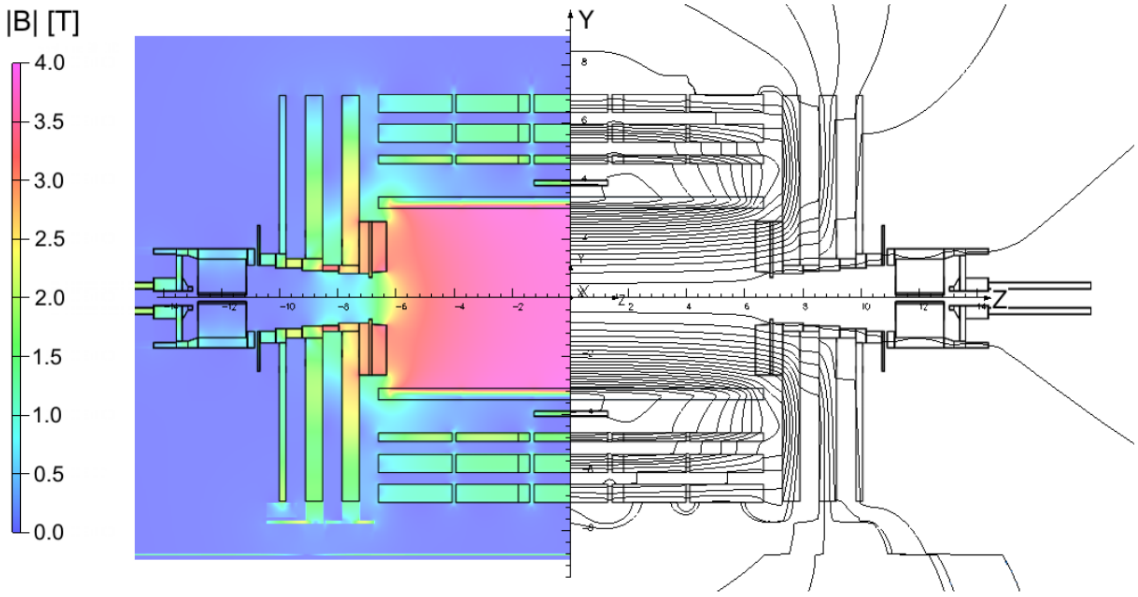

Figure 3.5: Magnetic flux density, values (left) and lines (right) on a longitudinal section of the CMS detector. The horizontal axis represents the z direction while the vertical axis represents the radial distance from the beam line [42].

3.3 Inner Tracking System

The pixel and strip trackers measure the tracks of charged particles very precisely. In order to be efficient they are built from multiple layers. As particles travel through the tracker the pixels and strips produce tiny electric signals that are amplified and digitalized. Figure 3.6 shows a schematic cross section through the CMS tracker in the r-z plane [43]. The tracker is a cylinder that surrounds the interaction points and is orientated along the axis of the beams. The tracker has a length of 5.8 m and a diameter of 2.5 m. The tracker covers the pseudorapidity range $-2.4 < \eta < 2.4$. The total area is 200 m^2, so it is the largest silicon tracker ever built. The tracker employs sensors with 75 million separate electronic read-out channels. The CMS tracker is composed of a silicon pixel detector with three barrel layers at radii between 4.4 cm and 10.2 cm and a silicon strip tracker with 4 (TIB) plus 6 (TOB) barrel layers extending outward to a radius of 110 cm. Each detector is completed by two endcaps, 2 disks in the pixel detector and 3 (TID) plus 9 (TEC) disks in the strip detector as shown in Figure 3.6. The principal characteristics of the tracker are summarized in Table 3.2.

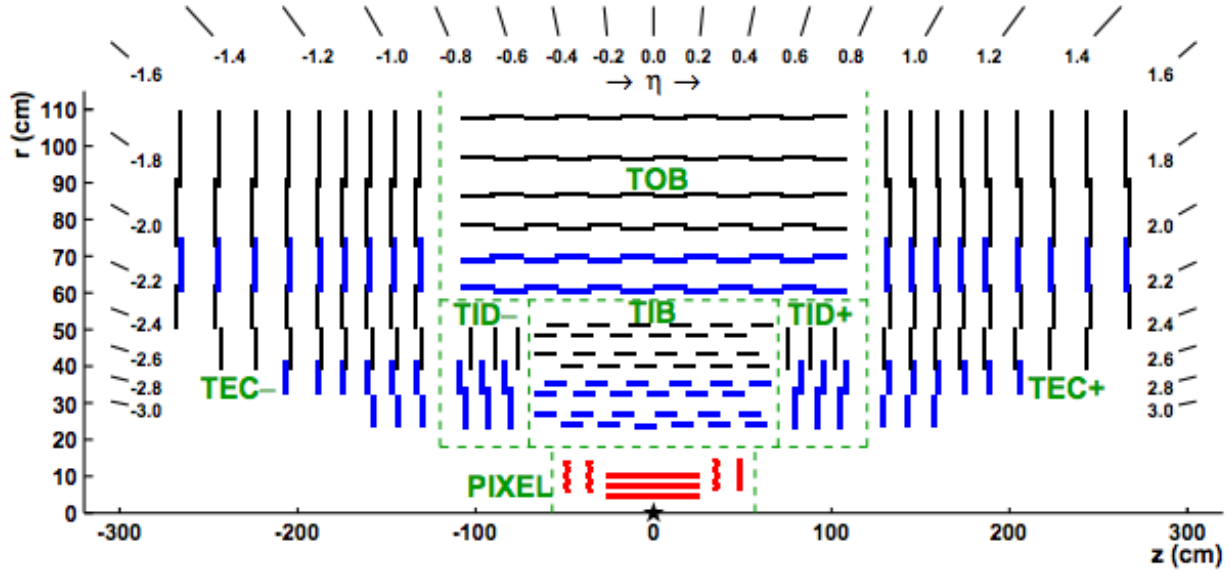

Figure 3.6: Schematic cross section through the CMS tracker. In this view, the tracker is symmetric about the horizontal line r = 0, so only the top half is shown here. The pixel tracker is shown in red while the tracker is shown in blue and black [43].

Tracker subsystem	Layers	resolution	Location
Pixel tracker barrel	3 cylindrical	$100 \times 150 \mu m^2$	$4.4 < r < 10.2cm$
Strip tracker inner barrel (TIB)	4 cylindrical	$80-120\ \mu m$	$20 < r < 55cm$
Strip tracker outer barrel (TOB)	6 cylindrical	$122-183 \mu m$	$55 < r < 116cm$
Pixel tracker endcap	2 disks	$100 \times 150 \mu m^2$	$34.5 < \|z\| < 46.5cm$
Strip tracker inner disks (TID)	3 disks	$100-141 \mu m$	$58 < \|z\| < 124cm$
Strip tracker endcap (TEC)	9 disks	$97-184 \mu m$	$58 < \|z\| < 124cm$

Table 3.2: A summary of the principal characteristics of the various tracker subsystems. The number of disks corresponds to that in a single endcap. The location specifies the region in r (z) occupied by each barrel (endcap) subsystem [43].

3.3.0.1 Silicon pixel detector

The pixel detector is a cylinder with three barrel layers at 4cm, 7cm and 11cm, and two endcap disks on each side of the interaction point. The total area of the pixel detector is $\approx 1\ m^2$. The pixel detector contains 66 million pixels and is the closest detector to the beam pipe. It tracks the paths of particles from the collision with extreme accuracy and is vital in reconstructing the tracks of very short-lived particles. The silicon pixel detector covers the pseudorapidity range $|\eta| < 2.5$.

Each layer is spilt into many silicon sensors. When a charged particle passes through a sensor it deposits energy that creates electron-hole pairs. Each pixel uses an electric voltage to collect these charges as a small electric signal. This signal is then amplified and digitized. This information is known as a hit. The tracking algorithm connects the hits in the tracker to form tracks. Figure 3.7 shows the geometrical layout of the pixel detector and its coverage as a function of pseudorapidity [44].

3.3.0.2 Silicon strip detector

The silicon strip detector surrounds the pixel detector and works in a similar way. Figure 3.8 shows a cross section of one quarter of the tracker in the longitudinal view. The total area of the silicon strip detectors is $200m^2$, and it comprises 9.6 million silicon strips. The strip detector has coverage up to $|\eta| < 2.4$.

The silicon strip detector is composed of four basic subdetectors. The barrel tracker region is

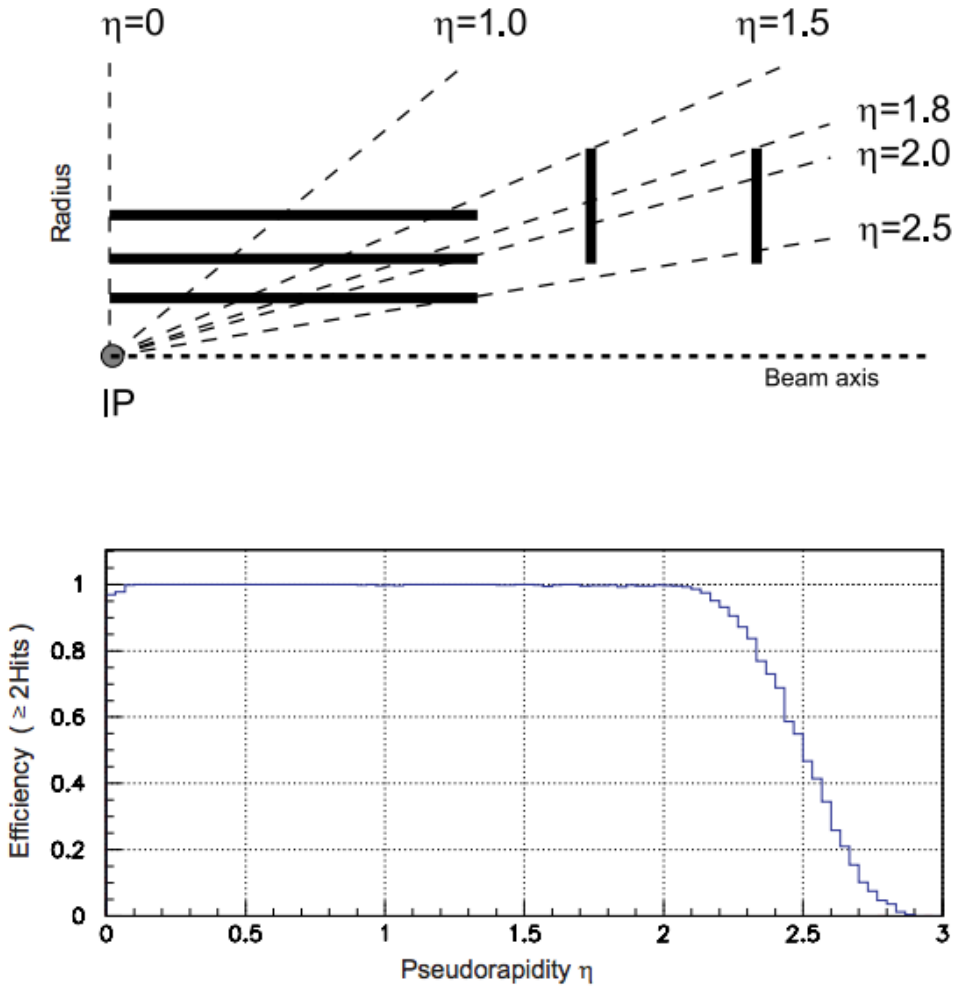

Figure 3.7: Geometrical layout of the pixel detector (top) and its coverage as a function of pseudorapidity (bottom) [44].

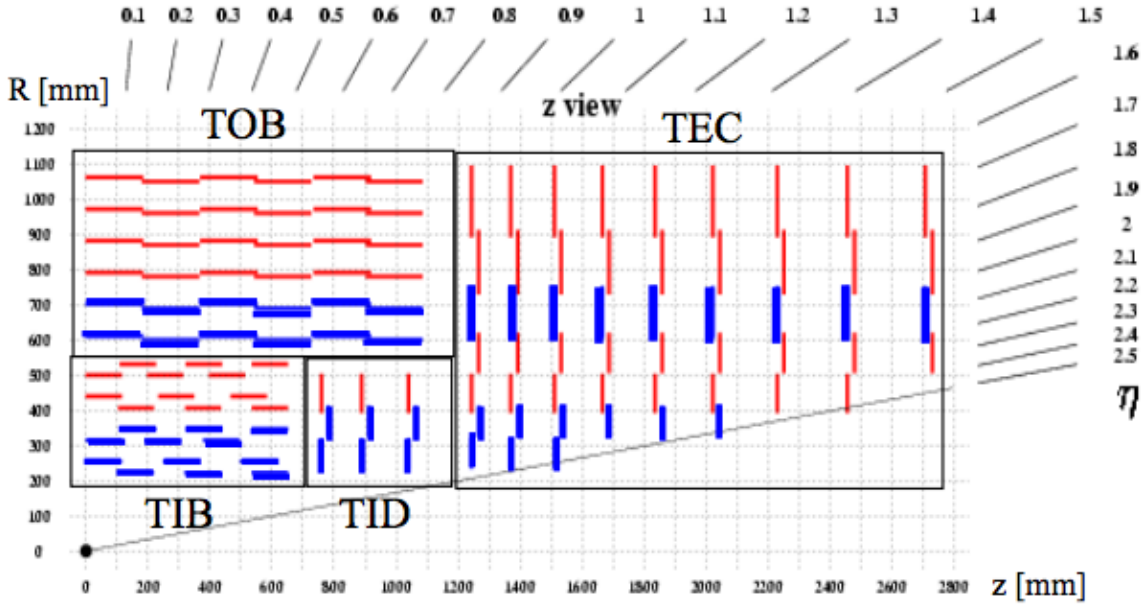

Figure 3.8: A sketch of the detector layout. The red and blue lines indicate the position and orientation of the detector modules in the r-z plane where r is the distance to the beam axes and z is the distance to the IP along the beam axes [41].

divided into 2 parts: a Tracker Inner Barrel (TIB) and a Tracker Outer Barrel (TOB). The TIB is made of 4 layers and covers up to $|z| < 65$ cm. The TOB comprises 6 layers and covers to $|z| < 110$ cm. The endcaps are divided into the Tracker End Cap (TEC) and Tracker Inner Disks (TID). Each TEC comprises 9 disks that cover the region 120 cm $< |z| <$ 280 cm, and each TID comprises 3 small disks that fill the gap between the TIB and the TEC. The TEC and TID modules are arranged in rings, centered on the beam line.

3.4 Electromagnetic Calorimeter

The Electromagnetic Calorimeter (ECAL) is designed to reconstruct the energy and position of photons and electrons, and in combination to the hadronic calorimeter, to perform a precise measurement of jets. It is the second innermost subdetector, just outside the tracker system. Figure 3.9 shows a $1/4$ slice through the ECAL. The ECAL also supplies information to the Level 1 trigger.

Electrons and photons create electromagnetic showers. For example, the effects of pair produc-

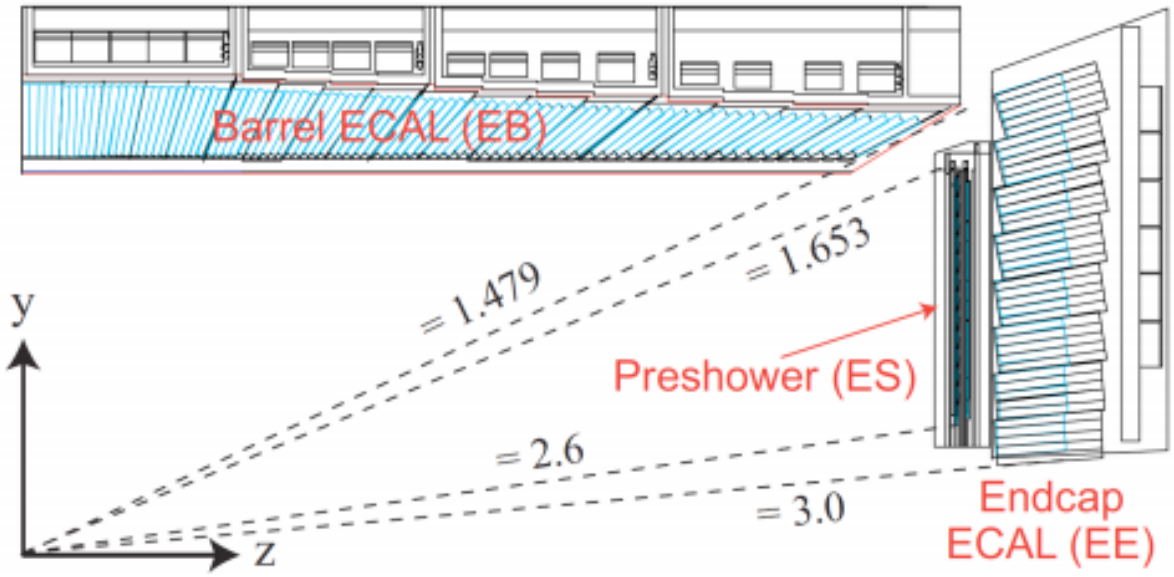

Figure 3.9: A quarter slice of the CMS ECAL detectors [45].

tion and bremsstrahlung lead to a cascade of photons and electrons. The $PbWO_4$ crystals absorb the energies of particles via Compton scattering and the photoelectric effect and scintillates (re-emits) that energy in the form of light (photons). The photons are captured by photodiodes and converted to digital signals. The number of scintillating photons is proportional to the energy deposited by the particle. The geometric acceptance of the ECAL extends to $|\eta| < 3$, where the barrel part (EB) covers the pseudorapidity range $|\eta| < 1.479$, while the endcap part (EE) covers $1.553 < |\eta| < 3.00$, as shown in Figure 3.9.

The ECAL is made up of crystals of lead tungstate, $PbWO_4$ which is a high density and transparent material. $PbWO_4$ has a short scintillation time, meaning that about 80% of the photons are remitted in less than $25ns$. It has a short radiation length $X_0 = 0.89cm$, which is needed to fit the calorimeter inside the magnetic coil. The barrel (EB) has 61200 crystals, and each endcap (EE) has 7324 crystals. to make a total of 75848 crystals. In the EB, the front face of the crystal is (22×22) mm^2 and the length is 23 cm equivalent to $\approx 26X_0$. In the EE, the front face of the crystal is (28.6×28.6) mm^2 and the length is 22 cm corresponding to $\approx 25X_0$. The granularity of the crystals is $\Delta\eta \times \Delta\phi = 0.0174 \times 0.0175$ in the barrel and $\Delta\eta \times \Delta\phi \approx 0.05 \times 0.05$ in the endcaps. A barrel and endcap crystal are shown in Figure 3.10. As can be seen in Figure 3.9 the geometry

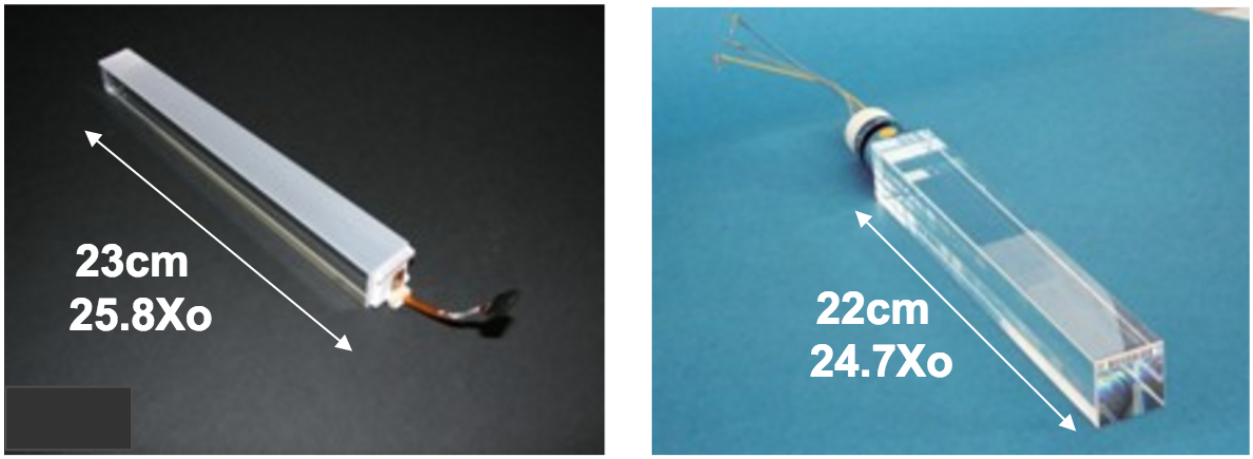

Figure 3.10: Lead tungstate crystals in the ECAL, left: Barrel crystal, right: Endcap crystal [41]

of the crystals is projective towards the center of CMS.

There is a pre-shower detector at the front of the endcaps. It is made of two layers of lead, followed by silicon strip detectors. The purpose of the pre-shower is to distinguish the isolated photons from neutral pions. The pre-shower covers the pseudorapidity range $1.65 < |\eta| < 2.6$.

The ECAL energy resolution was measured using an electron test beam. The resolution as a function of the electron energy is shown in Figure 3.11. The relative energy resolution of the ECAL improves with increasing energy and is parametrized by the following expression [41]:

$$(\frac{\sigma_E}{E})^2 = (\frac{N}{E})^2 + \frac{S^2}{E} + C^2, \tag{3.1}$$

where N, S and C are terms for noise, stochastic fluctuations, and the constant term, respectively. The values of the three parameters were determined by a fit to the test beam results to be $S = 0.028 GeV^{\frac{1}{2}}, N = 0.12 GeV$ and $C = 0.003$ [41].

3.5 Hadron Calorimeter

The Hadronic Calorimeter (HCAL) measures the energies of hadrons (protons, neutrons, pions, etc), and makes indirect measurements of invisible particles such as neutrinos. Additionally, it provides information to the level 1 trigger. HCAL is massive and thick. It is a sampling calorime-

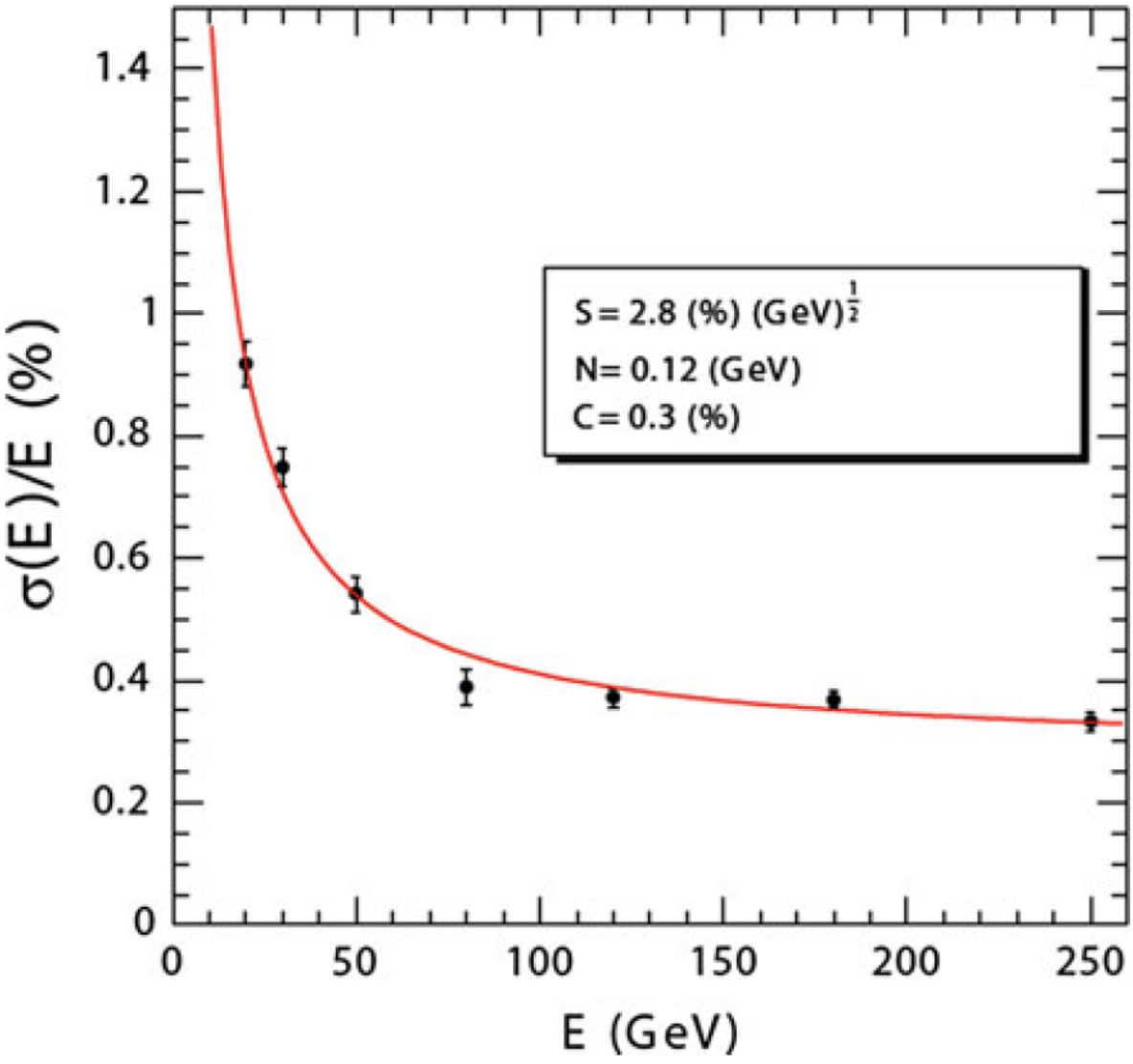

Figure 3.11: ECAL energy resolution as a function of the energy measured in electron test beam. The measured values of the stochastic (S), noise (N) and constant (C) parameters, from Equation 3.1 are displayed in the legend [41].

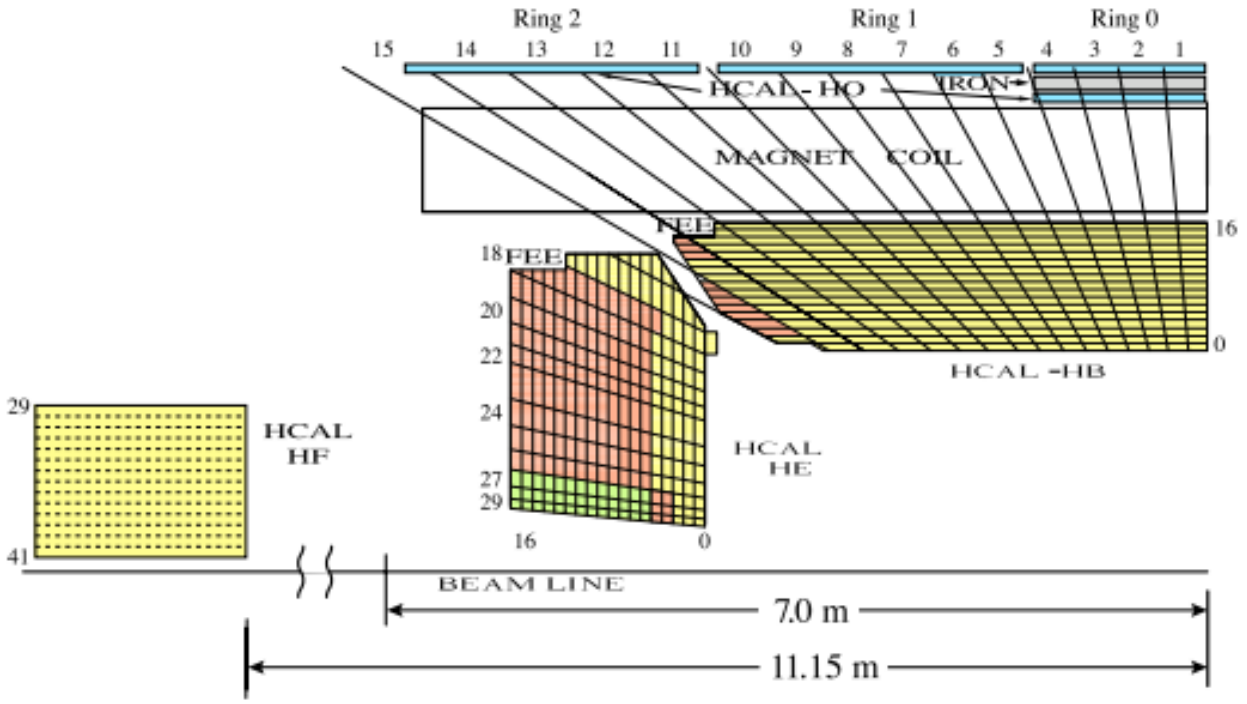

Figure 3.12: A quarter slice of the CMS HCAL detectors [41].

ter consisting of plastic scintillators, which serve as the active material, inserted between dense absorber plates. Figure 3.12 shows a quarter slice of the HCAL. The interaction of hadrons within HCAL produces a shower of secondary particles with gradually lower energy. A fraction of these particles deposit energy in the active medium which then scintillates. The total detected light signal is proportional to the energy of the incident particle [99].

HCAL has four major subdetectors: Hadronic Barrel (HB) ($|\eta| \leq 1.4$), two Hadronic Endcaps (HE) ($1.3 \leq |\eta| \leq 3.0$) and Hadronic Outer (HO) ($|\eta| < 1.26$). HB and HE sit between the ECAL and the magnet and use non-magnetic brass and copper as absorbers. HO catches the tail of the hadronic shower. It sits just outside the magnet and uses the steel return yoke of CMS as its absorber.

3.5.1 Hadron Barrel

Hadron Barrel (HB) covers the pseudorapidity range $|\eta| \leq 1.4$ and is divided into 36 identical wedges in ϕ. Each wedge is divided into 40 sectors along the z axis. The granularity of HB is

$\Delta\eta \times \Delta\phi = 0.087 \times 0.087$. The active material is plastic scintillator which is sandwiched between copper absorber plates that are 5 cm thick. The inner and outer plates are made of stainless steel 7 cm thick for more strength. Light collected from the scintillators is read out by the Hybrid Photodiodes (HPD). The energy resolution of HB is $\frac{\sigma}{E} = \frac{0.65}{\sqrt{E}} \otimes 0.05$ [100]. At $\eta = 0$, the depth of HB is 79 cm, which is equivalent to 5.15 interaction lengths λ_I. The HB is not deep enough to fully contain a hadronic shower. Thus, the outer calorimeter HO is used to catch the tails of a hadronic showers, as discussed below.

3.5.2 Hadronic Outer

Hadronic Outer (HO) is designed to catch the tails of hadronic showers that form in the HB. It is located inside the barrel muon system. It covers the region $|\eta| < 1.26$ and is divided into 5 rings along η. HO uses the solenoid and the iron of the return yoke as absorber material and contains scintillators with a thickness of 10 mm. At $\eta = 0$, HO increases the length of the HCAL to $11.8\lambda_I$.

3.5.3 Hadron Endcap

Hadron Endcap (HE) covers $1.3 \leq |\eta| \leq 3.0$ and lies within the influence of the 4T magnetic field. The absorber plates are made of nonmagnetic brass. The light from the scintillators is collected by wavelength shifting fibers. The signals are transferred to the photodetectors by optical cables. The granularity of HE is the same as HB for $|\eta| \leq 1.6$ but for $|\eta| > 1.6$ the granularity becomes $\Delta\eta \times \Delta\phi = 0.17 \times 0.17$. The length of HE is $10\lambda_I$ and the energy resolution is $\frac{\sigma}{E} = \frac{0.83}{\sqrt{E}} \otimes 0.05$ [100].

3.5.4 Hadron Forward

The Hadron Forward (HF) calorimeters are placed 11m away from the interaction point, as seen in Figure 3.12. The two calorimeters cover the pseudorapidity range $3.0 < |\eta| < 5.0$. They are Cherenkov calorimeters that use steel as the absorber and quartz fiber as the active material.

Each HF forms a cylinder around the beam with an inner radius of 25 cm and an outer radius of 1.4 m. HF extends 1.65 m along the z-direction. This depth corresponds to 10 λ_I. The transverse granularity of HF is $\Delta\eta \times \Delta\phi = 0.17 \times 0.17$. The fibers are embedded in the steel, run parallel to the beam direction, and are read out by phototubes on the back of HF. The are two kinds of fibers in HF. The long fibers, 1.65 m length, are sensitive to both the electromagnetic and hadronic parts of the showers while the short fibers, 1.43 m in length, are sensitive to only the hadronic parts of the showers. In HF, the energy resolution for electrons is $\frac{\sigma}{E_e} = \frac{1.5}{\sqrt{E}} \otimes 0.06$, for pions the energy resolution is $\frac{\sigma}{E_\pi} = \frac{2.7}{\sqrt{E}} \otimes 0.13$, and for jets the energy resolution is $\frac{\sigma}{E_{jet}} = \frac{3.0}{\sqrt{E}} \otimes 0.06$ [100].

3.6 Muon System

CMS has an excellent muon detection system. The muon detector has three main purposes, to identify the muons, to measure their momenta, and to provide information to the level 1 trigger. Because the muons are very penetrating the muon detector sits outside the calorimeters and magnetic coil and interleaves the iron plates of the magnet return yoke, see Figures 3.2 and 3.3. The muon detector consists of three types of gaseous chambers; Drift Tube (DT) chambers are used in the barrel, Cathode Strip Chambers (CSC) are used in the endcaps, and Resistive Plate Chambers (RPC) are used in both the barrel and endcaps. The muon detector covers a pseudorapidity range $|\eta| < 2.4$. The relative locations of the DT, CSC, and RPC of the muon detector are shown in Figure 3.13. The muon system contains of order 25000 m^2 of active detection planes, and nearly 1 million electronic channels.

The Muon Barrel (MB) consists of five wheels centered along the beam direction. Each section is 2.5m long and is divided into 12 sections that each cover 30^o in ϕ. Each section has 4 stations at radii of approximately 4.0 m, 4.9 m, 5.9 m and 7.0 m from the beam axis. The innermost station is inside the yoke, the stations at 4.9 and 5.9m are within the yoke, and the station at 7.0m is outside the yoke. Figure 3.14 shows a transverse view of CMS at z=0. Muon stations are denoted as MBZ/N/S, where $Z = -2, ... + 2$ is the barrel wheel number, $N = 1 - 4$ is the station number and $S = 1 - 12$ is the sector number. Similarly, the steel return yokes are denoted YBZ/N/S. Each of the

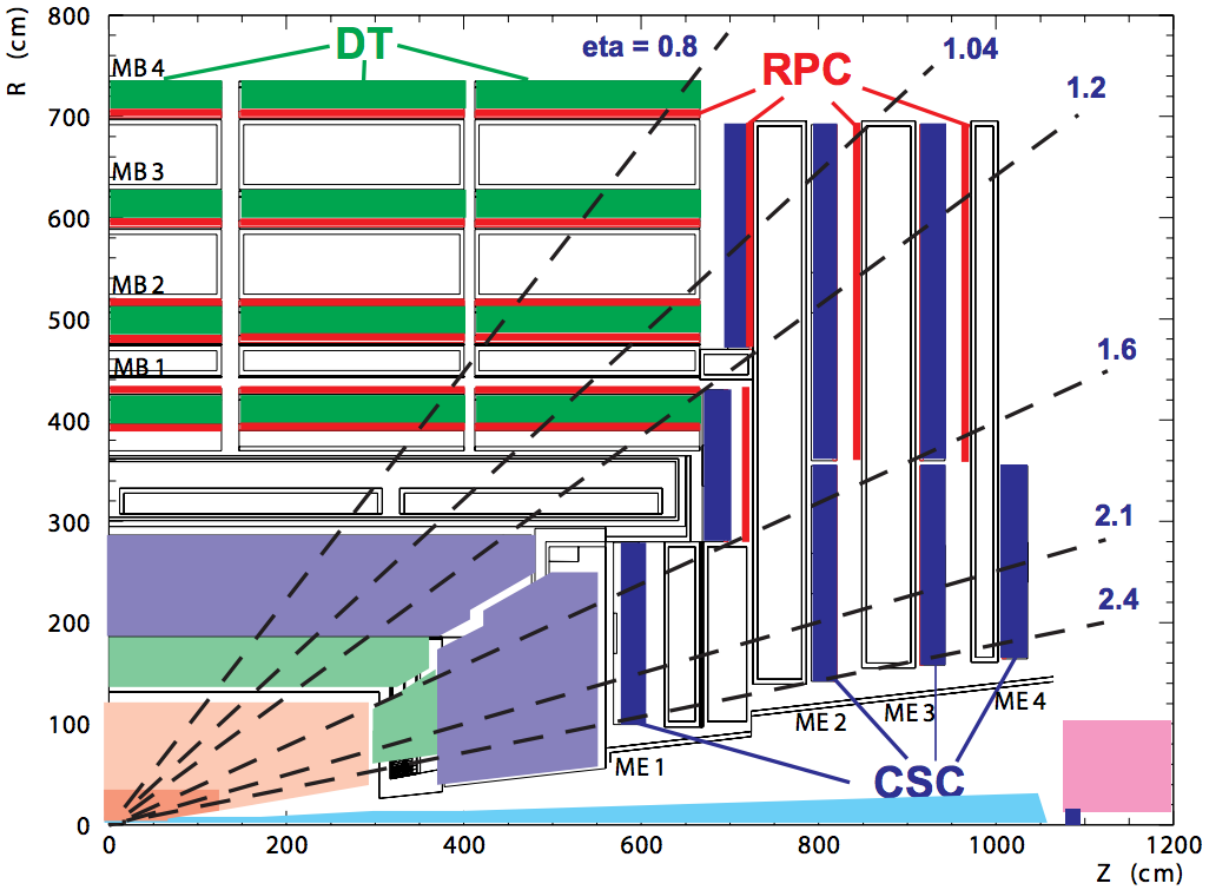

Figure 3.13: A schematic quarter-view of the CMS detector, ME stands for Muon Endcap, MB stands for Muon Barrel. The drift tubes (green), resistive plate chambers (red), and cathodes trip chambers (blue) are labelled [46].

stations MBZ/1/S and MBZ/2/S consists of one DT chamber between two RPC chambers. Stations MBZ/3/S and MBZ/4/S, each consists of one DT chamber and 1 RPC, as shown in Figure 3.13.

The muon endcap consists of 4 disk shaped stations, as shown in Figure 3.13. Each station consists of muon chambers (CSCs and RPCs) and iron disks of the flux return yoke. The first disk is divided into three rings, the remaining disks are divided to two rings. The chambers are labeled by ME$\pm$S/R, where ME is Muon Endcap, the $\pm$ sign indicates which endcap, S indicates the disk (station), and R is the ring number [50].

3.6.1 Drift Tubes

Figure 3.15 shows a cross-sectional view of a drift tube. When a muon traverses the tube it ionizes a gas. Electrons then drift under the influence of a shaped electric field to an anode wire where they produce a signal. The time of arrival of the pulse gives position information. The muon Drift Tubes detect muons in the pseudorapidity range $|\eta| < 1.2$, as shown in Figure 3.13. The drift tubes do not contribute to the level 1 trigger.

A total of 250 rectangular chambers are distributed in five wheels. Each wheel has four cylinders of chambers, that are interleaved in the iron yoke. There are 12 chambers in each one of three inner cylinders, and 14 chambers in the outer cylinder. Figure 3.16 shows a schematic view of one chamber. Each chamber is, on average 2.0 m x 2.5 m in size and consists of 12 aluminum layers grouped into three superlayers, two superlayers SL1, SL2 measure the (r-ϕ) coordinate, and the third, SL2 measures (r-θ) coordinate. A honeycomb structure separates the SL1 superlayer from the SL2 and SL3 superlayers. The chambers in the outer cylinder do not have the SL2 superlayer. Each superlayer has up to 60 drift tubes [47].

3.6.2 Cathode Strip Chambers

Cathode Strip Chambers, CSCs are gas detectors that operate in avalanche mode. Each CSC is trapezoidal in shape and consists of 6 gas gaps, each gap having a plane of radial cathode strips and a plane of azimuthal anode wires as shown in Figure 3.17. When a muon traverses the

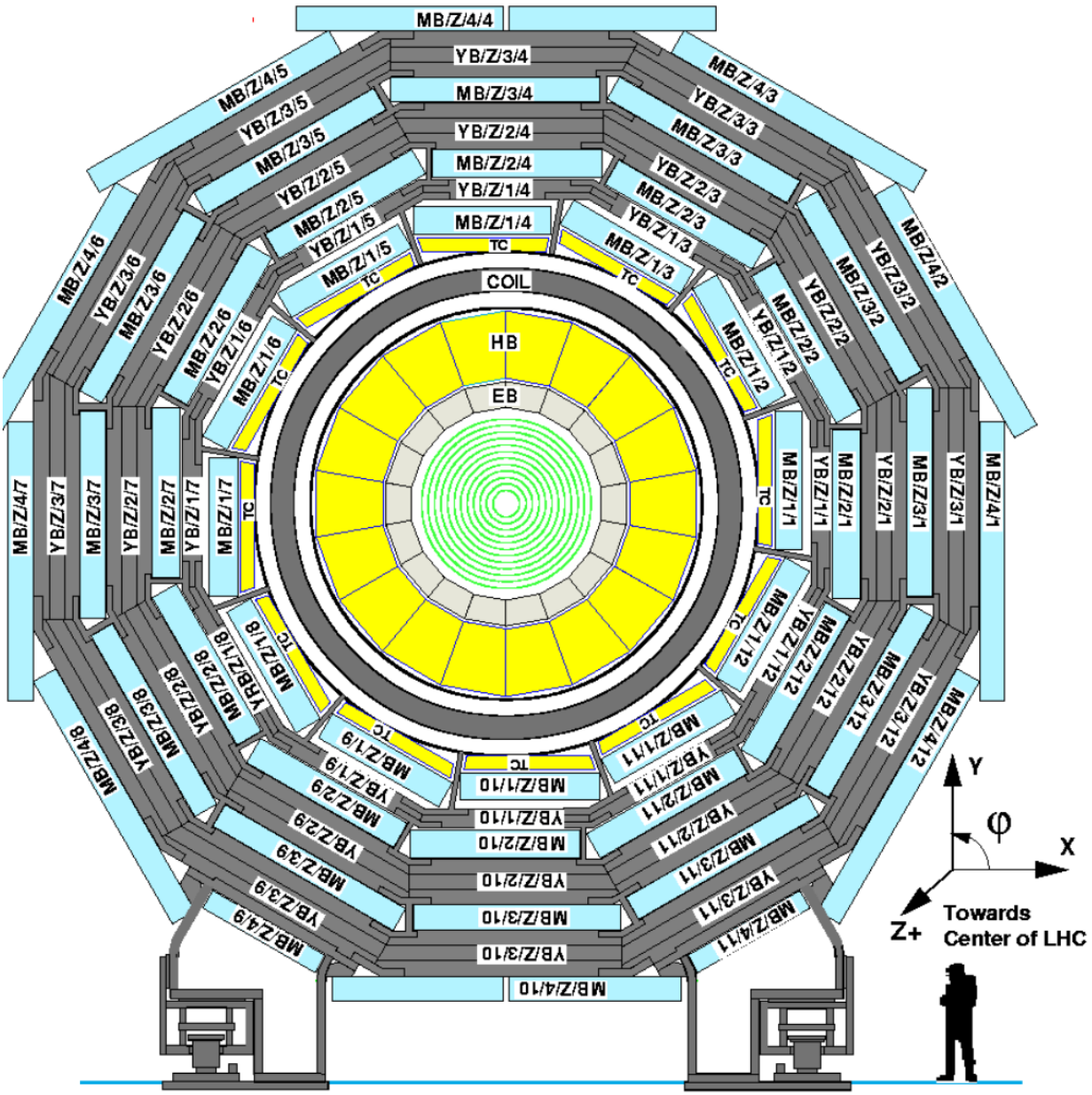

Figure 3.14: Transverse view at z=0.The barrel muon detector elements are denoted as MBZ/N/S, where z=-2,...+2 is the barrel wheel number, N=1-4 the station number and S=1-12 the sector number. Similarly, the steel return yokes are denoted YBZ/N/S [41].

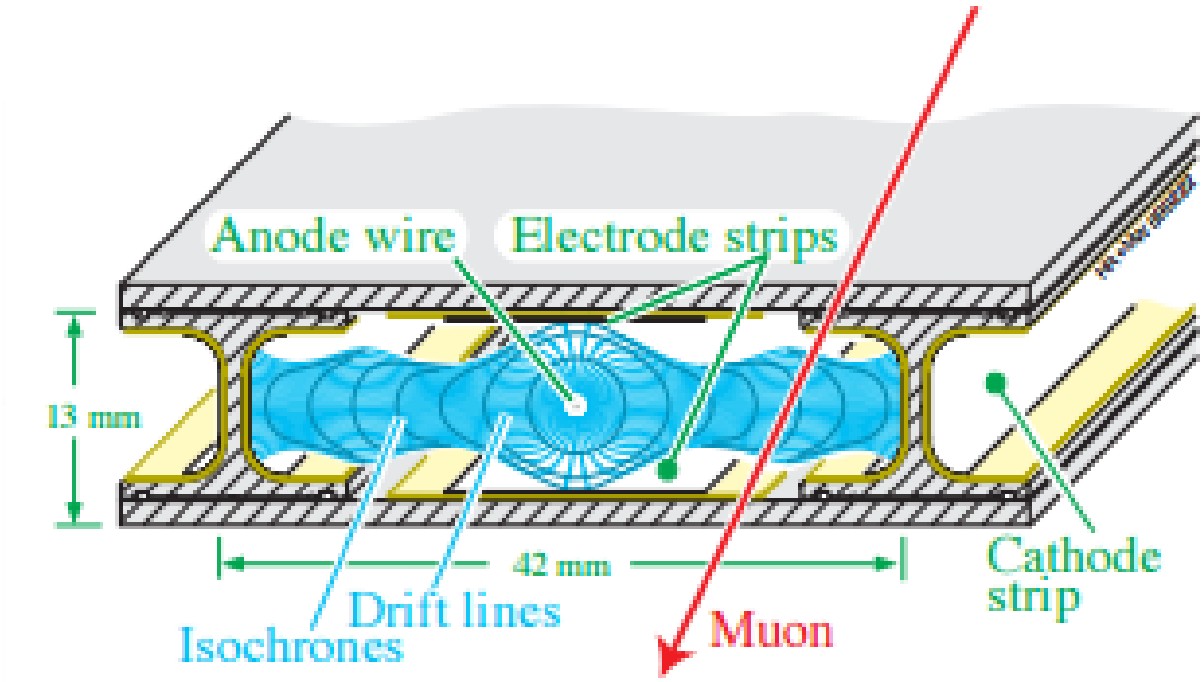

Figure 3.15: Cross sectional view of a drift tube [41].

CSC it ionizes the gas. The electric field in the gap is so strong that an avalanche of electrons is created. This avalanche produces a signal on anode wires and induces a charge on the cathode strips as shown in Figure 3.18. The signals from the wires and strips are then used to determine the position of the muon hit [101]. The strips and wires are almost perpendicular to each other with strips running along ϕ and the wires running along the radial coordinate $r-$. Therefore, when a muon passes through a chamber, the chamber provides six measurements of the ϕ (strips) and six measurements of r (wires).

The cathode strip chambers sit on the two endcaps of CMS and cover the pseudorapidity range ($0.9 < |\eta| < 2.4$), as seen in Figure 3.13. The CSCs do not contribute to the level-1 trigger. There are 234 CSCs in each of the two endcaps. There are 36 chambers in each ring of each muon station, except for the innermost rings of the second through fourth disks (ME2/1, ME3/1, and ME4/1) which have 18 chambers. Figure 3.19 shows a photograph of the CSCs in the second disk in ME+2. All CSCs, except those in the third ring of the first endcap disk (ME1/3), are overlapped in ϕ to avoid gaps in the muon acceptance.

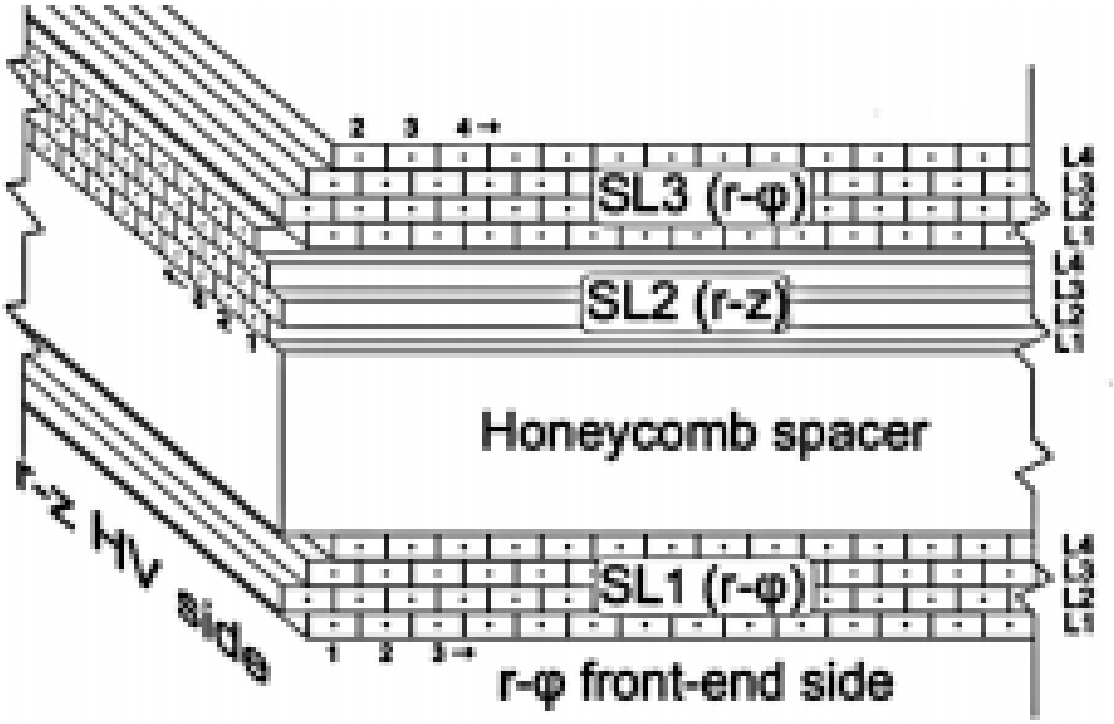

Figure 3.16: Schematic view of a DT chamber. It has three SuperLayers: SL1, SL3 measure the (r-ϕ) coordinate, while SL2 measures in (r-θ) plane. Each one consists of 4 planes of drift tubes [47].

3.6.3 Resistive Plate Chambers

Figure 3.20 shows a schematic view of the Resistive Plate Chambers, or RPCs. Each RPC consists of two plates made of very highly resistive material separated by a few millimeters of gas. One plate serves as an anode and the other serves as the cathode. When a muon passes through the chamber and ionizes the gas, the strong electric field causes an avalanche of electrons, which induces a charge on metallic strips. This charge is the output signal of the RPC [48]. The RPCs cover the pseudorapidity region ($|\eta| \leq 2.1$), as shown in Figure 3.13. There are 480 RPCs in the barrel and 378 chambers in each endcap. In the barrel, the RPCs are distributed in 5 wheels, with 6 stations in each wheel, see Figure 3.13. Moving outward from the beam there are two RPCs in front and behind each of the first two sets of DT chambers and one RPC on the inner sides of the third and forth DT chambers. For each endcap, the RPCs are distributed in four disks as shown in Figure 3.13. The first disk has three rings and each ring has 36 chambers. In each of disks 2, 3, and 4, there are two rings. The outer ring has 36 chambers and the inner ring has 18 chambers.

3.7 Muon Reconstruction

Muon reconstruction is performed in two stages, the first is stand-alone reconstruction, which is based on information from the muon system only. The second is global reconstruction, which uses information from the muon system and hit information from the silicon tracker. Stand-alone reconstruction is begun by finding track segments in the muon chambers. These segments are combined into muon trajectories using a Kalman Filter technique. In the global muon reconstruction the muon trajectories are extended to add hits that are measured by the tracker. The track parameters of a stand-alone reconstructed muon are compared to the track parameters of the tracker tracks. If the tracker track is consistent with the stand-alone muon track in momentum, position and di-

rection, the hit information of the tracker and the muon system are combined and refitted to form a global muon track. Then the resulting global tracks are checked for ambiguity and quality to choose the one global track that is the best fit for each stand-alone muon.

The precision of the momentum measurement in the muon system is determined by the measurement of the bending angle in the transverse plane at the exit point from the magnetic coil. For low momentum, the momentum resolution is improved by including the measurements from the silicon tracker, so the use of global muons is most valuable at low momentum. Figure 3.21 shows a comparison of the momentum resolution of the muon system stand-alone track, the tracker system and combined measurement (global muon track) for the barrel and the forward region. The combined tracks always have the best resolution [41].

3.8 CASTOR

The CASTOR detector measures the electromagnetic and hadronic energies of the particles in heavy ion and proton-proton collisions at CMS. CASTOR sits at 14.4m from the interaction point as shown in Figure 3.22 [102] and covers the pseudorapidity range ($5.2 < \eta < 6.6$). CASTOR consists of several sandwiches of two layers, a tungsten layer (W) as the absorber medium (providing the smallest shower size) and a quartz layer (Q) as the active medium. Incoming particles interact in the tungsten to produce showers of secondary particles. When these secondary particles pass the quartz plates, Cherenkov light is produced, and this light is collected by an air core light guide and transmitted to the photo-multiplier tubes (PMTs). To maximize the Cherenkov light the plates incline by 45^o relative to the beam axis.

Figure 3.23 [103] shows a sketch of CASTOR. CASTOR consists of two parts, an electromagnetic (EM) part a hadronic (HAD) part. The EM part has two longitudinal modules, where each module has 16 azimuthal sectors. The thicknesses of the W and Q plates in the EM part are 5.0 mm and 2.0 mm, respectively. The HAD part has 14 longitudinal modules, where each module has 16 azimuthal sectors. The thicknesses of the W and Q plates in the HAD part are 10.0 mm and 4.0 mm, respectively. CASTOR has 224 readout channels and a total depth of 10.3 interaction

lengths.[103]

3.9 Zero Degree Calorimeters

The Zero Degree Calorimeters (ZDC) measures the energy of neutrons and photons in the forward rapidity region, i.e. $\eta > 8.3$. There are two ZDCs of the same design. Each ZDC is located in the TAN absorber between the beam pipes at about 140m on each side of the interaction point. ZDCs cover the pseudorapidity range ($|\eta| > 8.3$). Figure 3.24 shows the locations of the ZDCs in CMS. Each ZDC consists of two parts: the electromagnetic (EM) and hadronic (HAD) sections. The EM section is positioned in front of the HAD section with respect to the interaction point. Figure 3.25 shows a side view of the ZDC with the EM section in front and the HAD section behind [50].

The EM section consists of 33 layers of 2-mm-thick tungsten plates and 33 layers of 0.7-mm-diameter quartz fibers. The plates are oriented vertically and arranged in five horizontal readout towers. The fibers from each tower are grouped in one readout bundle and coupled directly to a phototube. The HAD section consists of 24 layers of 15.5 mm thick tungsten plates and 24 layers of 0.7 mm diameter quartz fibers. The plates are inclined by 45^o relative to the beam axis and grouped in four longitudinal read-out bundles to four phototubes via light guides, as shown in Figure 3.25. The interaction length for HAD is $5.6\lambda_I$ and for EM is $19X_0$.

The ZDC detects neutrons and photons, the photons interact with the dense tungsten plates in the EM part and the neutrons interact with the dense tungsten plates in both the EM and HAD parts. This produces a shower of particles with velocities that, exceed the speed of light in quartz fibers, which causes the particles to generate Cherenkov light. The generated Cherenkov light is brought by the light guides to the phototubes, and the phototubes convert the light to an electrical signal. The signals from the 10 EM channels and the 8 HAD channels in the two ZDCs travel about 210 m through coaxial cable to the counting room [50]. For different positron energies, the energy resolution can be parametrized as [50]

$$(\frac{\sigma}{E})^2 = (\frac{70\%}{\sqrt{E}})^2 + (8\%)^2, \tag{3.2}$$

For different pion energies, the energy resolution can be parametrized as [50]

$$\frac{\sigma}{E} = \frac{138\%}{\sqrt{E}} + 13\%, \tag{3.3}$$

where E is in GeV.

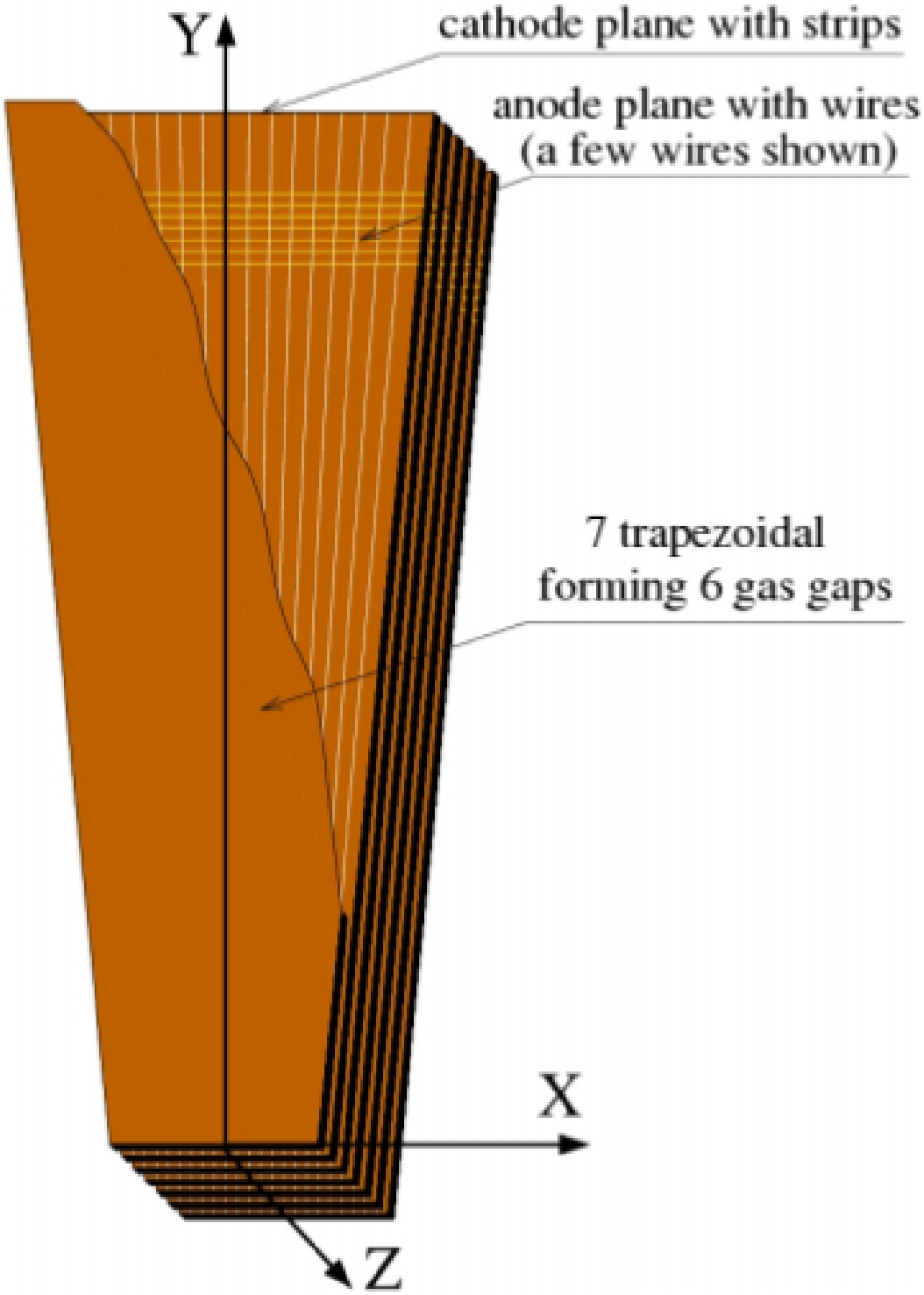

Figure 3.17: A schematic view of a CMS Cathode Strip Chamber [41].

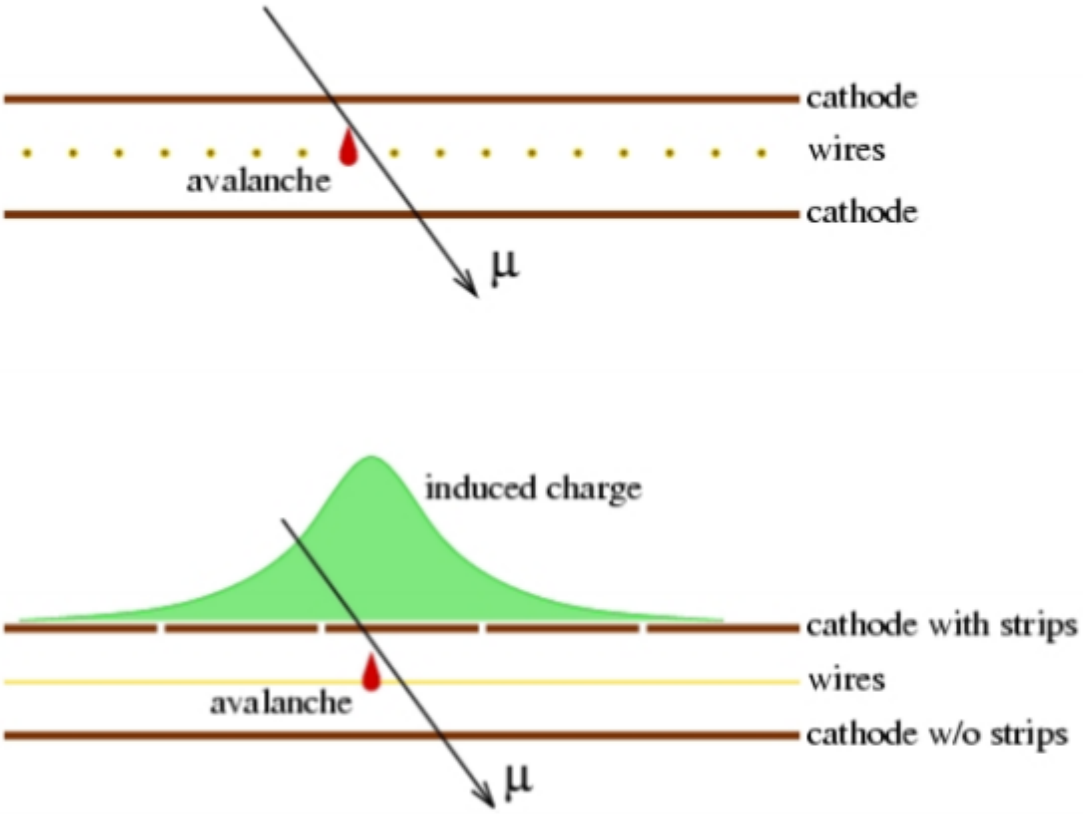

Figure 3.18: A schematic view of a single gap illustrating the principle of CSC operation. An electron avalanche resulting from a muon traversing a gas gap produces a signal on anode wires and induces a distributed charge on cathode strips [41].

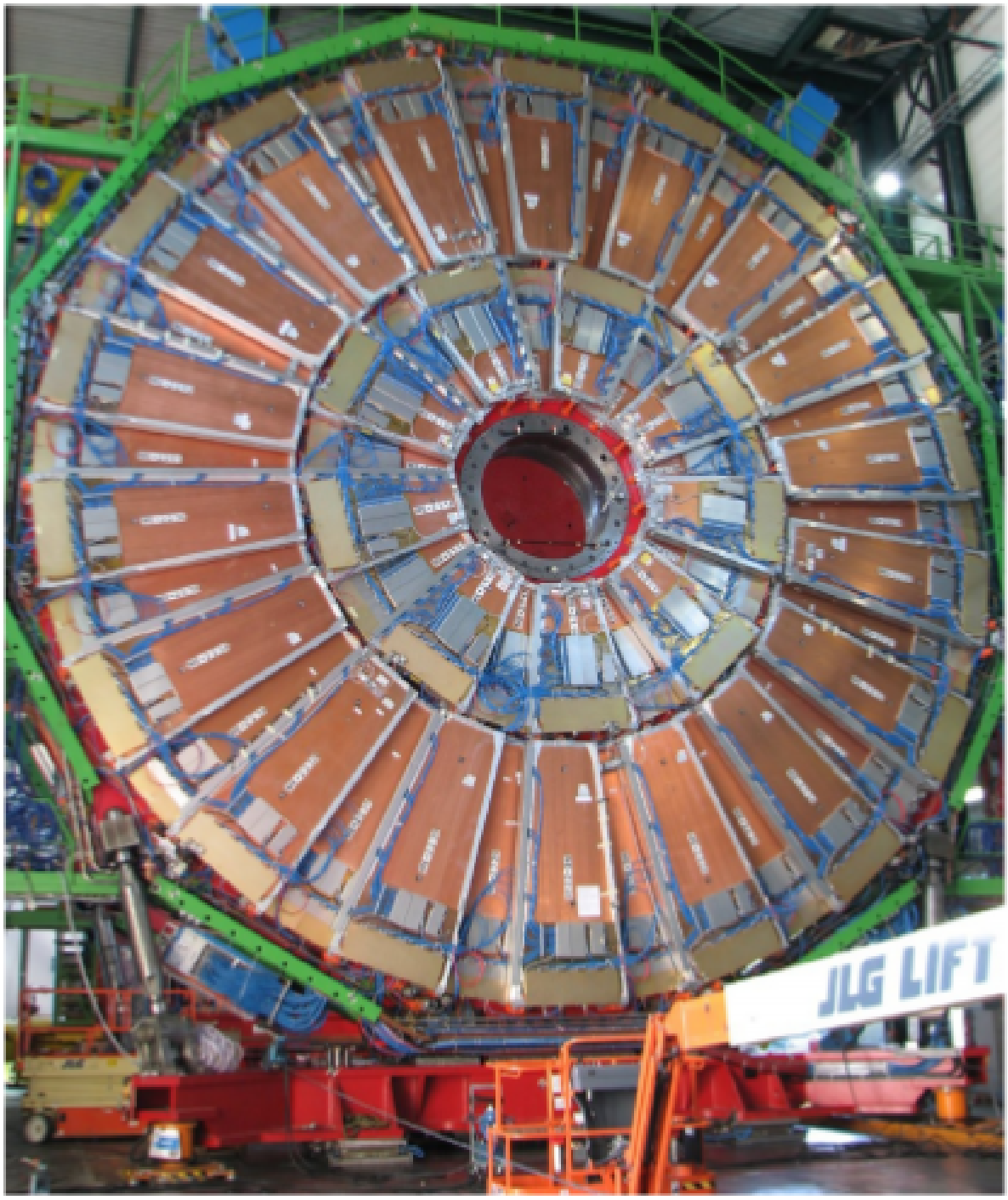

Figure 3.19: A photo of the second disk in positive side ME+2 [41].

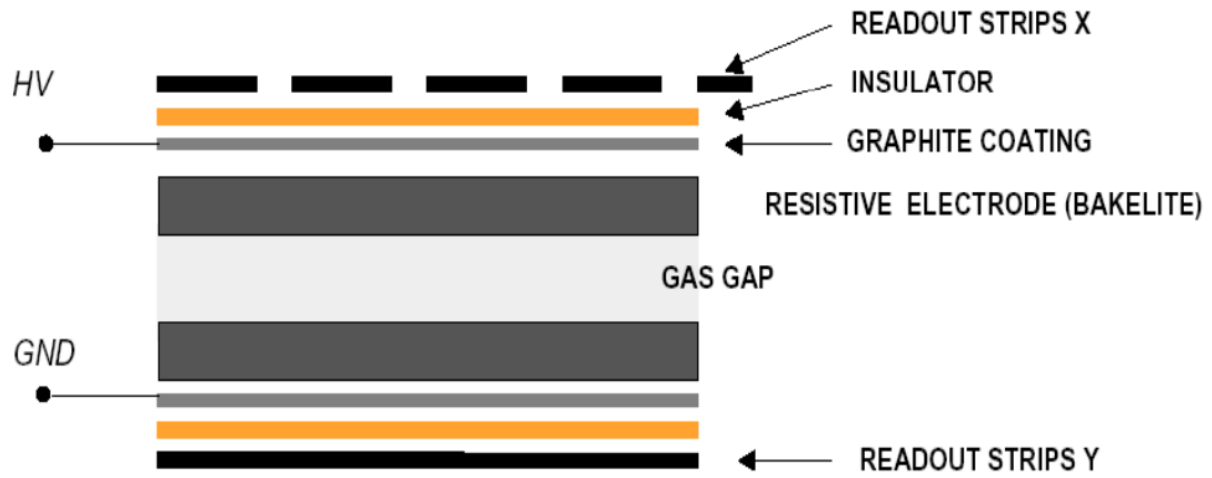

Figure 3.20: The cross section of the double-gap RPC chamber [48].

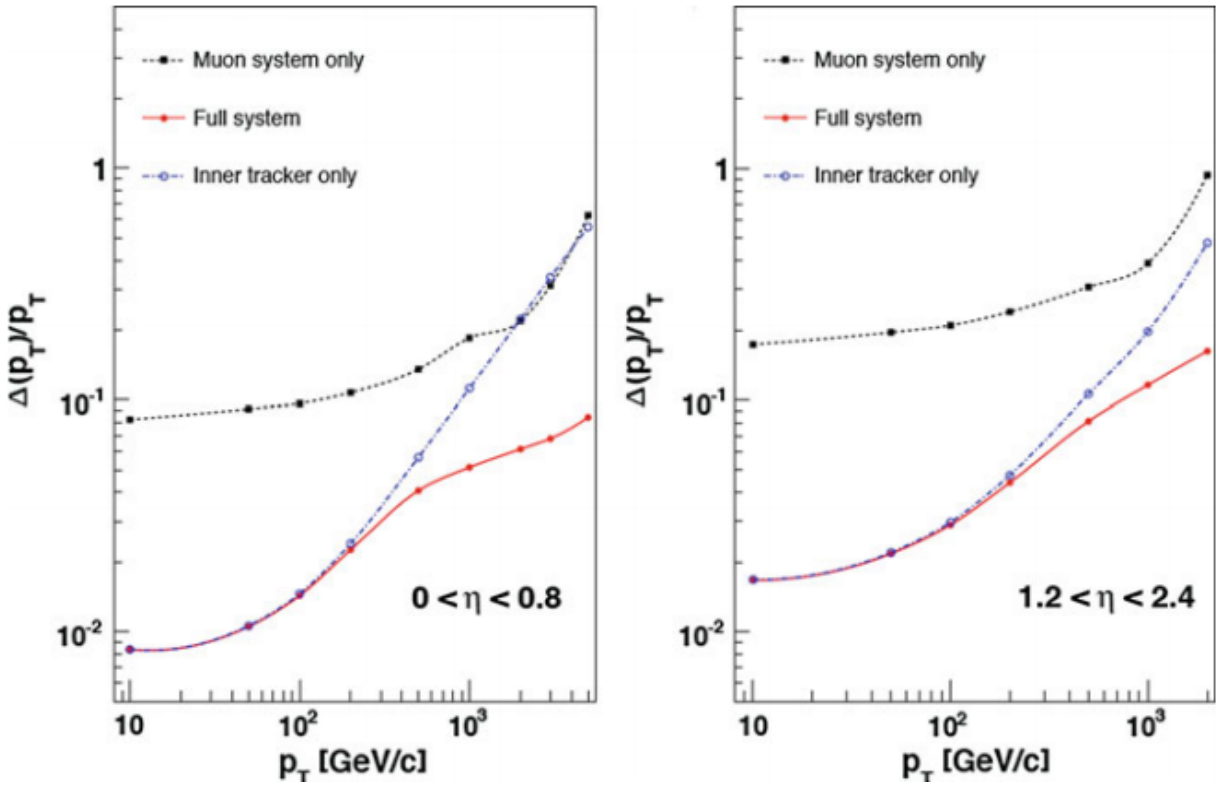

Figure 3.21: Muon transverse momentum resolution as a function of the transverse momentum for muons detected in the barrel (left) and the endcap (right) regions. The resolution is given for the measurement using the muon system only, the tracking system only, and for a combined method [41].

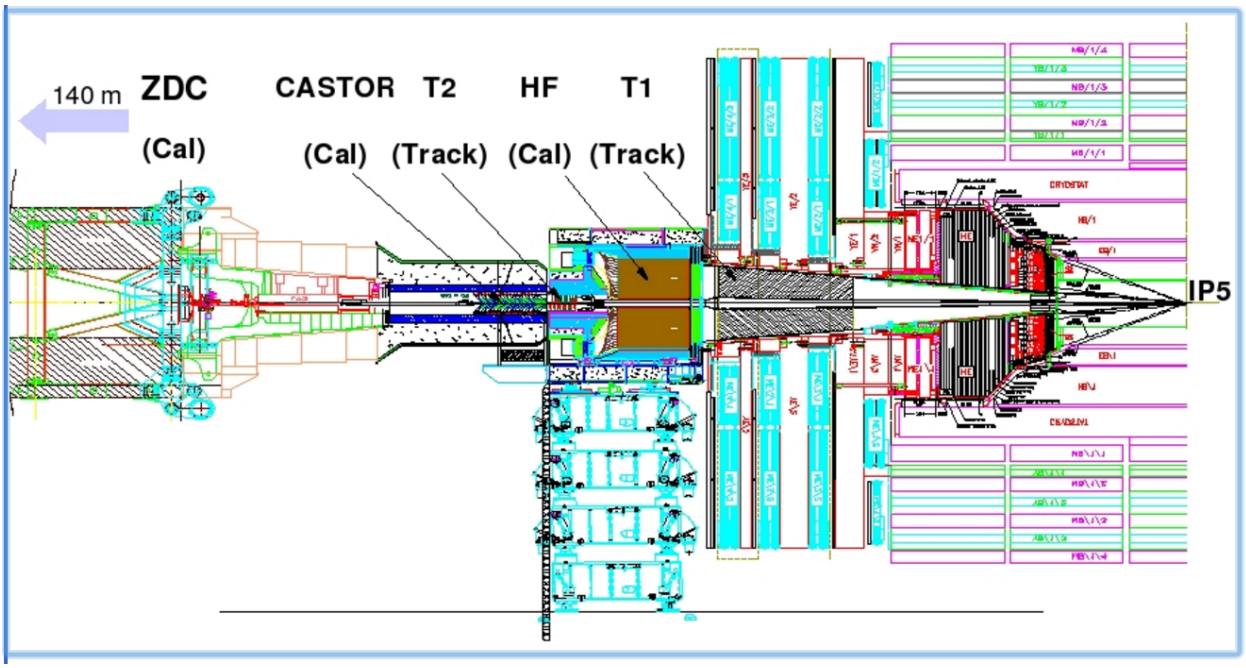

Figure 3.22: Sketch of the relative locations of the ZDC, CASTOR, and other parts of the CMS detector [41].

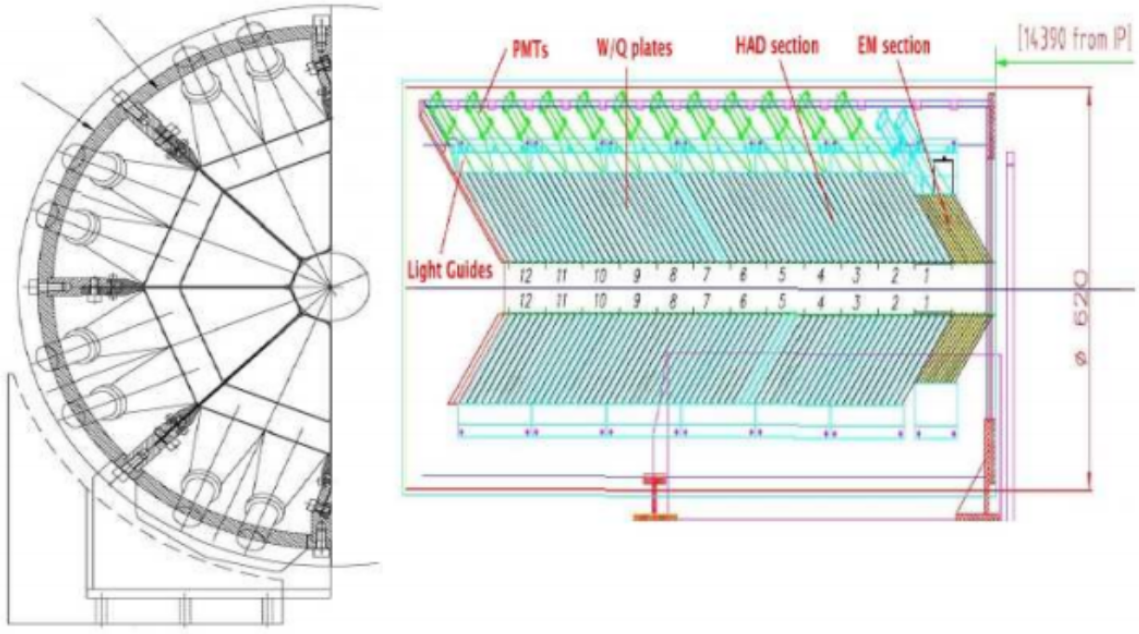

Figure 3.23: Sketch of the CASTOR calorimeter: front view (left) and longitudinal cross section(right) [41].

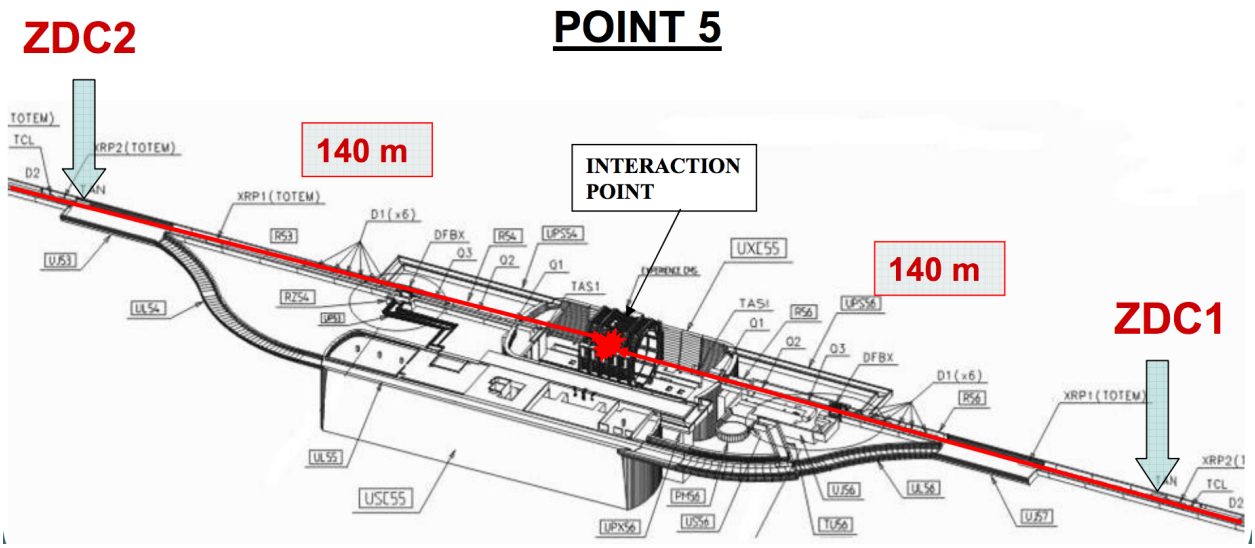

Figure 3.24: The ZDCs locations in CMS [49]

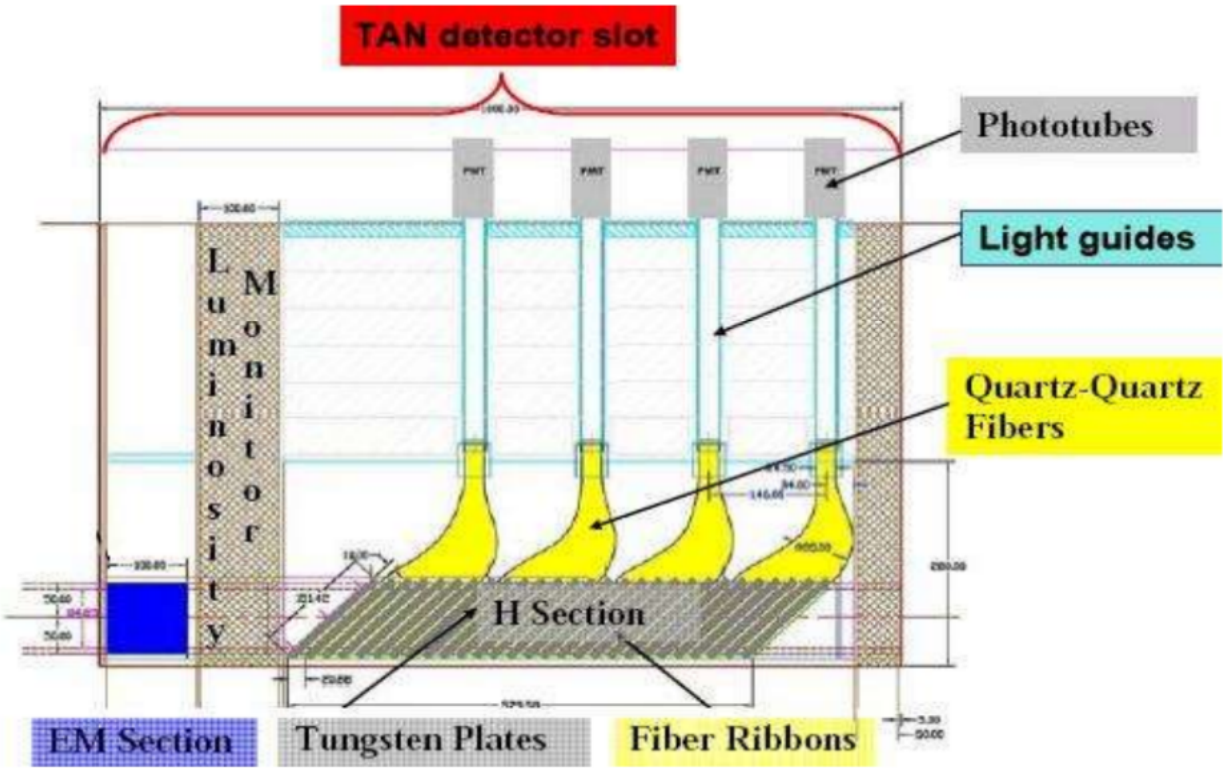

Figure 3.25: The side view of the ZDC showing the EM and HAD sections [50].

Chapter 4

The Trigger System

4.1 Introduction

The LHC was designed to reach an instantaneous proton-proton luminosity of about $10^{34} cm^{-2} s^{-1}$. Different bunches of protons or ions in the machine are separated by a minimum of 25 ns to give a maximum bunch-crossing rate of 40 MHz. CMS does not have sufficient offline storage to record the data from every bunch crossing. Therefore the trigger system is designed to select the most important events and so reduce the bunch crossing rate to an acceptable output rate of less than 1 kHz. To reach the design luminosity there must be multiple interactions per bunch crossing. In 2015 CMS recorded up to 70 pp interactions in one bunch crossing with an average closer to 20. Selecting the most interesting events under such conditions requires a very sophisticated and fast trigger.

The rejection power of $O(10^5)$ is split into two steps. The first step, Level-1, or L1, reduces the rate of accepted events to less then 100 kHz. The second step, known as the High Level Trigger, or HLT, reduces the L1 trigger rate to a final rate of a few hundred Hz. Figure 4.1 shows a schematic view of the CMS trigger and Data Acquisition system.

The L1 Trigger consists of specialized hardware and processors that use the data from the calorimetry and muon systems to select the most interesting events. The data from the detector are digitized and put into front-end pipelines. These pipelines have a latency of 3 μs. At the same time the data from the muon and calorimeter systems are sent to the L1 Trigger. After 1 μs the L1 accept flag for that event is set to be either true or false. If the L1 accept is true, the data from that event are sent to the readout buffers (RU) otherwise the data from the event are discarded forever.

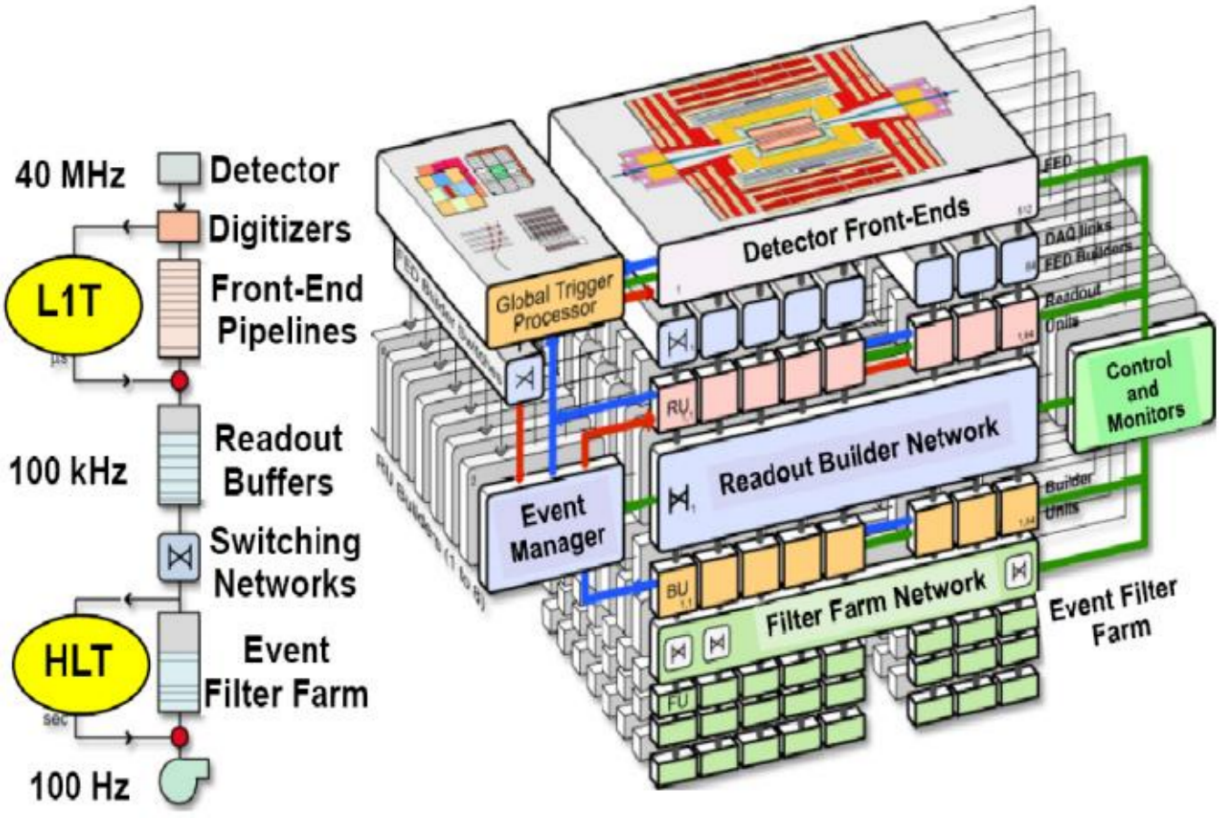

Figure 4.1: Schematic view of the data flow in the CMS trigger and DAQ system. Left: the successive stages. Right: the modularity (slices) of the system [51]

For events that are accepted at L1, the compete data for the event are collected in the event builder network. The builder network then sends completed events to the filter unit of the High Level Trigger (HLT). The HLT consists of a large number of processors, and performs a variety of physics selection algorithms on information from the whole detector, including the trackers. The results of these physics algorithms are then used to make the final decision on the data and store the accepted data permanently. These algorithms are as sophisticated as the offline analysis. The mean time for the HLT decision is on the order of $O(10)ms$ for pp events but is much larger for central heavy ion events. The results from the L1 trigger and HLT are sent to the Tier 0 center for storage on tape. A more detailed description can be found in Ref [104].

4.2 The Level-1 Trigger

Figure 4.2 shows the Level-1 trigger structure. The L1 trigger has local, regional and global components. The Local Trigger LT, also called Trigger Primitive Generator (TPG), is based on energy deposits in the calorimeters and hit patterns in muon chambers. Regional Triggers (RT) combine the trigger primitive information and use a logical process to rank and sort trigger objects such as electrons, muons, or jet candidates in limited spatial regions. A rank is determined as a function of energy, momentum and quality. The Global Calorimeter Trigger (GCT) and Global Muon Trigger (GMT) determine the highest rank calorimeter and muon objects across the entire experiment and transfer them to the global Trigger (GT). The GT takes the decision to reject or accept the event for more evaluation by the HLT [105].

4.2.1 Calorimeter trigger

In the Level-1 Trigger, the ECAL and HCAL calorimeters calculate energy deposits in trigger towers $(0.087\eta \times 0.087\phi)$ in the barrel. These energy deposits, known as trigger primitives, are sent to the Regional Calorimeter Trigger (RCT). The RCT identifies the total energy and the energies from electrons and photons in wider regions $(0.35\eta \times 0.35\phi)$ in the barrel. The e/γ and regional

sums are sent to the GCT. The GCT finds jets, total energy, energies of electrons and photons candidates, and calculates whether the electron and photon candidates are isolated. The GCT then sorts all of these objects by energy or momentum. After this is done, the GCT sends four isolated e, γ candidates, four non-isolated e/γ candidates, four central jets, four forward jets, four τ jets, and the total and missing energy to the Global Trigger GT.

4.2.2 Muon trigger

All three muon systems, the DT, CSC and RPC, participate in the trigger. The barrel DT chambers provide local trigger information in the form of track segments in the ϕ-projection and hit patterns in the η-projection. The endcap CSCs submit 3-dimensional track segments. All three chamber types identify the bunch crossing of the event. The Regional Muon Trigger consists of the DT Track Finder DTTF and the CSC Track Finder CSCTF. These join segments together to form complete tracks and determine the physical parameters of the tracks. The RPC Trigger chambers have an excellent time resolution. They submit the regional hit pattern of track candidates to the Global Muon Trigger. The GMT combines the information from the DT and CSC track finders and the RMT of the RPC to provide an improved momentum resolution and efficiency.

4.2.2.1 The Drift Tube Trigger

The read-out electronics of each DT performs a straight segment fit within superlayers. This fit requires hits in at least three of the four layers of drift cells. In r-z superlayers, only segments pointing to the interaction point are selected. In the two $r-\phi$ superlayers, the reconstructed segments in each chamber are matched by the Track Corrector (TRACO), to improve the angular resolution. Then the Trigger Server (TS) selects from the pairs of segments in each chamber the two corresponding to the highest p_T, and sends them to the DTTF. The DTTF matches the reconstructed segments in the four stations into a single muon track candidate and determines the quality and the track parameters p_T, η and ϕ. The candidates are sorted and the four highest p_T muon candidates are sent to the Global Muon Trigger GMT.

4.2.2.2 The CSC trigger

The CSC local trigger reconstructs track segments in three dimensions by using the strips and the wires in six layers of each chamber. The cathode strips reconstruct the ϕ coordinate and determine the p_T of the track. The anode wires reconstruct the η coordinate and assign a bunch crossing to the track. The determination of the bunch crossing requires two hits in different layers, whereas the reconstruction of segments requires four hits in the six CSC layers in each chamber. A time coincidence of anode and cathode segments is required to reconstruct the segment in three dimensions. The CSCTF receives and matches segments from different stations to reconstruct a candidate muon track and determine the track quality and its p_T, η and ϕ.

4.2.2.3 The RPC Trigger

Hits in each resistive plate chamber are collected directly by the Pattern Comparator Trigger PACT. PACT selects the hits that are correlated in space and time in the four RPC stations. The hits are matched with pre-defined patterns to identify and estimate the p_T of the muons. The PACT requires that muon tracks have hits in at least three of the four stations. A suppression algorithm is applied to reduce the effects of coincidences due to background hits. The four highest p_T muon candidates in the barrel and the four highest p_T of muon candidates in the endcap are sent directly to the GMT.

4.2.2.4 Global Muon Trigger

The GMT matches the muon candidates from the RMTs by comparing the spatial coordinates (ϕ, η) of the segments. This matching balances high efficiency and background suppression. The GMT sorts the muon candidates and passes the best four muon candidates with their parameters to the L_1 Global Trigger GT.

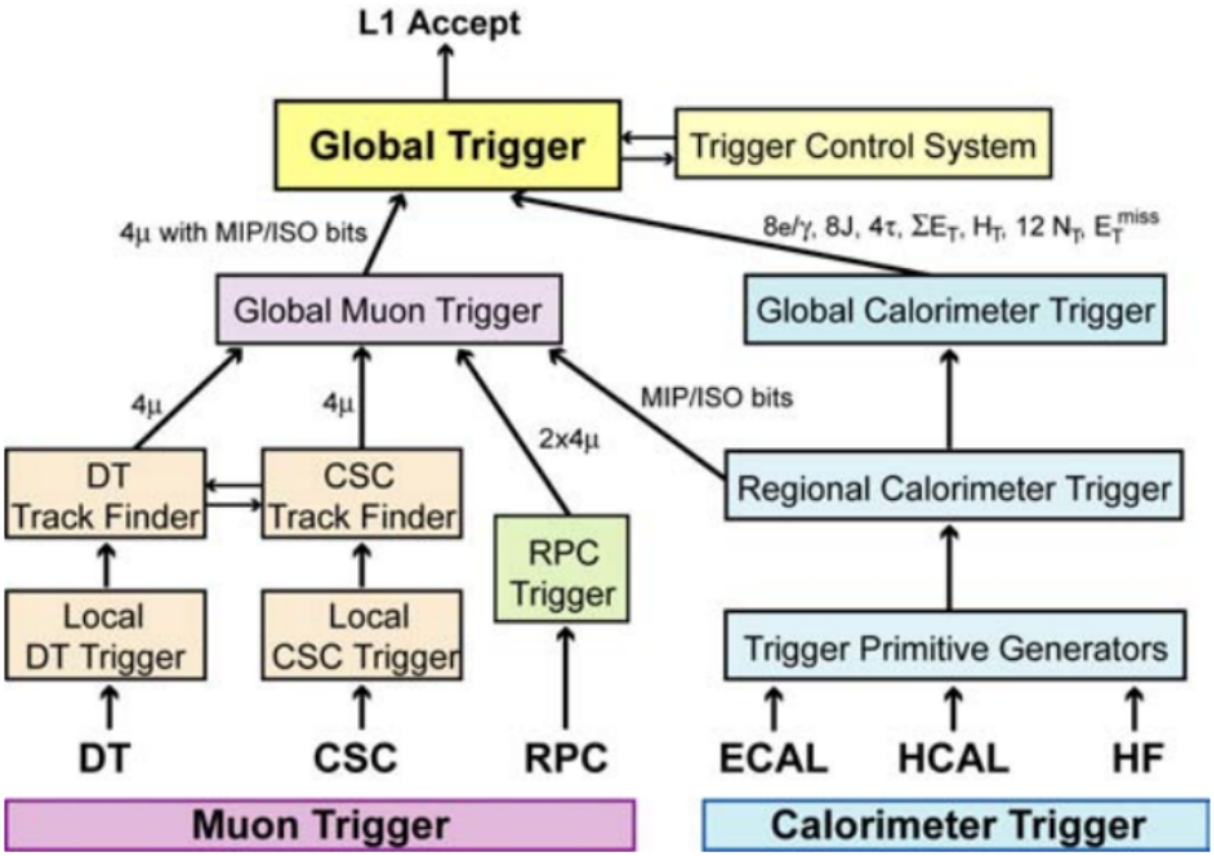

Figure 4.2: A schematic view of the CMS L1 Trigger [41]

4.2.3 Global trigger

The Global Trigger takes the final decision to accept or reject an event at Level-1. This decision depends on the inputs from the GMT and GCT and the trigger paths defined for a particular run.

4.3 HLT

The HLT software runs on a large computer farm of fast commercial processors. The algorithms have access to data from all CMS sub-detectors, including the tracker, with full granularity and resolution. The HLT reconstruction software is similar to what will eventually be used offline for CMS data analysis. Hence, the HLT algorithms, in contrast with the L1 trigger, calculate quantities with a resolution comparable to the final detector resolution. For example, tracking information from pixel and silicon strip detectors is combined with patterns of calorimeter energy deposition

to define electron candidates. Tau-jet candidates found in the calorimeter are combined with high p_T stubs in the tracker to form a hadronic τ trigger which has excellent efficiency and purity. These techniques enable the HLT to define its output objects very precisely and significantly reduce background. The HLT output quantities are similar to those of L1 but with far better resolution, purity and efficiency. The maximum HLT input rate is 100 KHz and the output rate is about 100 Hz [106].

4.4 Ultra-peripheral collisions (UPC) trigger

For the LHC PbPb Run in 2011, the Level-1 trigger selects ultra-peripheral events by requiring at least one hit in the muon chambers, energy deposits in the ZDC calorimeters (a hit due to a neutron in at least one ZDC), and a veto on hadronic activity. The output rate of the Level-1 trigger was 5 kHz. The HLT required at least one reconstructed track in the pixel tracker. The output rate at the HLT for this trigger was about 2 Hz [107].

For the LHC pPb Run in 2013, the Level-1 trigger selected ultra-peripheral events by requiring that at most one of the HF calorimeters had a signal above the noise threshold and at least one hit in the muon chambers. This trigger was designed to take muons with any transverse momentum. The output rate of this Level-1 trigger was 5 kHz. The HLT required at least one and less than 10 reconstructed tracks in the pixel tracker, and at least one track and less than 7 reconstructed tracks in the tracker (pixel and strips). The output rate of this trigger at the HLT was about 5 Hz[107].

Chapter 5

Lead-Lead Analysis

5.1 Introduction

In PbPb collisions the photon may be emitted from either nucleus. At forward rapidity this leads to a two-fold ambiguity in understanding the photon energy since, although the mass and rapidity constrain the energy of the photon and the parton with which it interacts, the direction of the photon is unknown. If the target nucleus breaks up when the J/ψ is created, there will be a correlation between the direction of the J/ψ and the neutron. Such an interaction is shown in Figure 5.1. This is expected to be the case when a photon interacts incoherently with a single proton in the nucleus to form a high p_T J/ψ. Although the neutron may be emitted in any direction in the rest frame of the target the extreme boost at the LHC energies means the neutron will end up in the ZDC that is being approached by the target nucleus.

Photons with wavelength on the order of the nuclear radius are emitted and absorbed coherently by the nuclei. For such photons the cross section is proportional to Z^2. The photon has $p_T \approx \hbar/R = 30$MeV. Since the transverse momentum of the photon is so low and is distributed to the nucleus as a whole, it is likely that the nucleus will stay intact. For neutron emission to occur it is then necessary that a second photon be exchanged between the nuclei. This photon produces a Giant Dipole Resonance (GDR) in the nucleus, which results in neutron emission. Since this second photon may strike either nucleus, the direction of the neutron is not correlated to that of the J/ψ. This process is shown in Figure 5.2. In this chapter the correlation between photo-produced J/ψ mesons and neutron emission is studied by analyzing the signal distribution in the ZDCs to determine the neutron direction, the rapidity distribution to determine the J/ψ direction, and the

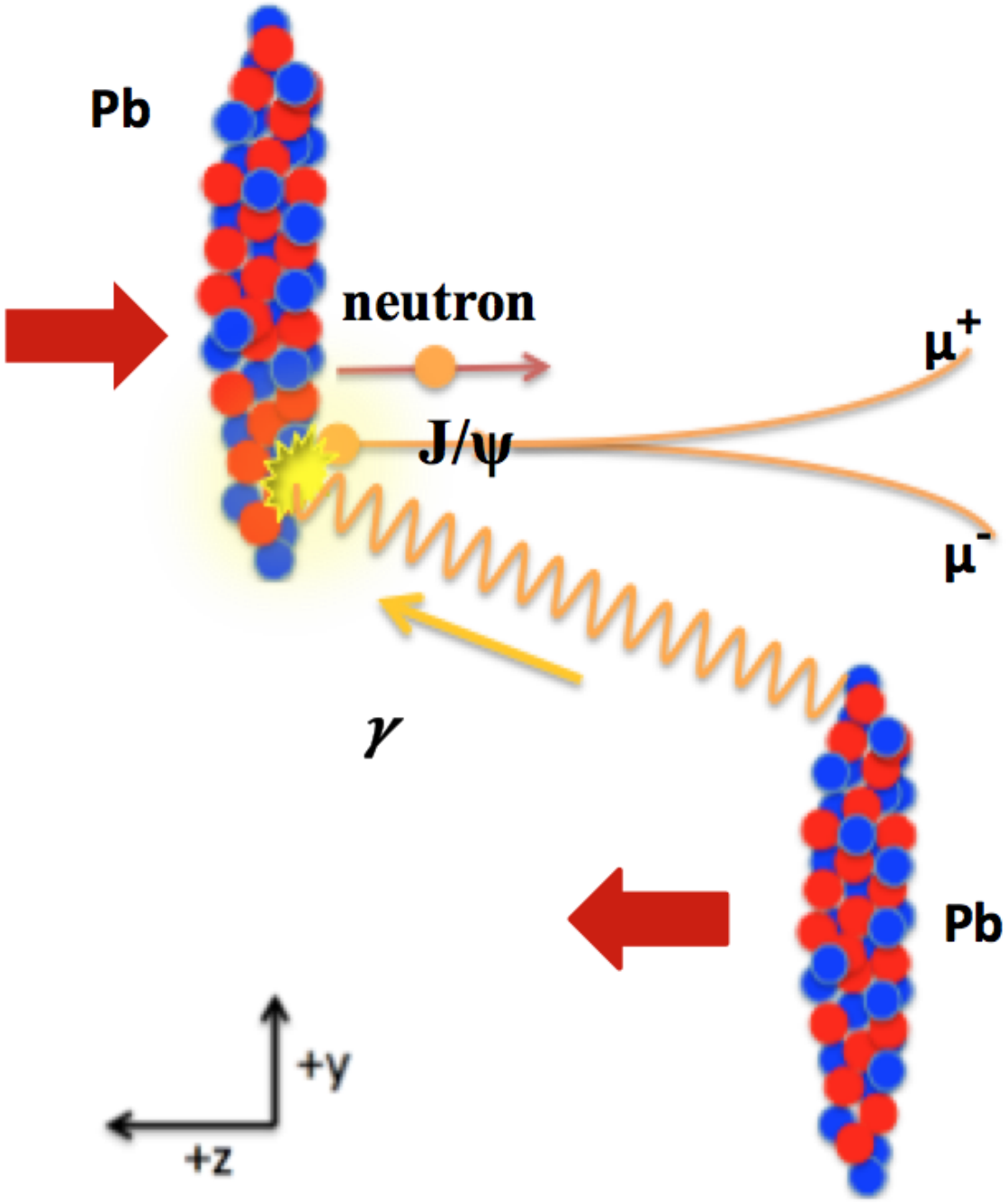

Figure 5.1: Incoherent Interaction: A photon collides with a single nucleon in the target nucleus, producing a J/ψ and a neutron simultaneously.

p_T distribution to determine whether the interaction was coherent or incoherent.

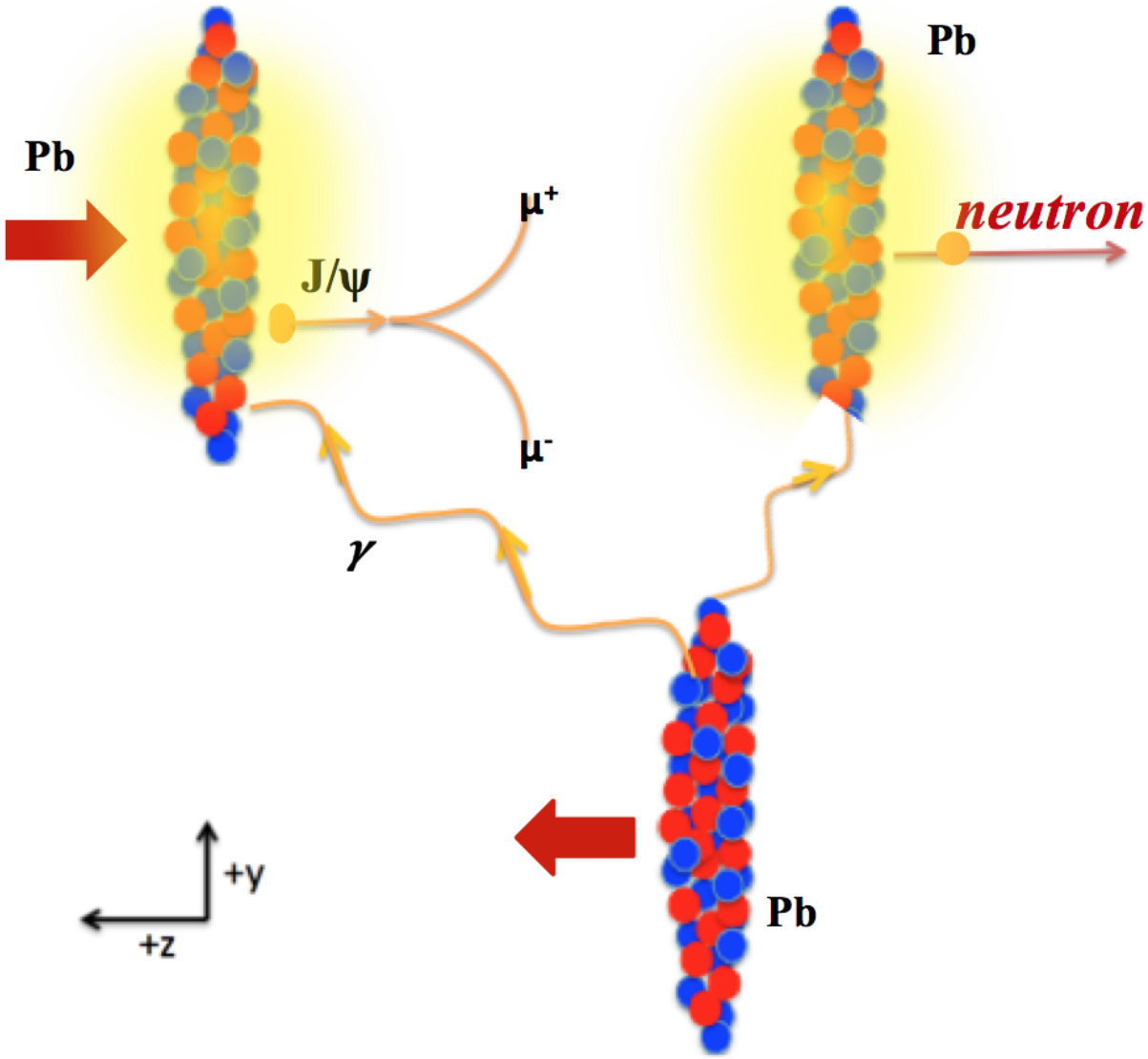

Figure 5.2: Coherent Interaction:A photon collides with the nucleus target as a whole, producing a J/ψ. Another photon causes the emission of a neutron from the target.

5.2 Data set and trigger

The data were collected during the 2011 Pb+Pb LHC runs. The momentum of each of the lead ions was 1.38 TeV per nucleon, which corresponds to a center of mass energy $\sqrt{s_{NN}} = 2.76$ TeV. The total luminosity collected in 2011 was $L_{int} = 159\mu b^{-1}$. The Level-1 trigger was $(L1-MuOpen\_ZdcCalo\_NotBscMinBiasThresh2\_BptxAND)$[107]. This trigger selects ultra-peripheral events by requiring at least one hit in the muon chambers, *MuOpen*, energy deposits in the ZDC

calorimeters (a neutron in at least one ZDC), $ZdcCalo$, a veto on hadronic activity, $NotBscMinBiasThresh2$, and two beams present in CMS, $BptxAND$. The output rate of the Level-1 trigger was 5 kHz. This trigger was used as input to the high level Trigger named $(HLT\_HIUPCNeuMuPixel\_SingleTrack\_v1)$ [107]. This trigger required at least one reconstructed track in the pixel tracker, $SingleTrack\_v1$. The output rate of this trigger at the HLT was about 2 Hz.

5.3 Event Selection

CMS has developed certain standard cuts to select clean physics events and to reject beam-gas and cosmic ray events. The first step in selecting good events is to require that the interaction vertex be within the fiducial region defined by the overlap of the two beams. Figure 6.2 shows the distribution of the event vertex along the z axis for all of the events collected by the UPC trigger and for the final event sample used in the analysis. The event vertex was required to have a transverse distance $D_{xy} \leq 2$ cm and a longitudinal distance $D_z \leq 20$ cm from the center of the beam spot.

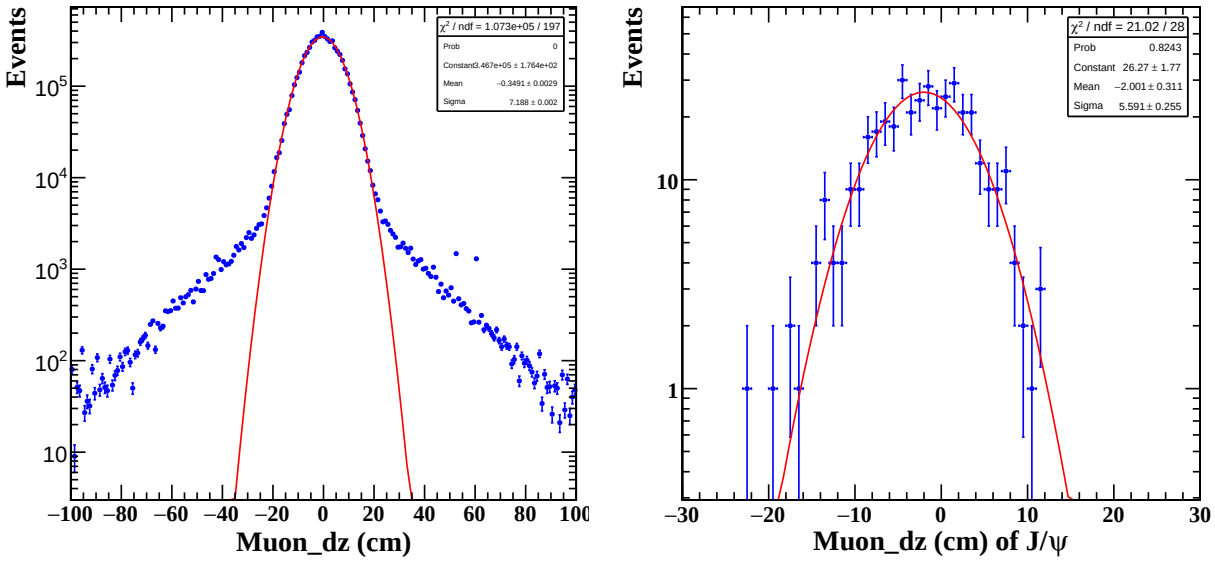

Figure 5.3: Distribution of the event vertex along the z axis for all of the events collected by the UPC trigger (left) and for the final event sample used in the analysis (right).

In order to select exclusive J/ψ candidates, only events with exactly two tracks of opposite sign were accepted. Each tracker track was required to be matched with at least one muon segment

and to have at least one hit in the silicon pixels. Figure 6.3 shows the distribution of pixel and tracker layer for all events and for events that pass the selection cuts.

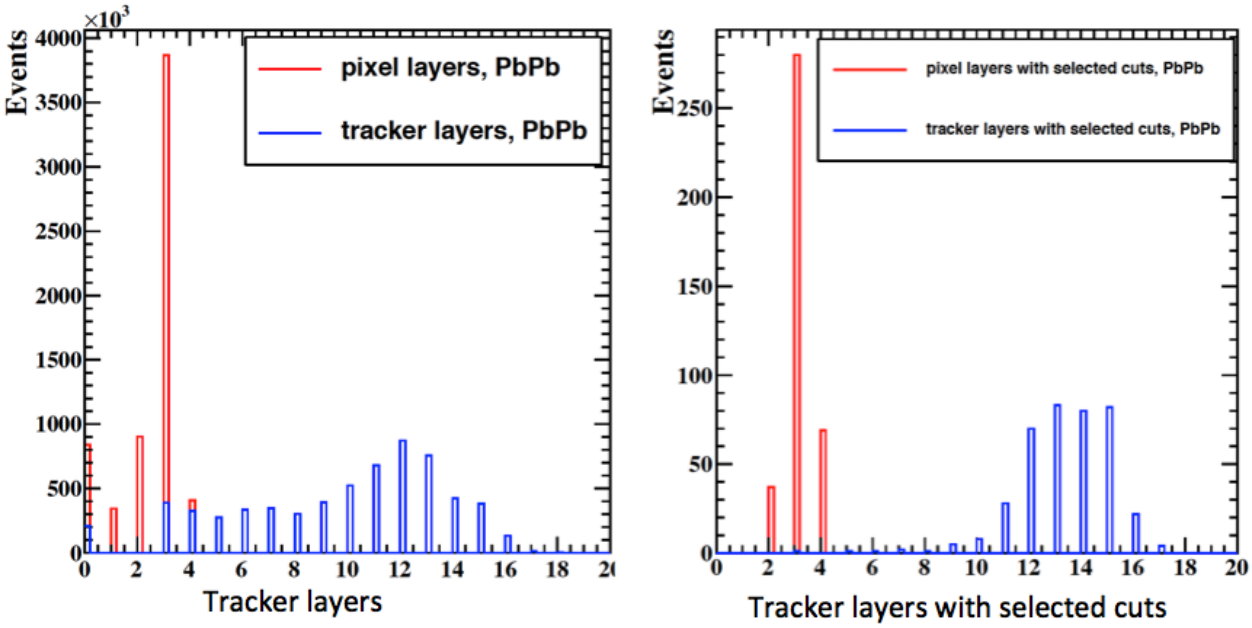

Figure 5.4: Distribution of number of pixel and tracker layers per muon for PbPb for all events (left) and for the events with selected muons (right).

For an ideal event there should only be two muons with opposite charge reconstructed in CMS and the signals in all the calorimeters should be consistent with noise. Figure 5.5 shows the energy distributions for $HF^{\pm}$, $HB^{\pm}$, $HE^{\pm}$ and $EB^{\pm}$. The vertical red lines show the noise thresholds used for the analysis cuts. These thresholds are listed in Table 5.1.

Threshold	HF-	HF+	HB-	HB+	HE-	HE+	EB-	EB+
Energy (GeV)	2.5	2.5	1.2	1.2	1.5	0.5	0.5	0.5

Table 5.1: Noise thresholds for each of the calorimeters used to select exclusive events.

5.4 Selection of breakup modes with the ZDCs

The ZDCs are used to select the breakup modes. Figure 5.6 shows the spectra of charge collected by the ZDCs for zero-bias events. For these events the only requirement was that two lead beams were present in CMS. Clear noise and signal neutron peaks are visible in both ZDC^{+} and ZDC^{-}.

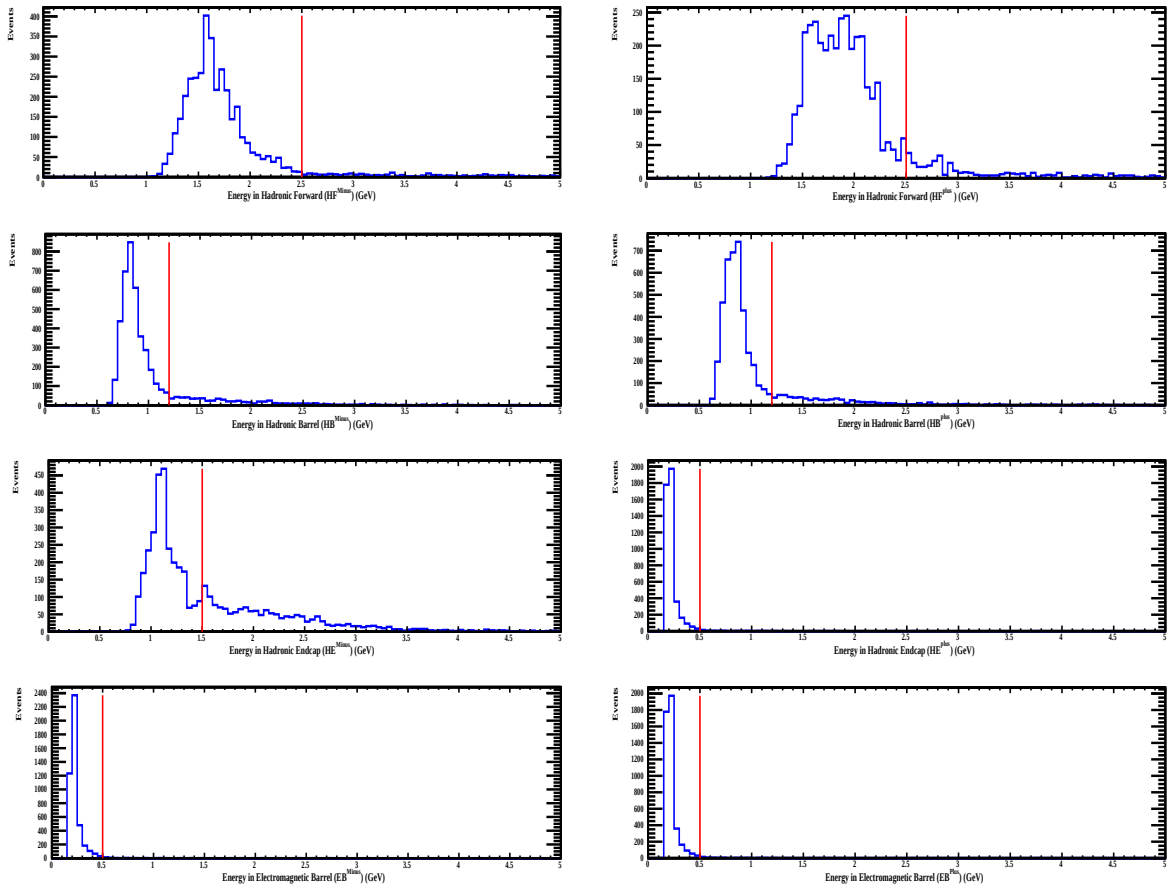

Figure 5.5: Energy distribution for UPC events for (top row) Hadronic Forward HF, (second row) Hadronic Barrel HB, (third row) Hadronic Endcap HE. (bottom row) Electromagnetic Barrel EB. The right column represents energy distributions at forward rapidity ($1.8 < y < 2.4$), and the left column represents energy distributions at backward rapidity ($-2.4 < y < -1.8$). The vertical red lines show the noise thresholds.

The red lines in Figure 5.6 show the thresholds used to select zero neutron or one or more neutron events. These thresholds are listed in Table 5.2.

	ZDC Minus	ZDC Plus
Charge (fC)	500	500

Table 5.2: Noise thresholds for ZDC^- and ZDC^+ for the PbPb data.

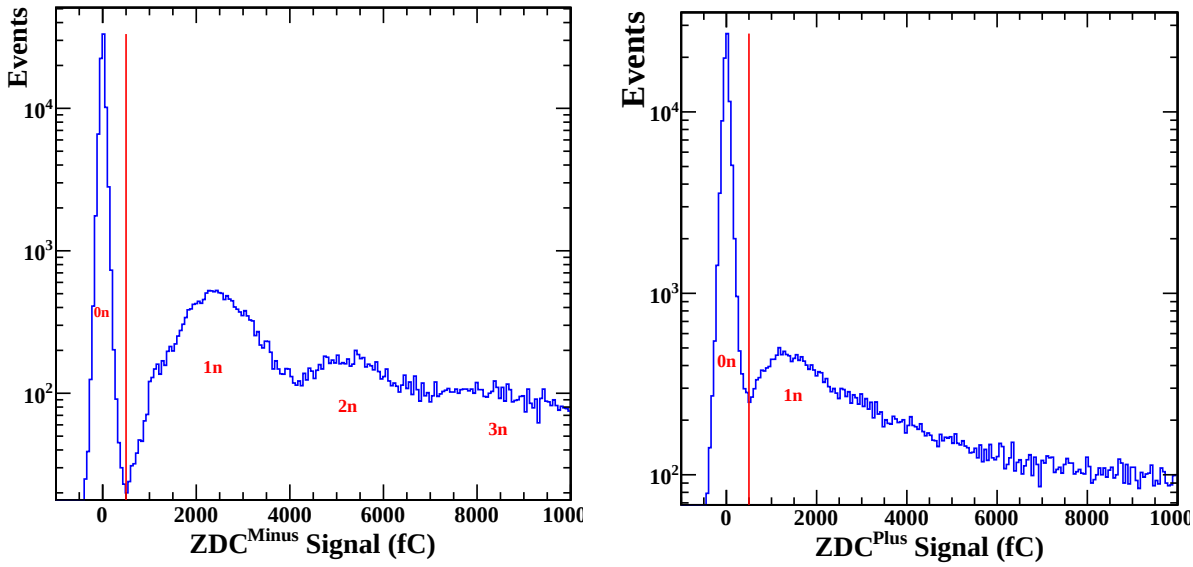

Figure 5.6: Spectrum of charge in femto-coulombs for ZDC^+ (right) and ZDC^- (left) for zero bias PbPb collisions at $\sqrt{s_{NN}} = 2.76$ TeV. The peaks around zero represent the electronic noise. In the ZDC^+, the peaks are corresponding to 1, 2 and 3 neutrons. In the ZDC^-, the resolution is worse because of a dead channel and only the 1 neutron peak is visible. The red vertical lines determine the noise thresholds in ZDC^- and ZDC^+

5.5 Signal Extraction

Figure 5.7 shows the mass distribution of all dimuon pairs from ultra-peripheral lead lead events. There are very clear J/ψ and $\psi(2s)$ peaks, as well as a continuum from the process $\gamma\gamma \to \mu^+\mu^-$. The distribution in Fig. 5.7 is fit to two Crystal Ball functions, one for the J/ψ and one for the $\psi(2s)$. The Crystal Ball function is described in Appendix 10.3. The continuum background is fit to a polynomial function of order two. Based on these fits a mass cut of $2.8 \leq M_{\mu\mu} \leq 3.3$ was chosen to select J/ψ events.

The p_T dependence of the $\gamma\gamma$ background in the J/ψ sample is estimated using a sideband subtraction technique. The first step is to define the ratio of the continuum in a sideband region to the continuum under the J/ψ peak

$$R_{sideband} = \frac{\int_{2.8}^{3.3} \frac{dN_{fit}}{dM} dM}{\int_{4.0}^{5.0} \frac{dN_{fit}}{dM} dM}. \tag{5.1}$$

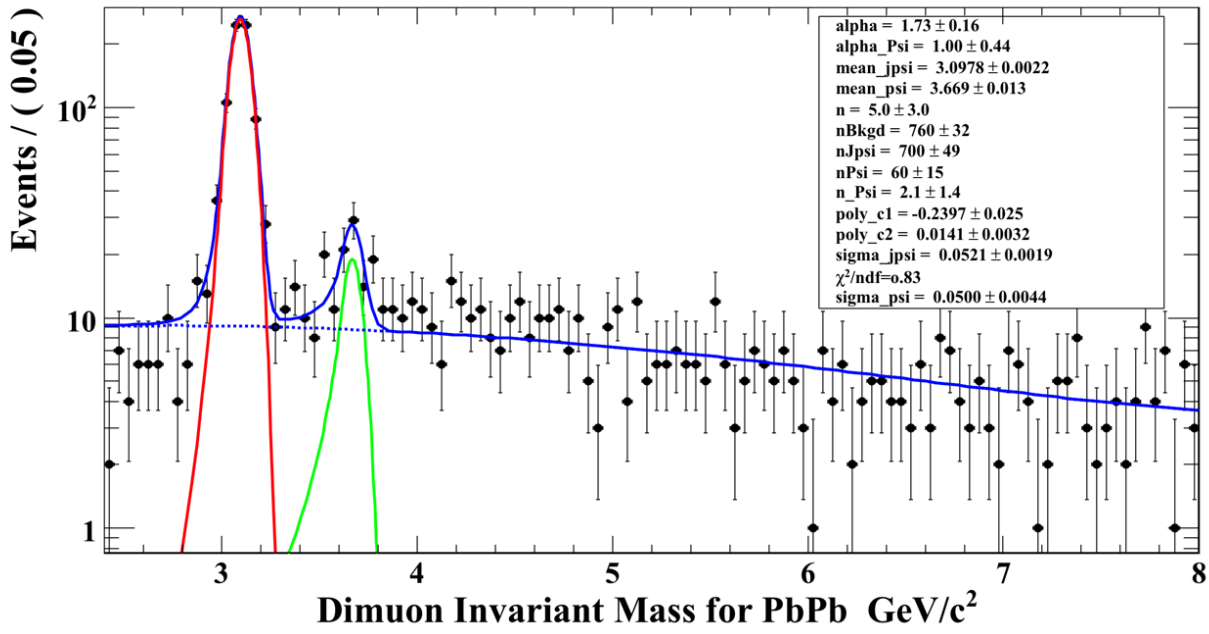

Figure 5.7: Invariant mass distribution for all dimuon pairs that pass the event selection and exclusivity cuts for PbPb collisions at $\sqrt{s_{NN}} = 2.76$ TeV. The solid blue line shows a fit to the distribution. This fit includes J/ψ (red line), $\psi(2s)$ (green line) components and a continuum background (dashed blue line).

Here dN_{fit}/dM is the fit to dimuon mass distribution, see for Example the dashed blue line in Fig. 5.7. The contamination of the J/ψ sample by the $\gamma\gamma$ continuum is then estimated to be

$$\frac{dN_{\gamma\gamma}}{dp_T} = R_{sideband} \cdot \frac{dN_{4-5}}{dp_T} \tag{5.2}$$

where $\frac{dN_{4-5}}{dp_T}$ is the p_T distribution of dimuon pairs with invariant masses between 4.0-5.0 GeV/c^2. Figure 5.8, shows the p_T distributions for the mass ranges (2.8 - 3.3) GeV/c^2 (black) and continuum background for same mass range (blue). The difference between these two spectra represents the J/ψ signal (red). A clear narrow coherent peak is seen at $p_T \approx 50$ MeV/c.

5.6 Correlation between J/ψ and neutron direction.

In order to help determine the direction of the photon that produced the J/ψ, events were selected with zero neutrons in one ZDC and at least one neutron in the other ZDC. This is known as the

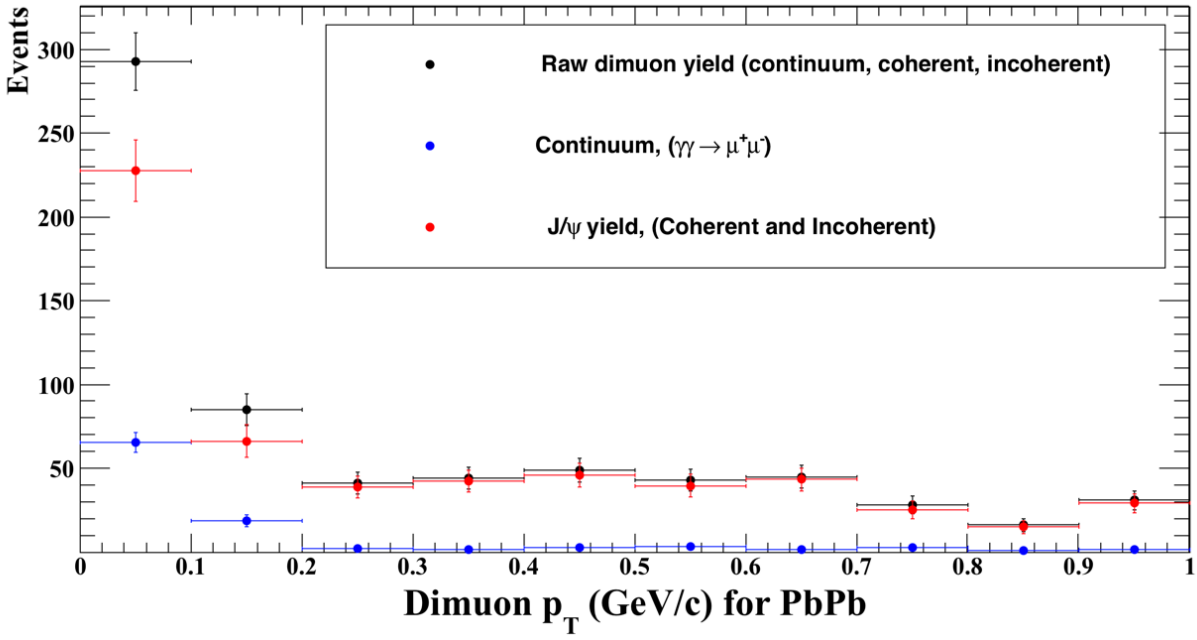

Figure 5.8: Distribution of dimuon p_T for the mass ranges (2.8 - 3.3) GeV/c^2 (black) corresponding to the J/ψ peak, continuum background for same mass range (blue).The difference between the total yield and the background represents the J/ψ signal (red).

(0n,Xn) breakup mode. Figure 5.9 shows the rapidity distribution of coherent (top) and incoherent J/ψ mesons (bottom) for events where the neutrons hit ZDC$^-$ (left) and ZDC$^+$ (right). At low p_T ($p_T < 0.15$ GeV/c), coherent production of J/ψ is dominant, and the distribution of J/ψ rapidity is not correlated with the neutron direction. At high p_T, where incoherent production is dominant, the J/ψ rapidity distribution depends strongly on the neutron direction.

Table 5.3 lists the numbers of events with neutrons in the ZDC$^-$ and ZDC$^+$ detectors and J/ψ mesons at positive and negative rapidity for $p_T < 0.15$ GeV/c (coherent production) and $0.15 < p_T < 1.0$ GeV/c (incoherent production). It is clear that the numbers of J/ψ events at low p_T are consistent for the cases where the neutron is on the same and opposite side, while at high p_T there is a clear difference between the opposite and same side cases. This can be explained by considering Figures 5.1 and 5.2. At low p_T, the photon collides with the target as a whole and the target stays intact. Neutron emission is caused by the exchange of a second photon, as shown in Figure 5.2. At higher p_T, the photon collides with a single nucleon in the target, producing the

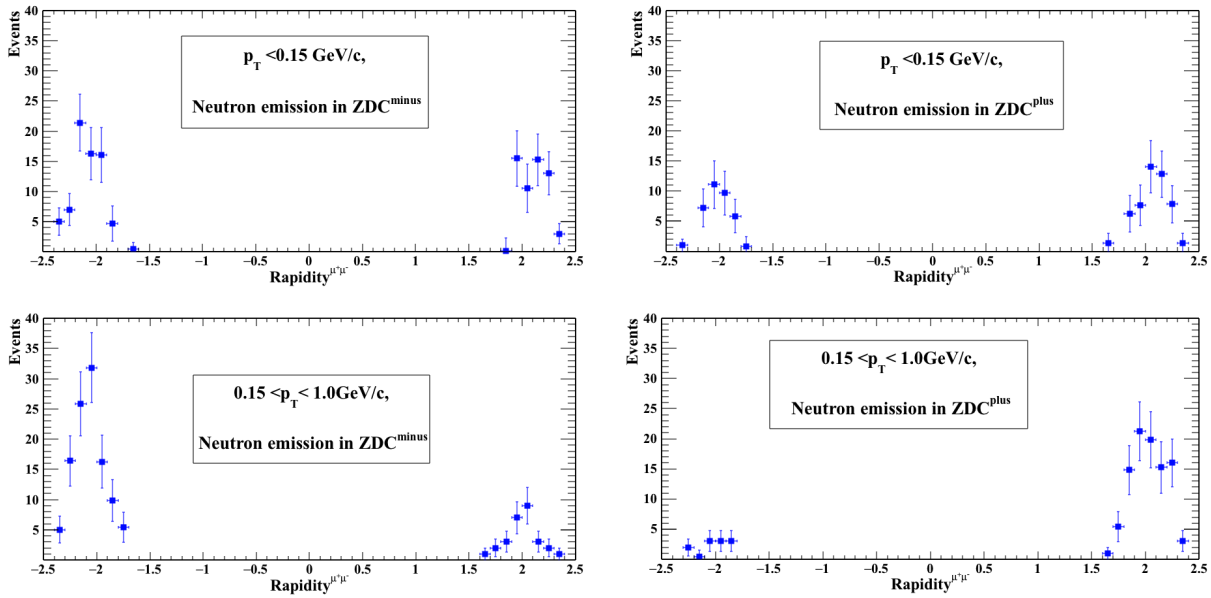

Figure 5.9: J/ψ rapidity distribution at low p_T ($p_T < 0.15$ GeV/c) (top row) and at high p_T ($0.15 < p_T < 1$) GeV/c (bottom row) for events with neutrons in ZDC^- (left column) and ZDC^+ (right column).

J/ψ and causing the emission of a neutron as in Figure 5.1. Since both the neutron and the J/ψ are produced by the same photon interaction there is a correlation between them.

	ZDC$^-$		ZDC$^+$	
J/ψ direction	Same	Opposite	Opposite	Same
Rapidity intervals	(-2.4,-1.8)	(1.8,2.4)	(-2.4,-1.8)	(1.8,2.4)
Coherent: $p_T < 0.15$ GeV/c	70.4 ± 9.1	57.3 ± 8.7	34.1 ± 7.1	50.1 ± 8.1
Incoherent: $0.15 < p_T < 1.0$ GeV/c	105.2 ± 8.1	25.0 ± 5.0	11.4 ± 3.5	90.2 ± 9.9

Table 5.3: The number of J/ψ events with the neutron in the same and opposite side for different p_T and y regions

Figure 5.10 shows the p_T distributions for events where the J/ψ and neutron are in the same and opposite directions. There is a clear difference between the two spectra. For $p_T < 150$ MeV/c, the numbers of J/ψ events are roughly consistent between the two distributions. For higher p_T, there are more J/ψ in the same direction as the neutron than opposite it.

In order to quantify the strength of the correlation between the direction of the J/ψ and the

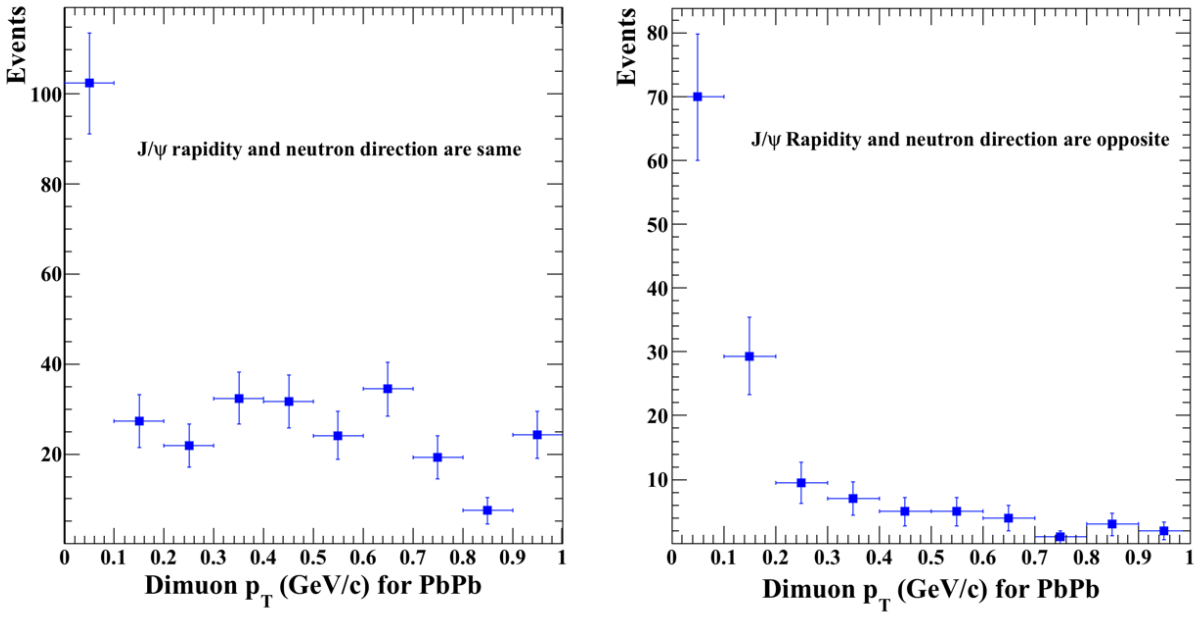

Figure 5.10: J/ψ p_T distribution. Left: J/ψ rapidity and neutron have the same direction. Right: J/ψ rapidity and neutron have opposite direction.

neutron the ratio $R(\frac{opposite}{same})(p_T)$ is defined by

$$R(\frac{opposite}{same})(p_T) = \frac{N^{opposite}(p_T)}{N^{same}(p_T)}, \tag{5.3}$$

where $N^{opposite}(p_T)$ and $N^{same}(p_T)$ represent the numbers of J/ψ with a given p_T that are moving in the opposite and same direction as the neutron, respectively. Figure 5.11 shows this ratio versus p_T. For $p_T \leq 150$ MeV/c the ratio is close to 1.0 while at higher p_T it is significantly lower. Thus for incoherent events there seems to be a strong correlation between the J/ψ and neutron directions while for incoherent events, i.e., $p_T \leq 150$ MeV/c the correlation is much weaker.

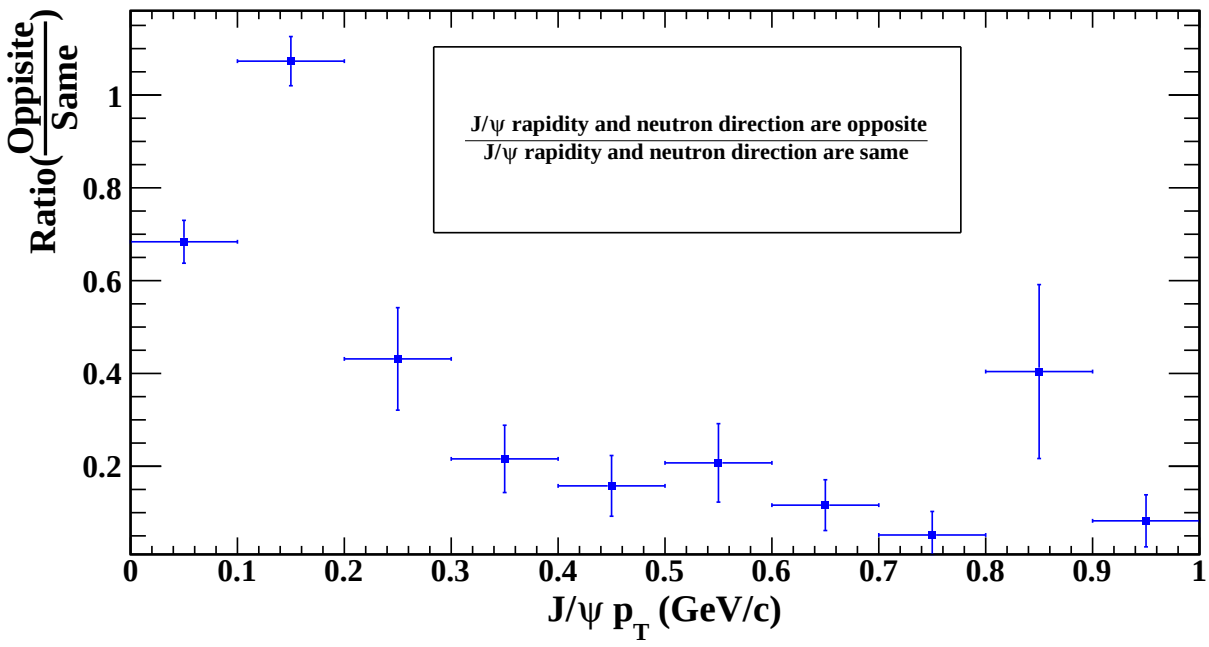

Figure 5.11: Ratio of numbers of events with the J/ψ and neutron on opposite sides to the number with the J/ψ and neutron on the same side

Chapter 6

Proton-Lead Analysis

This chapter focuses on the analysis the Pbp data. For ultra-peripheral Pbp collisions the dominant interaction is when photons collide with protons. The analysis of exclusive $\gamma p \to J/\psi$ is a very clean probe of the gluon distribution in the proton.

6.1 Data sets

The data analyzed in this thesis were collected during the 2013 pPb runs at the LHC. In 2013 the momentum of the proton beam was 4 TeV/c. Because of the design of the LHC the lead beam had the same rigidity, i.e. momentum/charge ratio, as the proton beam. This meant that the momentum of the lead beam was 4TeV * 82/208 = 1.58 TeV. The center of mass of the pPb system has an energy $\sqrt{s_{NN}} = 5.02$ TeV and is moving with a velocity of 0.503c in the direction of the proton beam. This corresponds to a offset of the center of mass rapidity with respect to the experiment of 0.465 towards the proton going direction.

For the first part of the 2013 data, donated pPb, the proton beam moved in the negative z direction (clockwise) and the Pb beam in the positive z direction (anti-clockwise). The integrated luminosity during this period was $L_{int} = 18.83$ nb^{-1} and the CMS run numbers ran from 210498 to 211256. During the second half of the run, which is donated Pbp, the LHC switched the direction of the beams. This period had an integrated luminosity of $L_{int} = 13.92$ nb^{-1} recorded in CMS runs 211313 to 211631. Figure 6.1 shows (a) a diagram of LHC, (b) the direction of proton-beam and Pb-beam in pPb collisions, and (c) the directions of the proton and Pb beams in Pbp collisions. The CMS convention is to consider that the proton beam has positive rapidity, so the results in this

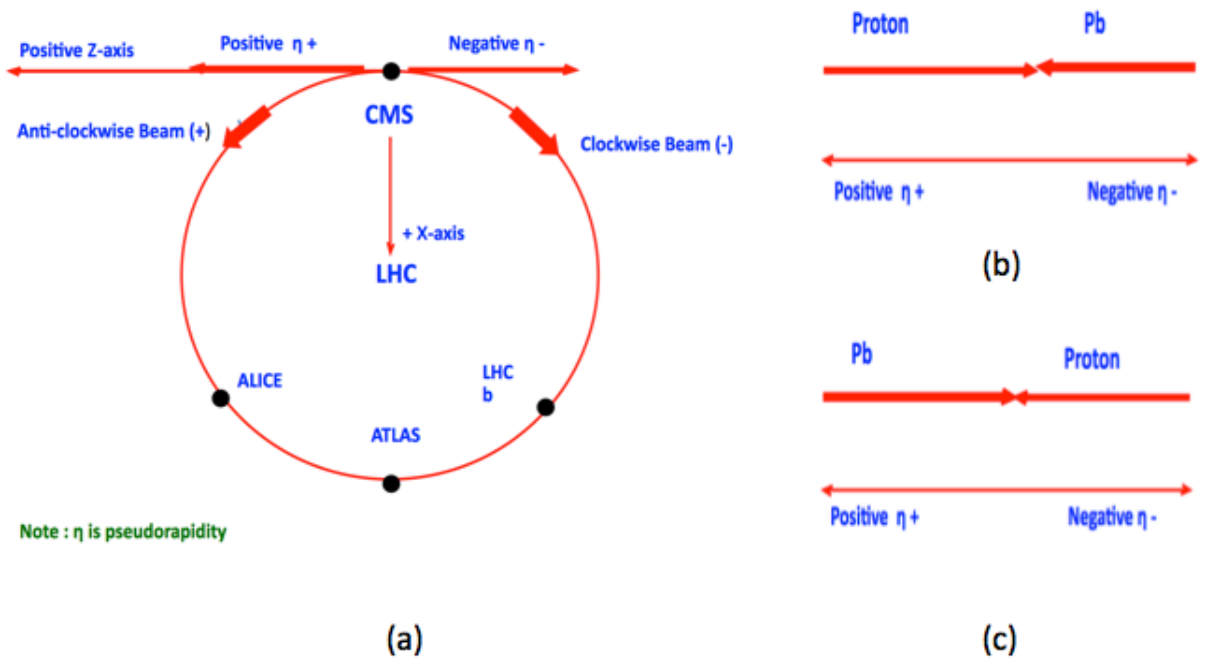

Figure 6.1: (a) A diagram of the LHC, (b) the directions of proton and Pb beams in pPb collisions, (c) the direction of proton and Pb beams in Pbp collisions

thesis are presented with the pPb data flipped in rapidity.

6.2 Trigger

The loosest possible trigger was developed to select very low p_T J/ψ mesons from ultra peripheral events.

The triggers used to collect this data selected events containing only low p_T J/ψ s and nothing else. The cross section for such events is about 10^5 times smaller than for ordinary nucleus-nucleus collisions. The Level-1 trigger used was (L1_SingleMuonOpen). This trigger selected ultra-peripheral events by requiring that at most one of the HF calorimeters had a signal above the noise threshold. The trigger also required at least one hit in the muon chambers. It was designed to take muons with any transverse momentum. The output rate of this Level-1 trigger was 5kHz. This trigger was used as input to the high level trigger (HLT_PAUpcSingleMuOpenFull_TrackVeto7_v1). The HLT required at least one and less than 10 reconstructed tracks in the pixel tracker, and at least

one track and less than 7 reconstructed tracks in the tracker (pixel and strips). The output rate of this HLT path was about 5Hz.

6.3 Standard Event Selection Cuts

CMS has developed certain standard cuts to select clean physics events and to reject beam gas and cosmic ray events.

The first step in selecting good events is to require that the interaction vertex be within the fiducial region defined by the overlap of the two beams. Figure 6.2 shows the distribution of the event vertex along the z axis for all of the events collected by the UPC trigger, described in Section 6.2 of pPb and for the final event sample used in the analysis. The event vertex was required to have a transverse distance $D_{xy} \leq 2$ cm and a longitudinal distance $D_z \leq 15$cm from the center of the beam spot. Because of the exclusivity requirement of only two tracks, see Section 6.4 there was at most one reconstructed vertex in the event. From the fits the efficiency of the vertex cut is estimated to be $98.7 \pm .2X\%$. The systematic error on this efficiency was estimated by redoing the fits with a different fit range.

In order to select exclusive J/ψ events exactly two tracks of opposite sign were required. Each tracker track was required to be matched with at least one muon segment. Each tracker track was required to have more than 5 hits in the tracker with at least one hit in the silicon pixels. Figure 6.3 shows the distribution of pixel and tracker layers for all events and for events that pass the selection cuts.

To eliminate cosmic muons and beam gas events a cut was made on the distance of closest approach between the muon tracks and the event vertex. Figure 6.4 shows the longitudinal and transverse distances of closest approach for pPb and Pbp events. For this analysis the closest longitudinal distance between the event vertex and the muon track is $|D_z| \leq 15$ cm and the closest transverse distance is $D_{xy} \leq 3$ mm.

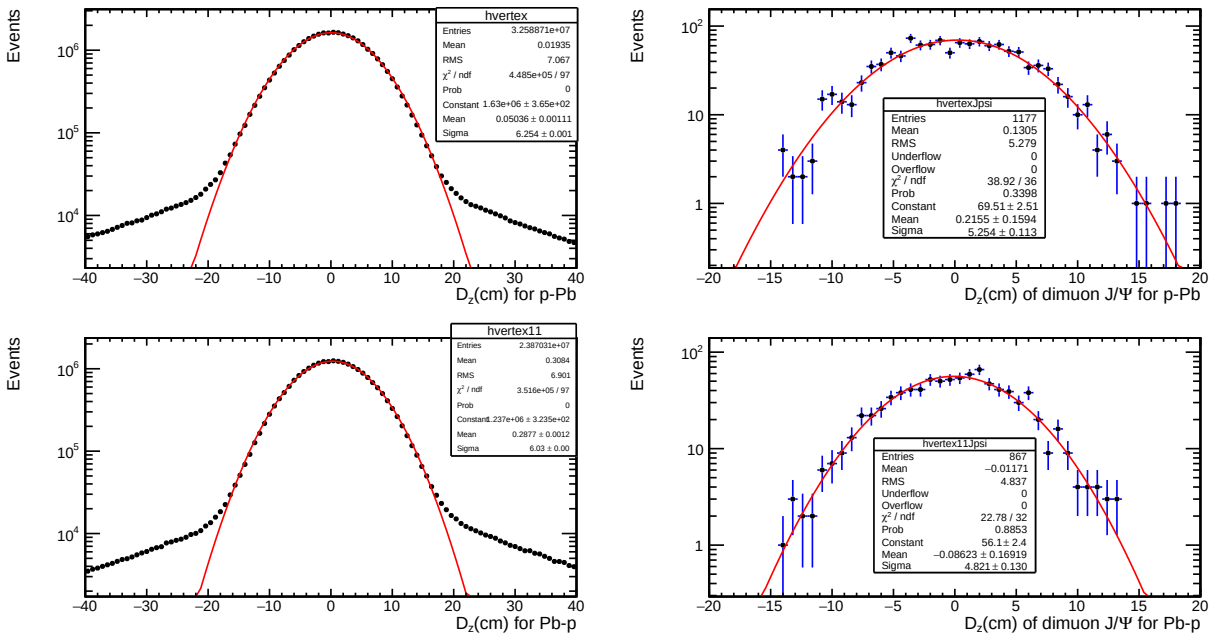

Figure 6.2: Distribution of the event vertex along the z axis for all of the events collected by the UPC trigger (left column) and for the final event sample used in the analysis (right column). The distributions for pPb data are shown in the top row and those for Pbp data in the bottom row.

6.4 Exclusivity Cuts.

For an ideal event there should only be two muons with opposite charge reconstructed in the CMS detector and the signals in all the calorimeters should be consistent with noise.

Figure 6.5 shows an event display for a typical J/ψ candidate. The two muons are very forward and have low p_T. Both muons punch through the CMS endcap and deposit a small amount of energy in EE+. The track of the top muon shows some jitter in the muon chambers. Muons that punch through the CMS material lose about 3 GeV of momentum in the endcap. For low momentum muons the multiple scattering in the steel of the muon chambers can be significant. There are no other reconstructed tracks but there is some noise in the calorimeters.

To select events such as the one shown in Figure 6.5 it is necessary to first determine the noise thresholds from the energy distribution in very quiet events. For both the pPb and Pbp data, Figures 6.6, 6.7, 6.8, and 6.9 show the distributions for $HB^{\pm}$, $HE^{\pm}$, $HF^{\pm}$ and $EB^{\pm}$ respectively. The noise distributions in ($HB^{\pm}$, $HE^{\pm}$, $HF^{\pm}$) were fitted to Gaussian functions and the ($EB^{\pm}$) noise

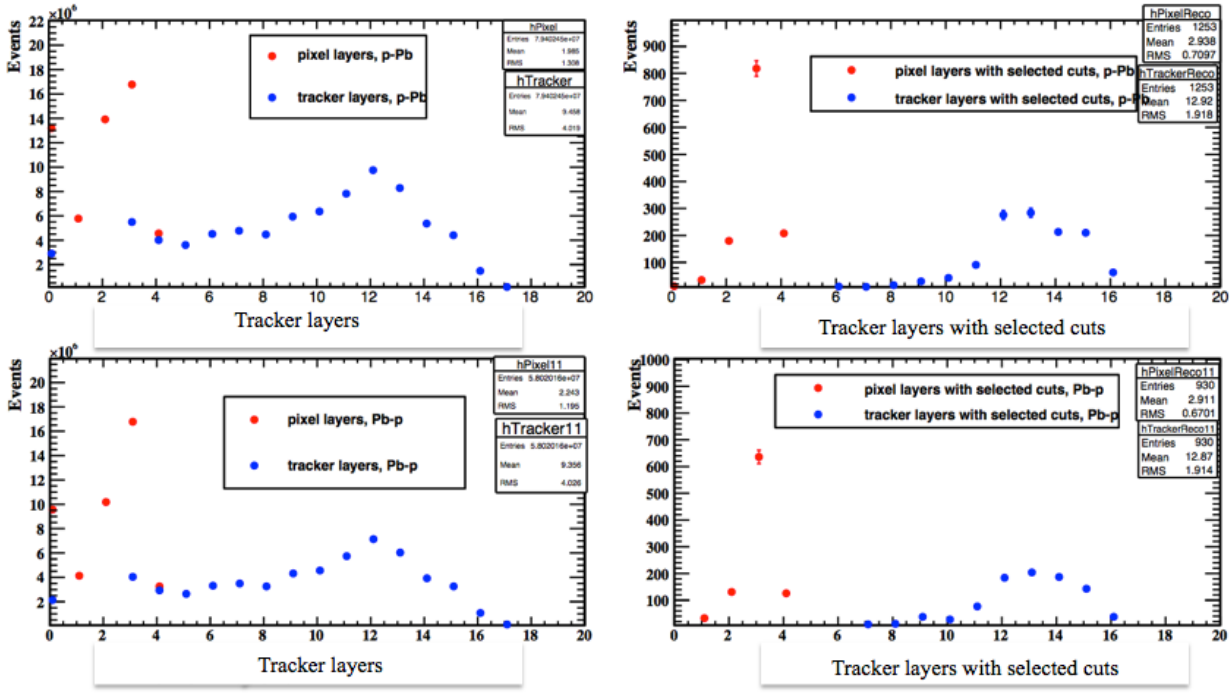

Figure 6.3: Distribution of number of pixel and tracker layers per muon for pPb (top) and Pbp (bottom) for all events (left) and for the events with selected muons (right).

“

distributions were fitted to an exponential function to determine the noise thresholds used for the exclusivity cuts. The deduced energy thresholds are listed in Table 6.1.

	HB^-	HB^+	HE^-	HE^+	HF^-	HF^+	EB^-	EB^+
Threshold Energy (GeV)	1.2	1.1	1.75	1.8	2	2	0.8	0.8

Table 6.1: Noise thresholds for each calorimeter used to select exclusive events.

For exclusive $\gamma p \to J/\psi + p$ events both the lead nucleus that emitted the photon and the proton should remain intact. For such events the signals in both of the ZDC^+ and ZDC^- should be consistent with noise. The energy distributions of neutrons in the ZDC^- (proton side) and in the ZDC^+ (Pb side) are shown in Figure 6.10 and Figure 6.11, respectively. The means of the noise peaks for both the p-side and Pb-side are around zero. The peaks in the ZDC^+ correspond to 1, 2 and 3 neutrons respectively. Since the ZDC^- is facing the proton beam we do not expect to see a single neutron peak.

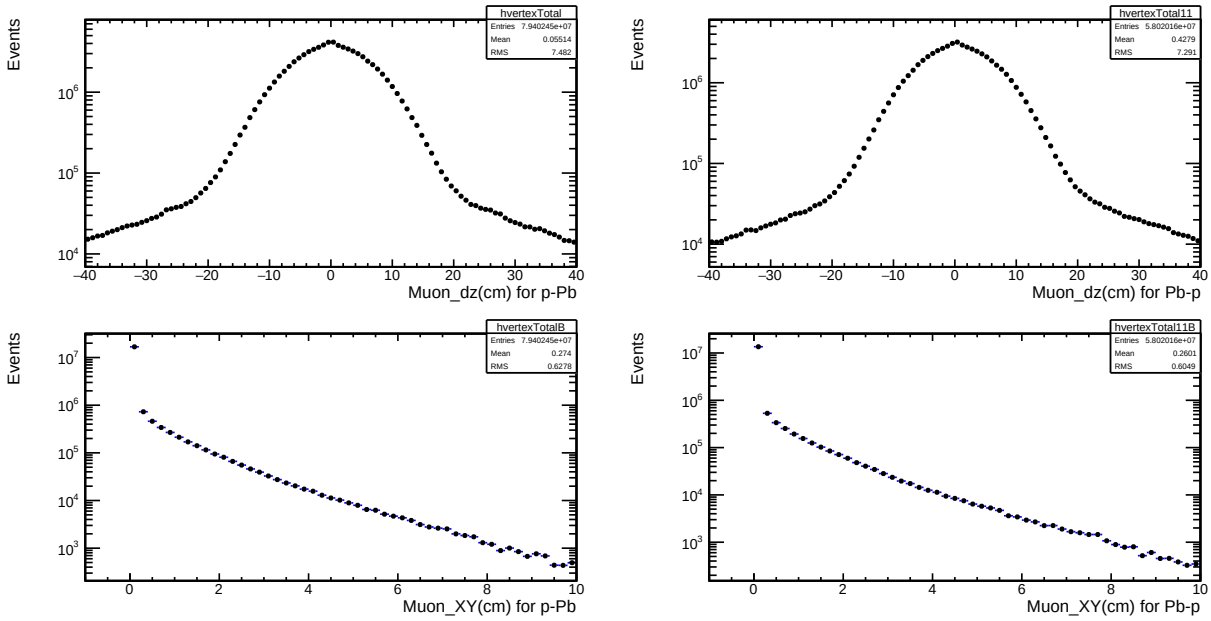

Figure 6.4: Distribution of the muon D_z (top row) and D_{xy} (bottom row) for pPb (left column) and Pbp (right column) for all of the events collected by the UPC trigger. For this analysis the closest longitudinal distance between the event vertex and the muon track is $|D_z| \leq 15$ cm and the closest transverse distance is $D_{xy} \leq 3$ mm.

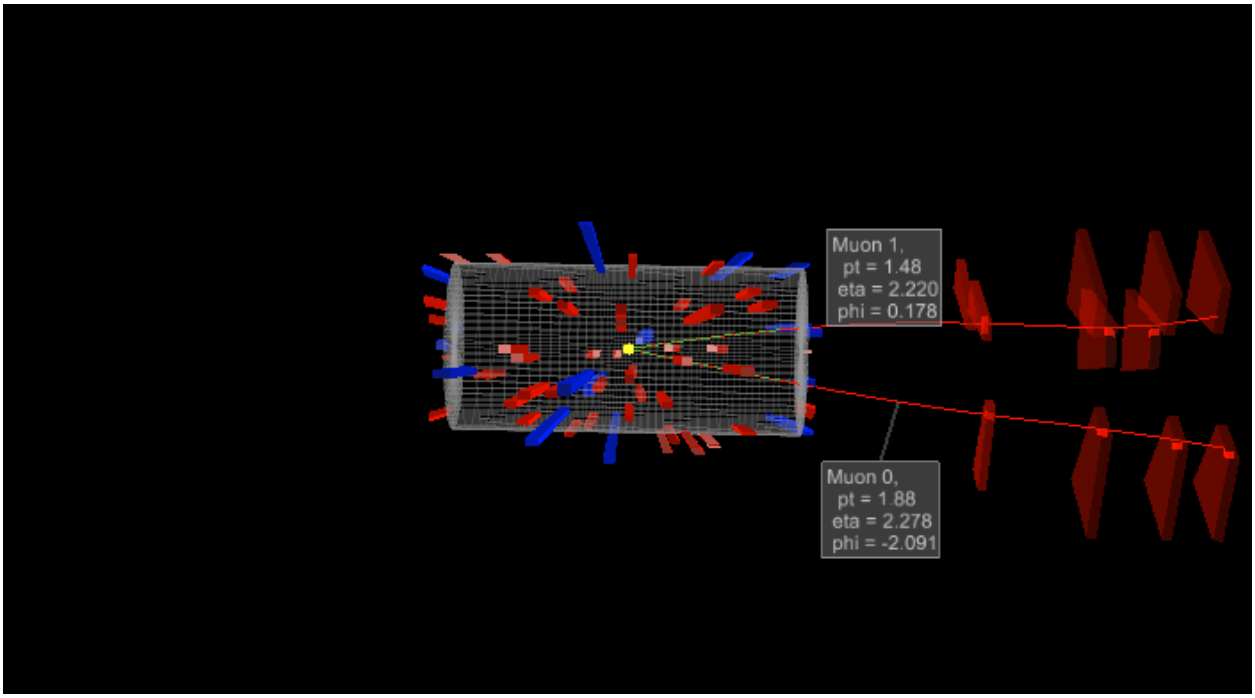

Figure 6.5: Event display for an exclusive J/ψ candidate

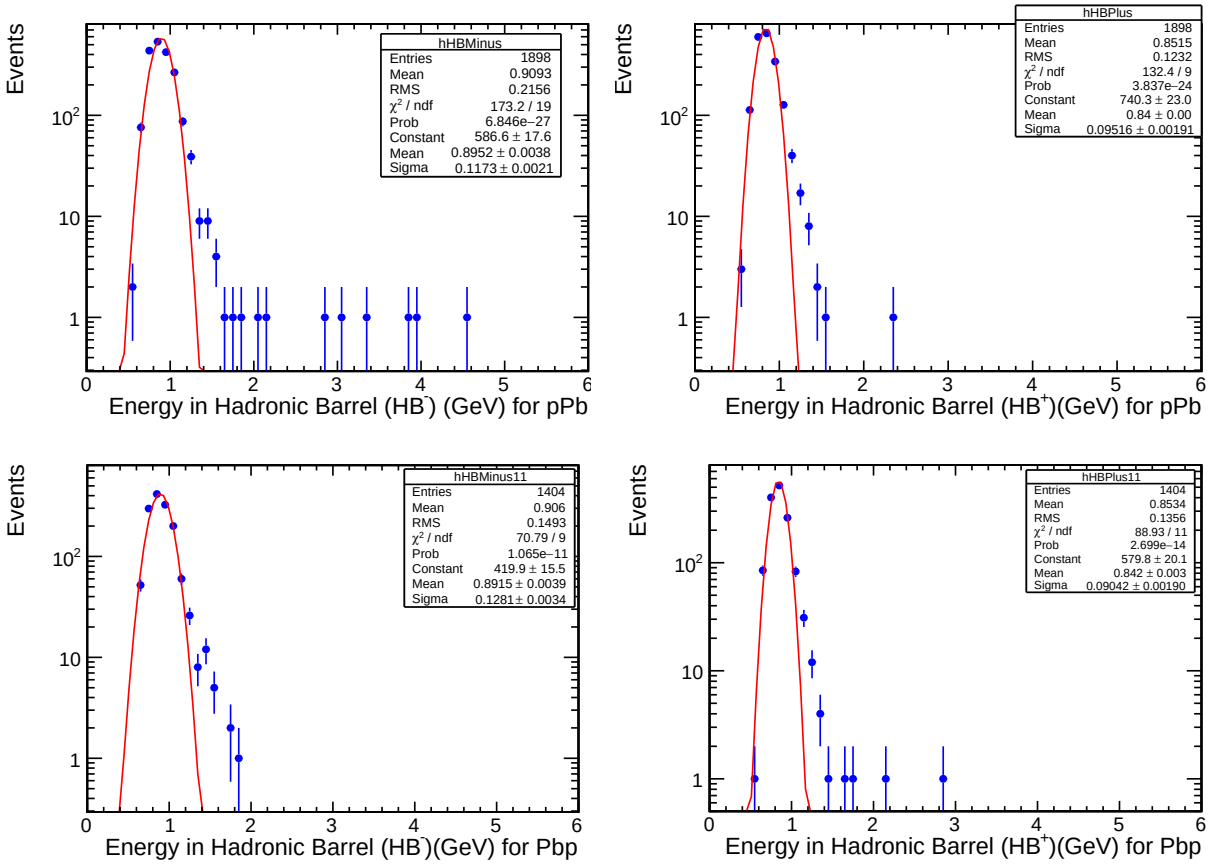

Figure 6.6: Hadronic energy distributions in Hadronic Barrel calorimeters, HB, for quiet events. The upper panels are for pPb collisions and the lower panels for Pbp collisions. The left column shows HB^- and the right column shows HB^+. The low end of the distributions are fitted to Gaussian functions in order to give an estimate of the noise thresholds.

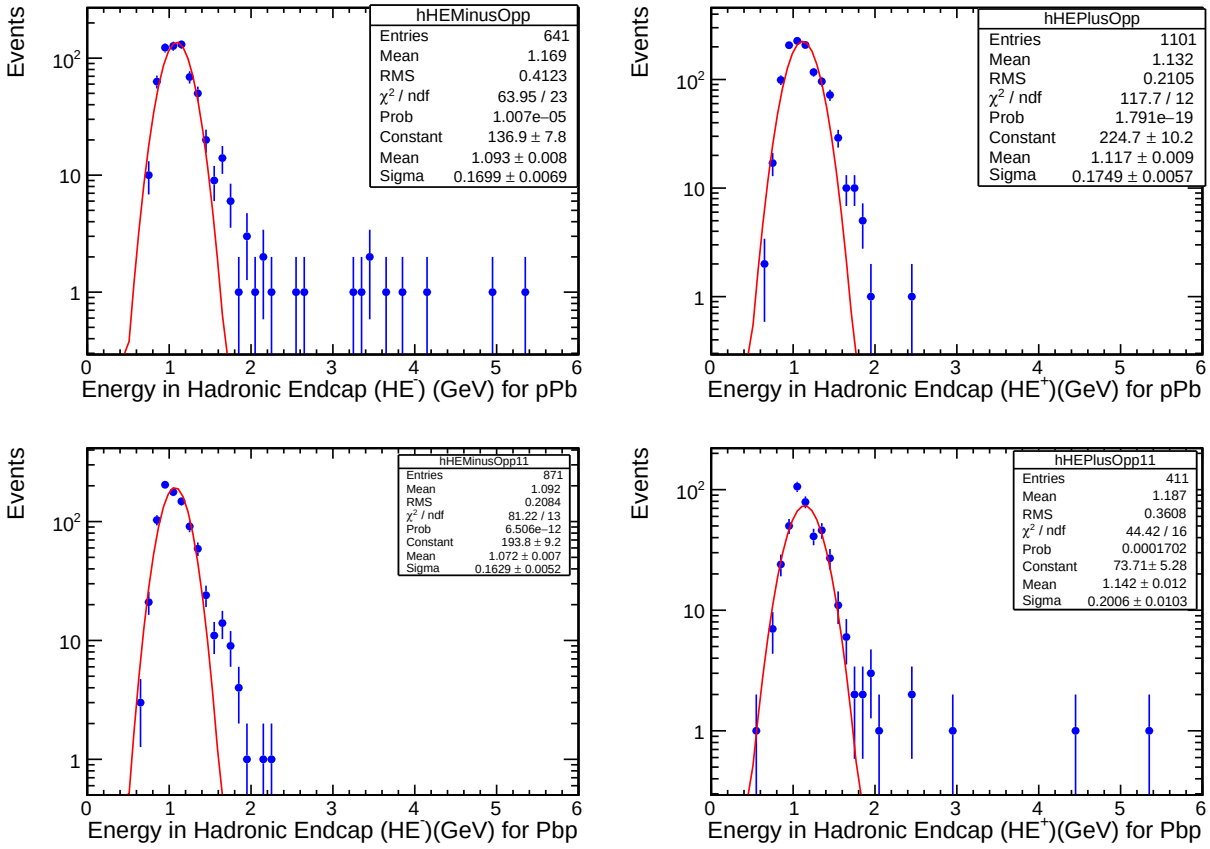

Figure 6.7: Hadronic energy distributions in Hadronic Endcap calorimeters, HE, for quiet events. The upper panels are for pPb collisions and the lower panels for Pbp collisions. The left column shows HE^{-} and the right column shows HE^{+}. The low end of the distributions are fitted to Gaussian functions in order to give an estimate of the noise thresholds.

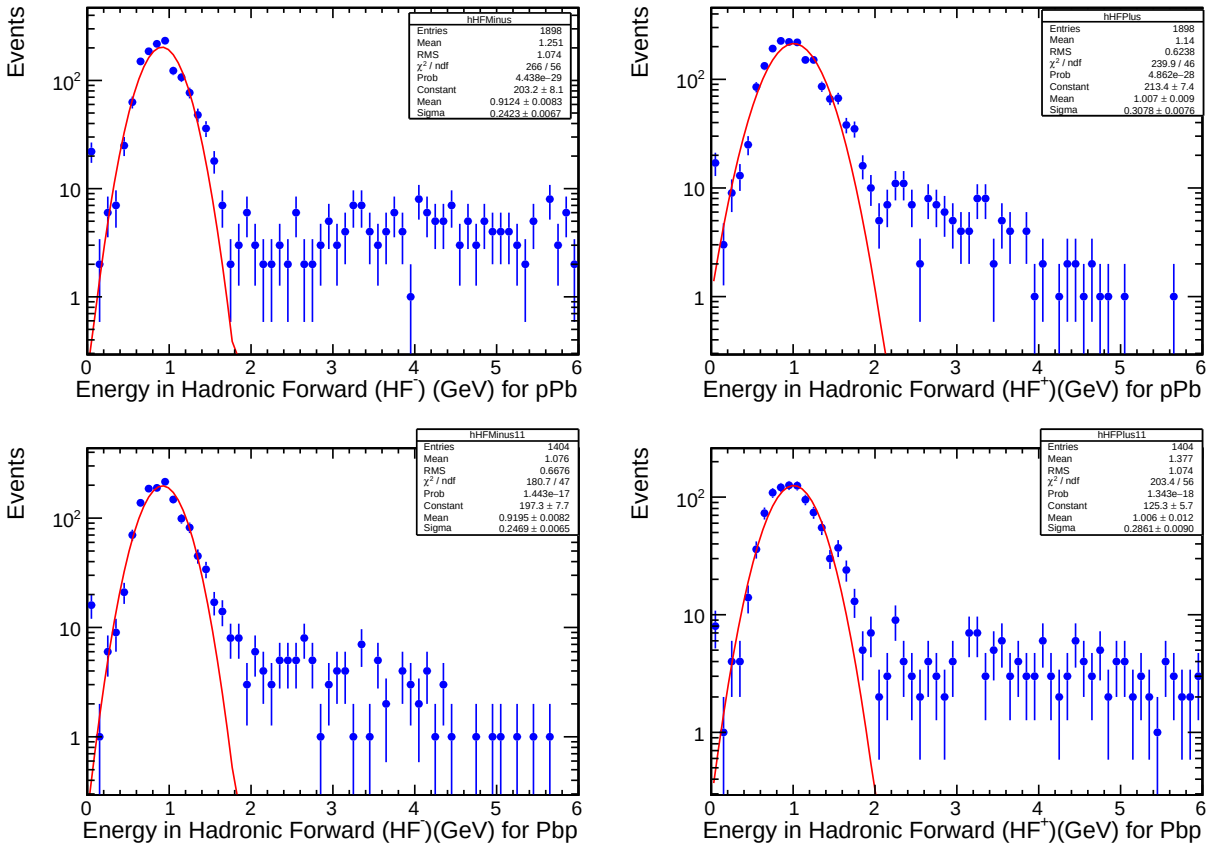

Figure 6.8: Hadronic energy distributions in the Hadronic Forward calorimeters, HF, for quiet events. The upper panels are for pPb collisions and the lower panels for Pbp collisions. The left column shows HF^{-} and the right column shows HF^{+}. The low end of the distributions are fitted to Gaussian functions in order to give an estimate of the noise thresholds.

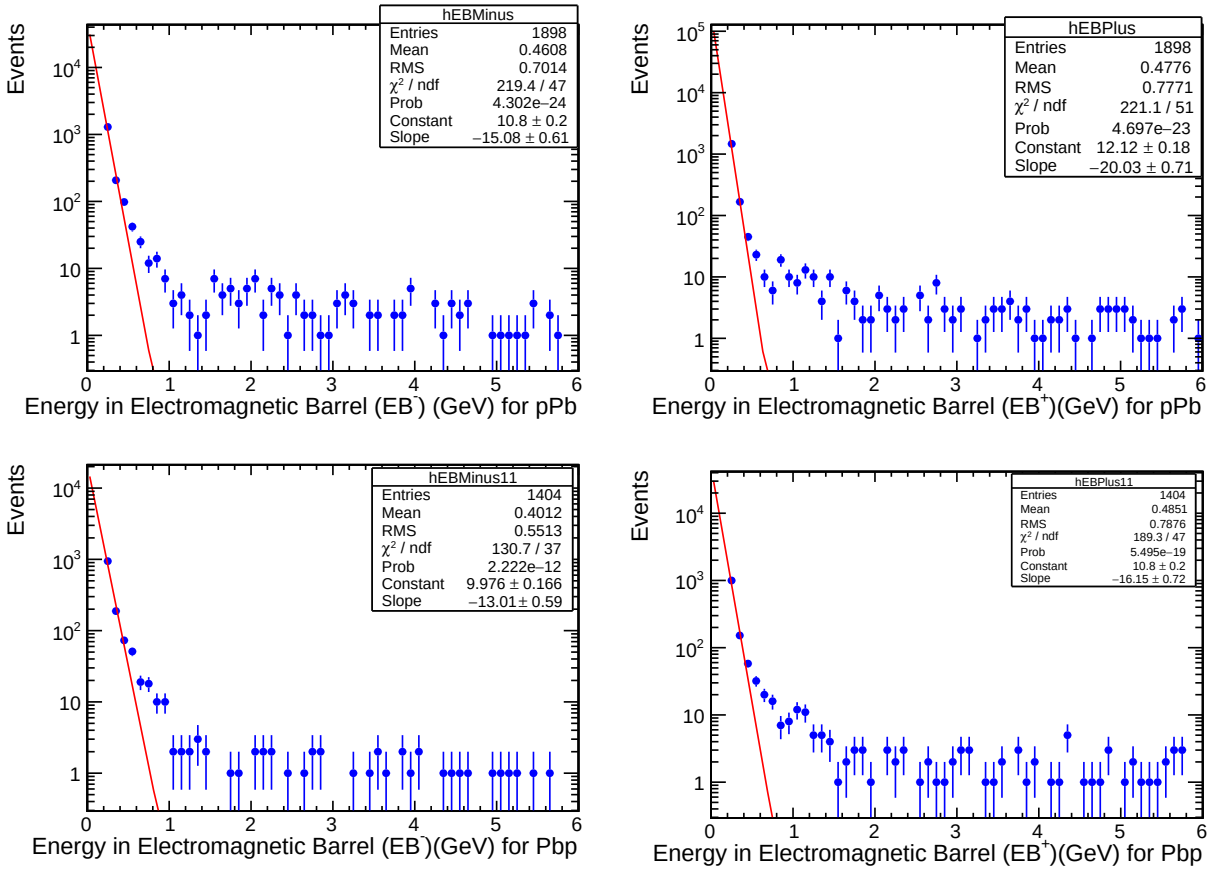

Figure 6.9: Electromagnetic energy distributions in the Electromagnetic Barrel calorimeters, EB, for quiet events. The upper panels are for pPb collisions and the lower panels for Pbp collisions. The left column shows EB^- and the right column shows EB^+. The low end of the distributions are fitted to exponential functions in order to give an estimate of the noise thresholds.

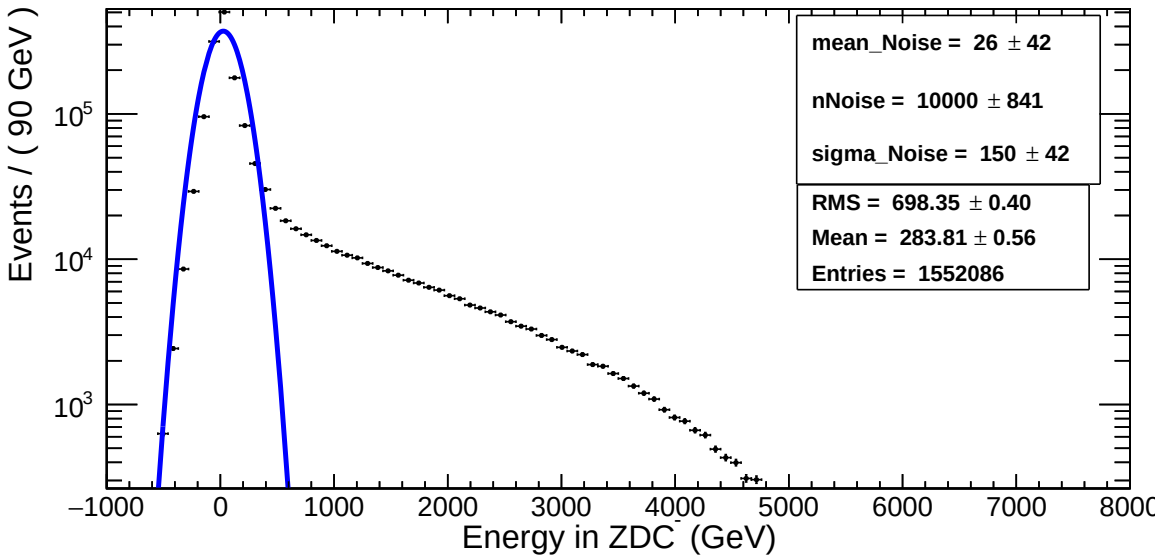

Figure 6.10: Total energy distribution in ZDC$^-$ p-side for Pbp collision at $\sqrt{s_{NN}} = 5.02$ TeV. Since ZDC$^-$ is facing the proton beam we do not expect to see a single neutron peak. The low end of the distribution is fitted to a Gaussian function, which corresponds to the noise distribution.

The noise in the proton side and lead side are fitted with Gaussian functions to determine the thresholds, which are used to reject events where there is energy in the ZDC detector. They are listed in Table 6.2. The numbers of events selected after each cut are shown in Table 6.3 for both the pPb and Pbp data. The total efficiency of all efficiency cuts is grater than 99%.

	ZDC Minus	ZDC Plus
Threshold Energy (fC)	900	2000

Table 6.2: Thresholds for exclusive selection in ZDC detector in Pbp.

6.5 Raw distributions in invariant mass, rapidity and p_T

After all the offline cuts have been applied the invariant mass, rapidity, and transverse momentum are determined for the each exclusive dimuon pair. Figure 6.12 left shows the distribution of events in invariant mass and p_T. Most events have low transverse momentum (p_T around 0.4 GeV/c) and are concentrated near the J/ψ mass region, ($2.8 < M_{\mu^+\mu^-} < 3.3$ GeV/c^2). Events with invariant mass in the continuum, i.e. $4 < M_{\mu^+\mu^-} < 8$ GeV/c^2, have low transverse momentum. Figure 6.12

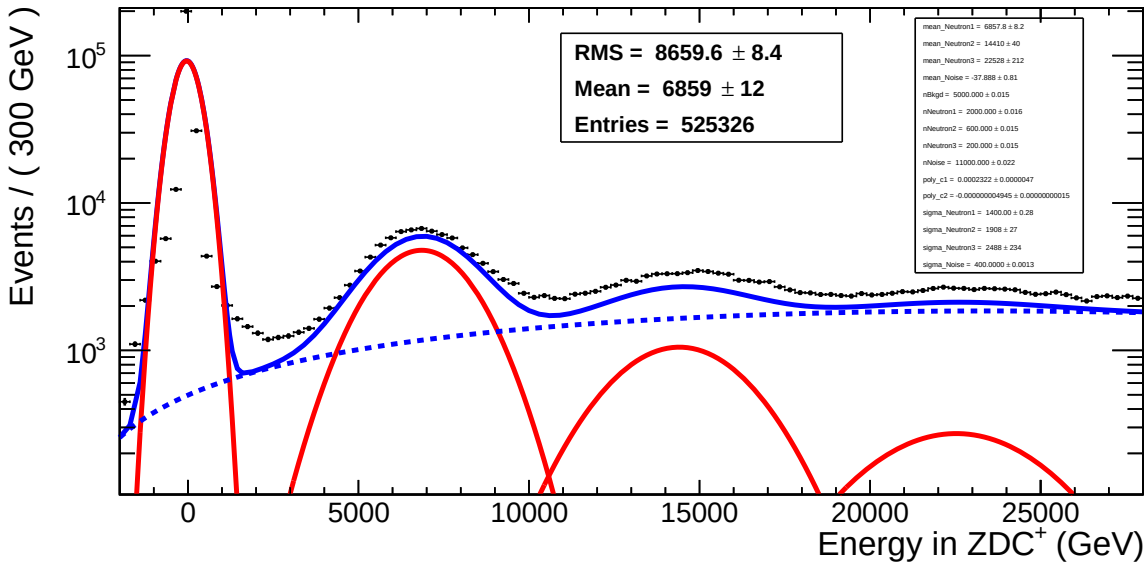

Figure 6.11: Total energy distribution in ZDC$^+$ Pb-side for Pbp collision at $\sqrt{s_{NN}} = 5.02TeV$. The peak around zero is noise, which is consistent with selected events. The other peaks in ZDC$^+$ correspond to 1, 2 and 3 neutrons respectively. The distribution is fitted to four Gaussian functions, the first for the noise signal (0n) which is consistent with selected events, the second for the first neutron signal (1n), the third for the second neutron signal (2n), and the forth for the third neutron signal (3n)

.

	Pbp		pPb	
Integrated luminosity	$13.92nb^{-1}$		$18.83nb^{-1}$	
Rapidity range	(-2.3,-1.8)	(1.8,2.3)	(-2.3,-1.8)	(1.8,2.3)
Total events	1,357,534	1,901,851	2,606,989	1,847,838
Applied cuts				
Vertex	4710	7915	9804	6928
Track purity	1966	3572	4209	2885
Two Tracks	607	1314	1570	873
Opposite Sign (OS)	403	797	898	564
No hadronic Activity in HF, HE,HB	383	715	889	530
No hadronic Activity ZDC	332	623	771	463
Mass Range (2.8, 3.3) GeV/c^2	271	490	594	399

Table 6.3: Number of events that pass the sequential analysis cuts.

right show the distribution of events with ($2.8 < M_{\mu^+\mu^-} < 3.3$ GeV/c^2) in rapidity and p_T. The events are concentrated around rapidities ($y \sim -2$) and ($y \sim +2$). There are also significantly more events on the proton going side 1281 ($y \sim +2$) 1281, than on the lead side at ($y \sim -2$) 811. This is expected from theoretical models since the momentum of the photon emitted by the lead nucleus is usually less than that of the parton that it hits. The analysis was done in 4 independent samples: pPb at forward rapidity, pPb at backward rapidity, Pbp at forward rapidity, Pbp at backward rapidity as shown in Table 6.3. For the final physics results, the Pbp results are merged with the pPb results that have been flipped in rapidity.

Figure 6.13 shows the mass distribution of all exclusive dimuon pairs. There are very clear J/ψ and $\psi(2s)$ peaks as well as a continuum from the process $\gamma\gamma \to \mu^+\mu^-$. The distribution in Fig. 6.13 is fit to two Crystal Ball functions, one for the J/ψ and one for $\psi(2s)$ and a second order polynomial for the background. The fit was done using the Roofit extended likelihood package for a binned histogram. The Crystal Ball function is described in the Appendix A. Based on these fits a mass cut of ($2.8 < M_{\mu^+\mu^-} < 3.3$ GeV/c^2) was chosen to select J/ψ events. From the fit in Fig. 6.13 the efficiency of this cut is estimated to by $99.75 \pm 0.05\%$ and the contamination from $\psi(2s)$ was estimated to be zero events.

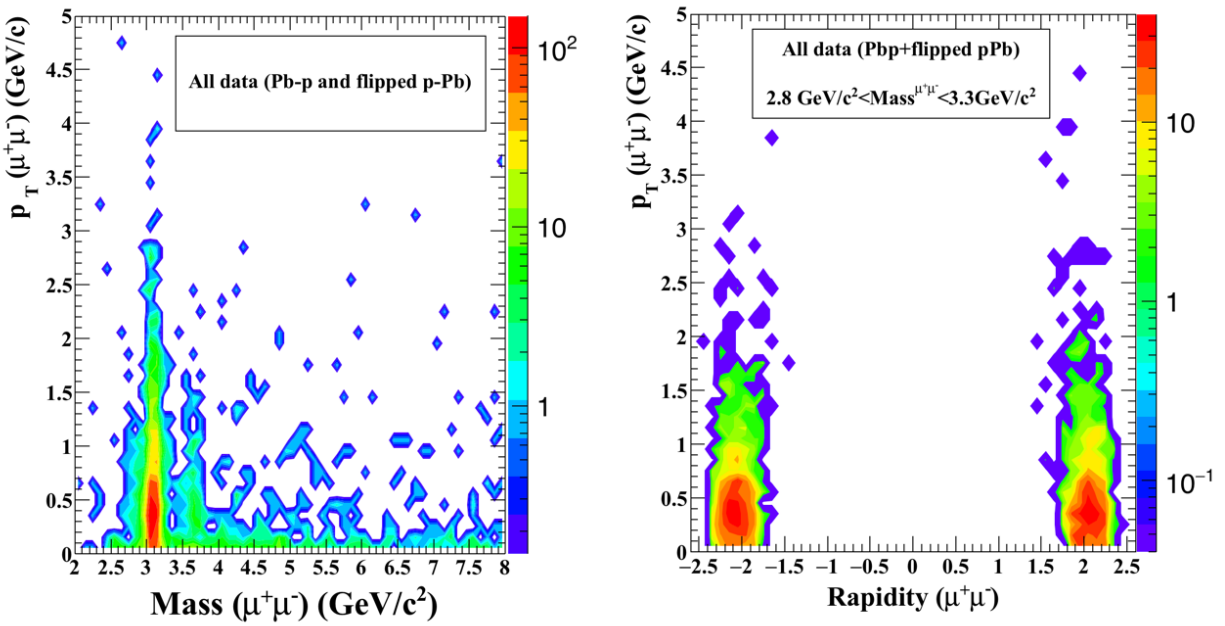

Figure 6.12: Left: distribution of p_T versus invariant mass for dimuon pairs. Right: distribution of p_T versus laboratory rapidity for dimuon pairs in the J/ψ mass range ($2.8 < M_{\mu^+\mu^-} < 3.3$ GeV/c^2). All events pass the event selections. The rapidity of the pPb events has been flipped to be consistent with the CMS convention.

6.6 Contamination in the J/ψ sample

The purpose of the selection and mass cuts is to select the cleanest possible sample exclusive J/ψ events. However, these events are still mixed with events from other physical processes, such as $\gamma\gamma \to \mu^+\mu^-$, $\gamma p \to \psi(2s) + p$, non-exclusive events such as $\gamma p \to J/\psi + X$, and photo-Pb interactions $\gamma Pb \to J/\psi + X$. All these processes have different distributions in dimuon p_T with $\gamma\gamma$ and γPb peaking at low p_T and non-exclusive J/ψ dominant at high p_T.Using information on the dimuon mass and the ZDCs and by looking at events that fail the exclusivity cuts described in Section 6.4, the fraction of each of these processes that are present in the final dataset is estimated.

One can see from the fit in Fig. 6.13 that about 6% of the events selected by the J/ψ mass cut are from the continuum background. The process $\gamma\gamma \to \mu^+\mu^-$ is a pure QED process and is expected to produce dimuons with a smooth distribution in mass with the events concentrated at very low p_T. Figure 6.14, shows the p_T distributions for the mass ranges 2.8 - 3.3 GeV/c^2 (blue)

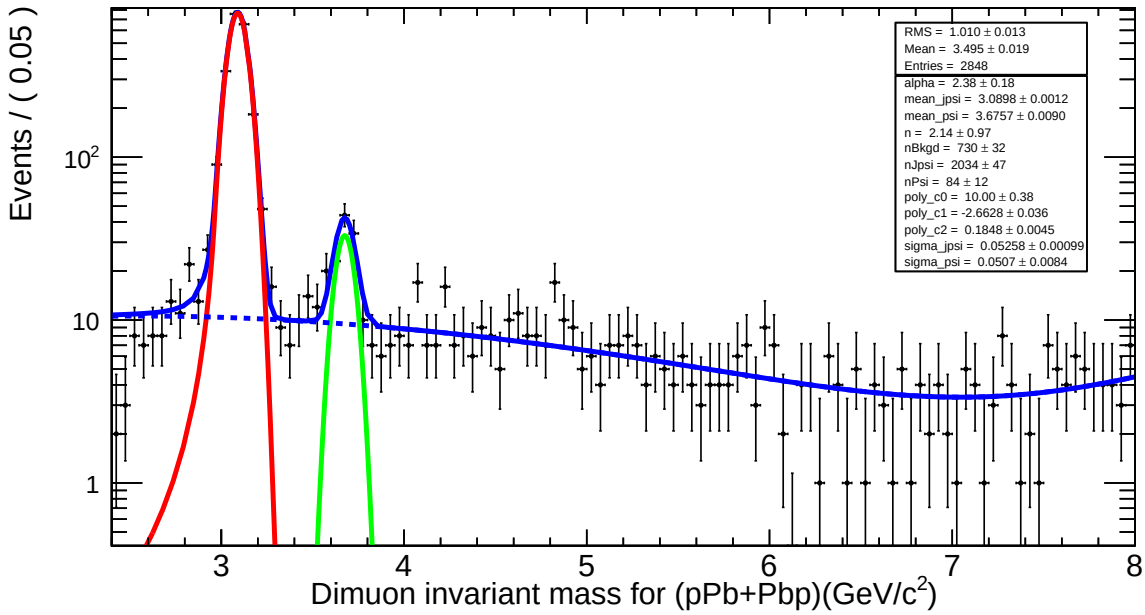

Figure 6.13: Mass distribution for all dimuon pairs that pass the event selection and exclusivity cuts. The red and green curves represent the J/ψ and $\psi(2s)$ signals and the dashed blue line the continuum background. The solid blue line is the sum of the three contributions.

and 4.0-8.0 GeV/c^2 (red) on Pb-side (left) and p-side (right). As expected the continuum events have a much lower mean p_T than those with invariant mass in the J/ψ region.

To estimate the fraction of $\gamma\gamma$ background in the J/ψ sample I defined the ratio of the continuum in a sideband region to the continuum under the J/ψ peak

$$R_{sideband} = \frac{\int_{2.8}^{3.3} \frac{dN_{fit}}{dM} dM}{\int_{4.0}^{5.0} \frac{dN_{fit}}{dM} dM}. \tag{6.1}$$

where M is the dimuon invariant mass and dN_{fit}/dM is the polynomial fit to the continuum, shown as the dashed blue line in Fig. 6.13. The contamination of the J/ψ sample by the $\gamma\gamma$ continuum is then estimated to be

$$\frac{dN_{\gamma\gamma}}{dp_T} = R_{sideband} \cdot \frac{dN_{4-5}}{dp_T} \tag{6.2}$$

where $\frac{dN_{4-5}}{dp_T}$ is the p_T distribution of dimuon pairs with invariant masses between 4.0-5.0 GeV/c^2.

The p_T distribution for $\gamma Pb \to J/\psi$ is estimated by studying events where the lead nucleus

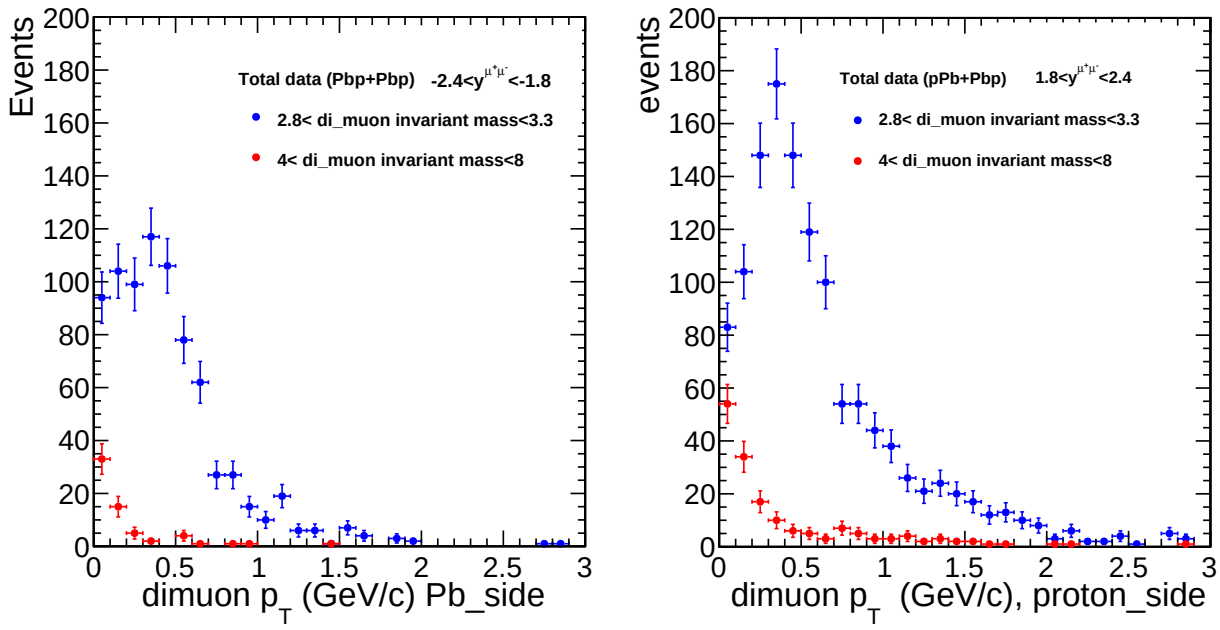

Figure 6.14: Distribution of dimuon p_T for the mass ranges 2.8 - 3.3 GeV/c^2 (blue) corresponding to the J/ψ peak, and 4.0-8.0 GeV/c^2 (red) corresponding to the continuum. Pb-side data are on the left and p-side data are on the right.

break ups and emits neutrons. Figure 6.15 shows the distribution of dimuon p_T for events where both a J/ψ and a neutron are emitted. As expected, the distribution peaks at very low p_T since J/ψ mesons produced in γPb events are generally produced by coherent collisions. The selection cuts described in Section 6.4 remove any events that contain neutrons. The distribution of $\gamma Pb \rightarrow J/\psi$ events in this sample is estimated using the equation

$$\frac{dN_{\gamma Pb}}{dp_T} = R_{0,N}(p_T) \cdot \frac{dN_{J/\psi+N}}{dp_T} \tag{6.3}$$

where $R_{0,N}(p_T)$ represents the fraction of $\gamma Pb \rightarrow J/\psi$ events with no neutrons compared to those with neutrons. This factor is estimated from STARLIGHT and checked with data.

To understand the contamination of the exclusive J/ψ sample by non-exclusive events, the exclusivity cuts on HF and the number of tracks were inverted to produce a non-exclusive sample. Figure 6.16 compares the p_T distributions of exclusive and non-exclusive J/ψ events for Pbp collisions at both backward (left) and forward rapidity (right). The non-exclusive events have

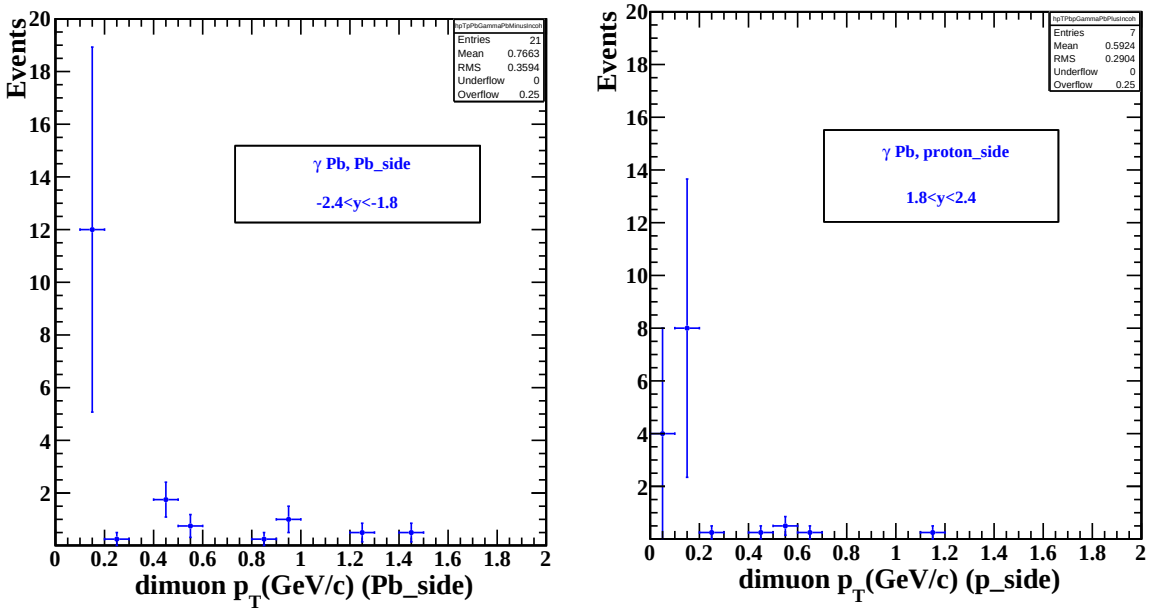

Figure 6.15: Distribution of dimuon p_T for events where both a J/ψ and a neutron are emitted. The left panel is for the negative rapidity, and the right panel for positive rapidity.

much broader p_T spectra than the exclusive events. The contamination of the exclusive sample by non-exclusive events is estimated by assuming that above a certain p_T the sample is dominated by non-exclusive events. Based on Figure 6.16 a threshold of $p_T = 2.5$ GeV/c was chosen. The non-exclusive sample was then scaled to the physics sample using the ratio

$$R_{non-exclu} = \frac{\int_{2.5}^{\infty} \frac{dN_{\text{non-exclusive}}}{dp_T} dp_T}{\int_{2.5}^{\infty} \frac{dN_{\text{exclusive}}}{dp_T} dp_T}. \tag{6.4}$$

The statistical error on $R_{non-exclu}$ was estimated from the number of events in both samples. The spectrum of non-exclusive events within the sample was then estimated to be

$$\frac{dN_{NoX}}{dp_T} = R_{\text{non-exclu}} \cdot \frac{dN_{\text{non-exclusive}}}{dp_T} \tag{6.5}$$

The statistical errors on $R_{non-exclu}$ and $\frac{dN_{non-exclusive}}{dp_T}$ were propagated to $\frac{dN_{NoX}}{dp_T}$. The systematic error on $\frac{dN_{NoX}}{dp_T}$ was estimated by varying the p_T limit used in Equation 6.4.

The final source of possible contamination in the sample is from misidentified muons. These

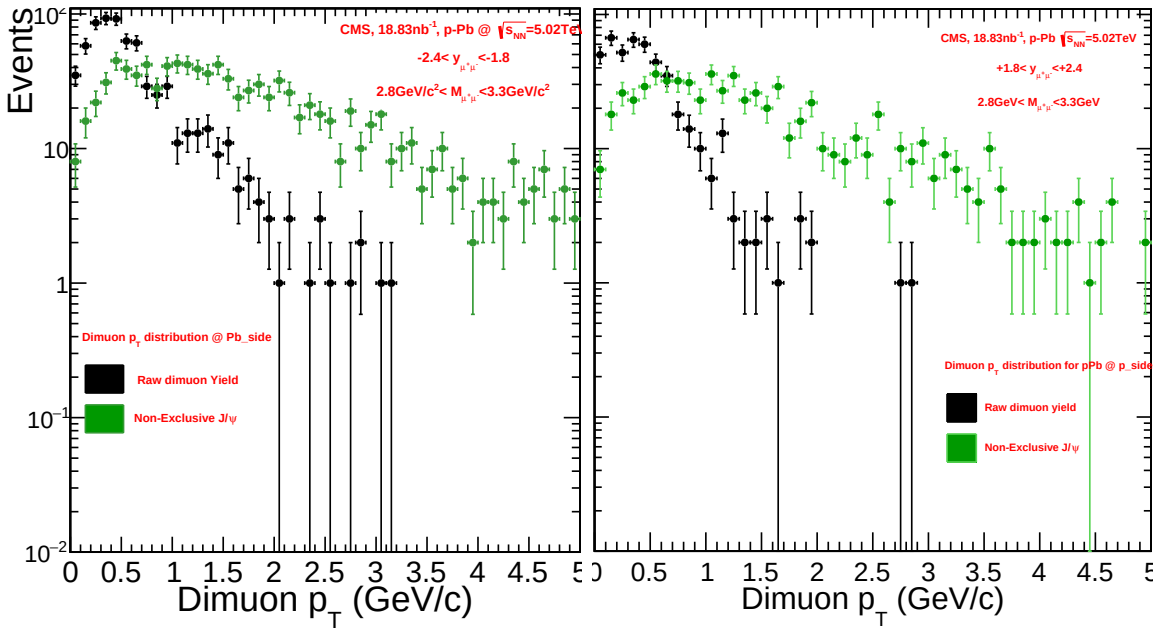

Figure 6.16: Distribution in p_T for exclusive (black) and non-exclusive (green) J/ψ events from Pbp collisions at both backward (left) and forward rapidity (right).

particles should be equally likely to be reconstructed as positive or negative particles and so the contamination can be estimated from the number of muons with the same sign, i.e., $++$ and $--$. No same sign pairs were found that passed the selection cuts and so this effect was ignored.

The left hand panel of Figure 6.17 shows the distribution in invariant mass for dimuons produced at forward rapidity in pPb events. The solid lines show fits to the J/ψ, $\psi^{'}$ and $\gamma\gamma$ continuum. The right hand panel of Figure 6.17 shows the p_T spectrum of dimuons with invariant mass between 2.8 and 3.3 GeV/c^2 together with estimates of the contamination from $\gamma\gamma \rightarrow J/\psi$, $\gamma Pb \rightarrow J/\psi$ and non-exclusive $\gamma p \rightarrow J/\psi + X$ derived using Equations 6.2,6.3 and 6.5, respectively. For p_T between 0.1 and 1.3 GeV/c the sample is very pure. Figures 6.18, 6.19 and 6.20 show the data for pPb collisions at backward rapidity and Pbp at forward and backward rapidity, respectively.

The purity of the exclusive J/ψ sample is defined by

$$purity(p_T) = \frac{\frac{dN}{dp_T} - \frac{dN_{\gamma\gamma}}{dp_T} - \frac{dN_{\gamma Pb}}{dp_T} - \frac{dN_{\mathrm{NoX}}}{dp_T}}{\frac{dN}{dp_T}} \tag{6.6}$$

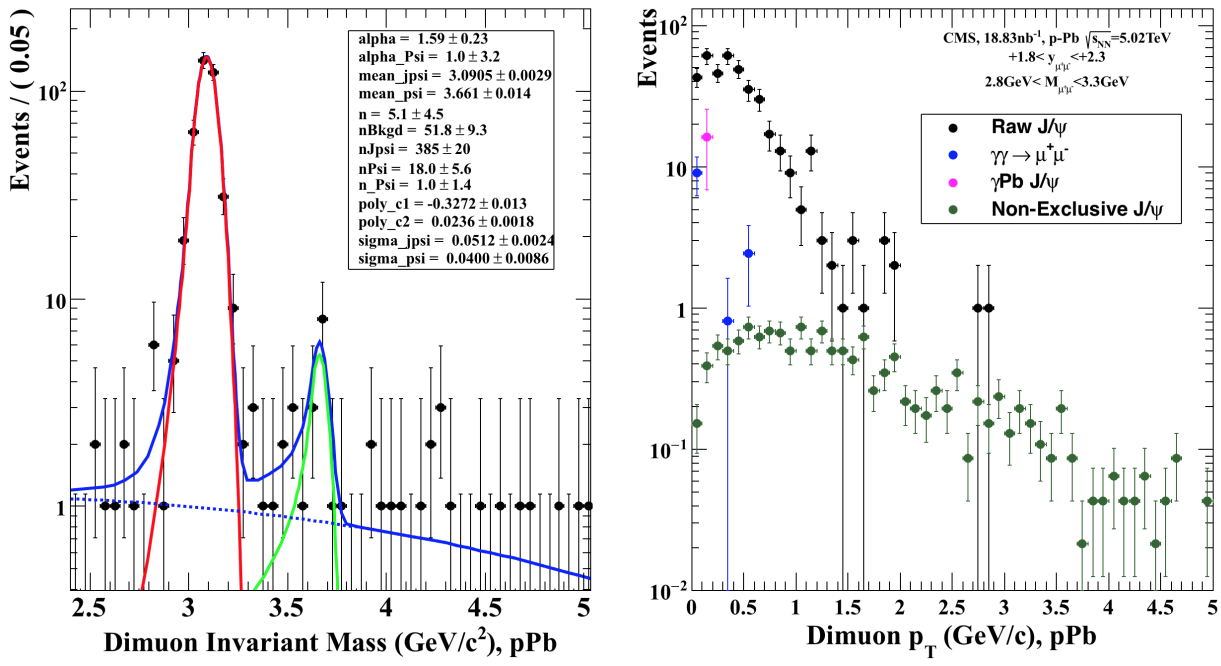

Figure 6.17: (Left) Dimuon invariant mass distribution for pPb at forward rapidity, the black points are the raw data, the blue curve is the fit for the total distribution, the red curve is the fit for the J/ψ resonance, the dashed curve is the fit for total background, the green curve is the fit for the ψ' resonance. (Right) The p_T distribution for dimuons with invariant masses between 2.8 and 3.3 GeV/c^2. The black data points are for the raw dimuon data, blue represents the $\gamma\gamma$ background, green represents the non-exclusive J/ψ production, and magenta represents the γPb production.

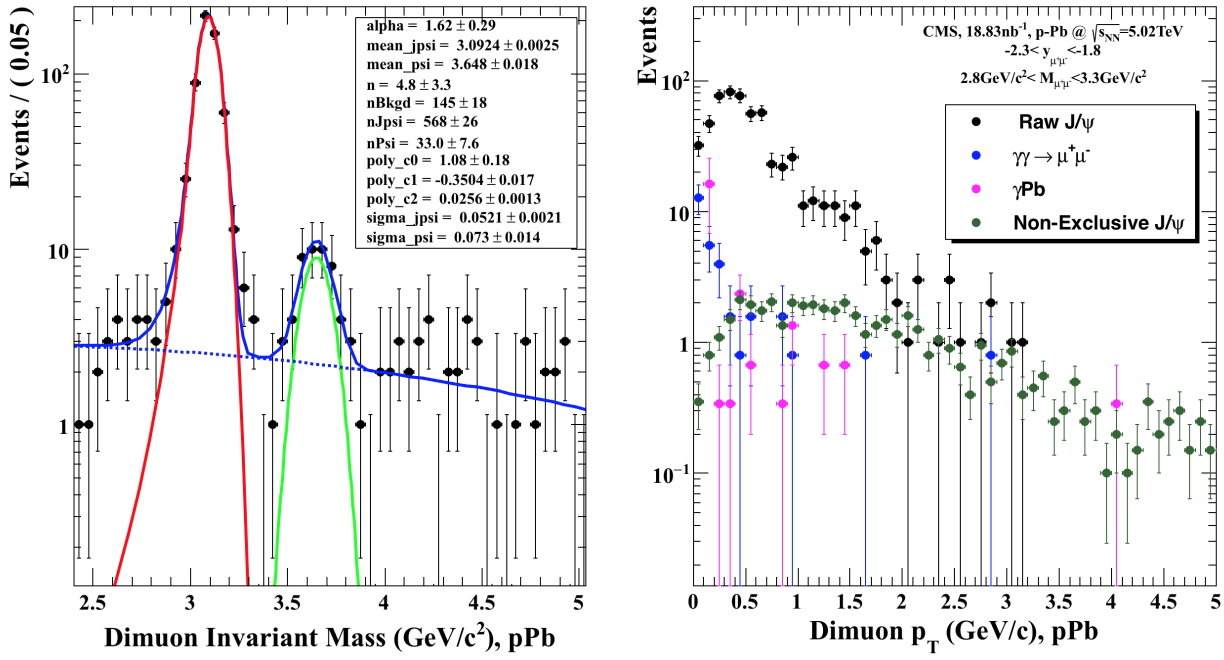

Figure 6.18: (Left) Dimuon invariant mass distribution for pPb at backward rapidity, the black points are the raw data, the blue curve is the fit for the total distribution, the red curve is the fit for the J/ψ resonance, the dashed curve is the fit for total background, the green curve is the fit for the ψ' resonance. (Right) The p_T distribution for dimuons with invariant masses between 2.8 and 3.3 GeV/c^2 for pPb at backward rapidity. The black data points are for the raw dimuon data, blue represents the $\gamma\gamma$ background, green represents the non-exclusive J/ψ production, and magenta represents the γPb production.

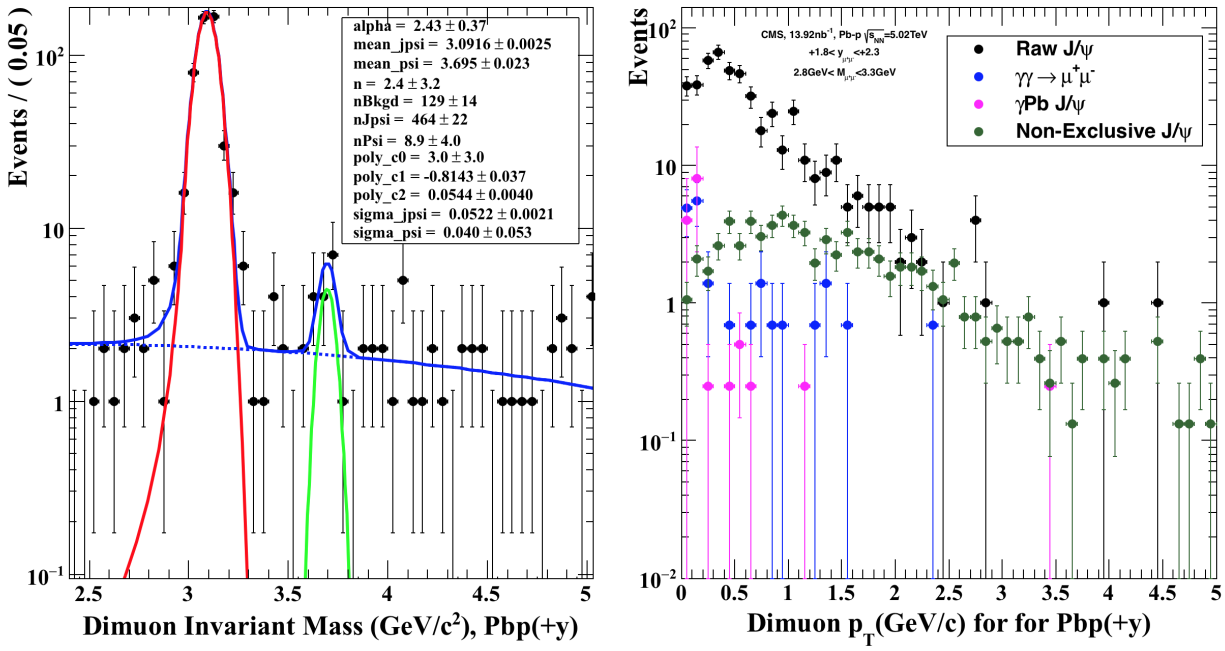

Figure 6.19: (Left) Dimuon invariant mass distribution for Pbp at forward rapidity, the black points are the raw data, the blue curve is the fit for total distribution, the red curve is the fit for the J/ψ resonance, the dashed curve is the fit for total background, the green curve is the fit for the ψ' resonance. (Right) The p_T distribution for dimuons with invariant masses between 2.8 and 3.3 GeV/c^2 for Pbp at forward rapidity. The black data points are for the raw dimuon data, blue represents the $\gamma\gamma$ background, green represents the non-exclusive J/ψ production, and magenta represents the γPb production.

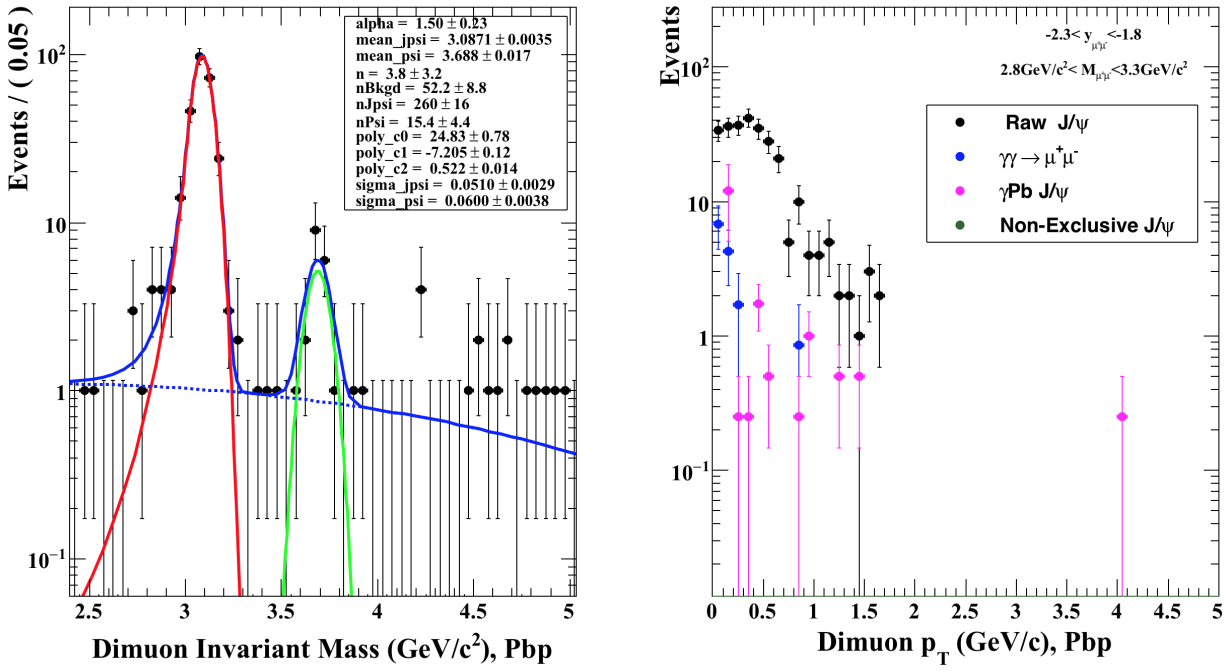

Figure 6.20: (Left) dimuon invariant mass distribution for Pbp at backward rapidity, the black points are the raw data, the blue curve is the fit for the total distribution, the red curve is the fit for the J/ψ resonance, the dashed curve is the fit for total background, the green curve is the fit for the $\psi^{'}$ resonance. (Right) The p_T distribution for dimuons with invariant masses between 2.8 and 3.3 GeV/c^2 for Pbp at backward rapidity. The black data points are for the raw dimuon data, blue represents the $\gamma\gamma$ background, green represents the non-exclusive J/ψ production, and magenta represents the γPb production.

Figure 6.21 shows that all samples have a high purity up to $p_T \approx 1.5$ GeV/c. The dip in the purity at low p_T is due to contamination from $\gamma\gamma$ and γPb events while the slow drop off above $p_T = 0.5$ GeV/c is caused by contamination from non-exclusive events.

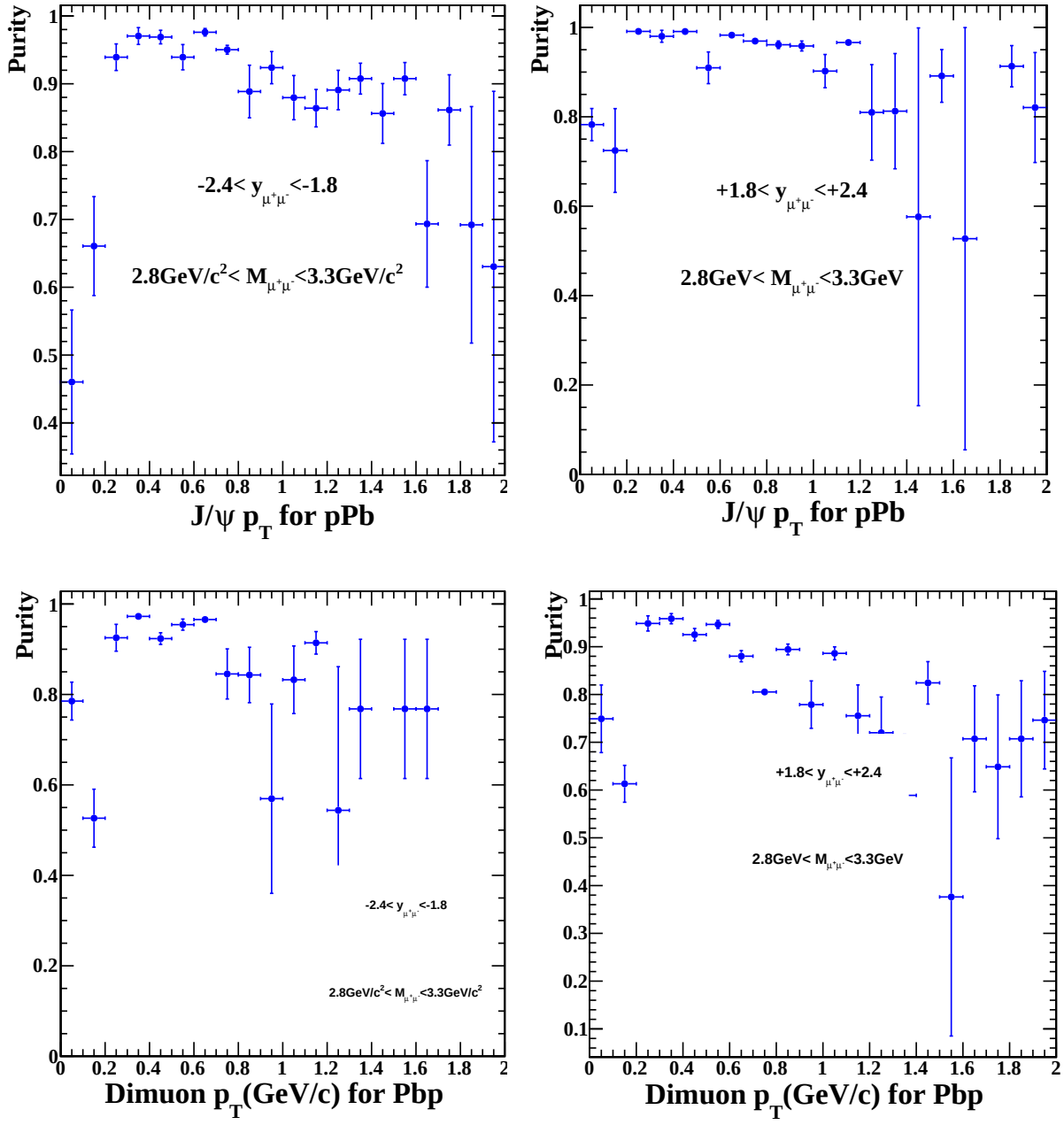

Figure 6.21: Purity of the J/ψ sample as a function of dimuon p_T for pPb (top) and Pbp (bottom). The left hand column shows the purity of the samples at negative rapidity and the right hand column the purity of the sample at positive rapidity.

Chapter 7

Comparison of Data and Monte Carlo Simulation for ultra-peripheral pPb collisions

7.1 Purpose of Monte Carlo Simulation

The purpose of the Monte Carlo is to correct the experimental results for the effects of acceptance and momentum resolution. The STARLIGHT package is used to generate $J/\psi \to \mu^+\mu^-$ and $\gamma\gamma \to \mu^+\mu^-$ events [93]. These events are then passed through a full GEANT4 [108] simulation of the CMS experiment. This simulation models how various particles pass through the detector, using random number generators to control whether or not a particle will interact with a given piece of matter. This simulated raw data is then reconstructed using the CMS software framework, CMSSW, exactly as if it was real data. In this way, the theoretical distribution and a realistic model of the detector's response are united. The goal of the MC simulation is to produce a set of corrections for the imperfections of the CMS detector that distort the data.

STARLIGHT is a MC simulation of ultra-peripheral heavy ion collisions, that calculates the cross sections for a variety of UPC final states and also generates events for use in determining detector efficiency. STARLIGHT simulates ultra-peripheral pPb collisions in three different physical processes:

- photo-production from γp processes where the nucleus acts as the source of photons and the proton as a target,
- γPb processes, where the proton acts as a source of photons and the Pb nucleus as a target, and

- the QED $\gamma\gamma$ processes, where a photon from the projectile (proton, Pb) interact with a photon from the target (proton,Pb).

The contribution of the γPb process is small relative to the γp process, but it is not negligible. The STARLIGHT MC events were reconstructed in CMSSW. The reconstructed J/ψ states for γp and γPb collisions and the reconstructed dimuons for $\gamma\gamma$ collisions were passed through the same selection cuts as the data.

Figure 7.1 shows the J/ψ p_T distributions for the MC simulations of the γp, γPb, and $\gamma\gamma$ physics processes at both forward and backward rapidity. It is clear from the plots that the concentration of the γPb, and $\gamma\gamma$ physics processes occurs at $p_T < 0.2$ GeV/c, but for γp, the distribution peaks at around $p_T \sim 0.4$ GeV/c. Figure 7.2 shows the J/ψ rapidity distributions for the MC simulations of the γp, γPb, and $\gamma\gamma$ physics processes, where each process is normalized to have a maximum value of one. It is clear that there is an asymmetry in the distributions in forward and backward rapidity for each process, and that acceptance for each process is concentrated around $y \sim 2$ and $y \sim -2$.

7.2 Data MC-Comparison

For the analysis used in this thesis the trigger efficiency is estimated using the data-driven Tag & Probe technique and the Monte Carlo is only used to correct for the acceptance of the detector. In order to make a fair comparison between Monte Carlo and data for the plots in this chapter the Monte Carlo events are weighted by the trigger efficiency. All cuts used on the data are also imposed on the Monte Carlo events. In the figures below the data from Pbp and flipped pPb are combined together and forward rapidity is defined to be in the proton-going direction.

Figure 7.3 shows the $\Delta\phi$ distribution, in $\Delta\phi$, the ϕ difference between the two muons, for uncorrected data (blue) and simulated γp events from STARLIGHT (red). Distributions from both data and STARLIGHT are peaked at $\phi = \pm\pi$. Figure 7.4 shows the two dimensional distributions of J/ψ p_T versus $\Delta\phi$ for data and γp MC. At low p_T, the muons are exactly back to back for both

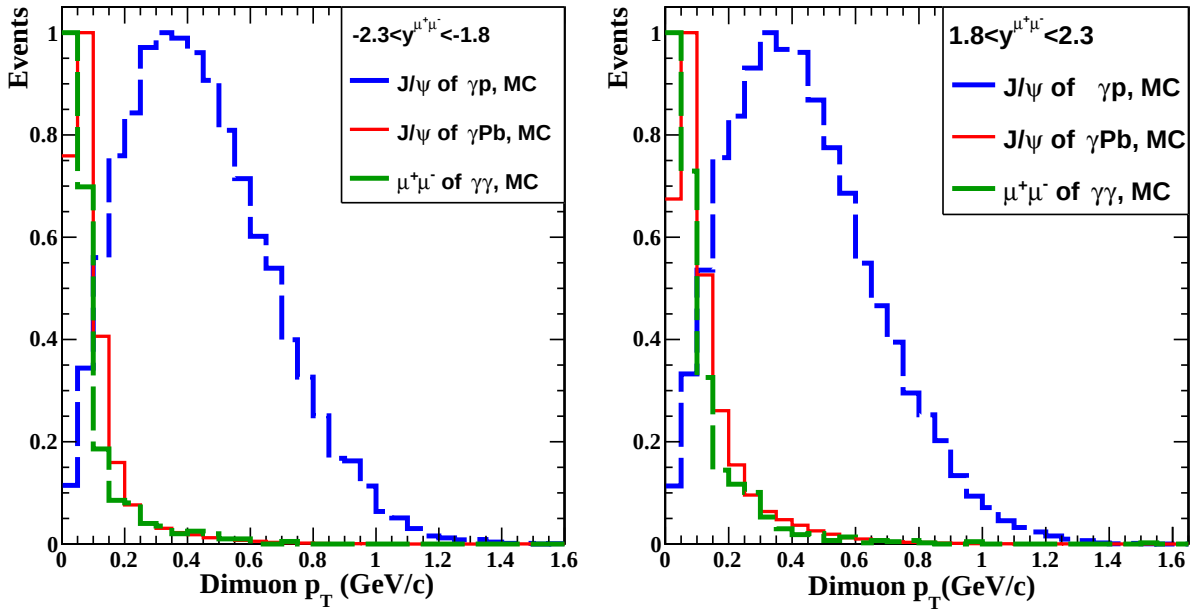

Figure 7.1: Dimuon p_T distributions for the MC simulation of γp, γPb, and $\gamma\gamma$ physics processes. The blue line is for γp, red is for γPb and green is for $\gamma\gamma$. The left hand plot shows the spectra at rapidity $-2.3 < y < -1.8$, while the right hand plot shows the spectra at rapidity $1.8 < y < 2.3$. All of the spectra are normalized to have a maximum value of one.

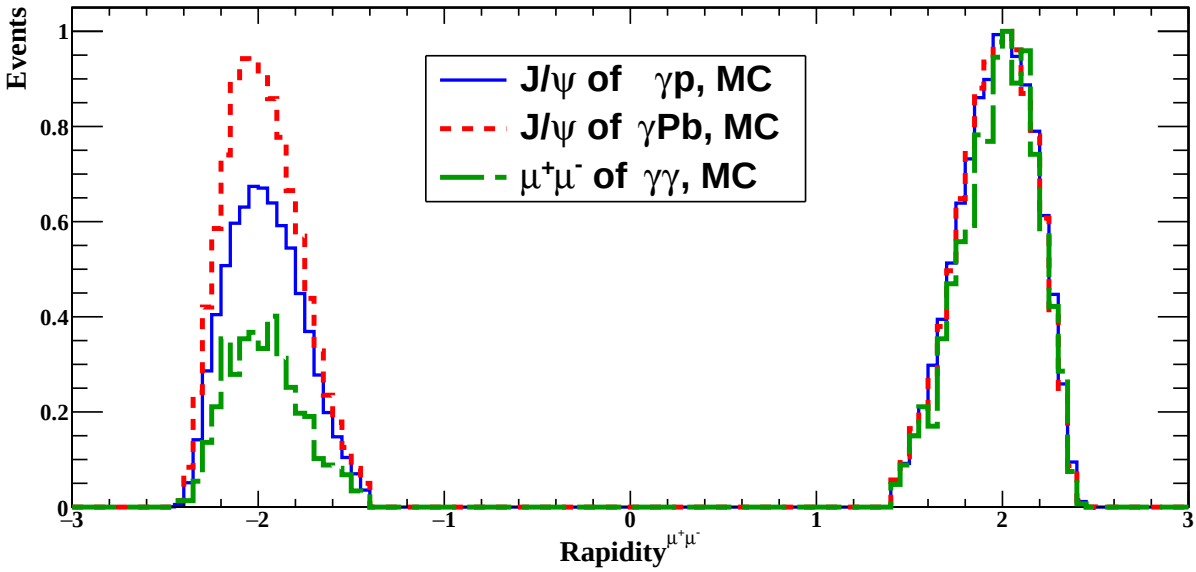

Figure 7.2: Rapidity distributions for MC simulation of γp, γPb, and $\gamma\gamma$ physics processes. The blue is for γp, red is for γPb and green is for $\gamma\gamma$. All of the spectra are normalized to have a maximum value of one.

data and MC. As the p_T of the J/ψ becomes comparable to its mass, the opening angle between the muons decreases. It is clear that the data and the MC are similar but that the data extends to higher p_T than the STARLIGHT simulation.

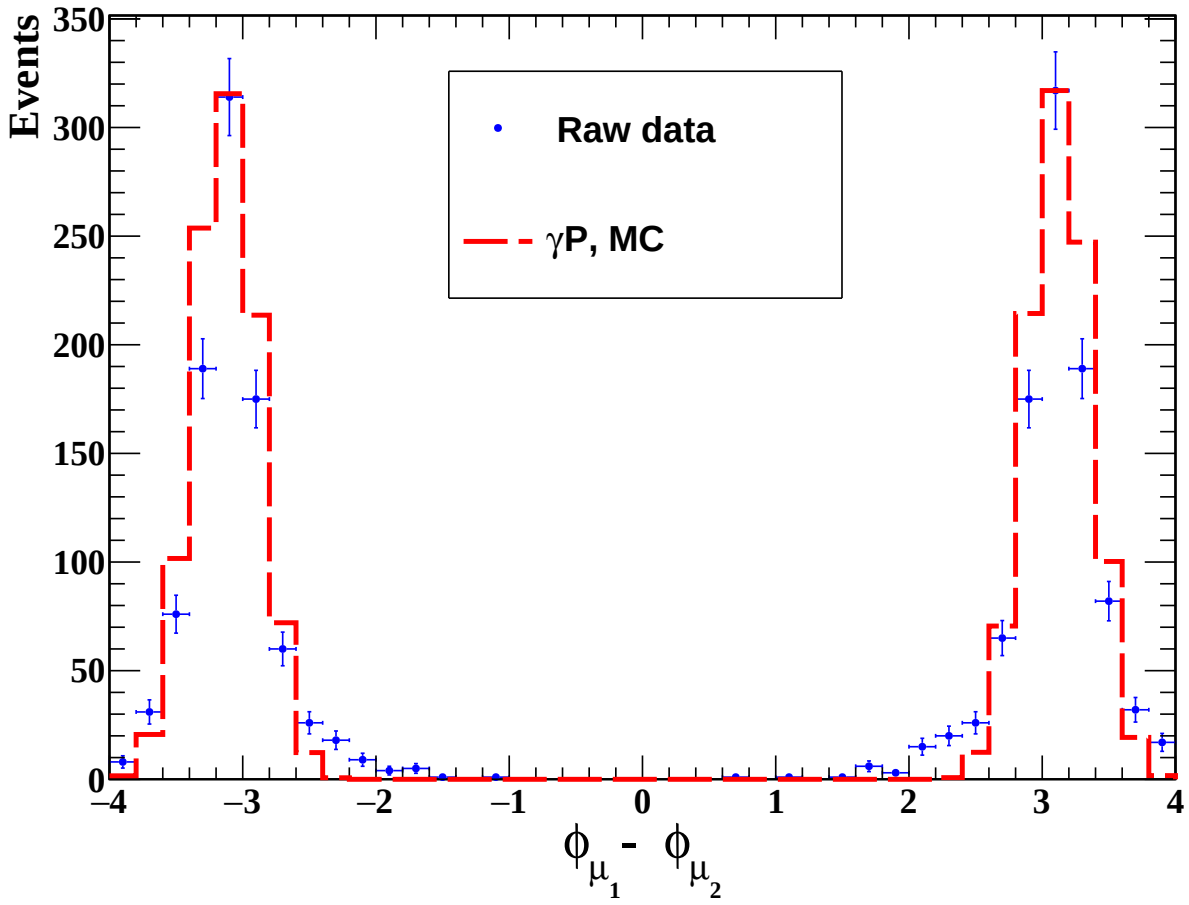

Figure 7.3: Distribution $\Delta\phi = \phi_{\mu_1} - \phi_{\mu_2}$ for data (blue points) and γp events from STARLIGHT (red curve)

Figure 7.5 compares the p_T spectra for data and MC for $\gamma\gamma, \gamma$Pb and exclusive γp samples at forward (top) and backward (bottom) rapidity. The techniques for producing these spectra in the data are described in the previous chapter. The $\gamma\gamma$ and γPb MC distributions are consistent with the data within statistical errors. For the exclusive γp spectra the MC is also generally consistent with the data except at forward rapidity and high p_T where the distribution falls more rapidly than the data.

Figure 7.6 shows the J/ψ rapidity distributions for data and γp MC. It is clear that the data and

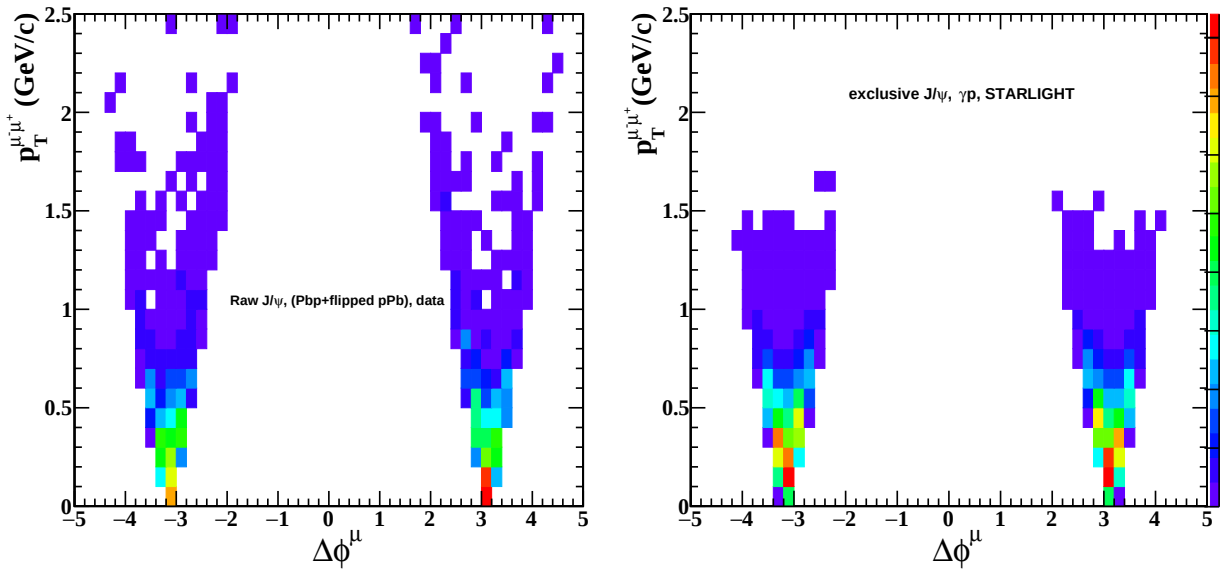

Figure 7.4: J/ψ p_T versus $\Delta\phi$ distribution for data (left) and γp MC (right).

the MC are similar, each distribution is asymmetric, and the concentrations are around $y \sim 2$ and $y \sim -2$. However, the data distributions are somewhat narrower than those from the MC. This may be because the $\gamma\gamma$, γPb and non-exclusive backgrounds have not been subtracted from the raw data.

Two-dimensional distributions of p_T versus rapidity for data and γp MC are shown in Figure 7.7. The MC plot has much higher statistics and so tends to be smoother than the data. Both the data and MC are asymmetric in rapidity and both distributions peak at similar values of p_T It is clear that the MC is significantly wider in rapidity than the data while the data goes to higher p_T than the MC.

Figure 7.8 shows the muon p_T versus η distribution for data and the γp MC. Both the data and MC are asymmetric in η but the data extend to higher p_T than the simulation. This may be due to the non-exclusive background that has not been subtracted from the data distribution.

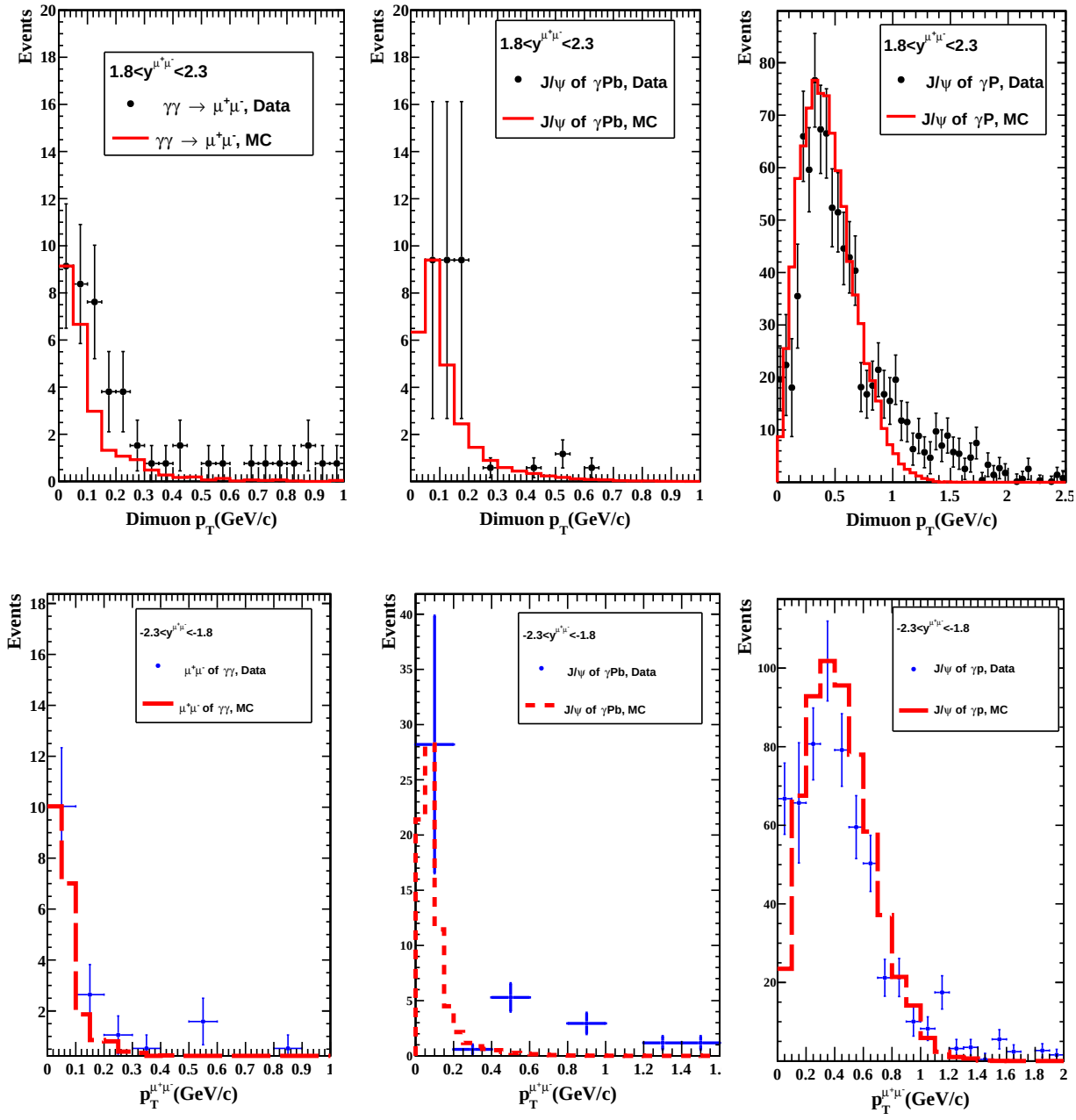

Figure 7.5: p_T spectra for data (black points) and MC (red curve) for $\gamma\gamma$ (left), γPb (middle) and exclusive γp collisions (right) for forward rapidity (top) and backward rapidity (bottom).

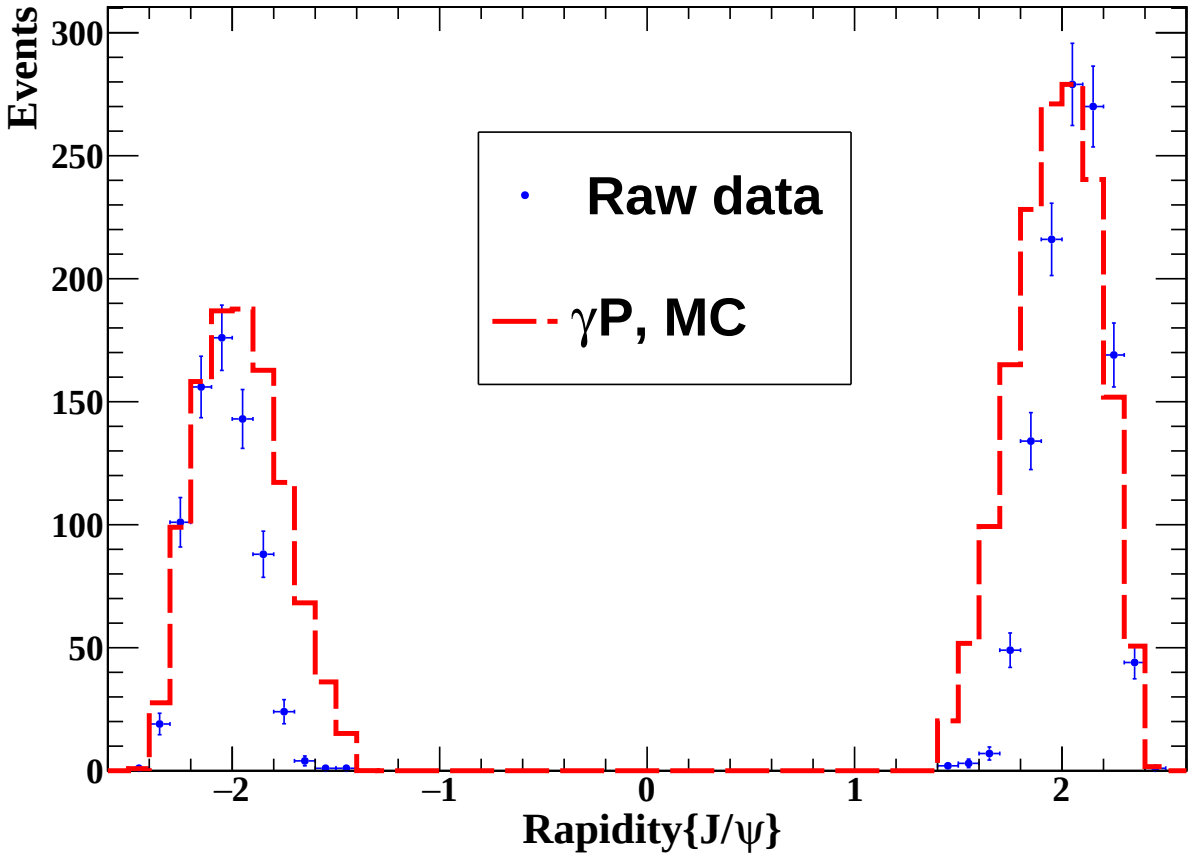

Figure 7.6: J/ψ rapidity distribution for data (blue points) and γp MC (red curve).

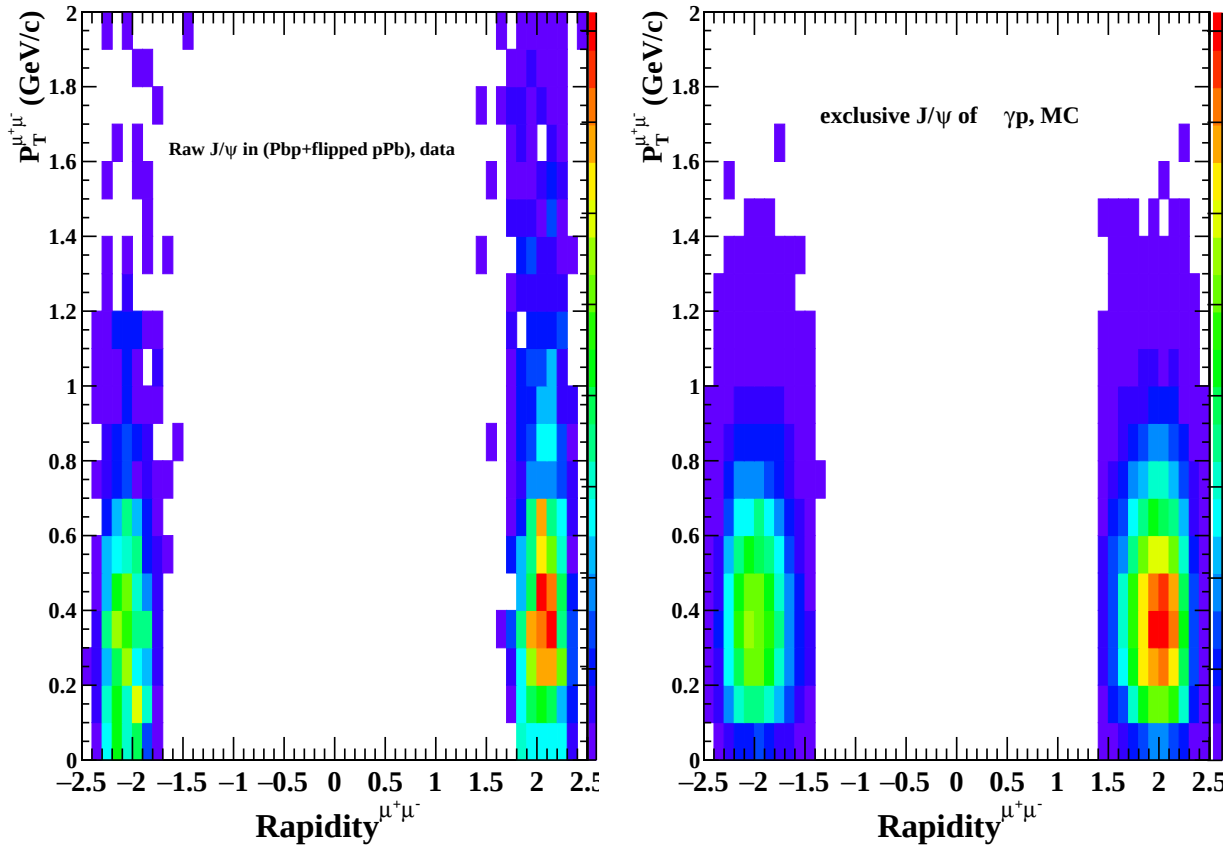

Figure 7.7: J/ψ p_T versus rapidity distribution for data (left) and γp MC (right).

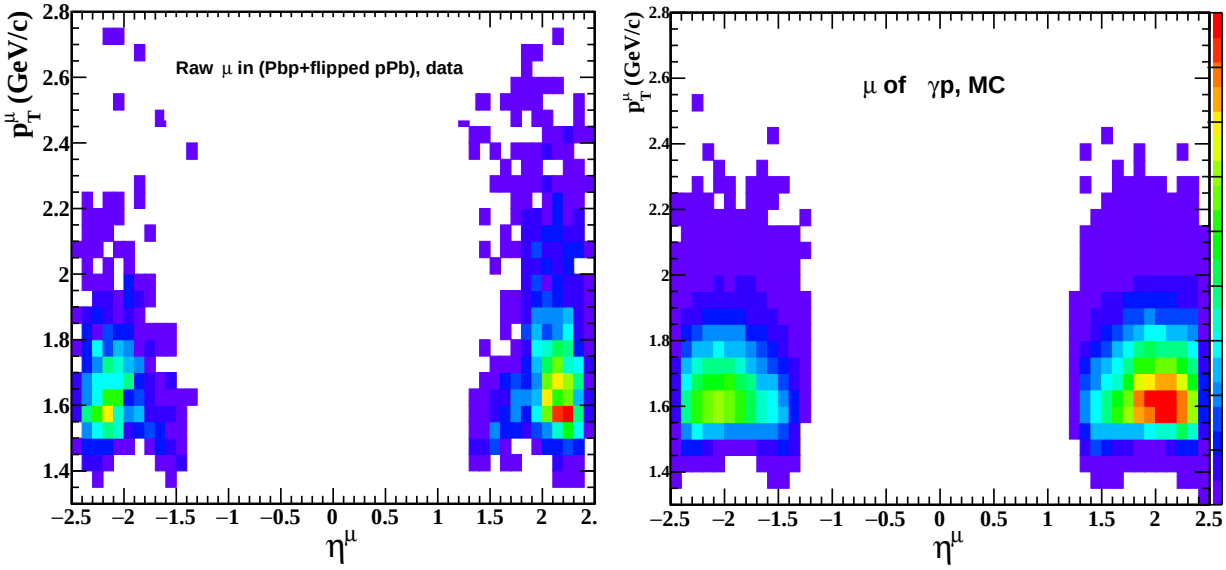

Figure 7.8: Muon p_T versus η distribution for data (left) and γp MC (right).

Chapter 8

Trigger Efficiency and Acceptance

8.1 Introduction

This chapter discusses the corrections for the dimuon trigger efficiency and acceptance of the CMS detector. The trigger efficiency is estimated from data while the acceptance corrections are estimated from Monte Carlo simulations.

8.2 Single muon trigger efficiency

The tag and probe method uses a sample of high quality muons that were not triggered on to investigate the efficiency of the muon trigger. For this study dimuon pairs in the J/ψ mass region, i.e., between 2.8 and 3.3 GeV/c^2, are used. In this region the signal-to-background ratio is greater than 15/1, as seen in Figure 6.13 . These events were selected with a trigger that required at least one hit in the muon chambers. For each dimuon event the trigger record is examined. Muons that produce triggers are known as “tags" and their partner muons are known as “probes." Probes that satisfy the trigger are then known as “passing probes" while those that fail the trigger are known as “failing probes." If both muons satisfy the trigger then they are both counted as tags and as passing probes. The single muon trigger efficiency is then given by

$$\varepsilon_{\mu}(p_T,\eta) = \frac{N_{passing\ probe}(p_T,\eta)}{N_{probe}(p_T,\eta)} \tag{8.1}$$

The statistical errors on ε_{μ} are calculated using binomial statistics.

Figure 8.1 shows the single muon efficiency ε_{μ} for pPb and Pbp data as a function of p_T and

pseudorapidity η. As expected, the efficiency increases with p_T and η since very low momentum muons are either bent into circles by the magnetic field or fail to punch through the iron of the muon absorbers.

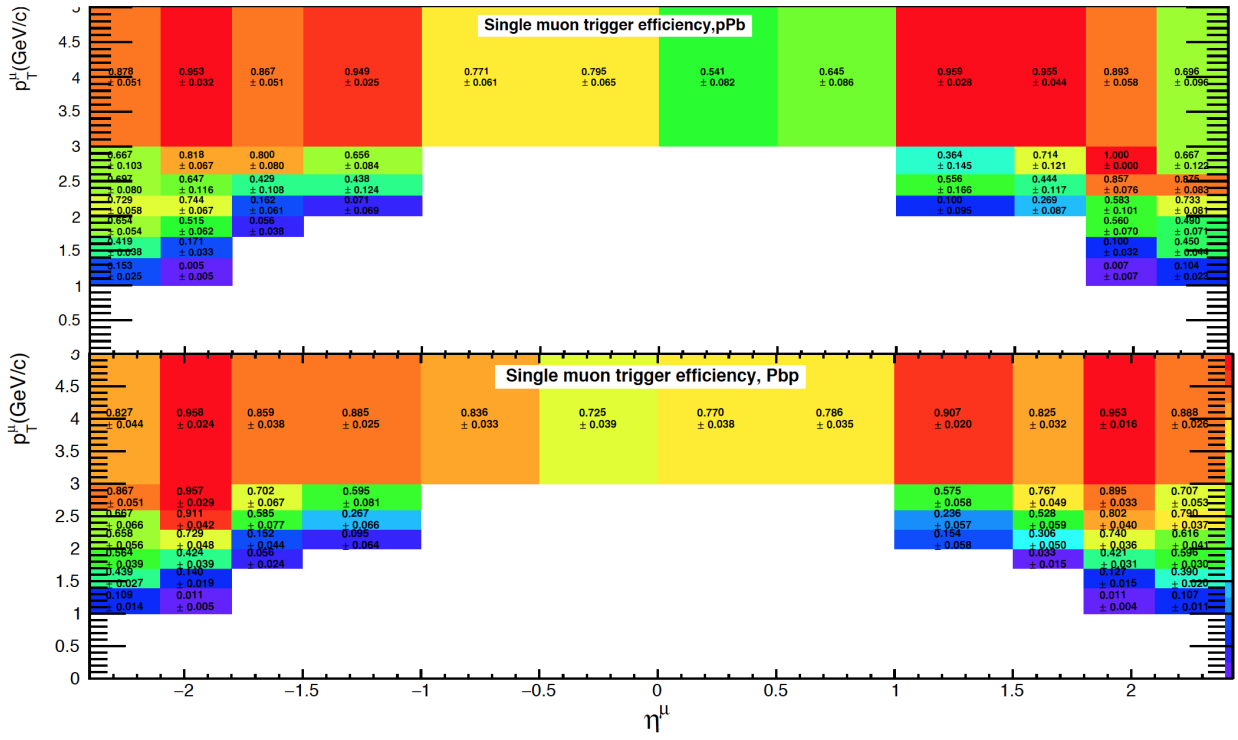

Figure 8.1: Single muon trigger efficiency versus η^μ and p_T^μ for pPb (top) and Pbp (bottom) data.

It is expected that the CMS muon system should be symmetric in η and that the efficiency should not change in the few weeks between pPb and Pbp running. Figure 8.2 shows the average single muon efficiency as a function of p_T at forward and backward η for both pPb and Pbp runs. The efficiency is symmetric in η and so to increase the statistical precision the efficiency is calculated as a function of $|\eta|$. Figure 8.3 shows ε_μ as a function of p_T for pPb and flipped Pbp. The distributions are symmetric and so the pPb and flipped pPb samples are merged.

Finally, Figure 8.4 shows ε_μ versus p_T for $0.9 < |\eta| < 2.4$ pPb and Pbp data. The distributions are statistically consistent and the binomial errors seem reasonable given the scatter of the points. Because ε_μ is consistent at positive and negative η and for the pPb and Pbp data it is reasonable to combine all the data to maximize the statistical precision of the efficiency. Figure 8.5 shows ε_μ as a function of p_T and $|\eta|$ for all data (pPb and flipped Pbp). For a J/ψ to be accepted in this analysis

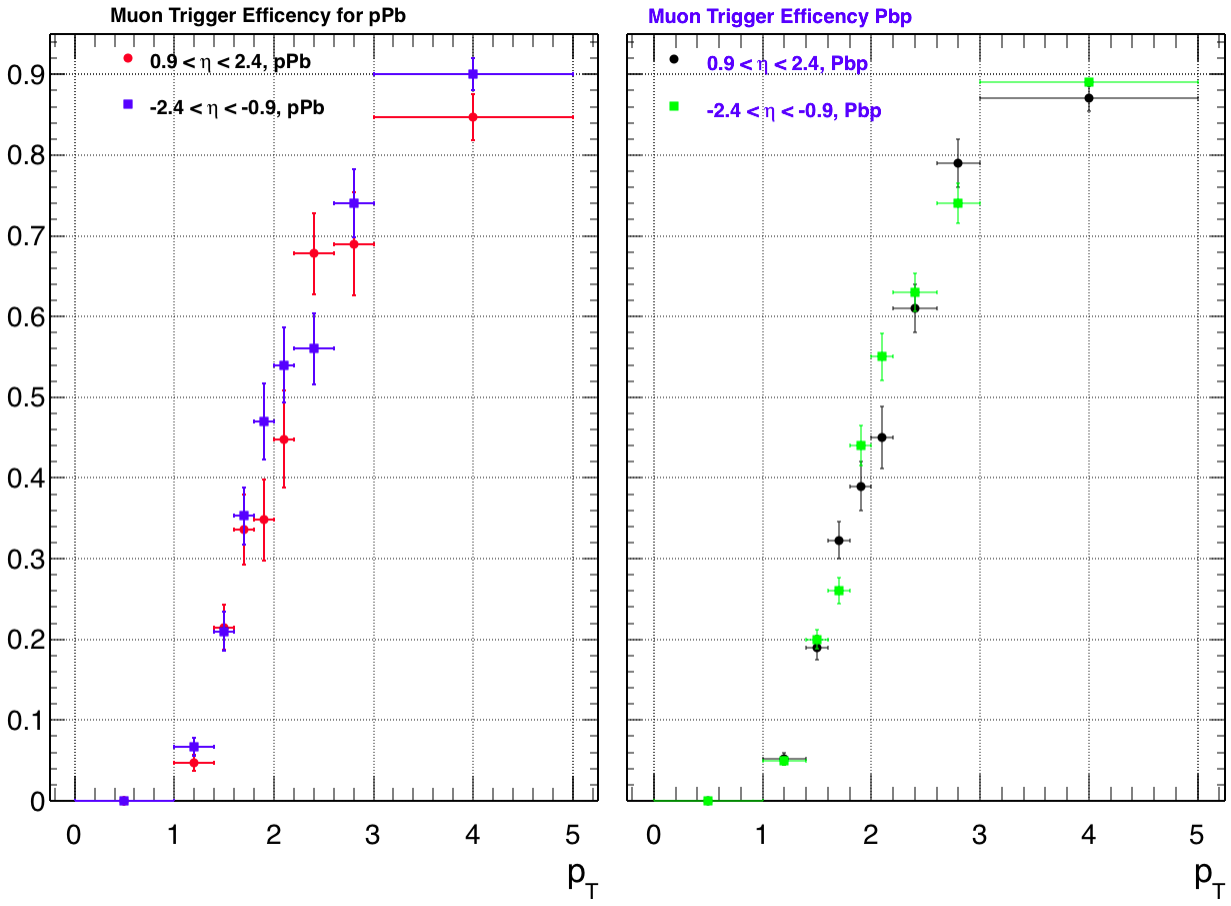

Figure 8.2: Single muon trigger efficiency averaged over a large η region versus the muon p_T. The left plot is for pPb data, $+\eta$ (blue) , $-\eta$ (red) and the right plot is for Pbp data, $+\eta$ (green), $-\eta$ (black).

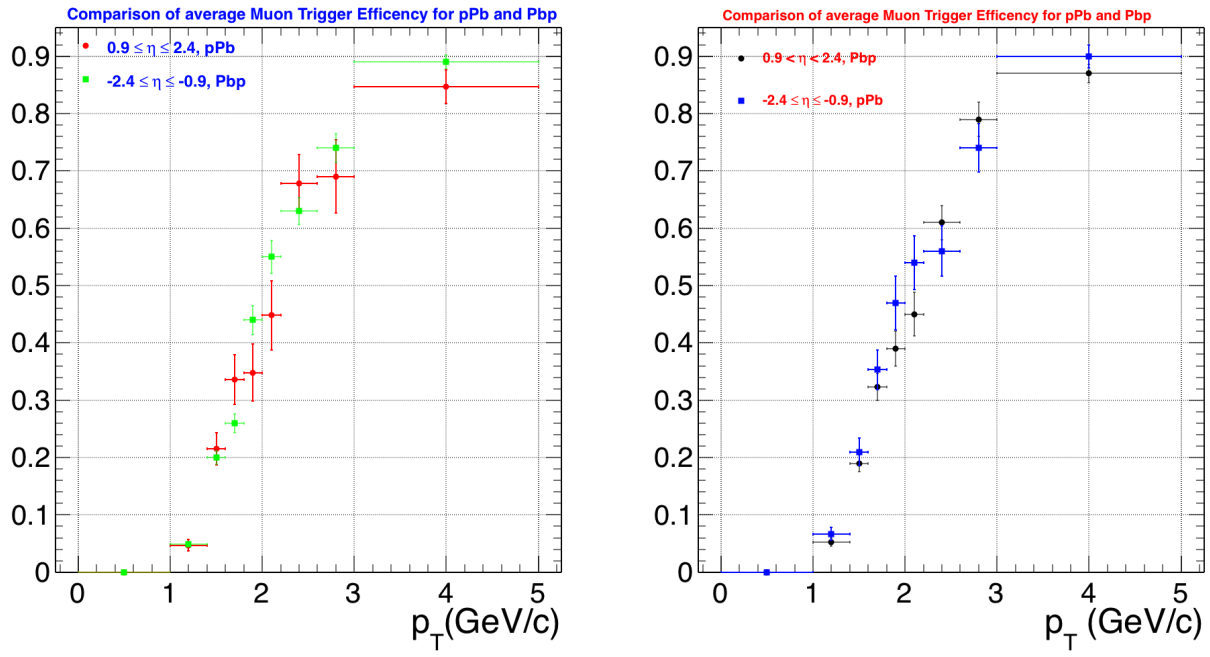

Figure 8.3: Single muon trigger efficiency ε_μ average over a large η^μ region versus p_T^μ. Left: pPb at $+\eta$ (red) and Pbp at $-\eta$ (blue). Right: pPb at $-\eta$ (blue) and Pb- at $+\eta$ (green).

it was required that each muon have a trigger efficiency of greater than 10%. This cut was used for both data and Monte Carlo events. This cut eliminates J/ψ which have one muon at the edge of the acceptance where the efficiency may not be estimated accurately. The muon trigger efficiency, $\varepsilon_\mu(|\eta|, p_T)$ shown in Figure 8.5 for all data (pPb and flipped Pbp) is summarized in Table 8.1.

	p_T (GeV/c)							
	0−1.0	1.0−1.3	1.3−1.6	1.6−1.9	1.9−2.2	2.2−2.5	2.5−3.5	3.5−5.0
$\|\eta\| < 1.0$	0	0	0	0	0	0	0.36±0.05	0.85±0.02
$1.0 < \|\eta\| < 1.8$	0	0	0	0.01±0.01	0.12±0.02	0.35±0.03	0.70±0.02	0.94±0.01
$1.8 < \|\eta\| < 2.4$	0	0.03±0.00	0.21±0.01	0.42±0.01	0.65±0.02	0.75±0.02	0.87±0.01	0.93±0.01

Table 8.1: Single muon trigger efficiency ε_μ as a function of the muon p_T and $|\eta|$ for the combined pPb and flipped Pbp data.

8.3 Dimuon Trigger efficiency

For ultra-peripheral J/ψ events the occupancy of the muon chambers is very low and the two muons are always in different ϕ regions of the muon chambers. This can be seen clearly in the event display shown in Figure 6.5. In such conditions, trigger efficiencies for each muon are

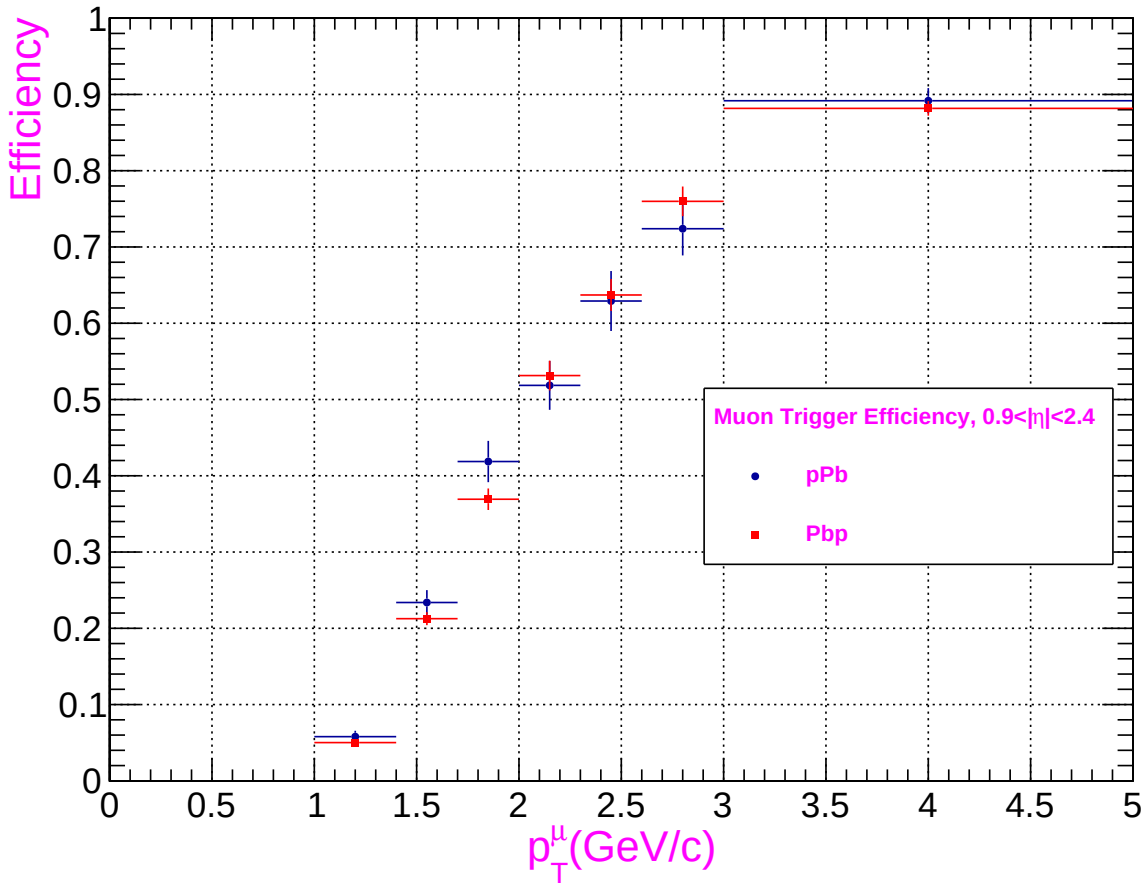

Figure 8.4: Single muon trigger efficiency ε_μ versus p_T in the range $0.9 < |\eta| < 2.4$. For pPb (blue) for Pbp (red) data.

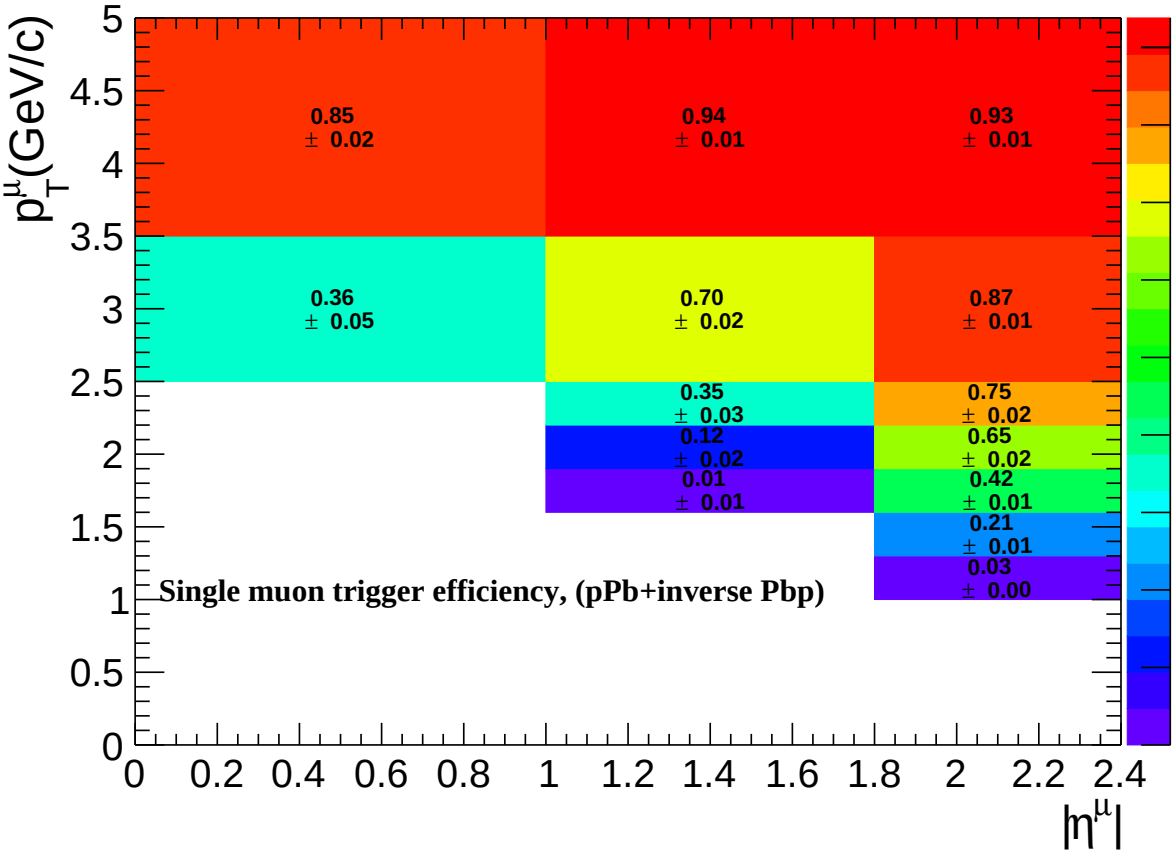

Figure 8.5: Single muon trigger efficiency ε_μ as a function of muon p_T and $|\eta|$ for the combined pPb and Pbp data.

independent and the chance for a J/ψ not to fire the trigger is just the product of the probabilities that muon 1 and muon 2 both fail the trigger. The trigger efficiency of dimuons $\varepsilon_{\mu_1\mu_2}$ is thus given by:

$$\varepsilon_{\mu_1\mu_2} = 1 - (1 - \varepsilon_{\mu_1}(p_{T1}, \eta_1))(1 - \varepsilon_{\mu_2}(p_{T2}, \eta_2)), \tag{8.2}$$

where ε_{μ_1} is the efficiency of muon 1 at $p_T^{\mu} = p_T^1$ and $\eta^{\mu} = \eta^1$ and ε_{μ_2} is the second muon trigger efficiency. The individual muon efficiencies are calculated on a grid as shown in Figure 8.5. Correcting for this trigger efficiency for each event gives

$$N_{TrigCorr} = \sum_{1}^{N_{events}} \frac{1}{\varepsilon_{\mu_1\mu_2}}, \tag{8.3}$$

where N_{events} is the number of events in the sample. Figure 8.6 shows corrected and uncorrected J/ψ p_T distributions for pPb and Pbp data at both forward and backward rapidity.

Although the correction for trigger efficiency is different for each event, it is possible to calculate an average trigger efficiency

$$\varepsilon_{J/\psi} = \frac{1}{N_{events}} \sum_{1}^{N_{events}} \frac{1}{\varepsilon_{\mu_1\mu_2}}. \tag{8.4}$$

The statistical error on $\varepsilon_{J/\psi}$ depends upon the individual statistical errors in the grid of individual muon efficiencies at different p_T and η. If the muon efficiency grid has N_{grid} elements then there are $N_{grid}^2/2$ different values of $\varepsilon_{J/\psi}$ that are averaged. As an alternative to calculating the full error matrix it was decided to evaluate the trigger efficiency in four independent samples. Figure 8.7 shows the J/ψ trigger efficiency $\varepsilon_{\mu_1}\varepsilon_{\mu_2}$ versus p_T for pPb and Pbp data at forward and backward rapidity. The central values are the averages of the four individual efficiencies. The error for each bin is determined by scaling the root mean square of individual efficiencies to the 67% confidence limit for a sample size of 4. The statistical error on the efficiency is reasonable up until a transverse momentum of 1.5 GeV/c.

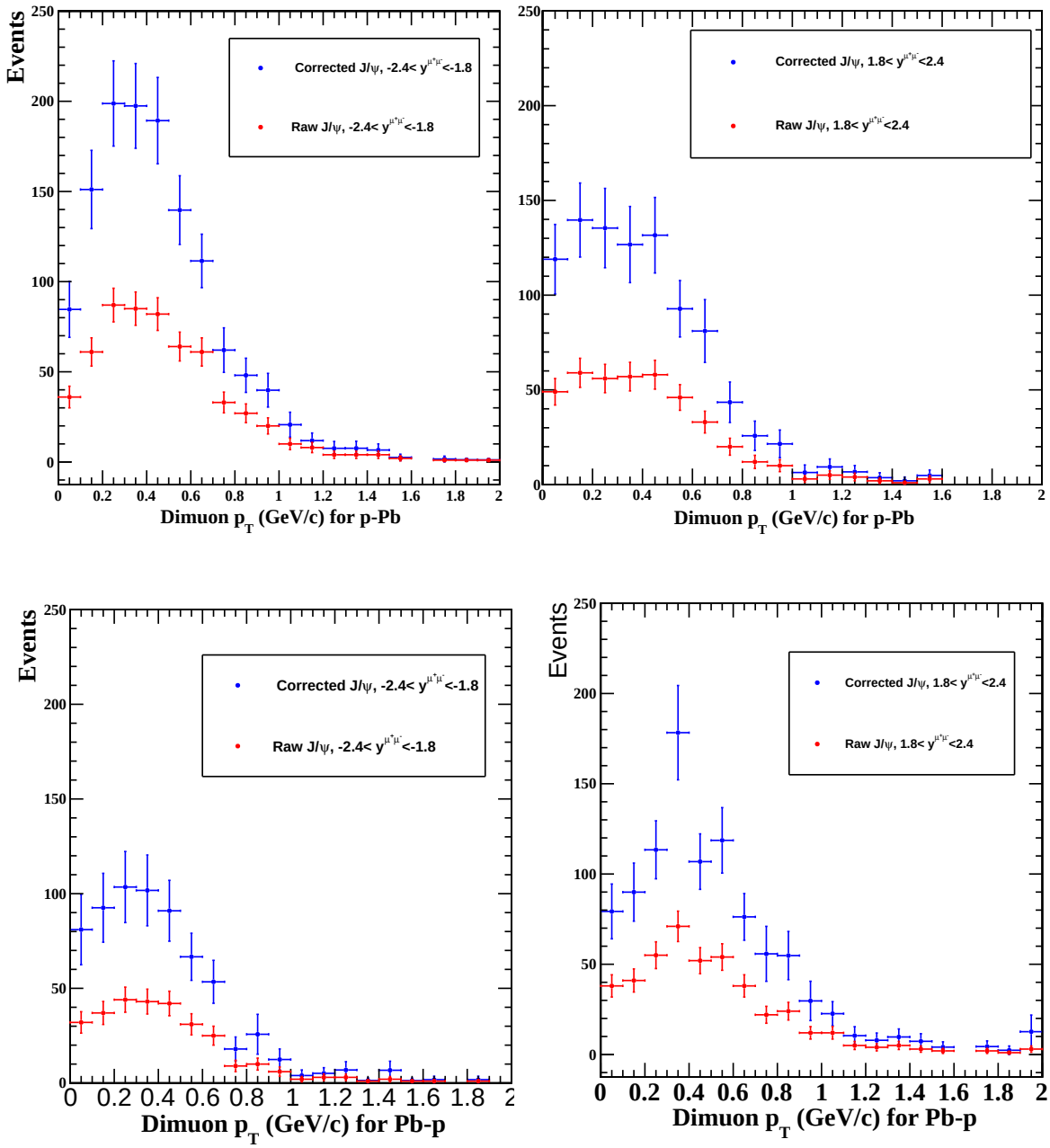

Figure 8.6: J/ψ p_T distributions of uncorrected (red) and corrected (blue) for trigger efficiency for pPb (top) and Pbp (bottom) data. The left column shows the spectra for $-2.4 < y < -1.8$ and the right column for $1.8 < y < 2.4$.

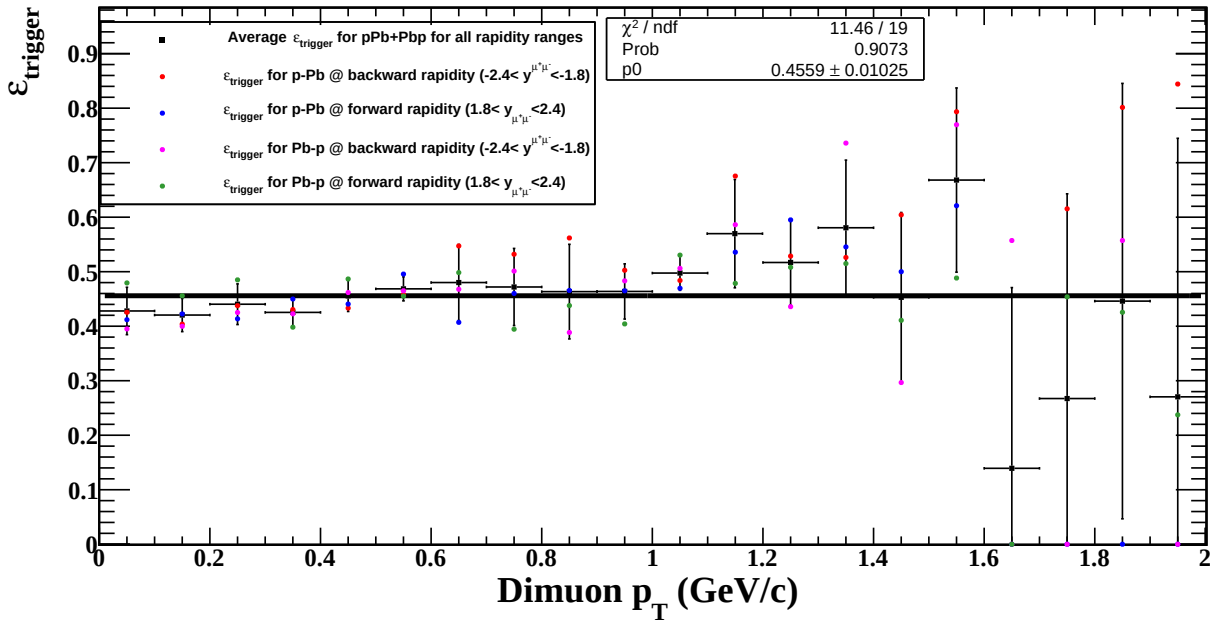

Figure 8.7: J/ψ trigger efficiency ε versus p_T. The central values are the average of four individual efficiencies in the data for pPb and Pbp at forward and backward rapidity. The error for each bin is determined by scaling the root mean square of the individual efficiencies to the 67% confidence limit for a sample size of 4.

8.4 Geometrical Acceptance

Figure 8.5 shows that CMS only detects muons in certain regions of p_T and η. Low momentum muons are bent into circles by the strong magnetic field and so never reach the muon chambers. In the forward region muons may not have enough momentum to punch through the iron in front of the muon chambers. Because of this not all the $J/\psi \to \mu^+\mu^-$ events produced in ultra-peripheral collisions are detected by CMS. To compensate for the missed J/ψ events it is necessary to use a simulation of the CMS detector to estimate the acceptance, A, defined by:

$$A(p_T, y) = \frac{N_{det}(p_T, y)}{N_{gen}(p_T, y)} \tag{8.5}$$

where N_{gen} is the number of J/ψ mesons generated by the Monte Carlo in a certain region of p_T and y and N_{det} is the number of reconstructed J/ψ in the same region. For this analysis, the UPC Monte Carlo STARLIGHT was used to estimate the acceptance A. The generated Monte

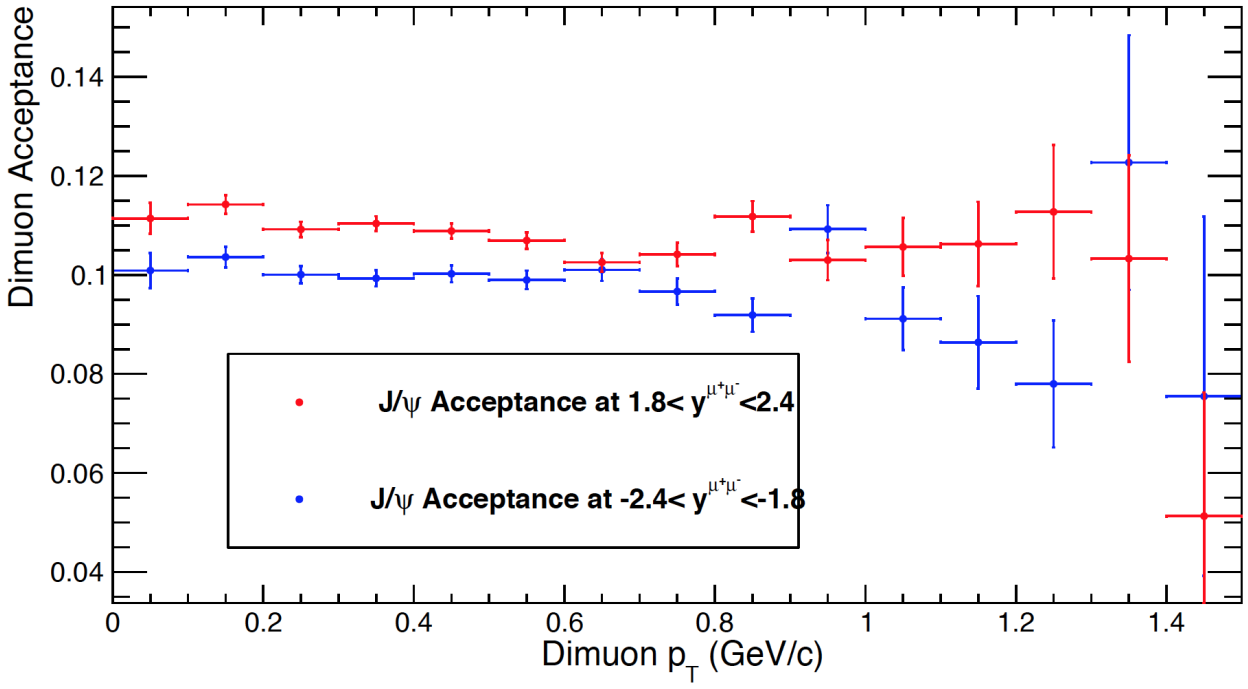

Figure 8.8: The acceptance versus p_T for forward rapidity (blue) ($1.8 < y < 2.4$) and backward rapidity (red) ($-2.4 < y < -1.8$)

Carlo events are put through a full GEANT4 simulation of CMS. These simulated events are then analyzed using the same cuts as the real data.

Figure 8.8 shows the acceptance versus p_T for two ranges of rapidity, backward rapidity at $-2.4 < y < -1.8$, and forward rapidity at $1.8 < y < 2.4$. The statistical error on A is estimated using the binomial formula. The acceptance does not depend strongly on p_T. There is a difference of about 9% in the relative acceptances on the two sides of CMS. To test this difference against data we compared the corrected yield of J/ψ events normalized by luminosity in pPb with those of Pbp in the flipped rapidity. This comparison will be discussed in the Results chapter. Figure 8.9 shows the dimuon acceptance versus rapidity for $0 < p_T < 1.5$ GeV/c. The dimuon acceptance is asymmetric; it is 0.1 in the rapidity range $-2.4 < y < -1.8$, while it is 0.11 in the rapidity range $1.8 < y < 2.4$.

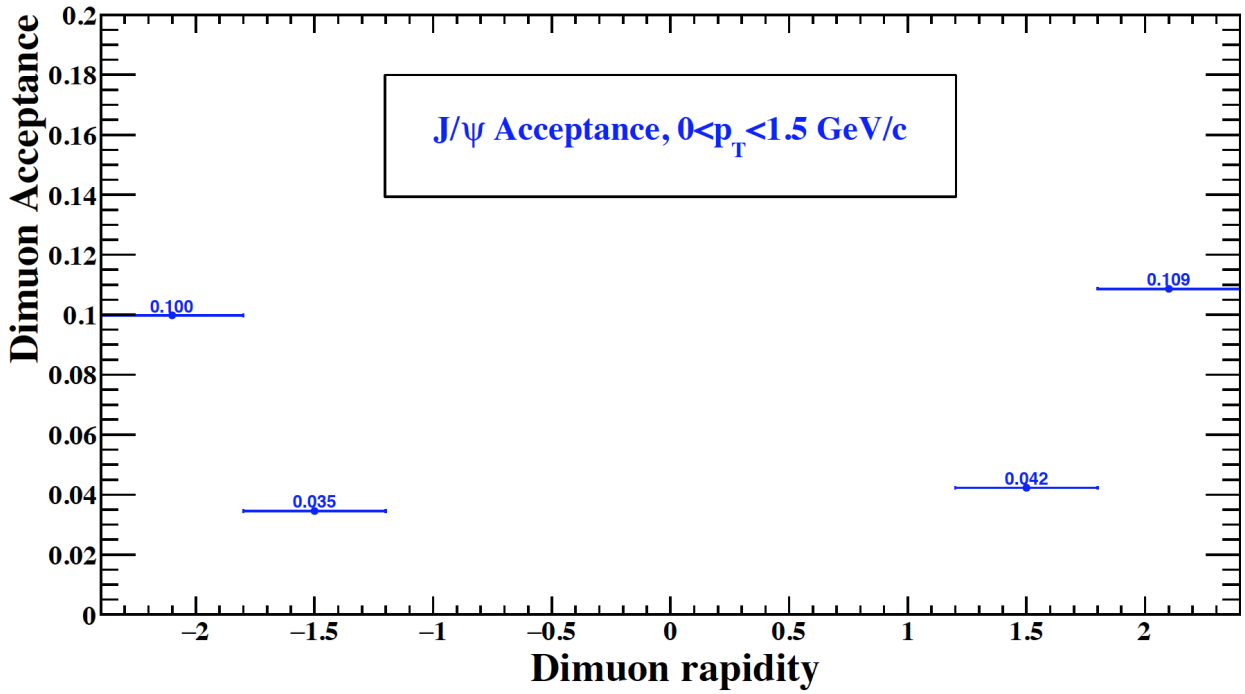

Figure 8.9: The $J/\psi \to \mu^+\mu^-$ acceptance versus rapidity for $0 < p_T < 1.5$ GeV/c. The statistical error is not clear, because the number of the events is large.

Chapter 9

Systematic Uncertainties and Cross Checks

9.1 Introduction

The double differential cross section in p_T and rapidity is calculated as

$$\frac{d\sigma}{dp_T dy}(\gamma p \to J/\psi p) = \frac{N^{exc}_{J/\psi}(p_T, y)}{\varepsilon_{J/\psi} \times A \times B.R \times L_{int}} \frac{1}{\Delta p_T} \frac{1}{\Delta y}, \tag{9.1}$$

where $N^{exc}_{J/\psi}(p_T)$ is the number of J/ψ events with a given p_T and y range, $\varepsilon_{J/\psi}$ is product of the J/ψ trigger efficiency and the efficiency of all the event selection cuts, A is the acceptance, $B.R$ is the branching ratio of $J/\psi \to \mu^+\mu^-$, and L_{int} is the integrated luminosity. Once the p_T spectrum is calculated one can take the mean to find $\langle p_T \rangle$. The integral gives

$$\frac{d\sigma}{dy} = \int_0^\infty \frac{d\sigma}{dp_T dy} dp_T. \tag{9.2}$$

The systematic uncertainties on $\frac{d\sigma}{dp_T dy}$ were estimated by changing each element of the analysis and quantifying how the change effected the final result. If the statistical difference between the two ways of doing the analysis is consistent with zero then no systematic error is added and the procedure is listed as a cross check. The systematic errors can be divided into two kinds, those that depend upon p_T such as the background subtraction, and global systematic errors such as the luminosity that are independent of p_T and only affect the overall normalization of the data. The total systematic error is takes to be the quadratic sum of all the systematic errors. In this chapter the p_T-dependent systematic errors are discussed first and the global errors are discussed second.

9.2 Background Subtraction

As discussed in Chapter 6 the p_T-dependent contributions of $\gamma\gamma$, γ-lead and non-exclusive reactions are subtracted from the raw distribution. The $\gamma\gamma$ and γ-lead spectra are concentrated at low p_T while the distribution of non-exclusive J/ψ is peaked at $p_T \approx 800$ MeV/c.

9.2.1 Subtraction of $\gamma\gamma$ background

The $\gamma\gamma$ background is estimated using a sideband region in the dimuon mass distribution slightly above the J/ψ peak. The main analysis uses the mass region 4-5 GeV/c^2 and the background was also estimated by taking the region 4-8 GeV/c^2. Using fits to the mass distribution two ratios are calculated

$$R_{\text{sideband1}} = \frac{\int_{2.8}^{3.3} \frac{dN_{fit}}{dp_T} dp_T}{\int_{4.0}^{5.0} \frac{dN_{fit}}{dp_T} dp_T}, \tag{9.3}$$

and

$$R_{\text{sideband2}} = \frac{\int_{2.8}^{3.3} \frac{dN_{fit}}{dp_T} dp_T}{\int_{4.0}^{8.0} \frac{dN_{fit}}{dp_T} dp_T}. \tag{9.4}$$

Note that both of these equations use the same polynomial fit to the continuum distribution. From these ratios two background distributions are extrapolated to the signal region

$$\frac{dN_{\gamma\gamma}^{4-5}}{dp_T} = R_{\text{sideband1}} \cdot \frac{dN_{4-5}}{dp_T}, \tag{9.5}$$

$$\frac{dN_{\gamma\gamma}^{4-8}}{dp_T} = R_{\text{sideband2}} \cdot \frac{dN_{4-8}}{dp_T}. \tag{9.6}$$

The difference between the two distributions is then taken as the systematic uncertainty from the $\gamma\gamma$ subtraction.

9.2.2 Subtraction of γPb background

For γPb collisions, there are two kinds of events, coherent and incoherent. For coherent events, the wavelength of the photon is close to the nuclear radius and the photon interacts with the nucleus

as a whole to produce a J/ψ. Neutrons may be produced by the exchange of a second photon, see Chapter 5 but this is not usual. The J/ψ mesons produced in these events have $p_T \approx 60$ MeV/c. If the wavelength of the photon is shorter then the nuclear radius, the photon interacts with one nucleon in the nucleus. In such cases the J/ψ is much more energetic, $p_T \approx 500$ MeV/c, and most events are accompanied by neutron production.

For this analysis γPb collisions were selected by requiring neutron emission on the lead side. Since in the main analysis we do not require neutron emission it is necessary to correct for the fraction of coherent and incoherent events that are accompanied by neutron emission. For the main analysis it was assumed that 20% of coherent events and 80% of incoherent events correlated with the emission of very low p_T forward neutrons. These factors were based on both experimental and theoretical estimates, [30, 37]. As an alternative it was assumed that 40% of coherent events and 60% of incoherent events correlated with neutron emission. The difference in the p_T distribution of the two estimates was treated as the systematic uncertainty.

9.2.3 Subtraction of non exclusive J/ψ events

The non-exclusive background in the sample was estimated by assuming that the high p_T tail of the distribution, i.e., $p_T > 2.0$ GeV/c was dominated by non-exclusive events. The spectrum of the non-exclusive events was then scaled to the raw data such that the number of both the raw J/ψ and the non-exclusive J/ψ were equal for $p_T > 2.0$ GeV/c. The scaled non-exclusive distribution was then used to subtract non-exclusive background at lower p_T. To estimate the systematic uncertainty on this subtraction, the p_T value above which I assumed all the data was non-exclusive was changed to $p_T = 2.5$ GeV/c and the difference in the distributions was treated as a systematic uncertainty.

9.3 Global systematic uncertainties

9.3.1 Efficiency of J/ψ mass cut

The dimuon mass distribution is fitted by a polynomial of order two for the $\gamma\gamma$ background distribution and two Crystal Ball functions to represent the J/ψ and $\psi(2s)$ signals. The Crystal Ball function depends upon four variables (mean, σ, n, α). For each of the four J/ψ signals, Pbp and pPb at forward and backward rapidity, the variables n and α were varied. In all cases this produced a negligible change in efficiency of the mass cut used for each J/ψ signal.

9.3.2 Geometric Acceptance

The acceptance at forward rapidity A^+ is a little different from the acceptance at backward rapidity A^-. Such a difference was not seen in the data. The systematic uncertainty on the acceptance was estimated from the difference in the average acceptance at positive and negative rapidity. This give $\frac{A^+-A^-}{A^++A^-} = 4.9\%$.

9.3.3 Luminosity

The luminosities for pPb and Pbp were estimated using dedicated Van de Waals scans. The uncertainties of the luminosity are 3.4% for pPb and 3.6% for Pbp [109]. These were combined using the measured luminosities to give a total error of 3.5%.

9.3.4 Trigger efficiency

The systematic uncertainties on the trigger efficiency were estimated by comparing the efficiencies measured in the forward and backward sides of CMS and for the pPb and Pbp data. From Fig. 8.7 it is clear that there is no statistically significant difference between these efficiencies and so this study was considered to be a cross-check.

9.3.5 Branching ratio

The measured branching ratio for $J/\psi \to \mu^+\mu^-$ is $(5.961 \pm .033) \cdot 10^{-2}$ [110]. This produces an additional uncertainty in the final cross section of 0.6%.

9.3.6 Flux of virtual photons $k\frac{dN_\gamma}{dk}$

The flux of virtual photons is calculated by STARLIGHT simulation. The Pb nucleus is the source of the photon flux, so the calculation of the systematic error is made by increasing and decreasing the radius of the Pb nucleus by ± 0.5 fm. The systematic error associated with the photon flux at low photon-nucleus center-of-mass energy W is 2% and it is 9% at high energy [33]. These uncertainty only effects the γp cross section $\sigma(\mathrm{W})$ and produce errors of 2% and it is 9% at low and high W respectively.

9.3.7 Total Normalization Uncertainty

Table 9.1 summarizes the normalization uncertainties for Pbp and pPb events at forward and backward rapidity.

Samples	Pbp		pPb	
Rapidity interval	(-2.3,-1.8)	(1.8, 2.3)	(-2.3,-1.8)	(1.8, 2.3)
Acceptance	4.9	4.9	4.9	4.9
Luminosity	3.6	3.6	3.4	3.4
Branching Ratio	0.6	0.6	0.6	0.6
Total for $d\sigma/dp_T dy$	6.1	6.1	6.0	6.0
Flux of virtual photons	9.0	2.0	9.0	2.0
Total for $\sigma(\mathrm{W})$	10.9	6.4	10.8	6.3

Table 9.1: Global systematic uncertainties for $d\sigma/dp_T dy$ and $\sigma(\mathrm{W})$ in %.

9.4 p_T Spectra

Figure 9.1 shows the J/ψ p_T spectra for Pbp and pPb collisions at backward and forward rapidity. The black markers represent the statistical errors and the blue boxes represent the p_T-dependent

systematic uncertainties. The systematic errors on the normalization are not included since they are common to all four systems. Table 9.2 lists the number of exclusive J/ψ events with both statistical uncertainties and systematic uncertainties from ($\gamma\gamma$, γPb and non-exclusive J/ψ) for different p_T ranges for Pbp and pPb at backward and forward rapidity.

p_T (GeV/c)	Pbp sample		pPb sample	
	-2.3 < y <-1.8	1.8 <y<2.3	-2.3 < y <-1.8	1.8<y < 2.3
0.0-0.1	27.2±6.3±0.1	28.0±7.6±1.9	19.0±6.5±13.7	33.4±7.2±7.4
0.1-0.2	19.8±9.4±3.1	23.2±8.7±2.7	24.5±11.8±17.6	44.4±12.2±3.1
0.2-0.3	35.1±6.2±0.7	54.6±7.7±0.8	70.6±8.9±1.3	45.5±6.8±0.6
0.3-0.4	41.8±6.5±0.5	64.4±8.2±1.6	78.6±9.1±0.8	59.6±7.9±0.4
0.4-0.5	33.3±6.0±0.4	44.1±7.1±1.4	71.7±8.9±0.5	48.4±7.0±0.3
0.5-0.6	27.5±5.3±0.1	43.9±6.9±1.1	51.8±7.6±0.5	31.7±6.1±1.2
0.6-0.7	21.0±4.6±0.5	27.1±5.8±1.3	55.3±7.6±0.2	29.4±5.5±0.3
0.7-0.8	5.0±2.2±0.1	13.6±4.4±1.0	21.0±4.8±0.8	16.3±4.1±0.2
0.8-0.9	8.9±3.3±0.4	19.6±5.0±1.2	18.7±4.8±0.5	12.3±3.6±0.2
0.9-1.0	3.0±2.1±0.2	8.0±3.8±1.4	21.9±5.2±0.5	8.5±3.0±0.52
1.0-1.1	4.0±2.0±0.1	21.3±5.1±1.2	9.1±3.3±0.8	4.3±2.2±0.2
1.1-1.2	5.0±2.2±0.1	7.5±3.4±1.1	10.1±3.5±0.8	12.5±3.6±0.3
1.2-1.3	1.5±1.5±0.1	5.3±3.0±0.7	8.5±3.4±0.5	2.3±1.7±0.2
1.3-1.4	2.0±1.4±0.1	4.7±3.2±1.2	9.3±3.3±0.2	1.5±1.4±0.1
1.4-1.5	0.5±1.1±0.1	8.8±3.4±0.8	6.3±3.1±0.5	0.5±1.0±0.1
1.5-1.6	3.0±1.7±0.1	1.0±2.4±1.1	9.4±3.3±0.2	2.6±1.7±0.1
0.0-1.6	238.4±18.2±3.2	374.9±22.9±5.3	485.5±26.0±22.4	353.2±22.1±8.2

Table 9.2: Number of exclusive J/ψ events with both statistical uncertainties and systematic uncertainties from ($\gamma\gamma$, γPb and non-exclusive J/ψ) for different p_T ranges for Pbp and pPb at backward and forward rapidity

Table 9.3 summarizes the numbers of events, luminosity, average acceptance and efficiency for each of the four data sets and Table 9.4 lists $\langle p_T \rangle$ for all four data sets. As expected the Pbp data at y- and the pPb data at y+ are consistent within the statistical errors and the spectra of Pbp at y=+2 and pPb at y=-2 are also consistent. Since the spectra from pPb and Pbp are consistent it is reasonable to combine the data. Since, according to CMS convention, the protons were moving in the positive direction for Pbp the pPb data is flipped in rapidity when it is combined with the Pbp data. Figure 9.2 shows $\frac{d\sigma}{dydp_T}$ versus p_T for the combined data (Pbp + flipped pPb).

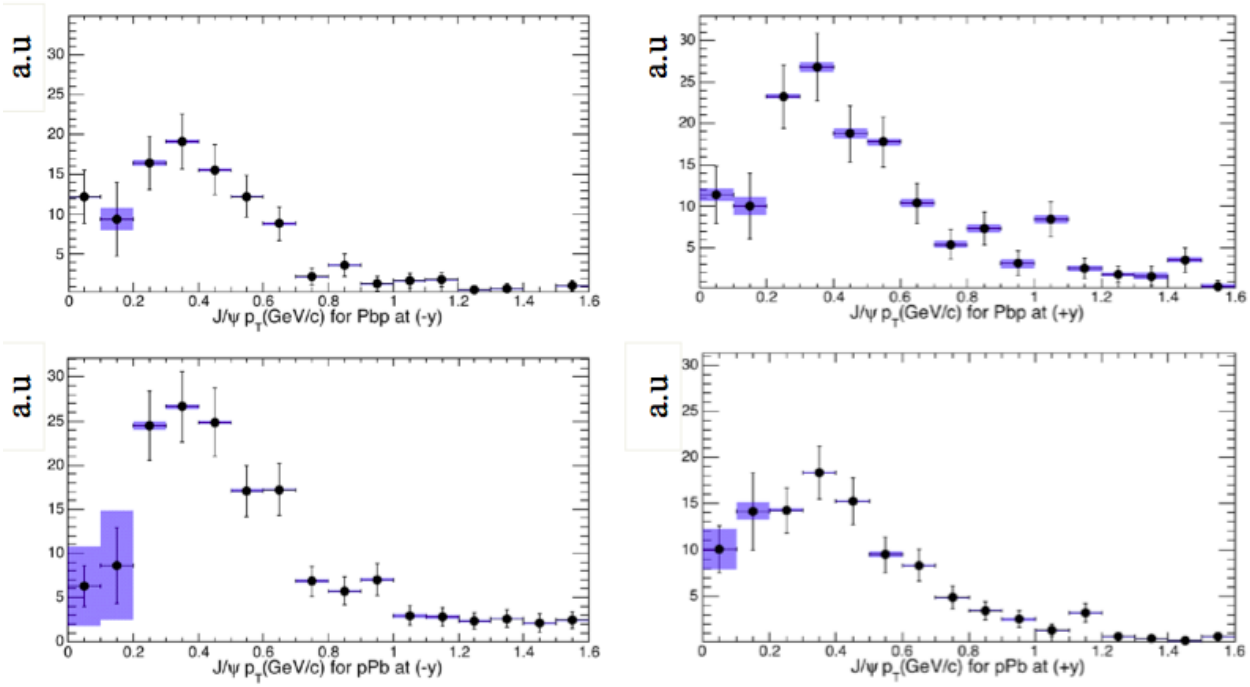

Figure 9.1: The double differential cross section $\frac{d\sigma}{dydp_T}$ versus p_T for exclusive J/ψ. The top row shows the Pbp spectra and the bottom one the pPb spectra. Spectra from negative rapidity are on the right and positive rapidity on the left. The black markers represent the statistical errors and the blue markers represent the p_T-dependent systematic uncertainties.

9.5 The γp cross section, $W_{\gamma p}$ and Bjorken-x

The photon-proton cross section $\sigma(\gamma p \to J/\psi p)$ is related to $\frac{d\sigma}{dy}$ by:

$$\frac{d\sigma}{dy}(\gamma p \to J/\psi p) = k\frac{dN_\gamma}{dk}\sigma(\gamma p \to J\psi p), \tag{9.7}$$

where $k\frac{dN_\gamma}{dk}$ is the flux of virtual photons. The lead ion is predominantly the source of the virtual photons. The flux was calculated using STARLIGHT. The energy of the photon-proton collision is given by

$$W_{\gamma p}^2 = 2E_p M_{J/\psi} e^{-y} \tag{9.8}$$

where $E_p = 4$ TeV is the energy of the proton beam in the laboratory frame, $M_{J/\psi}$ is the mass of the J/ψ and y is the laboratory rapidity of the J/ψ. $W_{\gamma p}$ is higher at negative rapidity and lower at positive rapidity. From Figure 7.6 it can be seen that the rapidity distribution can be described by

Sample	Pbp		pPb	
Rapidity interval	(-2.3,-1.8)	(1.8,2.3)	(-2.3,-1.8)	(1.8,2.3)
$\langle y \rangle$	-2.07 ± 0.13	2.06 ± 0.13	-2.07 ± 0.13	2.06 ± 0.13
N_{Raw}	269 ± 16.4	454 ± 21.3	563 ± 23.7	391 ± 19.8
$N_{\gamma\gamma}$	13.6 ± 3.4	19.2 ± 3.7	28.6 ± 4.8	12.9 ± 3.3
$N_{\gamma Pb}$	17 ± 7.0	13.5 ± 7.01	23.0 ± 9.5	16.2 ± 9.4
$N_{Nonexclusive}$	0 ± 0	46.4 ± 2.5	26.0 ± 1.1	8.74 ± 0.43
$N_{Exclusive}$	238 ± 18	375 ± 23	486 ± 26	353 ± 22
$\varepsilon_{J/\psi}$	0.504 ± 0.0176	0.504 ± 0.0176	0.504 ± 0.0176	0.504 ± 0.0176
A	0.1123 ± 0.0008	0.1238 ± 0.0007	0.1123 ± 0.0008	0.1238 ± 0.0007
$B.R$	0.0593	0.0593	0.0593	0.0593
$L_{int}(nb^{-1})$	13.92	13.92	18.83	18.83
Δy	0.5	0.5	0.5	0.5

Table 9.3: Summary of the number of events and various backgrounds for the four datasets, pPb and Pbp at forward and backward rapidity. The efficiencies, acceptances and luminosities are also shown. Note that the acceptance is a function of p_T and only an average value is listed here.

System	$\langle p_T \rangle$ (MeV/c)
Pbp y=-2.05	$429 \pm 25 \pm 4$
pPb y=+2.05	$434 \pm 21 \pm 7$
pPb y=-2.05	$532 \pm 21 \pm 16$
Pbp y=+2.05	$508 \pm 23 \pm 5$
(pPb + Pbp) y+	$431 \pm 17 \pm 4$
(pPb + Pbp) y-	$518 \pm 16 \pm 7$

Table 9.4: The $\langle p_T \rangle$ for pPb and Pbp at forward and backward rapidity. The first error is the statistical uncertainty and the second error is from the p_T-dependent systematic uncertainties.

two Gaussian curves centered around $y = \pm 2.05$ with widths 0.15. Rewriting Equation 9.8 gives

$$W_{\gamma p} = \sqrt{2E_p M_{J/\psi}} e^{-y/2}. \tag{9.9}$$

Differentiating with respect to y gives the dependence of W upon y,

$$\frac{dW_{\gamma p}}{dy} = -\frac{W_{\gamma p}}{2} \tag{9.10}$$

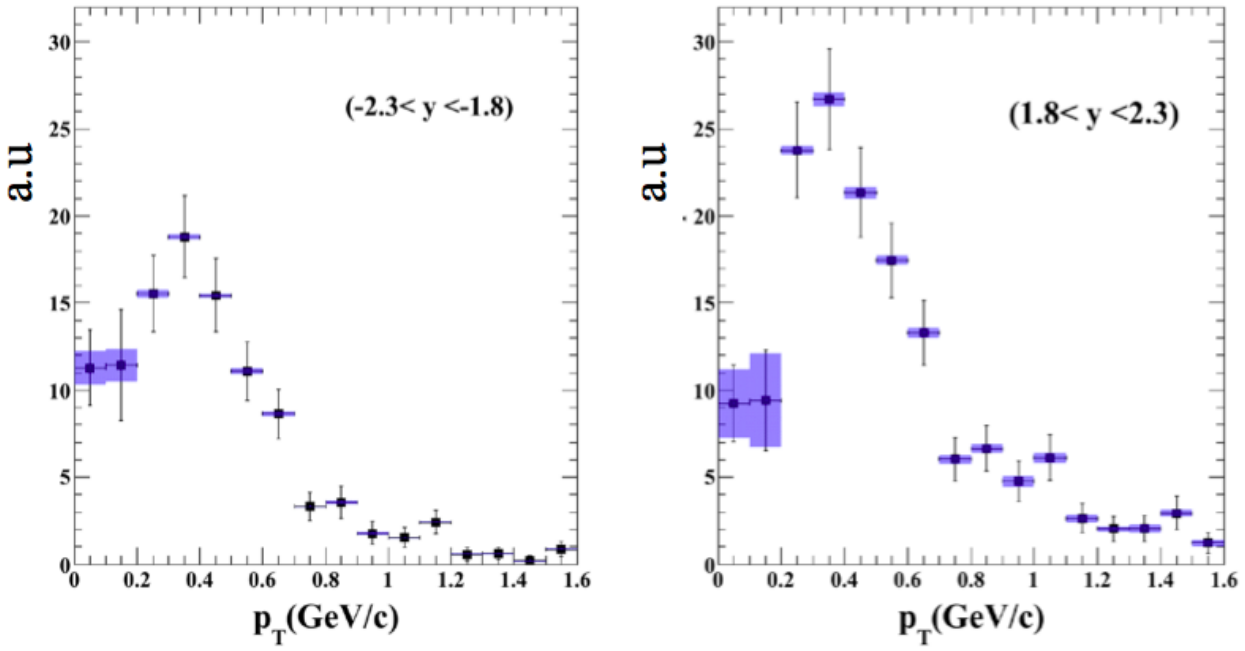

Figure 9.2: $\frac{d\sigma}{dydp_T}$ versus p_T for all events (Pbp and flipped pPb). Left : backward rapidity. Right: forward rapidity. The black markers represent the statistical errors and the blue boxes represent the local systematic errors.

Bjorken-x is related to $W_{\gamma p}$ by

$$x = (\frac{M_{J/\psi}}{W_{\gamma p}})^2 \tag{9.11}$$

$$x = \frac{M_{J/\psi}}{2E_p} e^y \tag{9.12}$$

Differentiating Eq. 9.12 with respect to y gives

$$\frac{dx}{dy} = x. \tag{9.13}$$

Equations 9.9, 9.10, 9.12 and 9.13 were used to calculate the values of W and x as well as their uncertainties. These values are listed in Table 9.5.

	Negative rapidity	Positive rapidity
$\langle y \rangle$	-2.05 $\pm$ .15	+2.05 $\pm$ .15
W	439 $\pm$ 32 GeV	56.5 $\pm$ 4.2 GeV
x	$(4.98 \pm .37)10^{-5}$	$(3.01 \pm .22)10^{-3}$
$k\frac{dN_\gamma}{dk}$	29.5 $\pm$ 2.7	158 $\pm$ 3

Table 9.5: Values of mean rapidity, W, and Bjorken-x and photon flux at negative and positive rapidity.

Chapter 10

Results and Summary

10.1 PbPb results

CMS and ALICE have both studied photoproduction of J/ψ mesons in ultra-peripheral PbPb collisions [28, 30, 33]. The CMS and ALICE results at $\sqrt{s_{NN}} = 2.76$ TeV are shown in Figure 10.1 along with theoretical predictions. The results strongly favor gluon shadowing in the lead nucleus. This thesis extends these studies to include both coherent and incoherent photoproduction of J/ψ in PbPb collisions in coincidence with neutron production. Figure 10.2 shows the ratio of the p_T distribution of J/ψs accompanied by neutrons emitted in the opposite direction to the p_T distribution of J/ψs accompanied by neutrons emitted in the same direction. This ratio depends strongly upon p_T. For $p_T < 100$ MeV/c where the spectra are dominated by coherent production, the ratio is close to one while for $p_T > 100$ MeV/c, where incoherent production dominates, the ratio falls to around 0.2.

In PbPb collisions the photon may be emitted from either nucleus. At forward rapidity this leads to a two-fold ambiguity in understanding the photon energy since, although the mass and rapidity constrain the energy of the photon and the parton with which it interacts, the direction of the photon is unknown. If the target nucleus breaks up when the J/ψ is created then there will be a correlation between the direction of the J/ψ and the neutron. Such an interaction is shown in Figure 5.1. This is expected to be the case when a photon interacts incoherently with a single proton in the nucleus to form a high p_T J/ψ. Although the neutron may be emitted in any direction in the rest frame of the target the extreme boost at the LHC energies means the neutron will end up in the ZDC detector on the side that is being approached by the target nucleus. Photons with wavelength

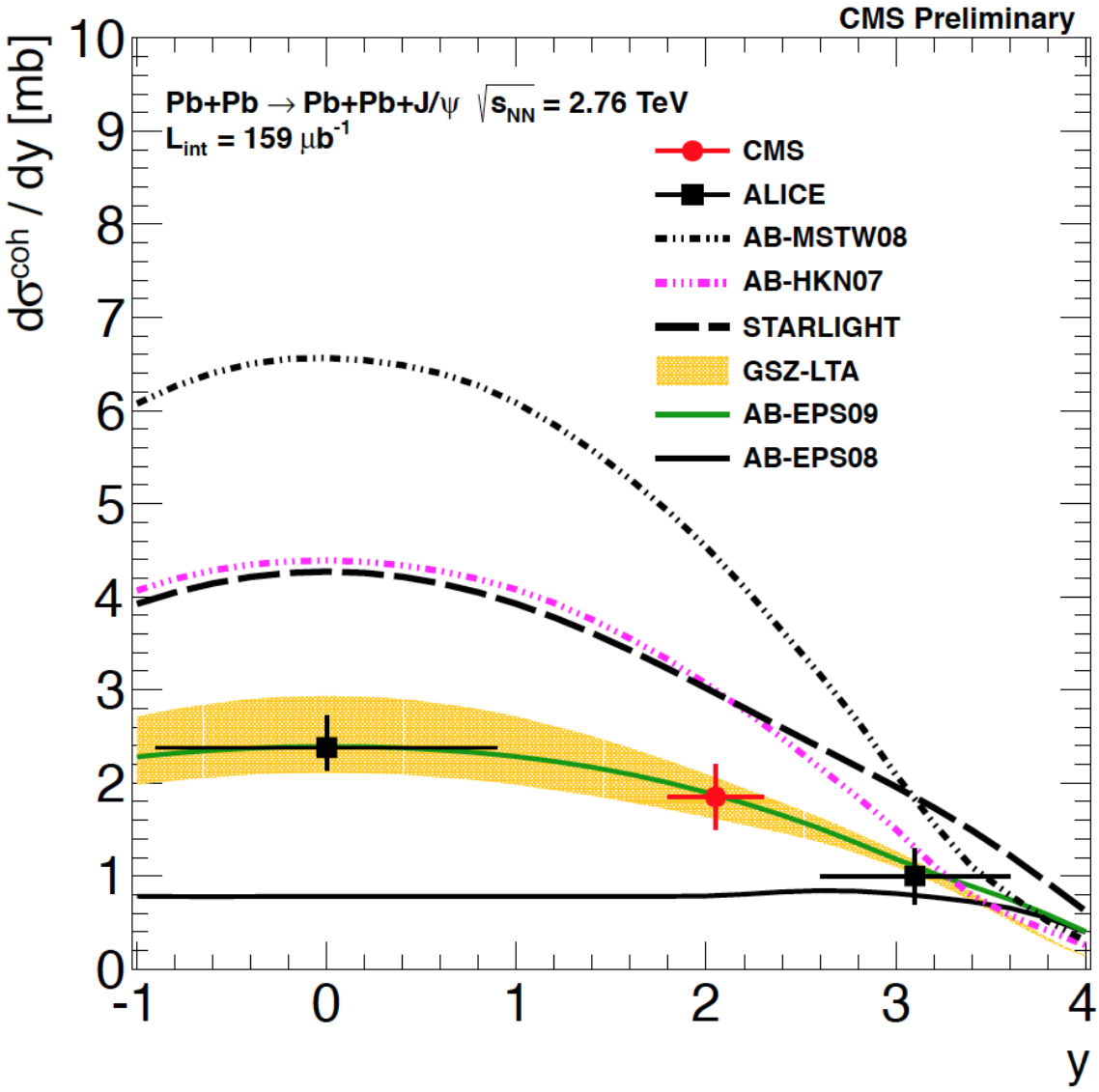

Figure 10.1: Cross section for coherent exclusive J/ψ production versus rapidity in ultraperipheral PbPb collisions at $\sqrt{s_{NN}} = 2.76$ TeV from CMS and ALICE compared to theoretical calculations [30].

of order of the nuclear radius, i.e, $p_T < 100$ MeV/c, are emitted and absorbed coherently by the two nuclei. Since the transverse momentum of the photon is so low and is distributed to the nucleus as a whole it is likely that the nucleus will stay intact. For neutron emission to occur it is then necessary that a second photon be exchanged between the two nuclei. This photon produces a Giant Dipole Resonance in the nucleus, which results in neutron emission. Since this second photon may strike

either nucleus, the direction of the neutron is not correlated to that of the J/ψ. This process is shown in Figure 5.2.

For $p_T > 100$ MeV/c, it is clear from Figure 10.2 that the J/ψ and neutron directions are correlated. This means that the neutron direction can be determined and the Bjorken x calculated. The ratio in Figure 10.2 depends upon the ratio of the gluon densities at $x = 1.8\ 10^{-4}$ to those at $x = 8.7\ 10^{-3}$. The figure also shows theoretical calculations from the leading twist approximation in the LTA model[37] for J/ψ production over a range of p_T. This model contains significant shadowing in the lead nucleus that is stronger at lower x. The model is at least in qualitative agreement with the data.

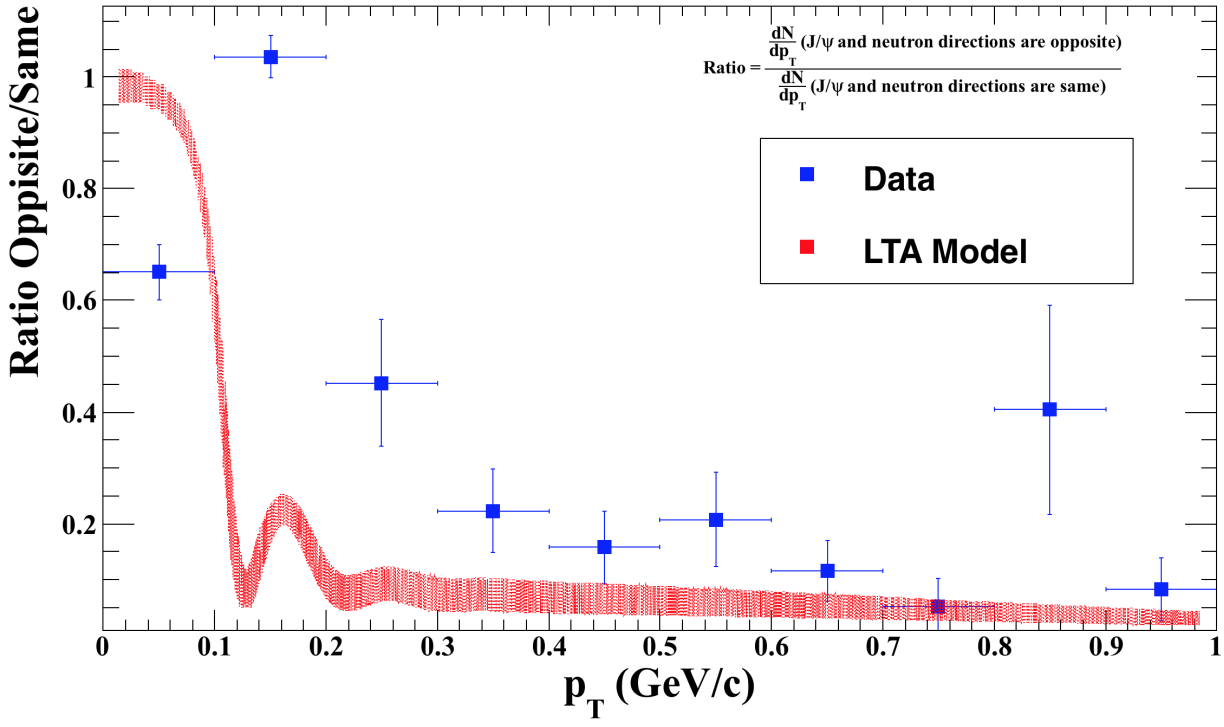

Figure 10.2: The ratio of the p_T distributions of J/ψ is that are accompanied by neutrons emitted in the opposite direction to those where the neutron is the same direction. The center of mass energy is $\sqrt{s_{NN}} = 2.76$ TeV and the rapidity of the J/ψ is in the region $1.8 < |y| < 2.3$. The data are in blue while red represents calculations using the leading twist approximation in the LTA model [37]. The theoretical calculations have not been convoluted with the p_T resolution of CMS. This resolution is of order 30 MeV/c.

10.2 pPb results

For the photoproduction of vector mesons it is expected that the cross section should have the form

$$\frac{d\sigma}{dt} = \frac{d\sigma}{dt}\bigg|_{t=0} |F(t)|^2 \tag{10.1}$$

where $t = -p_T^2$ and $F(t)$ is known as the form factor. The form factor is given by the Fourier transform of the proton density. At HERA, $F(t)$ was found to have an exponential form

$$|F(t)|^2 = e^{-b|t|}. \tag{10.2}$$

with b $\approx 4\ GeV^{-2}c^2$. For such a distribution it follows that

$$\frac{d\sigma}{dp_T dy} = \frac{d\sigma}{dy} \cdot b \cdot 2p_T \cdot e^{-b \cdot {p_T}^2}. \tag{10.3}$$

Equation 10.3 implies that b is related to the mean p_T by

$$b = \frac{\pi}{4} \cdot \frac{1}{\langle p_T \rangle^2}. \tag{10.4}$$

The values of $\langle p_T \rangle$ and b deduced from the spectra shown in Figure 10.3 are listed in Table 10.1. Curves based on these values and Equation 10.3 are shown in Figure 10.3. As the photon-proton center of mass energy W increases $\langle p_T \rangle$ decreases and b increases. The average of the two values of b is close to the HERA estimate of $b = 4$ GeV$^{-2}/c^2$.

Figure 10.3 shows $\frac{d\sigma}{dydp_T}$ versus p_T. It is clear that the yield of J/ψ mesons is greater at forward rapidity, than at backward rapidity. The integral of these spectra is $\frac{d\sigma}{dy}$ while the mean is $\langle p_T \rangle$ The values of $\langle p_T \rangle$ are shown in Table 10.1. Both $\frac{d\sigma}{dy}$ and $\langle p_T \rangle$ increase with rapidity.

Figure 10.4 shows the cross section arbitrary unit for photoproduction of J/ψ mesons versus center of mass energy $W_{\gamma p}$. The CMS results $\sigma_{\gamma p}$ increases with W. The rate of increase with W for CMS and ALICE is similar but the CMS results are significantly above those of ALICE.

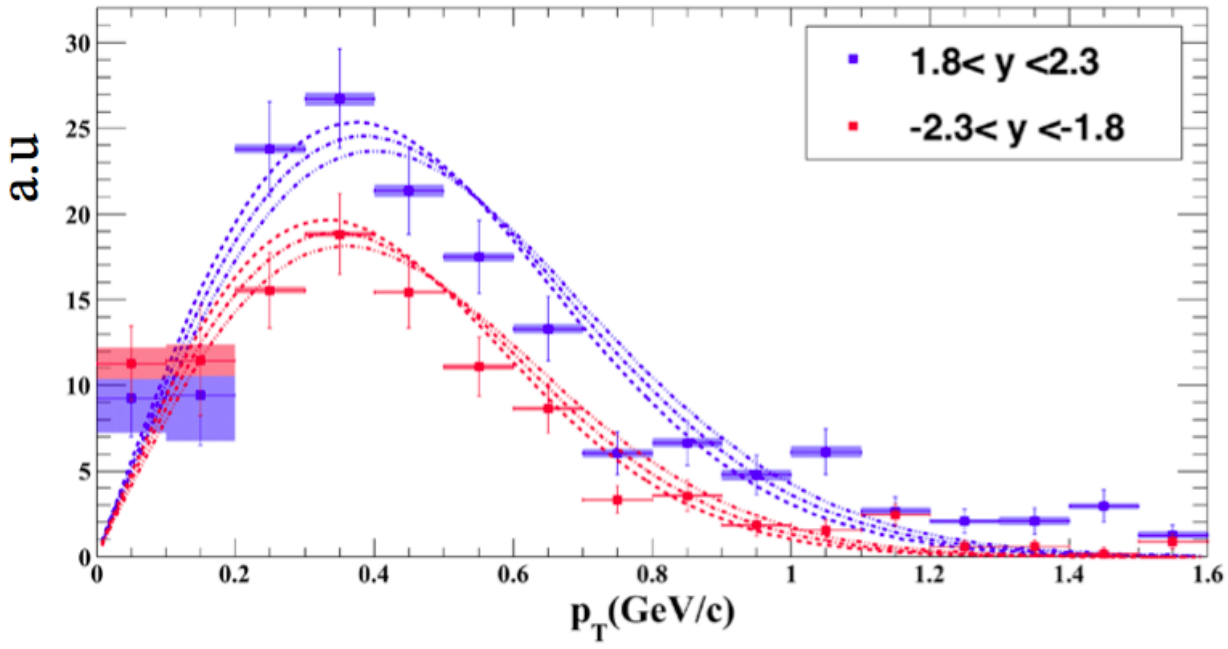

Figure 10.3: $\frac{d\sigma}{dydp_T}$ versus p_T for backward rapidity (red) and forward rapidity (blue). The markers represent the statistical errors, the boxes represent the local systematic errors. The systematic errors on the normalization are estimated to be 6.1%, as shown in Table 9.1. The curves represent fits to the spectra using the form found in Equation 10.3. For each rapidity three curves are shown. The central curve corresponds to the best fit while the other two curves show the effect of changing b by one standard deviation.

	W (GeV)	$\langle x \rangle$	$\langle p_T \rangle$ (MeV/c)	b GeV$^{-2}/c^2$
$y-$	439 ± 32	$(5.0 \pm 0.4)10^{-5}$	$431 \pm 17 \pm 4$	$4.23 \pm .33 \pm .08$
$y+$	56.5 ± 4.2	$(3.0 \pm 0.2)10^{-3}$	$518 \pm 16 \pm 7$	$3.37 \pm .20 \pm .09$

Table 10.1: Values for $\langle \mathrm{W} \rangle$, $\langle x \rangle$, $\langle p_T \rangle$, and b for at forward and backward rapidity. The errors on $\langle \mathrm{W} \rangle$ and $\langle x \rangle$, come from the distribution of events in rapidity. For $\frac{d\sigma}{dy}$ the first error is the statistical uncertainty, the second error is from the p_T dependent systematic uncertainties, and the third error is from the systematic uncertainty on the normalization of the spectra. This normalization uncertainty does not affect $\langle p_T \rangle$ or the inverse slope of the t distribution, b.

The ALICE results are consistent with data from HERA and so there is probably an uncorrected problem with the normalization of the CMS results. Because of the strong magnetic field of CMS the acceptance of the experiment for J/ψ at low p_T is quite small ($\approx 11\%$). This makes the acceptance correction particularly sensitive to the polarization of the J/ψ.

The study of exclusive photo-production of the heavy vector mesons J/ψ, $\psi(2s)$ and Υ began

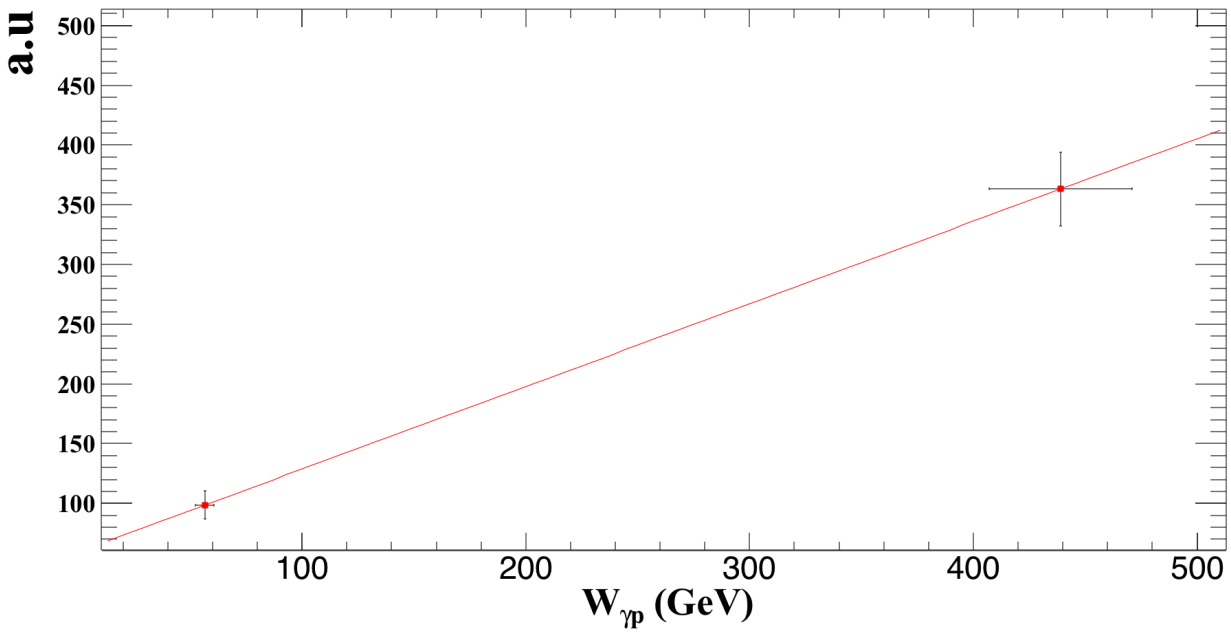

Figure 10.4: Cross section arbitrary unit of the photoproduction of J/ψ versus center of mass energy $W_{\gamma p}$ for CMS.

with fixed target experiments E401, E516, and E687 at FNAL in the 1980s [111–114]. These experiments covered values of $W_{\gamma p}$ in the range 10-20 GeV. Later the H1 and ZEUS experiments at the HERA ep collider and CDF at the Tevatron $(p\bar{p})$ collider extended the these measurements to values of W up to 400 GeV [96], [52], [115], [116], [94]. In reference [93] the authors of STARLIGHT fit these data to the form

$$\sigma(\gamma + p \to V + p) = \sigma_P \cdot \left[1 - \frac{(m_p + m_V)^2}{W_{\gamma p}^2}\right]^2 \cdot W_{\gamma p}^{\delta}, \tag{10.5}$$

where m_p and m_V are the masses of the proton and vector meson, respectively. In Equation 10.5 the power law controls the high energy growth of the cross section and the term in the square brackets describes the behavior near the kinematic threshold. In STARLIGHT δ is taken to be 0.65 for J/ψ and $\psi(2s)$ and 0.74 for the Υ family. Note for $W_{\gamma p} = 50$ GeV the threshold term in Equation 10.5 decreases the cross section by only 1.1% and so high energy data are typically fit to a simpler version of Eqn. 10.5, i.e,

$$\sigma(\gamma + p \to V + p) = a \cdot W_{\gamma p}^{\delta}. \tag{10.6}$$

When the LHC turned on measurements of the photoproduction of exclusive J/ψ were pushed up to W = 700 GeV by ALICE [33] and W = 2,000 GeV by LHCb [32, 117]. Figure 10.5 shows a compilation of data made by the LHCb experiment [117]. LHCb measures $d\sigma/dy$ for exclusive J/ψ mesons produced in pp collisions at $\sqrt{s} = 7$ and 13 TeV. Because pp collisions are symmetric it is not possible to know the direction of the photon. This is a problem since collisions at low and high W can contribute to the J/ψ yield at a particular rapidity. LHCb assumes that the low energy part of the cross section is given by a power law, i.e. $\sigma(W) \propto W^{\delta}$. They then use this constraint to subtract the low W part from $d\sigma/dy$ and so measure the high energy part of the cross section. This is another reason why it is very important to measure δ accurately.

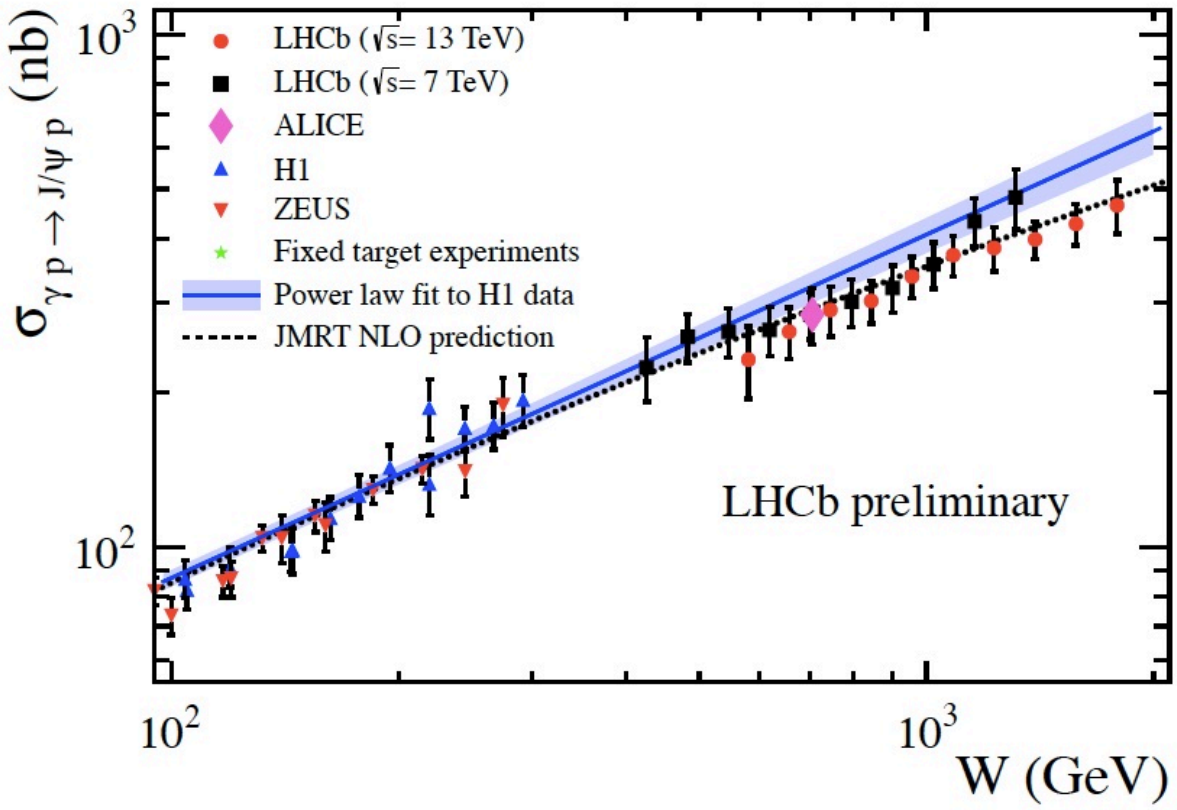

Figure 10.5: Cross section for the photoproduction of J/ψ mesons $\sigma(\gamma p \to J/\psi p)$ versus center-of-mass energy $W_{\gamma p}$ for several experiments.

Assuming a power law dependence as in Equation 10.6 the CMS data gives

$$\delta_{\mathrm{CMS}} = 0.636 \pm .053(\mathrm{stat}) \pm 0.013(\mathrm{sys}) \pm 0.001(\mathrm{norm}). \pm 0.032.(\mathrm{photon\ flux}) \qquad (10.7)$$

Here the first error comes from the statistical error on the cross sections, the second term is due to the point-by-point systematic errors on the spectra, the third term is due to the overall normalization errors on the cross sections and the forth term reflects the error on the photon flux estimated by STARLIGHT. Adding these terms in quadrature and following the CMS convention of keeping two digits for the error gives $\delta_{\mathrm{CMS}} = 0.636 \pm 0.063$. Figure 10.6 shows the values of δ obtained from H1 [52], ZEUS [53], ALICE [33], CMS, CDF [54] and LHCb [32]. For reference, the values are listed in Table 10.2. Before averaging the results it is important to realize that CMS and ALICE have a correlated error in the photon flux, since both use the same calculation from STARLIGHT. Taking this into account yields

$$\delta_{\mathrm{CMS+ALICE}} = 0.660 \pm .037(\mathrm{stat+sys}) \pm 0.032(\mathrm{photon\ flux}) \tag{10.8}$$

This gives $\delta_{\mathrm{CMS+ALICE}} = 0.660 \pm .054$. Note that the error from the photon flux is comparable to the combined statistical and systematic errors or the two experiments. Figure 10.6 shows that the CMS result is very consistent with the world data. Averaging H1, ZEUS, ALICE and CMS gives

$$\delta_{\mathrm{world}} = 0.674 \pm .022 \tag{10.9}$$

The CDF point was not published by the collaboration but deduced from a model fit by theorists [54]. For this reason that value was not used in the calculation of the average. The LHCb collaboration has recently published an updated analysis of their pp data at $\sqrt{s} = 7$ TeV [117] in which they claim that their results are consistent with the HERA parametrization. In this paper they do not derive a value of δ and so the result form their earlier paper [32] was also not used in the calculation of the average.

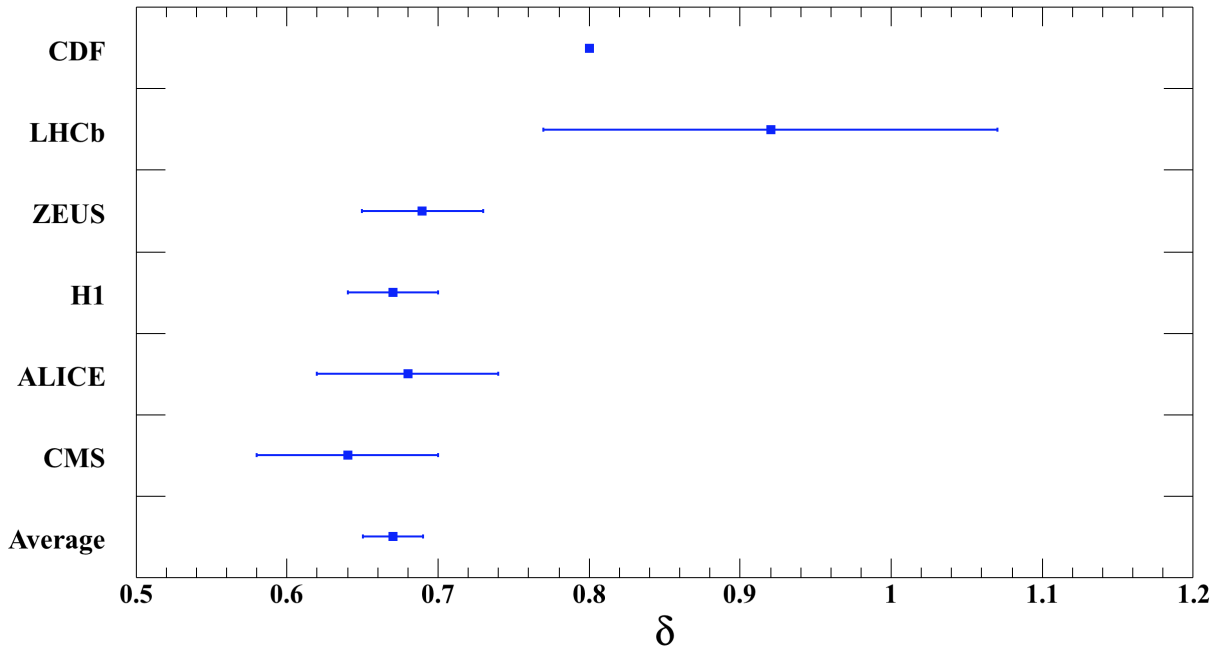

Figure 10.6: The parameter δ which represents the exponent of the cross section center of mass energy $W_{\gamma p}$ based on data from H1 [52], ZEUS [53], ALICE [33], CMS, CDF [54] and LHCb [32]. The statistical, systematic and theoretical errors have been added in quadrature.

Experiment	δ
CDF	0.80 [54]
LHCb	0.92 ± 0.15 [32]
H1	0.67 ± 0.03 [52]
ZEUS	0.69 ± 0.04 [53]
ALICE	0.68 ± 0.06 [33]
CMS	0.636 ± 0.063
Average	0.674 ± 0.022

Table 10.2: The values of δ derived from several experiments. The statistical, systematic and theoretical errors have been added in quadrature. Only the H1, ZEUS, ALICE and CMS results were used to calculate the average. This calculation took into account the correlation in the error from the photon flux between CMS and ALICE.

10.3 Summary

These measurements study the high energy limit of QCD. The question of when the gluon density inside a hadron becomes saturated is one of the most important goals of heavy ion physics. At very low values of Bjorken x it is expected that the gluons will form a new state of matter known as the

Color Glass Condensate. The detection and study of the Color Glass Condensate is one of the main goals of the proposed Electron Ion Collider. Until such a machine is built the photon production of vector mesons in ultra-peripheral, i.e., electromagnetic, collisions is one of the best ways to probe the density of gluons inside hadrons.

For ultra-peripheral lead PbPb collisions at $\sqrt{s_{NN}} = 2.76$ TeV, the data from the coherent production of J/ψ clearly show an effect of gluon shadowing. In such data it is not possible to tell the direction of the photon, but for incoherent collisions, i.e., where the J/ψ has $p_T > 100$ MeV/c the correlation between the directions of the J/ψ and the neutron allows the photon direction to be determined. Models incorporating gluon shadowing in the lead nucleus are able to fit these data. Inside a nucleus, the gluons from many difference nucleons can interact and merge and so it is expected that effects such as gluon shadowing or saturation should be visible at lower energies for photon-nucleus collisions as compared to photon-proton collisions. This boost factor has been roughly estimated to be $A^{1/6}$ where A is the atomic number of the nucleus. For lead this gives a value of 2.4. This suggests that for $W_{\gamma p}$ values above 1 TeV or so gluon recombination and suppression effects may become important.

For ultra-peripheral lead pPb collisions at $\sqrt{s_{NN}} = 5.02$ TeV, this thesis has reported on the photoproduction of exclusive J/ψ mesons for $W_{\gamma p} = 57$ and 439 GeV. The p_T spectra are consistent with the functional form found at HERA but with an exponent b that increases with $W_{\gamma p}$. For $W_{\gamma p}$ between 20 and 700 GeV the cross section for $\gamma p \to J/\psi + p$ increases with $W_{\gamma p}$ as a power law, i.e. $\sigma(W) \propto W^{\delta}$. In order to determine if new effects are present for $W_{\gamma p}$ values in the TeV region it is very important to measure δ precisely. The value of δ derived from these data has a precision that is comparable to the H1, ZEUS, and ALICE experiments.

The ALICE and CMS results make it clear that the LHC is an excellent facility for studying photon-nucleus and photon-proton collisions. This is important since it is unlikely that an Electron Ion Collider can be operational before 2030. In November of 2016, the LHC produced proton-lead collision with $\sqrt{s_{NN}} = 8.0$ TeV. During this run CMS collected more than 10 times the number of exclusive J/ψ than were available for this analysis. These data will allow a precise mapping of

the proton form factor and the energy dependence of the photoproduction of J/ψ, $\psi(2s)$ and the Υ states. To fully exploit such data it will also be important to improve the theoretical description of ultra-peripheral collisions. In particular it will be important to calibrate the “luminosity" of photons. This could possible by done by precisely measuring $\gamma\gamma \to e^+e-$ and $\gamma\gamma \to \mu^+\mu^-$.

Bibliography

[1] Universe expansion. [http://www2.lbl.gov/abc/wallchart/chapters/10/0.html].

[2] Experiments of large hadron collider. [https://cds.cern.ch/record/841555/files/lhc-pho-1998-349.jpg].

[3] The expansion of the universe and the experiment's role. [https://www.uni-giessen.de/fbz/fb07/fachgebiete/physik/einrichtungen/theorie/heavy-ions].

[4] A. K. Chaudhuri. *A short course on Relativistic Heavy Ion Collisions*. IOPP, 2014.

[5] Siegfried Bethke. Experimental tests of asymptotic freedom. *Prog. Part. Nucl. Phys.*, 58:351–386, 2007.

[6] Tapan K. Nayak. Heavy Ions: Results from the Large Hadron Collider. *Pramana*, 79:719–735, 2012.

[7] Jaroslav Adam et al. Differential studies of inclusive J/ψ and ψ(2S) production at forward rapidity in Pb-Pb collisions at $\sqrt{s_{\rm NN}} = 2.76$ TeV. *JHEP*, 05:179, 2016.

[8] Wei Xie. Heavy flavor Production and Interactions in Relativistic Heavy-Ion Collisions in CMS Experiment. *J. Phys. Conf. Ser.*, 779(1):012002, 2017.

[9] Serguei Chatrchyan et al. Azimuthal anisotropy of charged particles at high transverse momenta in PbPb collisions at $\sqrt{s_{NN}} = 2.76$ TeV. *Phys. Rev. Lett.*, 109:022301, 2012.

[10] K Aamodt et al. Elliptic flow of charged particles in Pb-Pb collisions at 2.76 TeV. *Phys. Rev. Lett.*, 105:252302, 2010.

[11] A. Andronic et al. Excitation function of elliptic flow in Au+Au collisions and the nuclear matter equation of state. *Phys. Lett.*, B612:173–180, 2005.

[12] Georges Aad et al. Measurement of charged-particle spectra in Pb+Pb collisions at $\sqrt{s_{\mathrm{NN}}} =$ 2.76 TeV with the ATLAS detector at the LHC. *JHEP*, 09:050, 2015.

[13] Serguei Chatrchyan et al. Study of high-pT charged particle suppression in PbPb compared to pp collisions at $\sqrt{s_{NN}} = 2.76$ TeV. *Eur. Phys. J.*, C72:1945, 2012.

[14] Betty Abelev et al. Centrality Dependence of Charged Particle Production at Large Transverse Momentum in Pb–Pb Collisions at $\sqrt{s_{\mathrm{NN}}} = 2.76$ TeV. *Phys. Lett.*, B720:52–62, 2013.

[15] B. Abelev et al. Measurement of charged jet suppression in Pb-Pb collisions at $\sqrt{s_{NN}} = 2.76$ TeV. *JHEP*, 03:013, 2014.

[16] Jaroslav Adam et al. Centrality dependence of high-p_T D meson suppression in Pb-Pb collisions at $\sqrt{s_{\mathrm{NN}}} = 2.76$ TeV. *JHEP*, 11:205, 2015.

[17] C. Gwenlan. Combined HERA Deep Inelastic Scattering Data and NLO QCD Fits. *Nucl. Phys. Proc. Suppl.*, 191:5–15, 2009.

[18] Larry McLerran. RHIC physics: The Quark gluon plasma and the color glass condensate: Four lectures. 2003.

[19] Edmond Iancu. QCD in heavy ion collisions. In *Proceedings, 2011 European School of High-Energy Physics (ESHEP 2011): Cheile Gradistei, Romania, September 7-20, 2011*, pages 197–266, 2014.

[20] Francois Gelis. The initial stages of heavy-ion collisions in the colour glass condensate framework. *Pramana*, 84(5):685–701, 2015.

[21] K. J. Eskola, H. Paukkunen, and C. A. Salgado. EPS09: A New Generation of NLO and LO Nuclear Parton Distribution Functions. *JHEP*, 04:065, 2009.

[22] K. J. Eskola, V. J. Kolhinen, and P. V. Ruuskanen. Scale evolution of nuclear parton distributions. *Nucl. Phys.*, B535:351–371, 1998.

[23] K. J. Eskola, V. J. Kolhinen, and C. A. Salgado. The Scale dependent nuclear effects in parton distributions for practical applications. *Eur. Phys. J.*, C9:61–68, 1999.

[24] Kari J. Eskola, Hannu Paukkunen, and Carlos A. Salgado. An Improved global analysis of nuclear parton distribution functions including RHIC data. *JHEP*, 07:102, 2008.

[25] D. de Florian and R. Sassot. Nuclear parton distributions at next-to-leading order. *Phys. Rev.*, D69:074028, 2004.

[26] M. Hirai, S. Kumano, and T. H. Nagai. Determination of nuclear parton distribution functions and their uncertainties in next-to-leading order. *Phys. Rev.*, C76:065207, 2007.

[27] Adeola Adeluyi and C. A. Bertulani. Constraining Gluon Shadowing Using Photoproduction in Ultraperipheral pA and AA Collisions. *Phys. Rev.*, C85:044904, 2012.

[28] E. Abbas et al. Charmonium and e^+e^- pair photoproduction at mid-rapidity in ultra-peripheral Pb-Pb collisions at $\sqrt{s_{NN}}$=2.76 TeV. *Eur. Phys. J.*, C73(11):2617, 2013.

[29] Jaroslav Adam et al. Coherent ρ^0 photoproduction in ultra-peripheral Pb-Pb collisions at $\sqrt{s_{\rm NN}} = 2.76$ TeV. *JHEP*, 09:095, 2015.

[30] Vardan Khachatryan et al. Coherent J/Psi photoproduction in ultra-peripheral PbPb collisions at sqrt(s[NN]) = 2.76 TeV with the CMS experiment. *Submitted to: Phys. Lett. B*, 2016.

[31] Adeola Adeluyi, C. A. Bertulani, and M. J. Murray. Nuclear effects in photoproduction of heavy quarks and vector mesons in ultraperipheral PbPb and pPb collisions at the LHC. *Phys. Rev.*, C86:047901, 2012.

[32] R Aaij et al. Exclusive J/ψ and ψ(2S) production in pp collisions at $\sqrt{s} = 7$ TeV. *J. Phys.*, G40:045001, 2013.

[33] Betty Bezverkhny Abelev et al. Exclusive J/ψ photoproduction off protons in ultra-peripheral p-Pb collisions at $\sqrt{s_{\rm NN}} = 5.02$ TeV. *Phys. Rev. Lett.*, 113(23):232504, 2014.

[34] S. Afanasiev et al. Photoproduction of J/psi and of high mass e+e- in ultra-peripheral Au+Au collisions at s**(1/2) = 200-GeV. *Phys. Lett.*, B679:321–329, 2009.

[35] Betty Abelev et al. Coherent J/ψ photoproduction in ultra-peripheral Pb-Pb collisions at $\sqrt{s_{NN}} = 2.76$ TeV. *Phys. Lett.*, B718:1273–1283, 2013.

[36] V. Guzey, E. Kryshen, M. Strikman, and M. Zhalov. Evidence for nuclear gluon shadowing from the ALICE measurements of PbPb ultraperipheral exclusive J/ψ production. *Phys. Lett.*, B726:290–295, 2013.

[37] V. Guzey, M. Strikman, and M. Zhalov. Disentangling coherent and incoherent quasielastic J/ψ photoproduction on nuclei by neutron tagging in ultraperipheral ion collisions at the LHC. *Eur. Phys. J.*, C74(7):2942, 2014.

[38] Lhc map. [http://area-map.web.cern.ch/area-map/AreaMap.html].

[39] Cms view. [https://cds.cern.ch/record/1626816/plots].

[40] Cms slice. [http://www.thestargarden.co.uk/History-of-CERN.html].

[41] *The CERN Large Hadron Collider: Accelerator and Experiments*. CERN, Geneva, 2009.

[42] S Chatrchyan et al. Precise Mapping of the Magnetic Field in the CMS Barrel Yoke using Cosmic Rays. *JINST*, 5:T03021, 2010.

[43] Serguei Chatrchyan et al. Description and performance of track and primary-vertex reconstruction with the CMS tracker. *JINST*, 9:P10009, 2014.

[44] A. Dominguez, D. Abbaneo, K. Arndt, N. Bacchetta, A. Ball, E. Bartz, W. Bertl, G. M. Bilei, G. Bolla, H. W. K. Cheung, et al. CMS Technical Design Report for the Pixel Detector Upgrade. 2012.

[45] Addendum to the CMS ECAL technical design report: Changes to the CMS ECAL electronics. 2002.

[46] Min Suk Kim. CMS reconstruction improvement for the muon tracking by the RPC chambers. *PoS*, RPC2012:045, 2012. [JINST8,T03001(2013)].

[47] S Chatrchyan et al. Performance of the CMS Drift Tube Chambers with Cosmic Rays. *JINST*, 5:T03015, 2010.

[48] CMS, the Compact Muon Solenoid. Muon technical design report. 1997.

[49] Zdc location. [https://image2.slideserve.com/4791983/description-of-zdc-n.jpg].

[50] Oleg A. Grachov, M. J. Murray, A. S. Ayan, P. Debbins, E. Norbeck, Y. Onel, and David G. d'Enterria. Status of zero degree calorimeter for CMS experiment. *AIP Conf. Proc.*, 867:258–265, 2006. [,258(2006)].

[51] V. Halyo, A. Hunt, P. Jindal, P. LeGresley, and P. Lujan. GPU Enhancement of the Trigger to Extend Physics Reach at the LHC. *JINST*, 8:P10005, 2013.

[52] C. Alexa et al. Elastic and Proton-Dissociative Photoproduction of J/ψ Mesons at HERA. *Eur. Phys. J.*, C73(6):2466, 2013.

[53] S. Chekanov et al. Exclusive photoproduction of J/ψ mesons at HERA. *Eur. Phys. J.*, C24:345–360, 2002.

[54] L. Motyka and G. Watt. Exclusive photoproduction at the Tevatron and CERN LHC within the dipole picture. *Phys. Rev.*, D78:014023, 2008.

[55] Crystal ball function. [https://en.wikipedia.org/wiki/CrystalBallfunction].

[56] J. A. Crittenden. Exclusive production of neutral vector mesons at the electron - proton collider HERA. 1997.

[57] Ramona Vogt. *Ultrarelativistic heavy-ion collisions*. Elsevier, Amsterdam, 2007.

[58] Lawrence W. Jones. A Review of Quark Search Experiments. *Rev. Mod. Phys.*, 49:717, 1977.

[59] Roel Aaij et al. Observation of J/ψ p Resonances Consistent with Pentaquark States in $\Lambda_b^0 \to J/\psi K^- p$ Decays. *Phys. Rev. Lett.*, 115:072001, 2015.

[60] T. Matsui and H. Satz. J/ψ Suppression by Quark-Gluon Plasma Formation. *Phys. Lett.*, B178:416–422, 1986.

[61] N. Armesto and E. Scomparin. Heavy-ion collisions at the Large Hadron Collider: a review of the results from Run 1. *Eur. Phys. J. Plus*, 131(3):52, 2016.

[62] S. Voloshin and Y. Zhang. Flow study in relativistic nuclear collisions by Fourier expansion of Azimuthal particle distributions. *Z. Phys.*, C70:665–672, 1996.

[63] J. Adams et al. Transverse momentum and collision energy dependence of high p(T) hadron suppression in Au+Au collisions at ultrarelativistic energies. *Phys. Rev. Lett.*, 91:172302, 2003.

[64] Jerome I. Friedman and Henry W. Kendall. Deep inelastic electron scattering. *Ann. Rev. Nucl. Part. Sci.*, 22:203–254, 1972.

[65] R. Brandelik et al. Evidence for Planar Events in e+ e- Annihilation at High-Energies. *Phys. Lett.*, B86:243–249, 1979.

[66] Yuri V. Kovchegov and Eugene Levin. *Quantum chromodynamics at high energy*, volume 33. Cambridge University Press, 2012.

[67] M. Arneodo et al. Shadowing in Deep Inelastic Muon Scattering from Nuclear Targets. *Phys. Lett.*, B211:493–499, 1988.

[68] Enrico Fermi. On the theory of collisions between atoms and electrically charged particles. *Nuovo Cim.*, 2:143–158, 1925. [,243(1925)].

[69] C. F. von Weizsacker. Radiation emitted in collisions of very fast electrons. *Z. Phys.*, 88:612–625, 1934.

[70] V. P. Goncalves and C. A. Bertulani. Peripheral heavy ion collisions as a probe of the nuclear gluon distribution. *Phys. Rev.*, C65:054905, 2002.

[71] Carlos A. Bertulani and Gerhard Baur. Electromagnetic Processes in Relativistic Heavy Ion Collisions. *Phys. Rept.*, 163:299, 1988.

[72] Gerhard Baur, Kai Hencken, Dirk Trautmann, Serguei Sadovsky, and Yuri Kharlov. Coherent gamma gamma and gamma-A interactions in very peripheral collisions at relativistic ion colliders. *Phys. Rept.*, 364:359–450, 2002.

[73] J. Reinhardt and W. Greiner. Theoretical aspects of quantum electrodynamics in strong fields. *Lect. Notes Phys.*, 440:153–194, 1994.

[74] Gerhard A. Schuler and Torbjörn Sjöstrand. A scenario for high-energy $\gamma\gamma$ interactions. *Zeitschrift für Physik C Particles and Fields*, 73(4):677–688, Dec 1997.

[75] Gerhard A. Schuler and Torbjorn Sjostrand. Towards a complete description of high-energy photoproduction. *Nucl. Phys.*, B407:539–605, 1993.

[76] Spencer R. Klein and Joakim Nystrand. Exclusive vector meson production in relativistic heavy ion collisions. *Phys. Rev. C*, 60:014903, Jun 1999.

[77] Anthony J. Baltz, Spencer R. Klein, and Joakim Nystrand. Coherent vector-meson photoproduction with nuclear breakup in relativistic heavy-ion collisions. *Phys. Rev. Lett.*, 89:012301, Jun 2002.

[78] Spencer R. Klein and Joakim Nystrand. Photoproduction of quarkonium in proton-proton and nucleus-nucleus collisions. *Phys. Rev. Lett.*, 92:142003, Apr 2004.

[79] Bruce Mellado. *Measurement of Diffractive Heavy Vector Meson Photoproduction at HERA with the ZEUS Detector*. PhD thesis, Columbia U., 2002.

[80] A. Donnachie and P.V. Landshoff. Total cross sections. *Physics Letters B*, 296(1):227 – 232, 1992.

[81] J. Breitweg et al. ZEUS results on the measurement and phenomenology of F(2) at low x and low Q**2. *Eur. Phys. J.*, C7:609–630, 1999.

[82] A. Donnachie and P.V. Landshoff. Small x: two pomerons! *Physics Letters B*, 437(3):408 – 416, 1998.

[83] J. G. Contreras and J. D. Tapia Takaki. Ultra-peripheral heavy-ion collisions at the LHC. *Int. J. Mod. Phys.*, A30:1542012, 2015.

[84] A. Cisek, W. Schafer, and A. Szczurek. Exclusive coherent production of heavy vector mesons in nucleus-nucleus collisions at LHC. *Phys. Rev.*, C86:014905, 2012.

[85] T. Lappi and H. Mantysaari. Incoherent diffractive J/Psi-production in high energy nuclear DIS. *Phys. Rev.*, C83:065202, 2011.

[86] T. Lappi and H. Mantysaari. $J/|psi$ production in ultraperipheral Pb+Pb and p+Pb collisions at energies available at the CERN Large Hadron Collider. *Phys. Rev.*, C87(3):032201, 2013.

[87] V. P. Goncalves and M. V. T. Machado. Vector Meson Production in Coherent Hadronic Interactions: An update on predictions for RHIC and LHC. *Phys. Rev.*, C84:011902, 2011.

[88] M. B. Gay Ducati, M. T. Griep, and M. V. T. Machado. Diffractive photoproduction of radially excited psi(2S) mesons in photon-Pomeron reactions in PbPb collisions at the CERN LHC. *Phys. Rev.*, C88:014910, 2013.

[89] Brian Foster. Low x physics. *Phil. Trans. Roy. Soc. Lond.*, A359:325–378, 2001.

[90] Adeola Adeluyi and Carlos Bertulani. Gluon distributions in nuclei probed at the CERN Large Hadron Collider. *Phys. Rev.*, C84:024916, 2011.

[91] A. D. Martin, W. J. Stirling, R. S. Thorne, and G. Watt. Parton distributions for the LHC. *Eur. Phys. J.*, C63:189–285, 2009.

[92] M. Hirai, S. Kumano, and T. H. Nagai. Nuclear parton distribution functions and their uncertainties. *Phys. Rev.*, C70:044905, 2004.

[93] Spencer R. Klein, Joakim Nystrand, Janet Seger, Yuri Gorbunov, and Joey Butterworth. STARlight: A Monte Carlo simulation program for ultra-peripheral collisions of relativistic ions. *Comput. Phys. Commun.*, 212:258–268, 2017.

[94] T. Aaltonen et al. Observation of exclusive charmonium production and $\gamma+\gamma$ to $\mu^+\mu^-$ in $p\bar{p}$ collisions at $\sqrt{s} = 1.96$ TeV. *Phys. Rev. Lett.*, 102:242001, 2009.

[95] L. Motyka and G. Watt. Exclusive photoproduction at the fermilab tevatron and cern lhc within the dipole picture. *Phys. Rev. D*, 78:014023, Jul 2008.

[96] A. Aktas et al. Elastic J/ψ production at HERA. *Eur. Phys. J.*, C46:585–603, 2006.

[97] S. Chekanov et al. Exclusive photoproduction of j/ψ mesons at hera. *The European Physical Journal C - Particles and Fields*, 24(3):345–360, Jul 2002.

[98] S. Chatrchyan et al. The CMS Experiment at the CERN LHC. *JINST*, 3:S08004, 2008.

[99] J. Man, J. Anderson, B. Dahmes, P. de Barbaro, J. Freeman, T. Grassi, E. Hazen, J. Mans, R. Ruchti, I. Schimdt, et al. CMS Technical Design Report for the Phase 1 Upgrade of the Hadron Calorimeter. 2012.

[100] S Chatrchyan et al. Performance of CMS Hadron Calorimeter Timing and Synchronization using Test Beam, Cosmic Ray, and LHC Beam Data. *JINST*, 5:T03013, 2010.

[101] V. Barashko, A. Drozdetskiy, A. Korytov, Guenakh Mitselmakher, and Yu. Pakhotin. Fast algorithm for track segment and hit reconstruction in the CMS cathode strip chambers. *Nucl. Instrum. Meth.*, A589:383–397, 2008.

[102] Salim Cerci and David d'Enterria. Low-x QCD studies with forward jets in proton-proton collisions at s**(1/2) = 14-TeV. *AIP Conf. Proc.*, 1105:28–32, 2009.

[103] Dmytro Volyanskyy. Physics Potential of the CMS CASTOR Forward Calorimeter. In *Physics at the LHC2010. Proceedings, 5th Conference, PLHC2010, Hamburg, Germany, June 7-12, 2010*, pages 421–423, 2010.

[104] Vardan Khachatryan et al. The CMS trigger system. *JINST*, 12(01):P01020, 2017.

[105] A. Tapper and Darin Acosta. CMS Technical Design Report for the Level-1 Trigger Upgrade. 2013.

[106] *CMS The TriDAS Project: Technical Design Report, Volume 2: Data Acquisition and High-Level Trigger. CMS trigger and data-acquisition project*. Technical Design Report CMS. CERN, Geneva, 2002.

[107] R. Patrick Kenny III and Michael Joseph Murray. *J/ψ photoproduction in ultra-peripheral PbPb collisions at* $\sqrt{s_{NN}}$ *= 2.76 TeV with CMS*. PhD thesis, Kansas U., 2014.

[108] S. Agostinelli et al. GEANT4: A Simulation toolkit. *Nucl. Instrum. Meth.*, A506:250–303, 2003.

[109] CMS Collaboration. Luminosity Calibration for the 2013 Proton-Lead and Proton-Proton Data Taking. 2014.

[110] K. A. Olive et al. Review of Particle Physics. *Chin. Phys.*, C38:090001, 2014.

[111] Morris E. Binkley et al. J/ψ Photoproduction from 60-GeV/c to 300-GeV/c. *Phys. Rev. Lett.*, 48:73, 1982.

[112] Morris E. Binkley et al. Psi-prime Photoproduction at a Mean Energy of 150-GeV. *Phys. Rev. Lett.*, 50:302, 1983.

[113] P. L. Frabetti et al. A Measurement of elastic J/ψ photoproduction cross-section at fermilab E687. *Phys. Lett.*, B316:197–206, 1993.

[114] Bruce H. Denby et al. Inelastic and Elastic Photoproduction of J/ψ (3097). *Phys. Rev. Lett.*, 52:795–798, 1984.

[115] C. Adloff et al. Diffractive photoproduction of ψ(2S) mesons at HERA. *Phys. Lett.*, B541:251–264, 2002.

[116] S. Aid et al. Elastic and inelastic photoproduction of J/ψ mesons at HERA. *Nucl. Phys.*, B472:3–31, 1996.

[117] Roel Aaij et al. Updated measurements of exclusive J/ψ and ψ(2S) production cross-sections in pp collisions at $\sqrt{s} = 7$ TeV. *J. Phys.*, G41:055002, 2014.

Appendix A

Crystal Ball Function

The Crystal Ball function is composition of a Gaussian of mean $\bar{m}$ and standard deviation σ_m and a power law tail towards lower mass with power n. Both functions are continuously joined at a point m_1. The Crystal Ball function (CB) is given by equation:

$$CB(m) = \begin{cases} e^{[\frac{-(\bar{m}-m)^2}{(2\sigma_m)^2}]} & ,m \geq m_1 \\ A[\frac{\sigma_m}{m^{'}-m)}]^n & ,m < m_1 \end{cases}$$

Where the parameters m_1, A and $m^{'}$ are :

$$m_1 = \bar{m} - \alpha\sigma_m$$

$$A = (\frac{n}{\alpha})^n e^{\frac{-\alpha^2}{2}}$$

$$m^{'} = \bar{m} + \sigma_m(\frac{n}{\alpha} - \alpha)$$

The CB function is determined by the 4 parameters mean $\bar{m}$ and width of the Gaussian standard deviation σ_m and tail parameters α and n. Figure A.1 shows the CB functions at specific mean and width with different tail parameters α and n.

In the fitting, the parameters mean $\bar{m}$ and standard deviation σ_m are left free, while the tail parameters α and n are fixed.

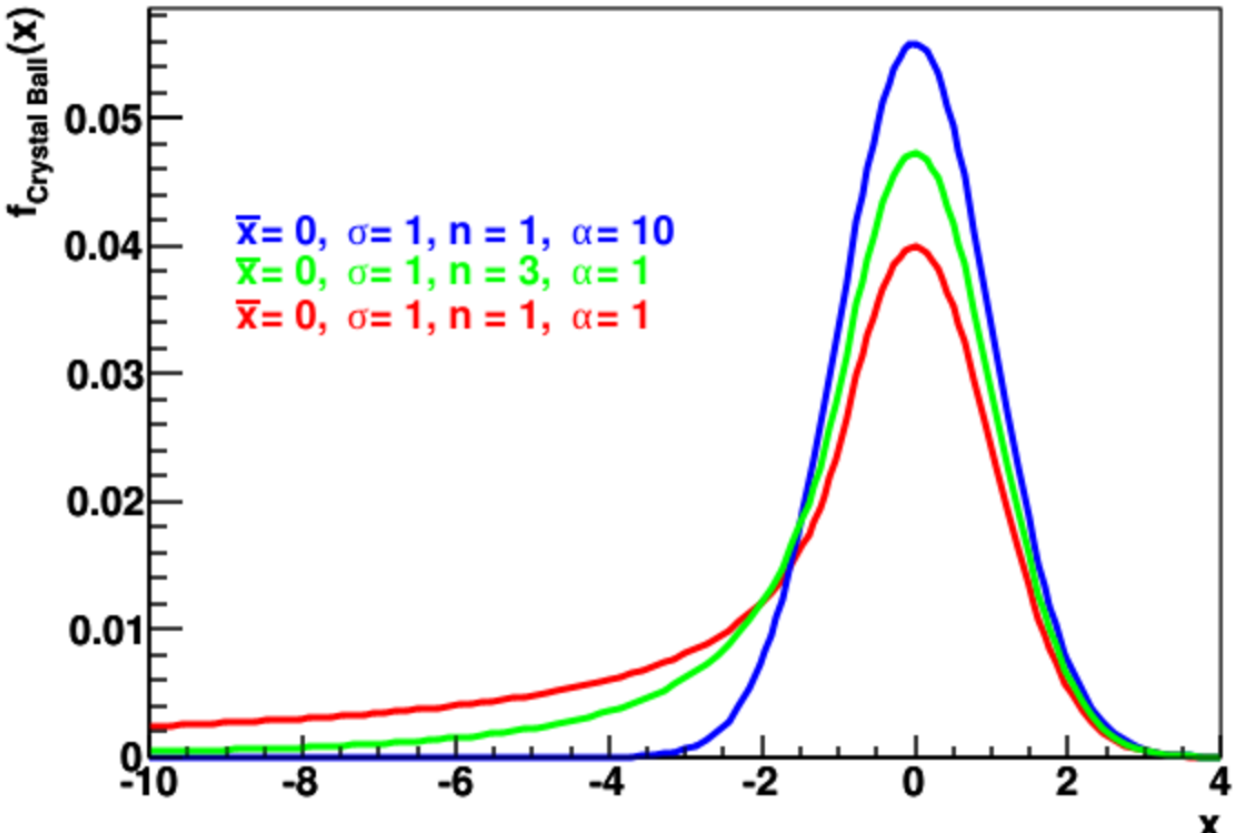

Figure A.1: the crystal ball functions at specific mean=0 and width =1 with different tail parameters, (blue) $\alpha = 10$ and $n = 1$, (green) $\alpha = 1$ and $n = 3$, (red) $\alpha = 1$ and $n = 1$ [55]